MEASUREMENT OF THE RMS PARITY VIOLATING MATRIX ELEMENT IN ^{239}U

by

Xianzhou (Joe) Zhu

Department of Physics
Duke University

Date: June 13, 1991

Approved:

N. Russell Roberson, Supervisor

William D. Walker

Lawrence E. Evans

John E. Thomas

Dissertation submitted in partial fulfillment of
the requirements for the degree of Doctor
of Philosophy in the Department of
Physics in the Graduate School
of Duke University

1991

ABSTRACT

(Physics-Nuclear)

MEASUREMENT OF THE RMS PARITY VIOLATING MATRIX ELEMENT IN ^{239}U

by

Xianzhou (Joe) Zhu

Department of Physics
Duke University

Date: June 13, 1991

Approved:

N. Russell Roberson, Supervisor

William D. Walker

Lawrence E. Evans

John E. Thomas

An abstract of a dissertation submitted in partial fulfillment of the requirements for the degree of doctor of philosphy in the Department of Physics in the Graduate School of Duke University

1991

ABSTRACT

We report the first determination of the Root-Mean-Square (RMS) parity violating matrix element in a compound nucleus (CN) system, ^{239}U. The experiment was performed using the intense pulsed epithermal neutron beam available at the Los Alamos Neutron Scattering Center (LANSCE). The helicity dependence of neutron transmission through a spin zero target (^{238}U) is measured for neutron energies from 6 eV to 300 eV. Parity violation is analyzed on 17 p-wave resonances among which five show 2σ or larger effects. The largest is a 7σ effect at the 63.5 eV resonance which shows a parity violating asymmetry of $p = 2.6\%$. A likelihood analysis is performed on these 17 parity violating asymmetries, and the RMS parity violating matrix element is determined for the first time to be $M = 0.59\ ^{+0.50}_{-0.25}$ meV which corresponds to a parity violating spreading width of $\Gamma^{PV} = \left(1.0\ ^{+1.7}_{-0.8}\right) \times 10^{-7}$ eV. Using statistical nuclear spectroscopy, we are able to relate M to the effective nucleon-nucleon (NN) interaction. The result is $|\alpha_p| \approx \left(4\ ^{+4}_{-2}\right) \times 10^{-7}$ where α_p is the ratio of the parity violating strength to the parity conserving strength in the effective NN interaction. This agrees qualitatively with the estimate of free NN interaction.

The consistency of the experimental measurement with expectation suggests that the manifestation of parity violating NN interaction in CN is understood. It is a challenging problem for the theorists to relate the RMS matrix element in the CN to the underlying NN interaction, therefore providing alternative ways to determine the Desplanques-Donoghue-Holstein (DDH) parameters of the NN interaction. The success of the parity violation study also validates the proposed experiment of studying the time reversal symmetry violation utilizing the large enhancement in the CN.

ACKNOWLEDGEMENTS

I am very grateful to the members of the TRIPLE collaboration: Dr. C. D. Bowman, Dr. J. D. Bowman, Miss J. E. Bush, Dr. P. P. J. Delheij, Dr. C. R. Gould, Dr. D. G. Haase, Dr. J. N. Knudson, Dr. G. E. Mitchell, Dr. S. I. Penttila, Dr. H. Postma, Dr. N. R. Roberson, Dr. S. J. Seestrom, Dr. J. J. Szymanski, Dr. B. Tippens, Dr. S. H. Yoo, Dr. V. Yuan and Mr. C. M. Frankle. They deserve my appreciation for making this experiment possible.

Special thanks goes to my thesis advisor Dr. N. R. Roberson for his help and guidance throughout my graduate career at TUNL. His patience in reading and revising the manuscripts of the thesis is greatly appreciated. Only with his assistance is it possible to turn the manuscripts into the present form.

I can not over-express my appreciation to Dr. J. D. Bowman. As a teacher, he is patient; as a friend, he is encouraging. I learned a lot from him, in both experimental skills and intelligent thinking. It has been a pure pleasure to work with him.

I thank Dr. C. R. Gould and Dr. G. E. Mitchell for interesting discussions in physics. I appreciate the help of Dr. E. G. Bilpuch, the director of TUNL, for providing the necessary travel fund.

The technical assistance of LAMPF personnel is greatly appreciated. I would like to thank Mr. R. N. Mortensen for his dedicated work on the cryostat, and Mr. Ron Richardson for his timely help in fixing the broken electronics modules.

I would like to acknowledge Miss Karen Mitchell for her help in forwarding my mails while I was running experiment at LANSCE.

Finally, I would like to thank my parents for their sacrifice, love and encouragement throughout my life. I am grateful to my friend, Dr. Saihong Fu, for her friendship and encouragement.

This work is supported by the United States Department of Energy.

ABBREVIATIONS

ADC	Analog-to-Digital Converter
CFC	Current-to-Frequency Converter
CN	Compound Nucleus
DAC	Digital-to-Analog Converter
DWELL	Time-Of-Flight Bin Width
FWHM	Full-Width-at-Half-Maximum
LAMPF	Los Alamos Meson Physics Facility
LANSCE	Los Alamos Neutron Scattering Center
LMN	Lanthanum Magnesium Nitrate
NMR	Nuclear Magnetic Resonance
NN	Nucleon-Nucleon
PMT	Photo-Multiplier-Tube
PSR	Proton Storage Ring
rf	radio frequency
RMS	Root-Mean-Square
TOF	Time-Of-Flight
TRIPLE	Time Reversal Invariance and Parity at Low Energies

Contents

List of Figures

List of Tables

Chapter 1

Introduction

1.1 The discovery of parity violation

One of the fundamental symmetries of nature is that of parity. It is connected with the physical invariance under the change from a right-handed coordinate system to a left-handed coordinate system. Under a parity operation, the space coordinates are reversed $\vec{r} \rightarrow -\vec{r}$, so parity operation is also called space inversion. Until 1956, parity was believed to be conserved in all physical processes.

By the mid-fifties, two particles, called τ^+ and θ^+, had been discovered with the following properties:

$$\begin{aligned} m_{\tau+} &\approx m_{\theta+} \\ \tau_{\tau+} &\approx \tau_{\theta+} \\ S_{\tau+} &= S_{\theta+} = 0 \end{aligned}$$

where m, τ and S are mass, lifetime and spin, respectively. On the other hand, they decayed as follows:

$$\begin{aligned} \theta^+ &\rightarrow \pi^+\pi^0 \\ \tau^+ &\rightarrow \pi^+\pi^+\pi^-. \end{aligned}$$

From the conservation of parity and angular momentum, one can determine the parity of τ^+ to be $-$ and the parity of θ^+ to be $+$ (The spin and parity of the pions are 0^-). How could two particles have the same physical properties but opposite parity ? Historically this was known as the "$\tau - \theta$ puzzle".

In their pioneering work on parity violation, Lee and Yang[Lee56] suggested a simple explanation: the τ^+ and the θ^+ are different decay modes of the same particle (K^+ as we know today), and parity is not conserved in weak interactions. Several experiments were proposed to test this hypothesis. The β-decay of polarized ^{60}Co was carried out by Wu et al. [Wu57], and a parity violating asymmetry was observed. Parity violation in the weak interaction was now established.

In the following year, Feynman and Gell-Mann predicted [Feyn58, Mars58], on the basis of their universal current-current theory of weak interactions, there should be a first order (and parity violating) weak interaction between two nucleons. It is then important to observe parity violation in the nucleon-nucleon (NN) interaction. Wilkinson[Wilk58] considered the experimental possibilities and suggested two groups of experiments. The first group of experiments involves searching for the violation of absolute selection rules, which is second order in α_p, the relative strength of parity violation in the NN interaction. The second group of experiments involves the interference of nuclear states of opposite parity and is first order in α_p. The second group of experiments measures the longitudinal analyzing power A_L, the γ-ray circular polarization P_γ, the γ-ray asymmetry A_γ, the neutron spin rotation ϕ, etc. The longitudinal analyzing power for reactions induced by polarized nucleons is defined as $A_L = 1/P_z[\sigma^+(\theta) - \sigma^-(\theta)]/[\sigma^+(\theta) + \sigma^-(\theta)]$, where P_z is the longitudinal polarization of the beam, and σ^+ and σ^- are cross sections for positive and negative helicity[1] projectiles, respectively. In other words, the longitudinal analyzing power A_L measures the $\vec{\sigma} \cdot \vec{k}$ dependence of the cross section, where $\vec{\sigma}$ is the nucleon spin and $\vec{k}$ is the nucleon momentum. The γ-ray circular polarization for the decay of

[1]helicity $\equiv \vec{\sigma} \cdot \hat{k}$, where $\vec{\sigma}$ is the nucleon spin and $\hat{k}$ is the direction of the nucleon momentum

unpolarized nuclei is defined as $P_\gamma = \langle \vec{\sigma_\gamma} \cdot \hat{k_\gamma} \rangle$, where $\vec{\sigma_\gamma}$ and $\hat{k_\gamma}$ are the directions of the spin and momentum of the γ-ray, respectively. The γ-ray asymmetry A_γ is defined for the decay of polarized nuclei. Consider a polarized nucleus produced by capturing a polarized thermal neutron on an unpolarized target, the asymmetry A_γ is defined as

$$W(\theta) = \text{const}\,(1 + f_n A_\gamma \cos\theta)$$

where $W(\theta)$ is the angular distribution of the capture γ's, f_n the neutron polarization, and θ the angle between the direction of neutron beam polarization and the direction of the γ-ray momentum. In other words, A_γ measures the $\vec{I} \cdot \vec{k_\gamma}$ dependence of the γ-ray angular distribution, where $\vec{I}$ is the target spin and $\vec{k_\gamma}$ is the γ-ray momentum. Since the angular momentum is P-even ($\vec{\sigma} \to \vec{\sigma}$, $\vec{I} \to \vec{I}$ under parity) and the linear momentum is P-odd ($\vec{k} \to -\vec{k}$ under parity), the quantity $\vec{\sigma} \cdot \vec{k}$ (and $\vec{\sigma_\gamma} \cdot \hat{k_\gamma}$, $\vec{I} \cdot \vec{k_\gamma}$) is P-odd. The detection of such terms indicates that parity is violated in the process.

1.2 Parity violation in light nuclei

The weak interaction Hamiltonian can be divided into three parts: pure leptonic, semi-leptonic and non-leptonic (p. 7, [Blin73]). The semi- and non-leptonic interactions can be further divided into strangeness conserving ($\Delta S = 0$) and strangeness non-conserving ($\Delta S = \pm 1$) parts. Effects generated by the $\Delta S = 0$ non-leptonic interaction are virtually impossible to observe in elementary particle processes since they form only a small ($\leq 10^{-6}$) background to the overwhelming strong interaction processes. As a result, this term can only be studied in nuclear processes. The parity violating NN potential has been parameterized by Desplanques, Donoghue and Holstein [Desp80] in terms of the parity violating coupling constants for pseudoscaler (π) and vector (ρ, ω) meson exchanges.

The study of parity violation with few nucleon and light nuclei systems is to experimentally determine the DDH parameters. In these systems, the nuclear structure is

relatively simple, and reliable calculations can be made to relate the observed effects to the underlying NN interaction ([Adel85]).

In the p-p system, Nagle et al. [Nagl79] obtained $A_L = (-1.7 \pm 0.8)10^{-7}$ at $E_p = 15$ MeV, and Balzer et al. [Balz84] observed $A_L = (-2.31 \pm 0.89)10^{-7}$ at $E_p = 45$ MeV. In the n-p system, thermal neutron capture on proton target has been performed. Knyazkov et al. [Knya84] observed $P_\gamma = (1.8 \pm 1.8)10^{-7}$, and Caviagnac et al. obtained $A_\gamma = (0.6 \pm 2.1)10^{-7}$. Experiments have been carried out on few-nucleon systems as well ([Adel85]). In general, these are very hard experiments because of the tiny asymmetries involved, and are difficult to improve.

Beyond the few-body systems, the calculation becomes very complicated. But for certain carefully chosen levels in light nuclei, good shell-model calculations are possible. The parity-mixed doublets in light nuclei (^{18}F, ^{19}F, and ^{21}Ne) have been studied. The two levels in these doublets are closely spaced, and are far from other levels except the ground state. Therefore, the perturbation calculation can be greatly simplified by using the two level approximation for parity mixing. The small spacing of the doublets and large amplification factor ([Adel85]) combine to give parity violating effects roughly 10^2-10^4 times larger than those in NN and few-nucleon systems, i. e. between 10^{-3} and 10^{-5}. These make the experiments more accessible. The circular polarization of the 1081 keV γ-transition of ^{18}F has been measured by Barnes et al. [Barn78], Bizetti et al. [Bize80], and Ahrens et al. [Ahre82], and the average value is $P_\gamma(1081\text{keV}) = (8 \pm 39)10^{-5}$ ([Adel85]). The asymmetry of the 110 keV γ-transition of ^{19}F has been measured by Adelberger et al. [Adel83] and Elsener et al. [Else84]. The average is $A_\gamma(110\text{keV}) = (-7.4 \pm 1.9)10^{-5}$. The circular polarization of the 2789 keV γ-transition of ^{21}Ne has been measured by Snover et al. [Snov78, Earl83] to be $P_\gamma(2789\text{keV}) = (80 \pm 140)10^{-5}$. From these measurements, Adelberger and Haxton [Adel85] were able to determine the DDH parameters. The π-exchange coefficient is smaller than expected and possibly zero, and parameter h_ρ^0 is non-zero, $\sim (2-3)10^{-6}$.

This determination is nevertheless not conclusive and more and better experiments are needed to improve it. The study of parity violation in light nuclei is limited by the number of cases available and these experiments are also very difficult to improve.

1.3 Parity violation in heavy nuclei

The primary interest of studying parity violation in heavy nuclei is in finding alternative ways of determining the DDH parameters. Because of large enhancements (see chapter 2), the parity violating effects in heavy nuclei are typically in the range of 10^{-3} to 10^{-1}, and are much easier to be observed.

Historically, the first successful observation of parity violation in the nucleon-nucleus interaction was made in 1964 by Abov et al. at ITEP[2] [Abov64, Abov73]. The γ-asymmetry of thermal neutron capture on ^{113}Cd was measured to be $A_\gamma = -(4.1 \pm 0.8)10^{-4}$. This result was confirmed by Danilyan et al. [Dani76]. Alberi et al. [Albe72] measured $P_\gamma = (6.0 \pm 1.5)10^{-4}$ for neutron capture on a ^{113}Cd. For neutron capture on ^{117}Sn, Danilyan et al. [Dani76] at ITEP measured $A_\gamma = (8.1 \pm 1.3)10^{-4}$ and Benkoula et al. [Ben77] at ILL[3] measured $A_\gamma = (4.4 \pm 0.6)10^{-4}$. The difference in the two measurements was never explained. All these experiments were done with thermal neutrons. The idea of these experiments is essentially the same as in those with few-nucleon and light nuclei systems, and the observed parity violating effects are also comparable.

Another approach of studying parity violation in NN interaction is the neutron optics. In 1964, Michel [Mich64] showed that, as a transversely polarized neutron beam passes through a substance, the rotation of neutron spin around its momentum can be detected. Later Stodolsky[Stod74] noticed another effect: the buildup of longitudinal polarization as an initially unpolarized neutron beam passes through a

[2]ITEP: Institute of Theoretical and Experimental Physics (Moscow, USSR)

[3]ILL: Institut Laue-Langevin (Grenoble, France)

medium. These effects are very small in pure form. In 1976, Forte [Fort76] observed that these effects may be enhanced in the vicinity of the one-particle p-wave resonance, and proposed an experiment to measure the angle of neutron spin rotation through a ^{124}Sn specimen. As a surprise, they did not find any parity violation in ^{124}Sn, but observed a parity violation in the control experiment which was traced to the ^{117}Sn nuclei in the target [Fort80]. The spin rotation for ^{117}Sn was found to be $\phi = -(3.67 \pm 0.27)10^{-5}$ rad/cm. Shortly thereafter, Kolomensky et al. [Kolo81] at Leningrad measured the helicity dependence of the total cross sections and radiative capture cross sections of polarized thermal neutrons on ^{117}Sn and ^{139}La targets. In this work, it was established that the parity violating effects were associated with the compound nuclear states.

The next generation of experiments uses neutrons with energies in the few eV region and measures the helicity dependence of the total cross sections of p-wave resonances. In this case, the parity violating asymmetry is defined as $p = (\sigma^+ - \sigma^-)/(\sigma^+ + \sigma^-)$, where σ^+ and σ^- are the resonance cross sections for positive and negative helicity neutrons, respectively. Alfimenkov et al. [Alfi82] conducted experiments on four target nuclei: ^{81}Br, ^{111}Cd, ^{117}Sn, and ^{139}La. The observed parity violating asymmetries are about four orders of magnitude greater than those seen in the thermal experiments. The largest occurs at the 0.7 eV p-wave resonance of ^{139}La which is about 10%. The large asymmetry was reproduced by Masuda et al. [Masu89], Bowman et al. [Bowm89], and Yuan et al. [Yuan91]. A summary of the experimental results with heavy nuclei is given in Table 1.1. The large effects were first explained by Sushkov and Flambaum [Sush80]. These authors used a model in which the parity violating effect is due to the parity mixing of a s-wave resonance and a nearby p-wave resonance in the compound nucleus (CN). The parity violation was predicted to be considerably enhanced. Sushkov and Flambaum noticed that in some cases, the effects could be as large as 10%.

Table 1.1: Parity violation in heavy nuclei †

Compound Nucleus	A_γ(thermal) (10^{-6})	$\Delta\phi$(thermal) (10^{-6} rad/cm)	A_L(thermal) (10^{-6})	p(resonance) (10^{-6})
^{82}Br	-19.5 ± 1.6		9.8 ± 1.0	24000 ± 4000
			9.5 ± 1.7	
^{112}Cd				-8600 ± 1200
^{114}Cd	-410 ± 80			
	-500 ± 120			
^{118}Sn	810 ± 130	-37 ± 2.5	6.2 ± 0.7	4500 ± 1300
	440 ± 60		11.2 ± 2.6	
^{140}La	-17.8 ± 2.2	-219 ± 29	9.0 ± 1.4	97000 ± 5000‡

† These values were taken from [Krup87], pp. 82, 123, 127.

‡ This value was taken from [Masu89].

1.4 Advance of physics by this experiment

Previous data on the helicity dependence of the neutron-nucleus cross sections was limited in several respects: (i) parity violation was observed for at most one resonance per nuclei; (ii) all observed effects were for neutrons with energy < 10 eV; (iii) All observed effects were for targets with spin I$\neq$0. These severely limit our understanding of parity violation in the compound nucleus, as will be discussed below.

Because parity violation was observed for only one p-wave resonance per nucleus, one can extract at most one parity violating matrix element for each nucleus. As Weidenmüller [Weid88,Weid89] pointed out, the compound nucleus is a chaotic system, and the individual parity violating matrix element carries very little information beyond the fact that parity violation is observed. The important quantity in the CN is the variance of the parity violating matrix elements.

Since parity violation was observed only for neutron energy less than 10 eV, one

may suspect that parity violation in compound nucleus is a threshold effect.

For targets with spin $I \neq 0$, one can not reliably determine the parity violating matrix element without the knowledge of the j-spin mixing ratio [Goul90]. The j-spin mixing ratios are difficult to obtain and are not available for most compound nuclear levels. In the absence of the j-spin mixing ratio, the best one can do is to determine an upper limit of the parity violating matrix element which is not very useful [Alfi84].

All of these obstacles are removed in this experiment. (i) A zero spin target, ^{238}U, is studied, so we are free of the j-spin mixing ratio problem. (ii) Our measurements take advantage of the intense epithermal neutron flux available at the Los Alamos Neutron Scattering Center (LANSCE), and we can study many p-wave resonances simultaneously. (iii) We have developed techniques which allow us to extract the parity violating root-mean-square (RMS) matrix element. And (iv), the RMS matrix element can be related to α_p, the ratio of the parity violating part of the effective NN interaction to the parity conserving part. For the first time, useful information can be extracted from heavy nuclei in a rather model independent manner.

The remaining of the thesis will be organized as follows: chapter 2 explains the theory, chapter 3 the experimental details; chapters 4 and 5 the extraction of the parity violating asymmetries. Chapter 6 determines the parity violating RMS matrix element, and relates it to the effective NN interaction; and chapter 7 concludes this work.

Chapter 2

Theory

2.1 Introduction

Consider the scattering of an epithermal neutron (0.1 eV − 1 keV) from a ^{238}U target nucleus. The scattering takes place through the CN mechanism (p. 340, [Blat54]) which proceeds in two steps: first the incident neutron is captured by the target nucleus to form a compound nucleus; then the compound nucleus decays into the final states, as shown below

$$\begin{aligned} & & n + ^{238}U \\ n + ^{238}U \rightarrow ^{239}U^* \rightarrow & & \gamma + ^{239}U \\ & & \vdots \end{aligned}$$

For direct reactions, the reaction time can be estimated as the time for the projectile to pass through the target nucleus. For a 10 eV neutron, the interaction time is approximately

$$\begin{aligned} t &= \frac{2R}{v} \equiv \frac{R}{c}\sqrt{\frac{2m_nc^2}{E_n}} \\ &\sim 5 \times 10^{-19}\ \text{s} \end{aligned}$$

where we have used $R = 10$ fm as a typical radius for heavy nuclei, c=3 $\times$ 10^8 m/s, and m_nc^2=940MeV.

In the CN reactions, the reaction time can be estimated from the resonance width as, using the uncertainty principle,

$$\Delta t \sim \frac{\hbar}{\Gamma} \sim 10^{-14} \text{ s}$$

where we have used $\hbar = 6.58 \times 10^{-16}$ eV·s and Γ=50 meV, the typical width of s-wave resonances of ^{238}U. Therefore in the CN reactions, neutrons spend several orders of magnitude more time interacting with the nucleons in the target nucleus. The parity violating NN interaction can be greatly enhanced in this process, as we will see later in the chapter.

The total cross section of neutrons on a ^{238}U target is shown in Figure 2.1. One observes that the total cross section consists of resonance scattering cross section and potential scattering cross section. The potential scattering cross section changes slowly with neutron energy, and the resonance cross section changes very rapidly with neutron energy. The total cross section can then be written as

$$\sigma_{total} = \sigma_{potential} + \sigma_{resonance} + \sigma_{interference}$$

where $\sigma_{potential}$ is the potential scattering cross section, and $\sigma_{resonance}$ is the resonance scattering cross section, and $\sigma_{interference}$ is the interference between the potential scattering and the resonance scattering.

In the scattering of a neutron from a nucleus, the contributing orbital angular momentum can be estimated as

$$l_{max}\hbar = m_n v R = \sqrt{2 m_n E_n} R$$

where l_{max} is the maximum orbital angular momentum, m_n, v and E_n are the neutron mass, speed and kinetic energy, respectively. If $E_n = 500$eV, $R \approx 10$fm, One finds

$$l_{max} \approx 0.05.$$

Therefore, one expects $l = 0$ to be the dominant orbital angular momentum, with some contribution from $l = 1$. A resonance with $l = 0$ is called a s-wave resonance,

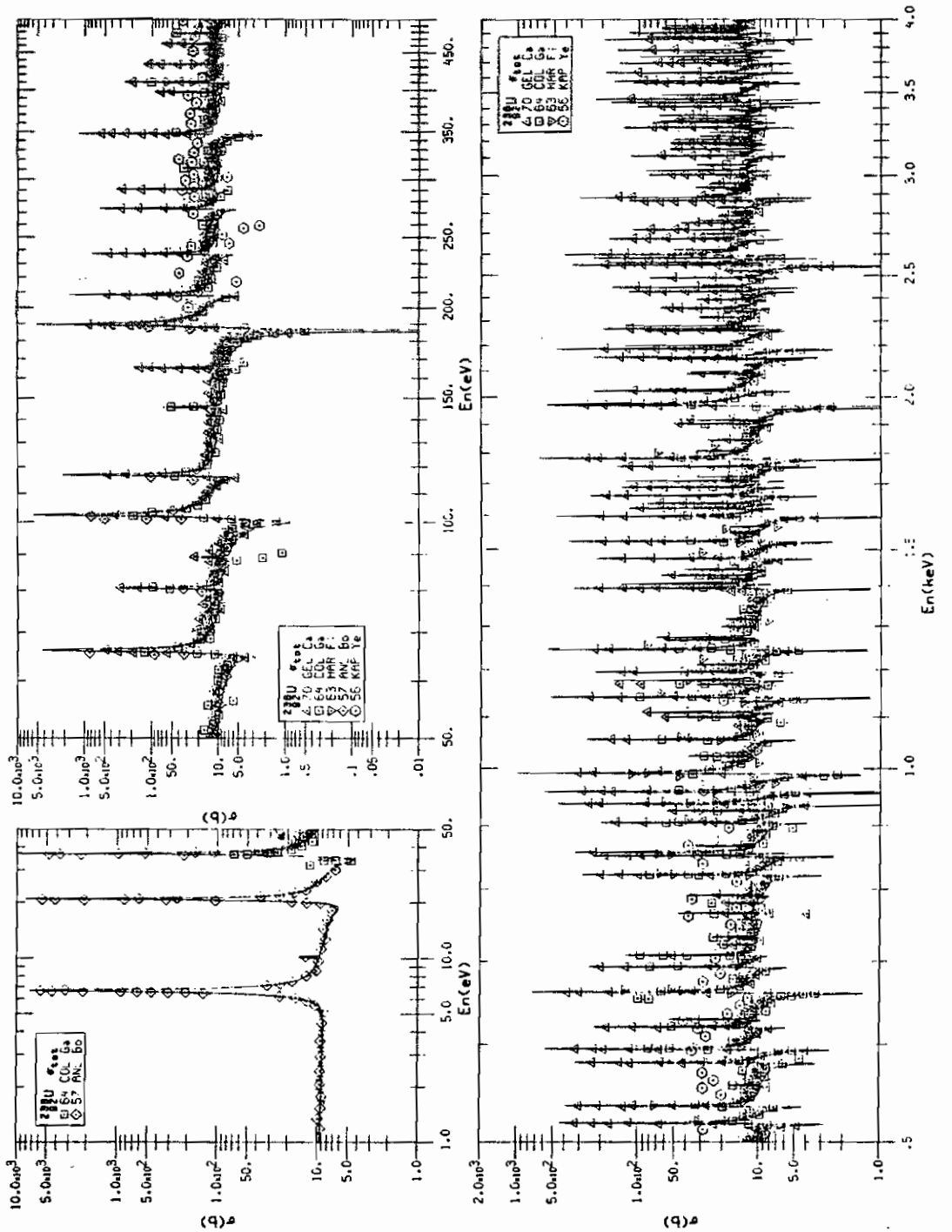

Figure 2.1: The total cross section of neutron on ^{238}U (taken from [Garb73])

while a resonance with $l = 1$ is called a p-wave resonance. For p-wave resonances, the interference term is small, and can be neglected.

In the presence of a parity violating interaction, the total cross section may depend on neutron helicity. As we will see later in the chapter, parity violation is greatly enhanced in the resonance cross sections. We introduce the parity violating asymmetry p for a p-wave resonance as

$$\sigma^{\pm} \equiv \sigma_p(1 \pm f_n p) \tag{2.1}$$

where $\sigma^{\pm}$ is the resonance cross sections for positive and negative helicity neutrons, respectively, σ_p is the p-wave resonance cross section for unpolarized neutrons, and f_n is the neutron polarization.

The analytical form of p and its relationship to the underlying parity violating matrix elements are the subjects of the following discussions.

2.2 Mixing of a p-wave resonance with one s-wave resonance: the enhancements

The parity violation at a p-wave resonance can be explained by the mixing of the p-wave resonance with nearby s-wave resonances which have opposite parity. For a target of spin 0, the total angular momentum is

$$\vec{J} = \vec{l} + \vec{s}$$

where $\vec{l}$ and $\vec{s}$ are the neutron orbital angular momentum and spin, respectively. For a s-wave resonance ($l = 0$), we have

$$J = \frac{1}{2};$$

while for a p-wave resonance($l = 1$), we get

$$J = \frac{1}{2}, \frac{3}{2}.$$

From the rotational invariance, the total angular momentum of the resonances has to be the same in order to mix. Therefore, only p-wave resonances with $J = \frac{1}{2}$ can mix with the s-wave resonances. The $J = \frac{3}{2}$ p-wave resonances do not mix with s-wave resonances, therefore do not show parity violation.

In the simplest case, let us assume that there is only one p-wave resonance and one s-wave resonance, each with $J = \frac{1}{2}$, in the CN. The Hamiltonian can be written as

$$H = H_0 + H_w$$

where H_0 is the parity conserving Hamiltonian and H_w is the small parity violating part. The parity violating H_w introduces mixing between the s- and p-wave resonances. If ψ_s and ψ_p are the unperturbed wavefunctions of the s- and p-wave resonances, respectively, the wavefunctions of the mixed states are, using the first order perturbation theory

$$\psi_s^{'} = \psi_s + \frac{V_{sp}}{E_s - E_p}\psi_p$$

$$\psi_p^{'} = -\frac{V_{sp}}{E_s - E_p}\psi_s + \psi_p$$

where $V_{sp} = \langle\psi_s|H_w|\psi_p\rangle$, and E_s, E_p are the energies of the s- and p-wave resonances, respectively.

The parity violating asymmetry has been worked out by many authors [Sush80, Alfi84, Vanh88, Goul90] using the two level mixing model. For a p-wave resonance, the resonance cross section can be written as

$$\sigma^{\pm} = \sigma_p \pm f_n \sigma_{PNC} \tag{2.2}$$

where $\pm$ denotes the helicities of the neutrons. Comparing equation (2.2) with equation (2.1), one finds

$$p = \frac{\sigma_{PNC}}{\sigma_p}.$$

For a spin 0 target such as ^{238}U, we have [Goul90]

$$\sigma_{PNC} = 2\pi\lambda^2 V_{sp}\sqrt{\Gamma_s^n \Gamma_p^n}\frac{(\Delta E_s \Gamma_p + \Delta E_p \Gamma_s)}{[S]^2[P]^2},$$

where

$$\begin{aligned} \Delta E_{s,p} &\equiv E_{s,p} - E \\ [S,P]^2 &\equiv \Delta E_{s,p}^2 + \frac{1}{4}\Gamma_{s,p}^2 \end{aligned}$$

and E is the kinetic energy of the neutron-nucleus pair in the center of mass system, Γ_s^n and Γ_p^n are the neutron widths, Γ_s and Γ_p are the total widths, and λ is the de Broglie length. At the p-wave resonance, where $E = E_p$ and $\Delta E_p = 0$, the parity violating asymmetry can be shown to be

$$p = 2V_{sp}\frac{E_s - E_p}{(E_s - E_p)^2 + \frac{1}{4}\Gamma_p^2}\sqrt{\frac{\Gamma_s^n}{\Gamma_p^n}} \tag{2.3}$$

$$\cong \frac{2V_{sp}}{E_s - E_p}\sqrt{\frac{\Gamma_s^n(E_p)}{\Gamma_p^n(E_p)}} \tag{2.4}$$

where we have used for the p-wave resonance cross section

$$\sigma_p = \pi\lambda^2\frac{\Gamma_p^n\Gamma_p}{[P]^2}. \tag{2.5}$$

Since Γ_p ($\ll 50$ meV in ^{238}U) is much smaller than the typical level spacing (~ 10 eV), the Γ_p^2 in the denominator of equation (2.3) can be dropped to obtain equation (2.4). The energy dependence of the s-wave neutron width is ([Hale89])

$$\Gamma_s^n(E) = \Gamma_s^n(E_s)\sqrt{\frac{E}{|E_s|}}.$$

The parity violating cross section σ_{PNC} at the peak of the s-wave resonance is about the same as at the peak of the p-wave resonance. Because the typical s-wave resonance cross section is of the order of a few hundred to a few thousand barns, and the typical p-wave resonance cross section is a few barns, the parity violating asymmetry at the s-wave resonance is several orders of magnitude smaller than at the p-wave resonance.

(1) Dynamic Enhancement

The ratio

$$\frac{V_{sp}}{E_s - E_p}$$

in equation (2.4) exhibits what has been called dynamic enhancement. This refers to an enhancement in its value over what is expected on the basis of single particle estimates.

Following Sushkov [Sush82], the wavefunction of any state in a compound nucleus may be expanded using the shell-model basis as

$$\psi = \sum_{i=1}^{N} a_i \phi_i$$

where ϕ_i corresponds to certain particle-hole excitations. The typical number of terms in the sum is determined by the strength of the residual internucleon interaction. If ΔE is the scale of this interaction, and D is the distance between levels of the compound nucleus, then the number of terms in the sum is $N \sim \Delta E/D$. In heavy nucleus, $D \approx 10\text{eV}$, and the typical value for ΔE is $\sim$1MeV, the distance between shell model states. Therefore we have $N \sim 10^5$. Because of the strong mixing, one expects the coefficients a_i to be of the same magnitude. By virtue of the normalization condition, we can write

$$|a_i| \sim \frac{1}{\sqrt{N}}.$$

We now turn back to the matrix element

$$\begin{aligned} V_{sp} &= \langle \psi_s | H_w | \psi_p \rangle \\ &= \langle \sum_i a_i \phi_i | H_w | \sum_k b_k \phi_k \rangle \\ &= \sum_{i,k} a_i^* b_k \langle i | H_w | k \rangle. \end{aligned} \tag{2.6}$$

For each fixed value of i, the matrix element is nonzero for only a few values of k, for which ϕ_i differs from ϕ_k by the state of a single particle. It is natural to assume that the signs of the individual terms in equation (2.6) occur at random. We thus have in equation (2.6) an incoherent sum of $\sim N$ terms each of the order of $\frac{\langle H_w \rangle}{N}$.

In general, for the incoherent sum of N terms, α_i, of equal magnitude but random sign

$$y = \sum_{i=1}^{N} \alpha_i,$$

the expectation value of y^2 is

$$\begin{aligned} \langle y^2 \rangle &= \sum_{i,i'} \langle \alpha_i \alpha_{i'} \rangle \\ &= \sum_{i} \langle \alpha_i^2 \rangle \\ &= N \langle \alpha^2 \rangle \end{aligned}$$

where $\langle \alpha^2 \rangle$ is the magnitude of $\langle \alpha_i^2 \rangle$. Therefore, the magnitude of the matrix element is

$$V_{sp} \sim \sqrt{N \left(\frac{\langle H_w \rangle}{N} \right)^2} \sim \langle H_w \rangle \frac{1}{\sqrt{N}}$$

where $\langle H_w \rangle$ is the magnitude of the matrix elements between shell model states. Recalling $N \sim \Delta E/D$, we have

$$\frac{V_{sp}}{E_s - E_p} \sim \frac{V_{sp}}{D} \sim \frac{\langle H_w \rangle}{\Delta E} \sqrt{N} = F\sqrt{N}$$

where F is the typical mixing of single particle states. In other words, the dynamic enhancement is approximately $\sqrt{N} \approx 3 \times 10^2$.

(2) Kinematic Enhancement

An additional enhancement, referred to as kinematic enhancement, comes from the term

$$\sqrt{\frac{\Gamma_s^n}{\Gamma_p^n}}.$$

The neutron widths of the s- and p-wave resonances can be expressed as (pp. 361,390, [Blat54])

$$\begin{aligned} \Gamma_s^n &\propto kR \\ \Gamma_p^n &\propto (kR)^3 \end{aligned}$$

where $\hbar k$ is the neutron momentum, and R is the radius of ^{238}U nucleus. Therefore

$$\sqrt{\frac{\Gamma_s^n}{\Gamma_p^n}} \sim \frac{1}{kR}.$$

For a 1 eV neutron, we have $k \sim 2.2 \times 10^{-4}$ fm^{-1}; for heavy nuclei, we have $R \sim 10$fm. Therefore, the kinematic enhancement is $\sim 1/kR \sim 5 \times 10^2$.

Combining the dynamic enhancement and the kinematic enhancement together, the over all enhancement can be as large as 10^5.

2.3 Mixing of a p-wave resonance with many s-wave resonances: the M^2

If there is only one s-wave resonance near the p-wave resonance, the parity violating asymmetry at the p-wave resonance is given by equation (2.4). If we label the p-wave resonance with index i and the s-wave resonance with index j, equation (2.4) can be rewritten as

$$p_i = A_{ij} V_{ij}$$

where $V_{ij} = \langle \psi_{s,j} | H_w | \psi_{p,i} \rangle$ is the parity violating matrix element, and

$$A_{ij} = \frac{2}{E_{s,j} - E_{p,i}} \sqrt{\frac{\Gamma_{s,j}^n(E_{p,i})}{\Gamma_{p,i}^n(E_{p,i})}}$$

is a constant depending on the resonance parameters.

For the compound nucleus formed by a neutron and a ^{238}U nucleus, there are many s-wave resonances in the system, as seen in Figure 2.1. In principle, all the s-wave resonances can mix with the p-wave resonance and contribute to the parity violation at the p-wave resonance. Therefore the parity violating asymmetry at the p-wave resonance should sum over the contributions from all the s-wave resonances as

$$p_i = \sum_j A_{ij} V_{ij}. \tag{2.7}$$

Our experiment measures the parity violating asymmetries, p_i, at the p-wave resonances. For convenience in data analysis, we introduce a new quantity Q_i as

$$Q_i = \frac{p_i}{A_i} = \sum_j B_{ij} V_{ij} \tag{2.8}$$

where

$$\begin{aligned} A_i &= \sqrt{\sum_j A_{ij}^2} \\ B_{ij} &= \frac{A_{ij}}{A_i}. \end{aligned}$$

As seen from equation (2.7), for each p_i measured, there are N_s new matrix elements, where N_s is the number of s-wave resonances in the system. It is impossible to determine the individual matrix elements. Instead, we can measure M, the RMS value of the matrix elements. To obtain M, we need to relate it to the statistical properties of the experimental observable p_i's (or Q_i's).

First we need to prove a theorem which states that(p. 59, [Eadi71])

Theorem 1 *if x_j, $j = 1, 2, \ldots, N$, are Gaussian distributed random variables with mean and variance*

$$\begin{aligned} \langle x_j \rangle &= \mu_j \\ \langle (x_j - \langle x_j \rangle)^2 \rangle &= \sigma_j^2, \end{aligned}$$

then the linear combination of the x_j's

$$X = \sum_{j=1}^{N} b_j x_j$$

is also a Gaussian distributed random variable, with mean and variance

$$\langle X \rangle = \sum_{j=1}^{N} b_j \mu_j \tag{2.9}$$

$$\langle (X - \langle X \rangle)^2 \rangle = \sum_{j=1}^{N} b_j^2 \sigma_j^2. \tag{2.10}$$

The proof of the theorem is conveniently done through the characteristic functions (p. 29, [Eadi71]). If x_j is a random variable with a probability density function $f(x_j)$, the characteristic function $\phi_{x_j}(t)$ is defined as the expectation value of e^{itx_j}

$$\begin{aligned}\phi_{x_j}(t) &= \langle \exp(itx_j) \rangle \qquad\qquad t \text{ real} \\ &= \int_{-\infty}^{+\infty} \exp(itx_j) f(x_j)\, dx_j.\end{aligned}$$

In other words, the characteristic function $\phi_{x_j}(t)$ is the Fourier transform of the probability function. For a Gaussian distribution with mean μ_j and variance σ_j^2, the probability density function is

$$f(x_j) = \frac{1}{\sqrt{2\pi}\sigma_j} \exp\left[-\frac{(x_j-\mu_j)^2}{2\sigma_j^2}\right],$$

and the characteristic function can be evaluated as

$$\begin{aligned}\phi_{x_j}(t) &= \int_{-\infty}^{+\infty} \exp(itx_j) \frac{1}{\sqrt{2\pi}\sigma_j} \exp\left[-\frac{(x_j-\mu_j)^2}{2\sigma_j^2}\right] dx_j \\ &= \exp(it\mu_j) \int_{-\infty}^{+\infty} \exp(ity) \frac{1}{\sqrt{2\pi}\sigma_j} \exp\left[-\frac{y^2}{2\sigma_j^2}\right] dy \\ &= \frac{1}{\sqrt{\pi}} \exp(it\mu_j) \int_{-\infty}^{+\infty} \exp(it\sqrt{2}\sigma_j z) \exp\left[-z^2\right] dz \\ &= \frac{1}{\sqrt{\pi}} \exp(it\mu_j) \int_{-\infty}^{+\infty} e^{-z^2} \left[\cos(\sqrt{2}\sigma_j tz) + i\sin(\sqrt{2}\sigma_j tz)\right] dz \\ &= \frac{1}{\sqrt{\pi}} \exp(it\mu_j) \int_{-\infty}^{+\infty} \exp\left[-z^2\right] \cos(\sqrt{2}\sigma_j tz)\, dz \\ &= \exp[it\mu_j - \frac{1}{2}t^2\sigma_j^2]. \qquad (2.11)\end{aligned}$$

Now we can calculate the characteristic function for variable $y = bx_j$ as

$$\begin{aligned}\phi_y(t) &= \langle \exp(ity) \rangle \\ &= \langle \exp(itbx_j) \rangle \\ &= \int_{-\infty}^{+\infty} \exp(itbx_j) \frac{1}{\sqrt{2\pi}\sigma_j} \exp\left[-\frac{(x_j-\mu_j)^2}{2\sigma_j^2}\right] dx_j \\ &= \phi_{x_j}(bt) \\ &= \exp[itb\mu_j - \frac{1}{2}t^2b^2\sigma_j^2],\end{aligned}$$

and the characteristic function for $X = \sum_{j=1}^{N} b_j x_j$ as

$$\begin{aligned}
\phi_X(t) &= \langle \exp(itX) \rangle \qquad (2.12)\\
&= \left\langle \exp\left(it \sum_{j=1}^{N} b_j x_j \right) \right\rangle \\
&= \left\langle \prod_{j=1}^{N} \exp\left(itb_j x_j\right) \right\rangle \\
&= \prod_{j=1}^{N} \langle \exp\left(itb_j x_j\right) \rangle \\
&= \prod_{j=1}^{N} \exp(itb_j\mu_j - \frac{1}{2}t^2 b_j^2 \sigma_j^2) \\
&= \exp\left(it \sum_{j=1}^{N} b_j\mu_j - \frac{1}{2}t^2 \sum_{j=1}^{N} b_j^2\sigma_j^2 \right). \qquad (2.13)
\end{aligned}$$

Comparing equation (2.13) with equation (2.11), we see that X is indeed a Gaussian distributed variable with mean and variance given by equations (2.9) and (2.10).

Now let us apply the theorem to the variable Q_i. Because of the chaotic nature of the compound nucleus, we can assume that the parity violating matrix elements V_{ij} are Gaussian distributed random variables with mean 0 and variance M^2

$$\begin{aligned}
\langle V_{ij} \rangle &= 0 \\
\langle V_{ij}^2 \rangle &= M^2.
\end{aligned}$$

By virtue of the theorem, one can see that the quantity Q_i, which is a linear combination of the V_{ij}'s, is also a Gaussian distributed random variable with mean 0 and variance M^2

$$\langle Q_i \rangle = 0 \qquad (2.14)$$

$$\langle Q_i^2 \rangle = M^2 \qquad (2.15)$$

where we have used the normalization property of the B_{ij}'s

$$\sum_j B_{ij}^2 = \sum_j \frac{A_{ij}^2}{A_i^2} = 1.$$

We will further discuss the extraction of M from the experimental p_i's in chapter 6.

We can relate M to the properties of the NN interaction by defining the parity violating spreading width

$$\Gamma^{PV} \equiv 2\pi \frac{M^2}{D} \tag{2.16}$$

where D is the level spacing. From the discussion on enhancement, the matrix element squared is proportional to the level spacing. Therefore one expects that Γ^{PV} is essentially independent of the atomic mass of the compound nucleus.

With the methods of statistical nuclear spectroscopy, French et al. [Fren88, Fren89] have established for time reversal invariance the connection between the symmetry breaking in CN and the symmetry breaking in the effective NN interaction

$$\Gamma^{TRV} \approx 2\pi 10^5 (\text{eV})\, \alpha_T^2 \tag{2.17}$$

where Γ^{TRV} is the time reversal invariance violating spreading width, and α_T is the ratio of the time reversal invariance violating strength to the time reversal invariance conserving strength in the effective NN interaction.

Equation (2.17) has a simple intuitive interpretation (Weid89]). For a symmetry-breaking NN interaction, the ratio of the symmetry-breaking spreading width (Γ^{SB}) to the strong interaction spreading width (Γ_{strong}) is approximately α^2, α being the ratio of the symmetry-breaking strength to the symmetry-conserving strength in the effective NN interaction

$$\Gamma^{SB}/\Gamma_{strong} \approx \alpha^2. \tag{2.18}$$

The strong interaction spreading width is roughly 1 MeV, as evidenced by the spreading widths of E1 giant resonances. Taking $\Gamma_{strong} = 2\pi 10^5$ eV, equation (2.18) can be written as

$$\Gamma^{SB} \approx 2\pi 10^5 (\text{eV})\, \alpha^2,$$

which holds for any symmetry breaking. For parity violation, we can write

$$\Gamma^{PV} \approx 2\pi 10^5 (\text{eV})\, \alpha_p^2, \tag{2.19}$$

where α_p is the ratio of the parity violating strength to the parity conserving strength in the effective NN interaction.

Therefore by measuring the parity violating asymmetry on many p-wave resonances simultaneously, one can extract the RMS parity violating matrix element M, and understand how the parity violating NN interaction manifests itself in the presence of large number of nucleons.

Chapter 3

Experimental Details

3.1 Overview

This experiment measures the helicity dependence of the neutron transmission through a ^{238}U target. Therefore, we need an intense epithermal neutron source, a mechanism to prepare the neutrons in the desired helicity states, a ^{238}U target, and a detector which can record the high neutron flux.

The intense epithermal neutron beam is provided by the Los Alamos Neutron Scattering Center (LANSCE) spallation source. The LANSCE neutrons are produced as follows: A 800 MeV proton beam from the Los Alamos Meson Physics Facility (LAMPF) linac is injected into a Proton Storage Ring (PSR) with a rate of 20 Hz and with a pulse width of $\sim 800\mu$s. The PSR compresses these pulses to a single pulse of width 250 ns. After extraction, the beam is directed to a tungsten production target. The spallation neutrons are moderated and collimated to produce a beam of epithermal neutrons.

The neutron beam is polarized longitudinally by transmitting through a sample containing polarized protons. The spin reversal is accomplished by passing the neutrons through a spin flipper which has a magnetic field varying in space. The spin flipper can operate in two configurations: the neutron spin direction is not changed,

or the neutron spin direction is changed by 180°, therefore preparing the neutrons in the desired helicity states. The ^{238}U target is located in a guide field at the end of the spin flipper.

The detector consists of an array of 7 ^{6}Li-loaded glass scintillators with photomultiplier tubes (PMT), located 56 meters from the spallation source. With the high neutron flux at the detector, the conventional method of pulse counting fails. Instead, the currents from the anodes are used as a measure of the neutron flux.

It should be noticed that, because the proton beam from the PSR is pulsed, neutrons of different energy can be separated by time-of-flight (TOF).

The details of the various components are discussed in the following sections.

3.2 The pulsed neutron beam

A schematic view for LANSCE neutron production is shown in Figure 3.1. The 800MeV H^- beam from the LAMPF linac is deflected to line D through a kicker magnet. The deflected beam has a length of $\sim 800\mu s$, and a repetition rate of 20 Hz. In the PSR where the beam is accumulated, the H^- beam is first converted to a H^0 beam in a high field stripper magnet with 100% efficiency, then the H^0 beam enters the lattice of the ring, and is stripped to H^+ beam with $\approx 92\%$ efficiency in a 200 g/cm^2 carbon foil. Up to 2800 turns can be injected and accumulated before the proton beam is extracted in a single turn, with a width of 250 ns. The protons are then transported to the LANSCE tungsten production target, where approximately 17 spallation neutrons are produced by each incident proton. More detailed discussion of the PSR can be found in references [Mace88] and [Lawr85].

The spallation neutrons are moderated by a target-moderator-reflector-shield (TMRS) system. A vertical cut-away view of the TMRS is shown in Figure 3.2. The TMRS consists of two tungsten targets in split geometry, an inner beryllium/nickel reflector region, and an outer nickel reflector region. Three water slab-moderators

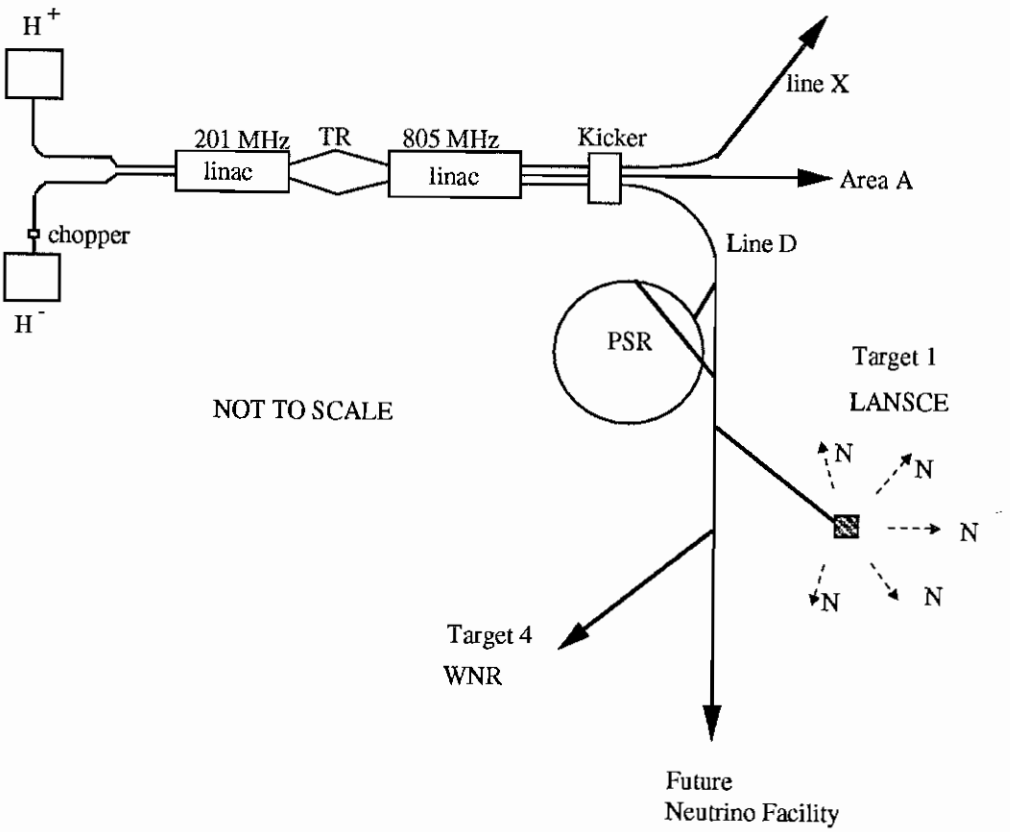

Figure 3.1: LANSCE facility

and a liquid hydrogen slab-moderator are in flux-trap geometry between the two tungsten targets. The plan view of the LANSCE beam line arrangements is shown in Figure 3.3. Our beamline, FP-2, is served by a high resolution moderator.

The flux of epithermal neutrons has been measured (see appendix C). It can be represented by

$$\Delta N = 0.01 \frac{\Delta E_n}{E_n} \left(\frac{E_n}{19eV} \right)^{0.13} \frac{i}{eg} f\Omega \qquad \text{neutrons/burst} \qquad (3.1)$$

where E_n is the neutron energy in eV, i the proton current in amps, e the electron charge in Coulombs, $g = 20$ Hz is the beam repetition rate, $f = A/169\text{cm}^2$ is the fraction of the moderator area viewed by the detector, and Ω is the solid angle into which the neutrons are emitted.

The proton beam width, neutron moderation, and detector dimension influence the time resolution, and therefore, the energy resolution. The proton beam burst has the shape of an isosceles triangle having a full-width-at-half-maximum (FWHM) of 125 ns. The FWHM of the moderated beam for the moderator used in this experiment can be approximated by [Wend90]

$$\Gamma_{th} = 6.58 E_n^{-0.394}/g \qquad \mu\text{s}$$

where g is a factor listed in Table 3.1. If, in addition, the transient time of the neutrons through the 1 cm thick ^{6}Li glass scintillators is taken into account, the energy resolution for the 56 meter flight path can be calculated. The result of the calculation is shown in Table 3.1 and is plotted in Figure 3.4.

The whole target assembly is surrounded by a biological radiation shield, and the neutrons can exit only through designated openings. A mercury shutter is mounted in a 84 inch long collimator which is constructed of iron and borated polyethylene. The beam is collimated to a 2 inch diameter.

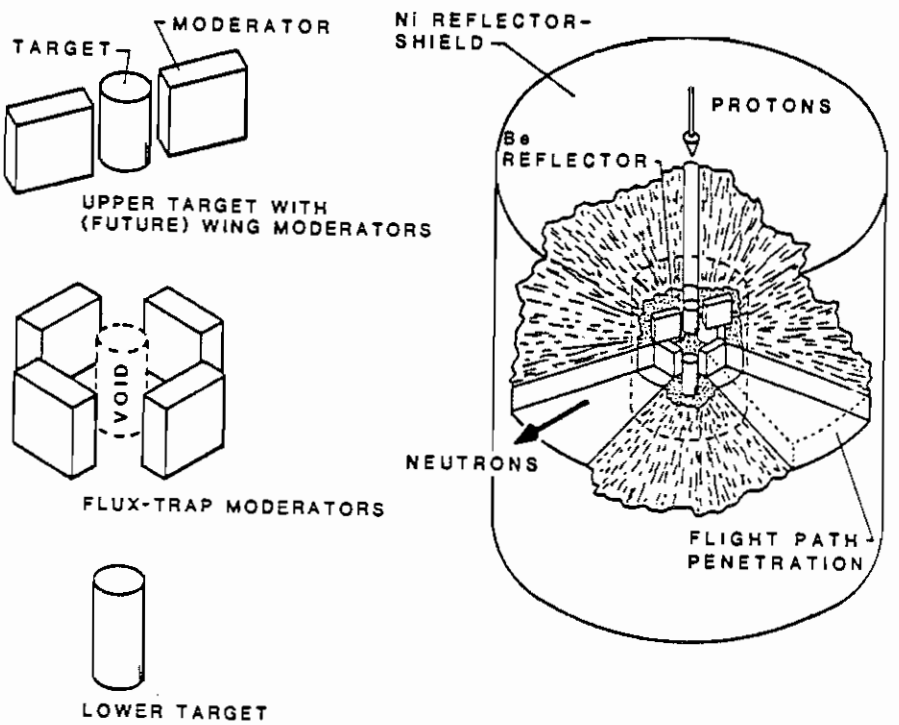

Figure 3.2: Illustration of the LANSCE target system

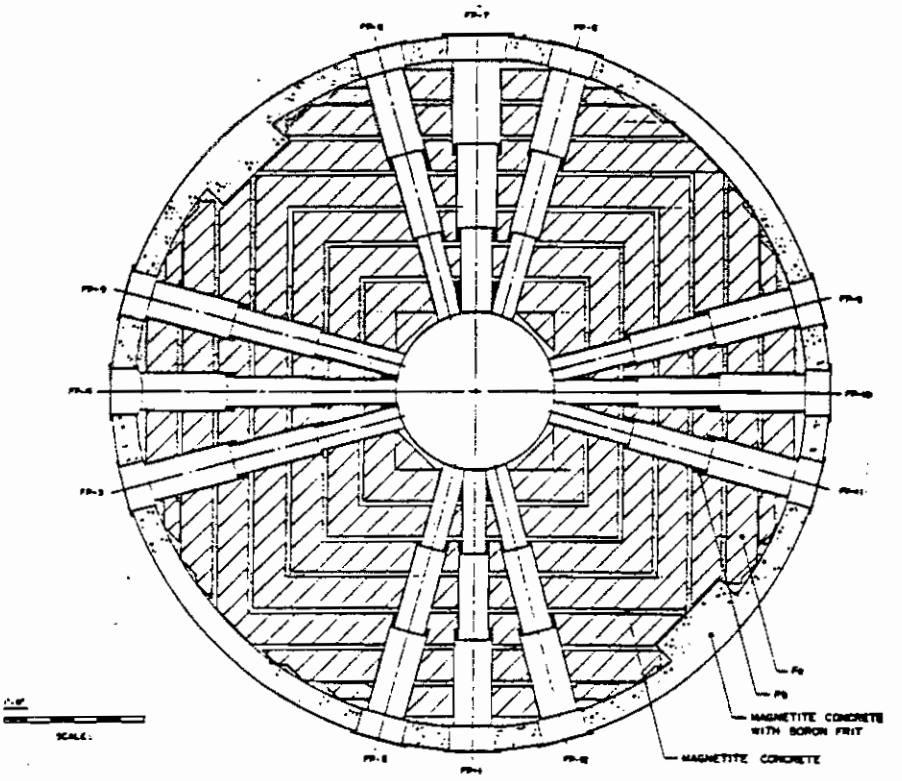

Figure 3.3: Plan view of the LANSCE beam line arrangements

Table 3.1: Energy resolution of the 56 meter flight path. E_n is the neutron energy, Γ_{th} the FWHM of the neutron moderation time, Γ_b the FWHM time of the proton beam, Γ_{det} the neutron transient time through the 1 cm thick scintillators, $\Gamma_{tot} = \sqrt{\Gamma_{th}^2 + \Gamma_b^2 + \Gamma_{det}^2}$ is the total width, and t_{56} is the neutron TOF over a 56 meter flight path. The energy resolution is calculated as $\Delta E/E = 2\Gamma_{tot}/t_{56}$. g is a correction factor for Γ_{th}.

E_n (eV)	g	Γ_{th} (μs)	Γ_b (μs)	Γ_{det} (μs)	Γ_{tot} (μs)	t_{56} (μs)	$\frac{\Delta E}{E}$
1	2.6	2.53	0.125	0.72	2.63	4047	1.3×10^{-3}
10	4.3	0.62	0.125	0.23	0.67	1280	1.0×10^{-3}
100	4.4	0.24	0.125	0.07	0.28	405	1.4×10^{-3}
1000	2.7	0.16	0.125	0.02	0.20	128	3.1×10^{-3}
10000	1.2	0.14	0.125	0.01	0.19	40	9.5×10^{-3}

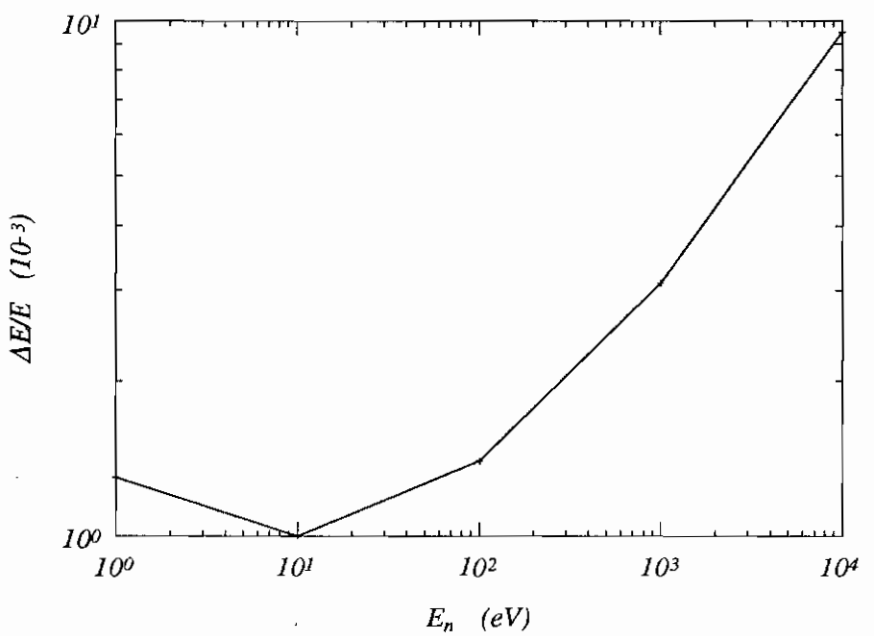

Figure 3.4: Energy resolution of the 56 meter flight path

3.3 Beamline

A block diagram of the beamline is shown in Figure 3.5. It consists of a beam monitor, a polarizer, a spin flipper, an unpolarized ^{238}U target and a ^{6}Li-loaded glass scintillator array. The total distance from the neutron source to the detector array is 56 meters.

The neutron beam is polarized by transmission through a sample containing polarized protons. The protons are located in the water of hydration of $La_2(0.05\%Nd)Mg_3(NO_3)_{12} \cdot 24H_2O$ (LMN) crystals, and can be polarized either parallel or anti-parallel to the beam direction. Six flat LMN crystals form a block $3.5 \times 3.5 cm^2$ by 1.8 cm thick located inside a cryostat. Inserts in the cryostat collimate the beam to a diameter of $1\frac{1}{8}$ inches. The spin flipper consists of two longitudinal solenoids and one transverse Helmholtz coil. The longitudinal magnetic fields serve as a guide field for neutron spins, and the transverse field is introduced to flip the neutron spin. The spin flipper operation will be discussed in detail in section 3.5. The polarized neutrons then pass through a metallic sample of ^{238}U ($49.3 g/cm^2$) located at the beam exit of the spin flipper. From 11 meter on, the beam is transported through an aluminum vacuum pipe.

The beam monitor, the polarizer, the spin flipper and the target are all enclosed in a concrete cave which provides sufficient radiation shielding to allow access to the area outside the cave while the shutter is open.

The expected instantaneous count rate at the detector is shown in Figure 3.6 (see appendix C for details), where we have taken into account the beam collimation by the cryostat, the beam attenuations by the LMN crystal, the air, an assumed two mean-free-path sample, and the efficiency of the ^{6}Li-loaded glass scintillators. The most significant factors which reduce the count rate are as follows.

1. Attenuation

   The polarizer and the 11 meter of air are significant in reducing the neutron

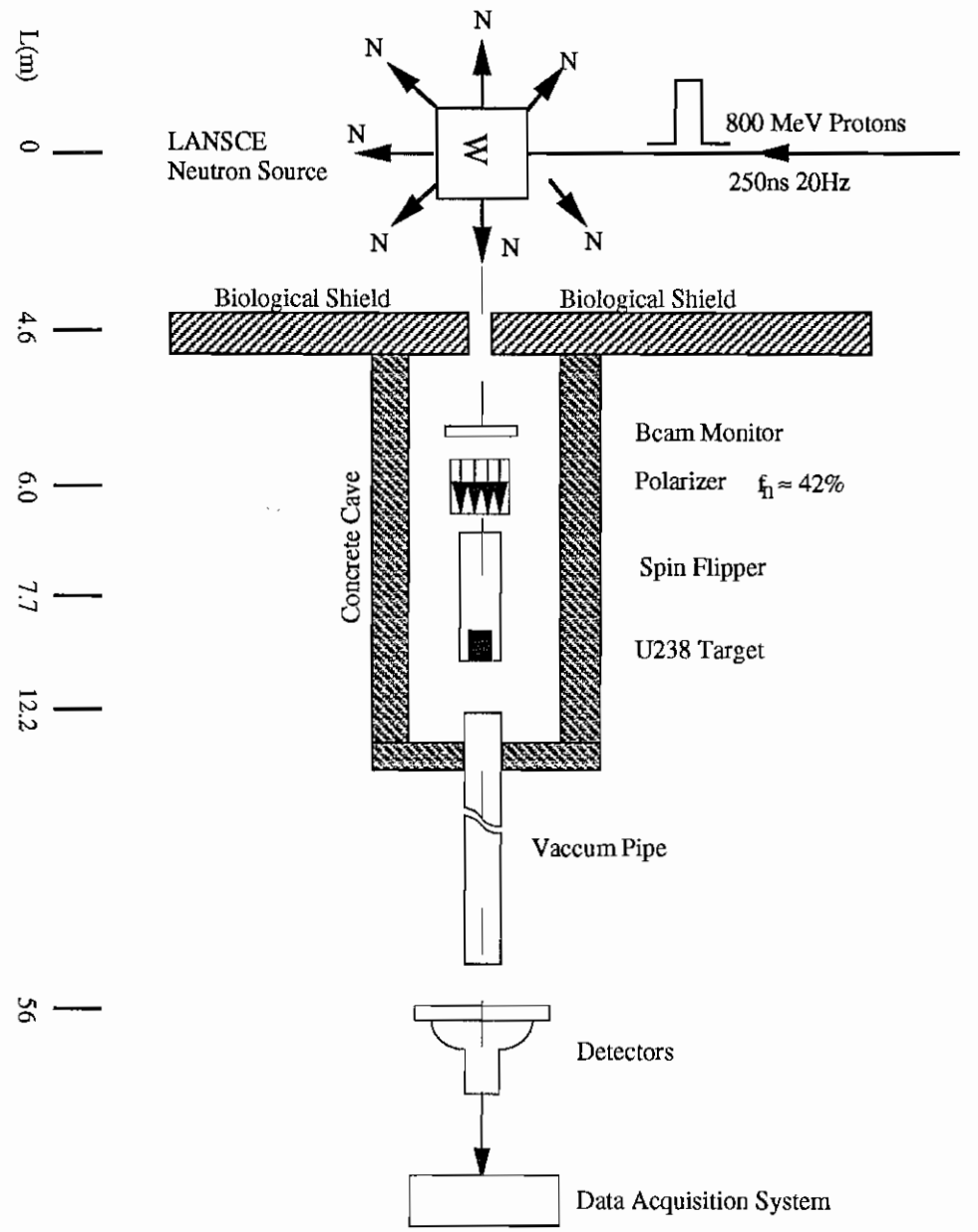

Figure 3.5: The beam-line

flux. In this experiment, typical neutron transmission through the LMN crystal is 15%, and typical transmission through 11 meter air is 70% (see Table C.2 for neutron mean-free-path in these materials). This reduces the beam by a factor of 10.

2. Collimation

   The collimation inside the cryostat reduces the neutron flux. The f-factor in equation (3.1) is 0.12 with no collimation, while it is 0.05 with the collimation in place. Therefore, the cryostat collimation reduces the beam by a factor of 2.

3. Detector Efficiency

   The neutron detecting efficiency of the ^{6}Li-loaded glass scintillator has a $\frac{1}{v}$ dependence where v is the velocity of neutrons. For 1 eV neutrons, the efficiency is $\sim 86\%$; while for 100 eV neutrons, the efficiency is reduced to $\sim 18\%$. Thus the number of detectable neutrons is significantly reduced at the higher energies.

In the following sections, we will describe the various components of the beamline in detail.

3.4 Polarizer

Polarized protons can be used as a neutron spin filter over a wide energy range from 0.1 eV to 10 keV, since the n-p spin-spin cross section is approximately constant. For this experiment, the neutron energy range of interest is from 6 eV to 400 eV.

The polarizer was build by Keyworth et al. [Keyw74] and was refurbished for use in this experiment. A cut-away view of the polarizer is shown in Figure 3.7. The LMN crystals are located at the center of a 2.7 Tesla superconducting magnetic field. Both the magnet and the crystals are immersed in a pumped 1.15 K liquid ^{4}He bath which is surrounded by 4 K liquid ^{4}He and liquid N_2. A valve feeds ^{4}He between the 4 K and the 1.15 K baths. Approximately 0.5 watts of microwave power is used to

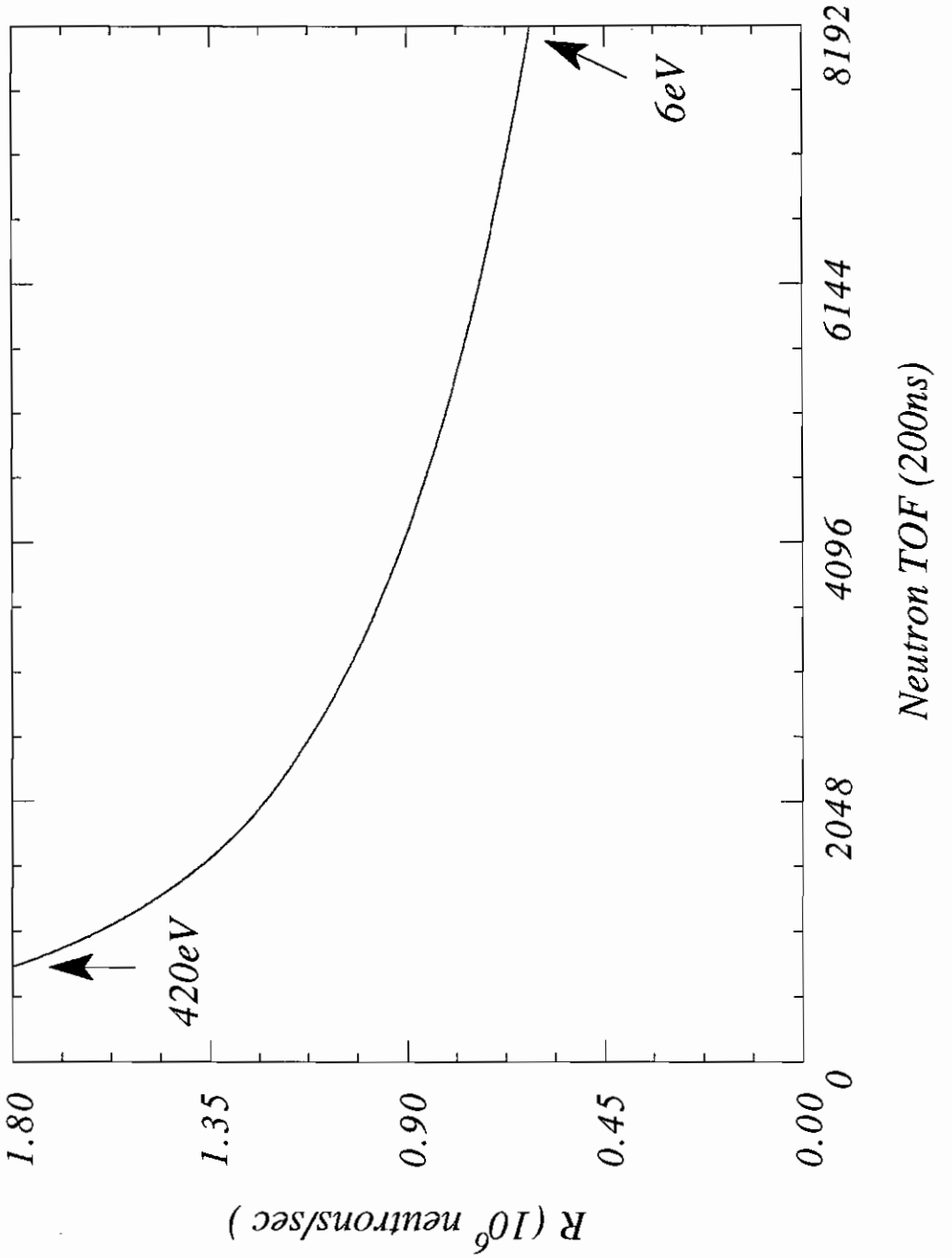

Figure 3.6: The expected instantaneous count rate of the detector. The proton current $i = 40\mu$A

polarize the protons in the LMN crystals. The magnetic field is in the beam direction, and as we will show later in this section, this arrangement will also cause the protons to be polarized in the beam direction.

Neutrons are polarized by transmitting through the polarized proton target, as shown below. Neutrons from the LANSCE spallation source are unpolarized, that

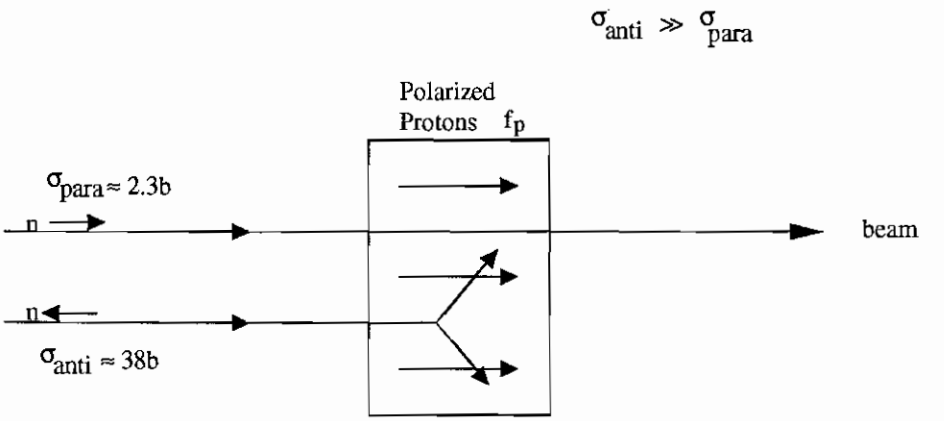

is, there are equal number of neutrons with spin parallel or anti-parallel to the beam direction. The spin anti-parallel n-p cross section (37.06 barn, see appendix A) is much bigger than the spin parallel cross section (3.66 barn). Therefore neutrons with spin anti-parallel to that of the protons are scattered more by the proton target than neutrons with spin parallel. Thus the transmitted neutron beam is polarized, and the polarization is given by (see appendix B)

$$f_n = \tanh(f_p n \sigma_p t)$$

where f_p is the proton polarization, n the proton number density in the LMN crystal, t the thickness of the crystal, and $\sigma_p = (\sigma_{anti} - \sigma_{para})/2$ is called polarization cross section. The physical quantities of the LMN crystals are summarized in Table 3.2,

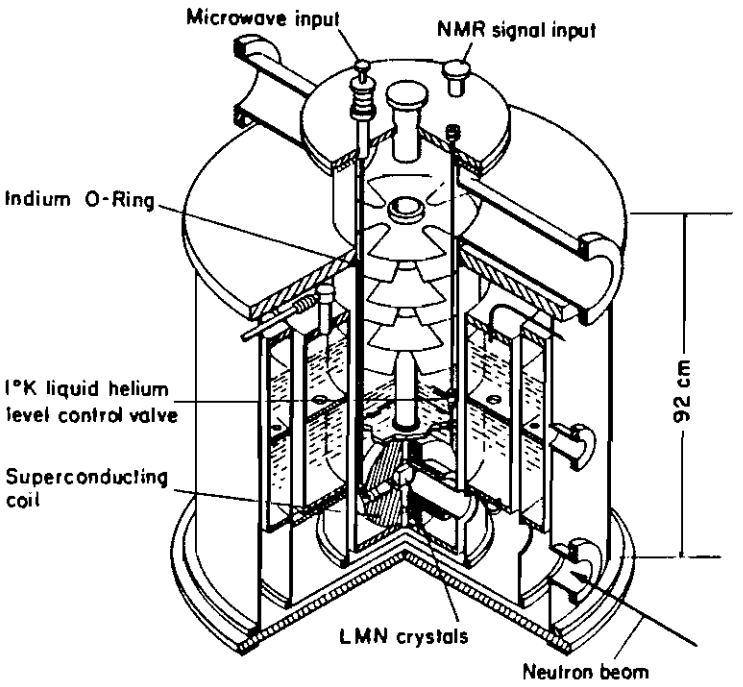

Figure 3.7: The Keyworth cryostat

Table 3.2: The LMN crystal: $La_2(0.05\%Nd)Mg_3(NO_3)_{12} \cdot 24H_2O$

density ρ (g/cm^3)	thickness t(cm)	cross section	nt(protons/barn)	σ_p (barn) (1eV–10keV)
2.07	1.8	3.5 cm × 3.5 cm	0.070	16.7

and the neutron polarization is plotted as a function of the proton polarization in Figure 3.8. The typical proton polarization was $\sim 43\%$ corresponding to a neutron polarization of $\sim 46\%$.

The protons in a LMN can be polarized under the combination of the following conditions: 1) a strong magnetic field which splits the spin states; 2) a low temperature which assures that more electron-proton pairs will occupy the lower energy states① and③ (see Figure 3.9) than the higher energy states② and④; 3) microwave pumping to induce forbidden transitions between the spin states.

LMN is a magnetically dilute crystal containing free protons and electrons ([Jeff63]). In an external magnetic field $\vec{B}$, the energy of a typical electron-proton pair is given by

$$E = 2\mu_B BM - g_p \mu_N Bm,$$

where μ_B is the Bohr magneton, $g_p = 5.586$ is the proton g-factor, μ_N is the nuclear magneton, and M, m are the z-components of the electron and proton spins, respectively.

The level diagram of the electron-proton pair is shown schematically in Figure 3.9. If the electron spin-lattice relaxation time τ_1 is small compared to the electron-proton spin-lattice relaxation time $\tau_2 = \tau_3$, pumping at microwave frequencies $\nu_e \pm \nu_p$ will result in a bulk proton polarization. The process works as follows. The microwave pumping induces a flip-flip transition of the electron-proton pair, then the electron relaxes thermally to its original state, leaving the proton in the spin-flipped state. The electron can then induce another flip-flip transition. As this process continues,

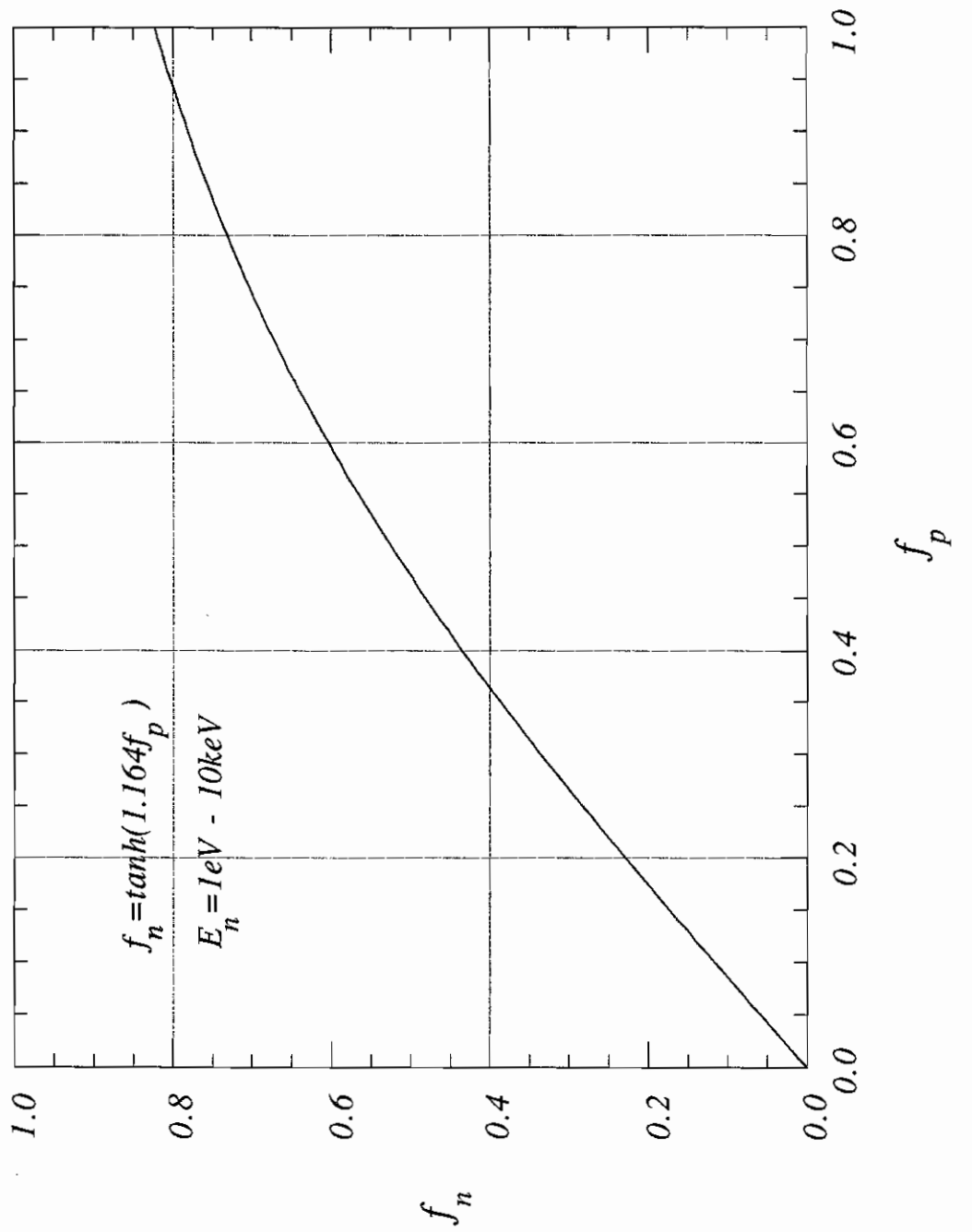

Figure 3.8: The neutron polarization vs the proton polarization

more and more protons are left in the spin-flipped state, which results in a net proton polarization.

As an example, pumping at the higher microwave frequency $f_h = \nu_e + \nu_p$ induces the transition from state① to state② . In the process, both electron spin and proton spin are flipped. In the subsequent thermal relaxation from state② to state③, the electron spin is flipped back to its original state while the proton is left in the spin flipped state with a z-component of $-\frac{1}{2}$. In this case , the proton polarization is anti-parallel to the magnetic field. Similarly, when pumping at the lower microwave frequency $f_l = \nu_e - \nu_p$, the resulting proton polarization is parallel to the magnetic field.

In this experiment, the direction of the superconducting magnet field is parallel to the beam, that is, pointing from the spallation source to the detector.

The proton polarization is monitored by the nuclear magnetic resonance (NMR) technique. A coil wraps around the LMN crystal, and a radio-frequency (rf) generator is connected to the coil. The rf-field introduces transition between the states① and ③. Depending on the pumping microwave frequency, ie., the relative population of the two states, the LMN crystal can either absorb or give out rf energy. So the NMR signal can be either positive or negative.

The NMR signal is measured by sweeping the rf frequency through the resonance region, as shown in Figure 3.10. An input voltage to the NMR module controls the rf frequency, so that a stair-step ramp voltage can be used to vary the frequency through the measuring range. The computer generates the ramp by stepping a 12-bit digital-to-analog converter(DAC) 8 units at a time. After each step, a gate, generated by the DAC strobe and delayed with a gate and delay generator, enables the linear gate of a 12-bit analog-to-digital converter (ADC) which measures the NMR signal. A delay time of 150μsec was chosen to allow the rf system to stabilize before the NMR signal is measured. After each measurement, the DAC again is stepped up by 8 units, and the cycle continues until the frequency sweep is completed.

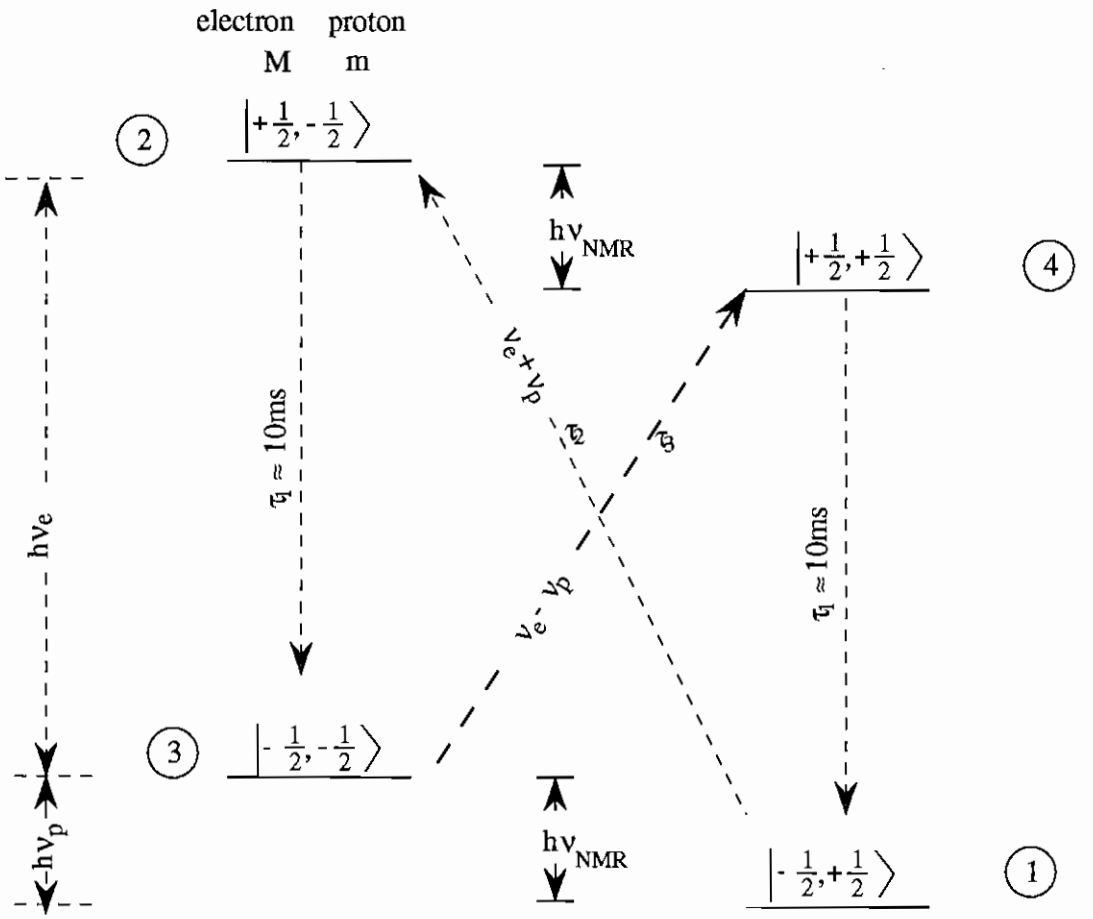

Figure 3.9: Energy levels of an electron-proton pair in a $\vec{B}$ field. $\nu_e = 2\mu_B B$, $\nu_p = g_p \mu_N B$, and the τ_i's are the spin-lattice relaxation time for the various transitions.

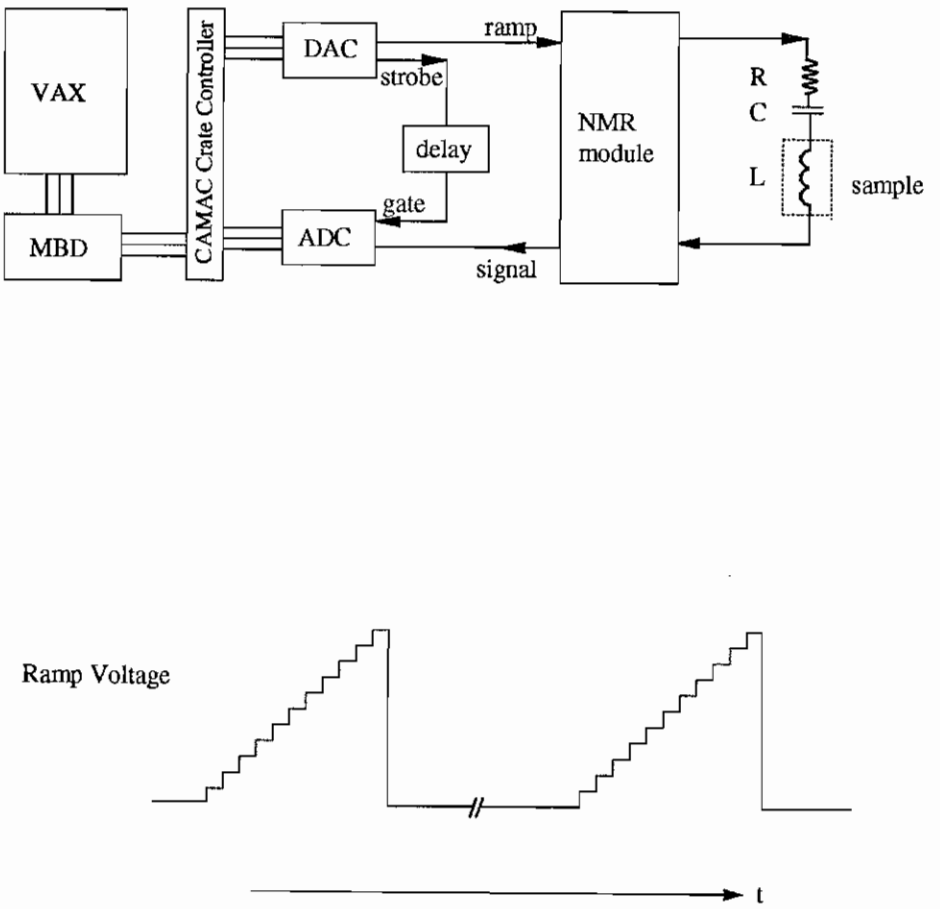

Figure 3.10: The circuit for NMR measurement

Typical NMR spectra are shown in Figure 3.11 for both microwave frequencies. The NMR signal, shown as the shaded area, is superimposed on the Q-curve of the NMR circuit. The NMR area is extracted by fitting the Q-curve with a third order polynomial. The NMR area is proportional to the proton polarization, and the determination of conversion factor is described in appendix B.

3.5 Spin flipper

The spin flipper consists of a pair of longitudinal solenoids and a pair of transverse Helmholtz coils, as shown in Figure 3.12(a). The solenoids are configured to produce longitudinal fields of the same amplitude but in opposite direction, as shown by B_z in Figure 3.12(a). The field direction of the first solenoid is chosen to be parallel to the direction of the superconducting magnetic field of the cryostat, so the neutrons enter the spin flipper with spins properly guided. The total length of the spin flipper is $2L = 2$ meters.

The operation principle of the spin flipper is to pass the neutrons through a magnetic field the direction of which rotates in space. The spin flipper can operate in two configurations: transverse coil off or on, corresponding to neutron spin not flipped or flipped, respectively.

In the first configuration, the transverse coil is off, and the total magnetic field is produced by the longitudinal solenoids only. Let us choose the z-axis to be the beam direction, and $z = 0$ to be the center of the spin flipper, as shown in Figure 3.12(a). The longitudinal magnetic field produced by the solenoids can be described by

$$B_z = \begin{cases} B_0 & -L < z < -\frac{L}{2} \\ -B_0 \sin \frac{\pi z}{L} & -\frac{L}{2} < z < +\frac{L}{2} \\ -B_0 & +\frac{L}{2} < z < +L \end{cases}$$

where B_0 is of the order of 100 gauss. A plot of B_z is shown in Figure 3.12(b).

Consider a neutron entering the spin flipper with spin parallel to the beam di-

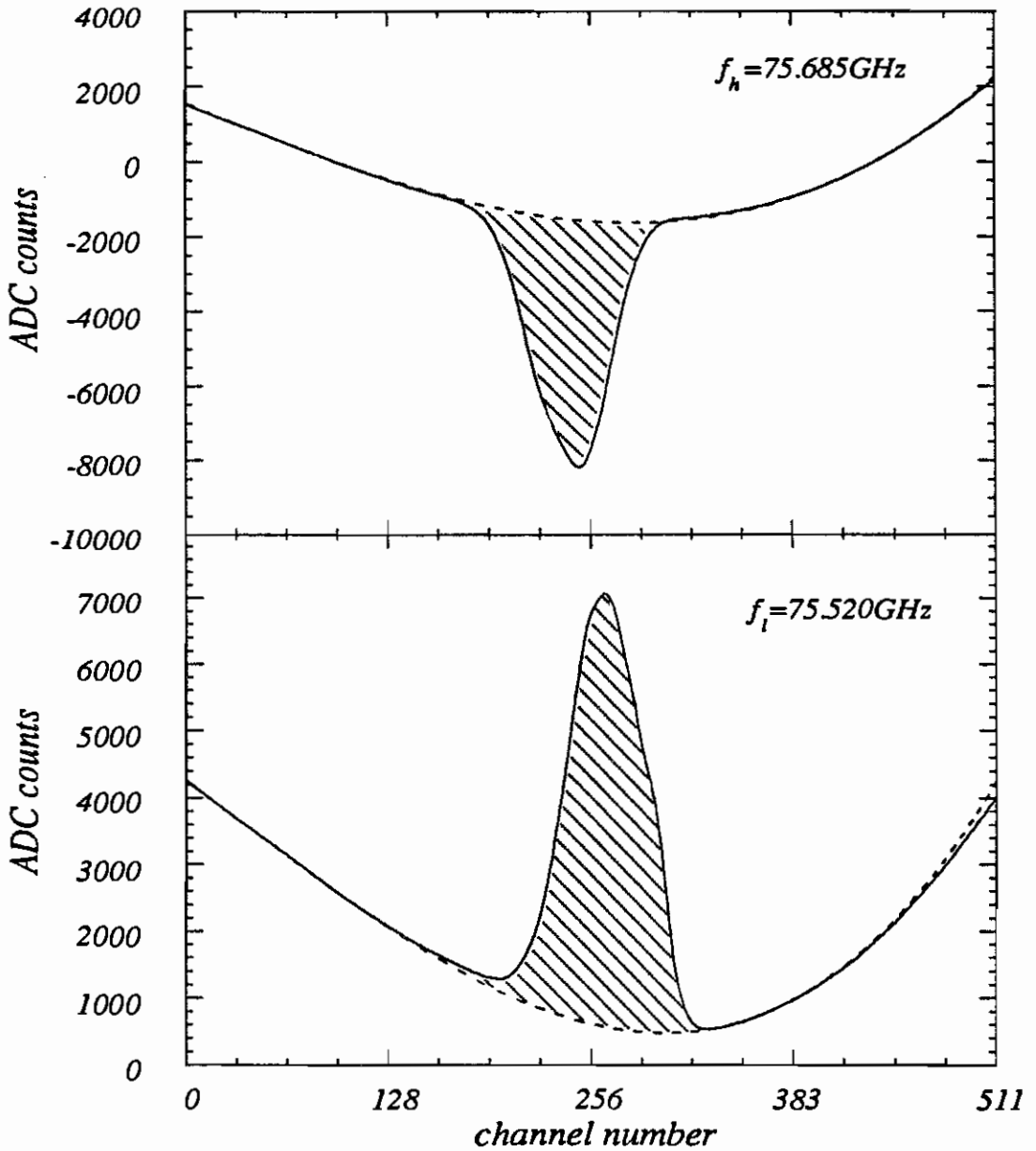

Figure 3.11: Typical NMR signals for both microwave frequencies

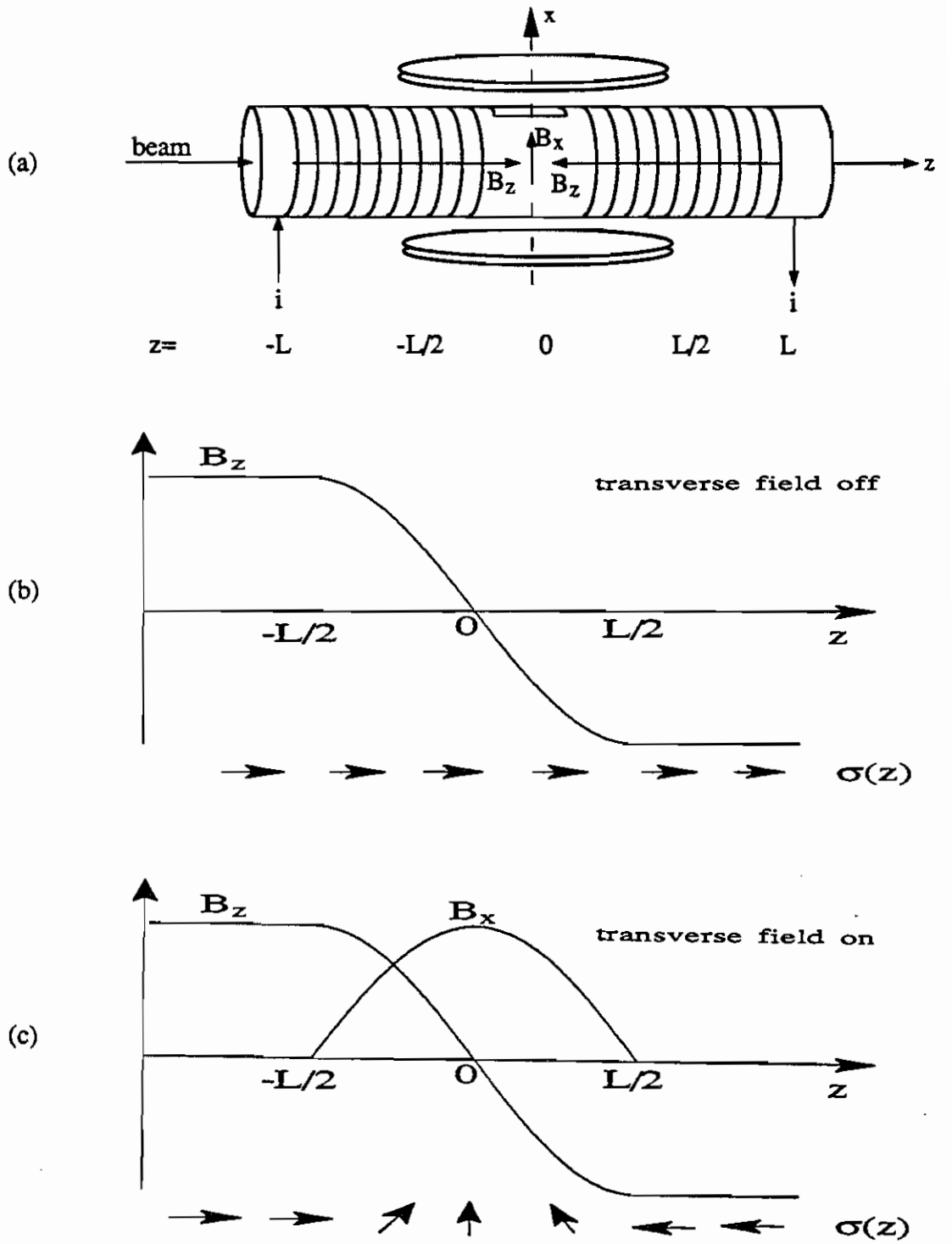

Figure 3.12: The spin flipper and its magnetic fields

rection. Since the magnetic field has only a longitudinal component, the torque experienced by the neutron is

$$\vec{\tau} = \vec{\mu} \times \vec{B} = 0$$

where $\vec{\mu}$ is the neutron magnetic moment. Therefore, the neutron passes through the spin flipper with spin direction unchanged, as shown by the $\sigma(z)$ row in Figure 3.12(b).

In the second configuration, the transverse coil is on, and the total magnetic field is the superposition of the longitudinal field produced by the solenoids and the transverse field produced by the Helmholtz coil. The transverse field can be represented by

$$B_x = \begin{cases} \pm B_0 \cos \frac{\pi z}{L} & -\frac{L}{2} < z < +\frac{L}{2} \\ 0 & \text{otherwise} \end{cases}$$

and is plotted in Figure 3.12(c), together with the longitudinal field. Here the x-axis is perpendicular to the beam, and the $\pm$ sign indicates that the transverse field can be either parallel or anti-parallel to the x-axis. The superposition of a sine longitudinal field and a cosine transverse field yields a combined field $\vec{B}_0$ of constant amplitude B_0 with direction rotating in space. For positive B_x, the field rotates counterclockwise from $+z$ at $z = -\frac{L}{2}$ to $-z$ at $z = \frac{L}{2}$.

Consider a neutron entering the spin flipper with velocity v. The time needed for the neutron to transverse from $z = -\frac{L}{2}$ to $z = \frac{L}{2}$ is $t = \frac{L}{v}$. As the neutron travels down the spin flipper, it experiences a magnetic field rotating with an angular speed $\omega_B = \frac{\pi v}{L}$.

The neutron spin also experiences a Larmor precession around the combined magnetic field. The Hamiltonian for this interaction is

$$H = -g_n \mu_N \vec{S} \cdot \vec{B}_0 = -g_n \mu_N B_0 \vec{S} \cdot \hat{n}$$

where $g_n = -1.913$ is the neutron g-factor, μ_N is the nuclear magneton, $\vec{S}$ is the neutron spin operator in unit of $\hbar$, and $\hat{n}$ is the unit vector in the direction of $\vec{B}_0$.

The Schrödinger equation can be written as

$$\frac{d}{d\,t}\psi = i\frac{g_n\mu_N B_0}{\hbar}\vec{S}\cdot\hat{n}\psi. \tag{3.2}$$

This equation describes a rotation of the wavefunction about the $\hat{n}$-axis at a rate of $\omega_L = \frac{|g_n|\mu_N B_0}{\hbar}$, the Larmor frequency.

The spin flipper is designed such that the rotation of the magnetic field is much slower than the Larmor spin precession

$$\omega_B \ll \omega_L,$$

so that the spin of the neutron can follow the direction of the rotating magnetic field. For a neutron entering the spin flipper with spin parallel to the beam direction, if B_x is positive, the spin direction will rotate counter-clockwise, as shown by the $\sigma(z)$ row in Figure 3.12(c); while if B_x is negative, the spin will rotate clockwise. In either case, the spin of the neutron will be flipped as it exits the spin flipper.

To understand the spin flipper quantitatively, one need to solve the Schrödinger equation (3.2), with $\hat{n}$ rotating at a rate of ω_B. The final result is as follows. The spin flipping efficiency r_{flip}, defined as the expectation value of the Pauli matrix σ_z at the exit, is [Bowm91]

$$r_{flip} = 1 - \sin^2(\theta)\left[1 - \cos\left(\pi\sqrt{\gamma^{-2}+1}\right)\right]$$

where

$$\begin{aligned}\gamma &= \frac{\omega_B}{\omega_L}\\ \tan(\theta) &= \gamma.\end{aligned}$$

The spin flipper is designed to work for small γ, so that r_{flip} can reach 1. As neutron energy becomes large, γ becomes large, and r_{flip} can reach -1. The neutron passes through the spin flipper so fast that its spin direction is not affected by the spin flipper field at all. The spin flipping efficiency r_{flip} is shown in Figure 3.13 for the neutron energies of interest 1 eV – 1 keV.

Bowman [Bowm91] has solved the Schrödinger equation for the off axis neutrons in the first configuration. In this case, the strength of the magnetic field at the center of the spin flipper is zero, and the z-gradient is non-zero, as shown in Figure 3.12(b). By virtue of the Maxwell equation,

$$\vec{\nabla} \cdot \vec{B} = 0,$$

the magnetic field develops transverse components off axis. For a neutron passing through the spin flipper off axis, the small transverse components tend to flip the neutron spin. For small beam radius R, one can show that, the spin preserving efficiency s_{flip}, which is defined as the expectation value of σ_z at the exit, is[Bowm91]

$$s_{flip} = 1 - \frac{\pi^3 R^2}{8\gamma L^2}.$$

The spin preserving efficiency s_{flip} is shown in Figure 3.13 for the neutron energies of interest 1 eV – 1 keV.

The on and off of the transverse coil is computer controlled. This control is accomplished by using a programmable power supply and a relay box. The computer can turn the power supply on and off, as well as select the direction of the transverse coil current through the relay box. The change of the neutron spin state can be completed in 60 ms.

In the experiment, the spin flipping follows a preprogrammed pattern which we called an 8-step-sequence: 0,+,−,0,+,0,0,−, where 0 stands for transverse field off, and +,− stand for positive and negative transverse fields, respectively. Each spin state lasts about 10 seconds (200 beam bursts). The fast spin flip is to reduce possible false asymmetries due to time dependent drifts in the system.

Since the detector runs in current mode, any gain change in the detector results in a change in the signal. The 8-step-sequence has the advantage of canceling any linear and quadratic gain drifts in the detecting system. This can be explained as follows. Assume that the detector has a quadratic gain drift, which leads to quadratic time

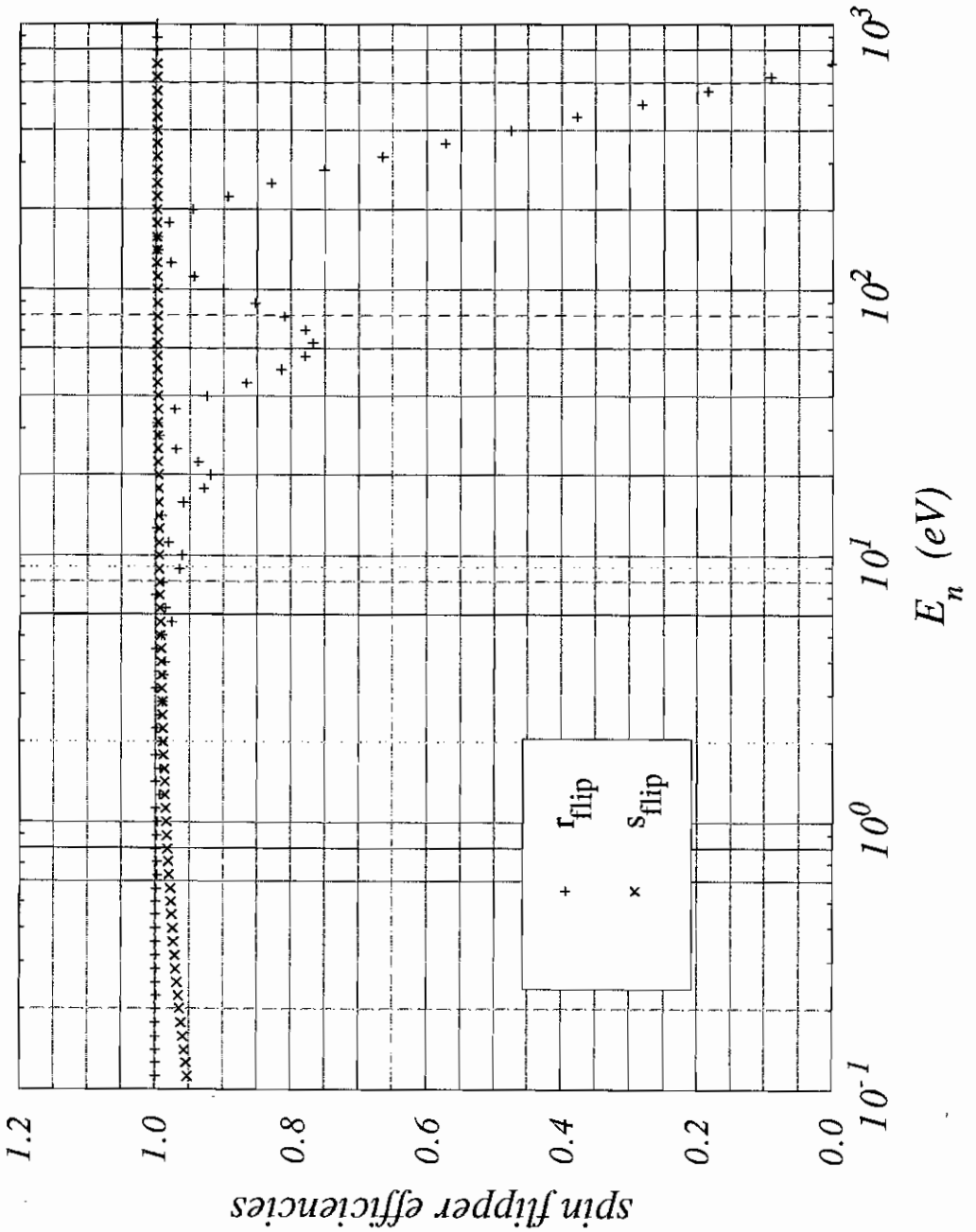

Figure 3.13: The spin flipper efficiencies, B_0=100 gauss, R=1.4 cm.

drift in the signal. A quadratic time drift can be represented by

$$y = at^2 + bt + c$$

where a, b, and c are arbitrary constants.

For a spin state which lasts from T to $T + \Delta$, the recorded signal is

$$\int_T^{T+\Delta} y\ dt = \frac{1}{3}at^3 + \frac{1}{2}bt^2 + ct \Big|_{T}^{T+\Delta} = g(T+\Delta) - g(T)$$

where $g(t) = \frac{1}{3}at^3 + \frac{1}{2}bt^2 + ct$.

For a 8-step-sequence starting at time T, the signal accumulated in the "flipped" data (transverse coil current + or −) is

$$\begin{aligned} F &= g(T+3\Delta) - g(T+\Delta) \\ &\quad + g(T+5\Delta) - g(T+4\Delta) \\ &\quad + g(T+8\Delta) - g(T+7\Delta), \end{aligned}$$

and the signal accumulated in the "noflipped" data (transverse coil current 0) is

$$\begin{aligned} N &= g(T+\Delta) - g(T) \\ &\quad + g(T+4\Delta) - g(T+3\Delta) \\ &\quad + g(T+7\Delta) - g(T+5\Delta). \end{aligned}$$

The difference in the "flipped" data and the "noflipped" data is

$$\begin{aligned} Z &= F - N \\ &= g(T) - 2g(T+\Delta) + 2g(T+3\Delta) - 2g(T+4\Delta) + 2g(T+5\Delta) \\ &\quad -2g(T+7\Delta) + g(T+8\Delta), \end{aligned}$$

which can be shown to be zero as follows.

Since $g(t)$ is a function of a, b, and c, Z should also be a function of a, b, and c. Notice that

$$\frac{\partial g}{\partial a} = \frac{1}{3}t^3$$

$$\begin{aligned}\frac{\partial g}{\partial b} &= \frac{1}{2}t^2 \\ \frac{\partial g}{\partial c} &= t,\end{aligned}$$

the derivatives of Z with respect to a, b, and c are

$$\begin{aligned}3\frac{\partial Z}{\partial a} &= T^3 - 2(T+\Delta)^3 + 2(T+3\Delta)^3 - 2(T+4\Delta)^3 + 2(T+5\Delta)^3 \\ &\quad -2(T+7\Delta)^3 + (T+8\Delta)^3 \\ &= 0; \\ 2\frac{\partial Z}{\partial b} &= T^2 - 2(T+\Delta)^2 + 2(T+3\Delta)^2 - 2(T+4\Delta)^2 + 2(T+5\Delta)^2 \\ &\quad -2(T+7\Delta)^2 + (T+8\Delta)^2 \\ &= 0; \\ \frac{\partial Z}{\partial c} &= T - 2(T+\Delta) + 2(T+3\Delta) - 2(T+4\Delta) + 2(T+5\Delta) \\ &\quad -2(T+7\Delta) + (T+8\Delta) \\ &= 0.\end{aligned}$$

Therefore Z is a constant. Since $Z(a=0, b=0, c) = 0$, we have $Z \equiv 0$, i. e. $F = N$, and any linear and quadratic time dependent gain drift will be canceled out.

One may be concerned about the false asymmetry arising from the dependence of the phototube gain on the spin flipper field. We have measured this effect quantitatively, and the result is negligibly small ($\sim 2 \times 10^{-10}$). The method is as follows. The gain of the phototube can be expanded in Taylor series as

$$G(B + \Delta B) = G_0 + G'\Delta B + \frac{G''}{2}(\Delta B)^2 + \cdots$$

where B is the local field, ΔB is the change in the local field, and G', G'' are the first and second derivatives, respectively.

For a non-symmetrized spin flipping pattern, +,−,+,−,$\cdots$, the asymmetry between the + and − spin states is

$$A_1 = \frac{G_+ - G_-}{G_+ + G_-} = \frac{G'}{G_0}\Delta B;$$

while for the 8-step spin flipping pattern, the asymmetry between the flipped and noflipped spin states is

$$A_2 = \frac{2G_+ + 2G_- - 4G_0}{2G_+ + 2G_- + 4G_0} = \frac{G''(\Delta B)^2}{4G_0}$$

where $\pm\Delta B$ is the change in magnetic field at the detector when the spin flipper field is $+$ or $-$ ($\Delta B = 0$ if the spin flipper is off).

Assume the gain of the phototube scales with the local field B as

$$G = G(0)\cos\left(\frac{B}{B_0}\right)$$

where B_0 is an (unknown) scaling field of the order of a few gauss which determines at what field the tube stop functioning. For B small compared to B_0, we get

$$\begin{aligned} A_1 &= -\frac{B}{B_0^2}\Delta B \\ A_2 &= \frac{1}{4}\frac{1}{B_0^2}(\Delta B)^2, \end{aligned} \tag{3.3}$$

and

$$A_2 = -\frac{1}{4}\frac{\Delta B}{B}A_1. \tag{3.4}$$

The magnetic field at the phototube has been measured to be 0.3 gauss. The ΔB is obtained by measuring the field change 3 meters away from the center of the spin flipper as the transverse field changes from $+$ to $-$, and scaling it down to the detector which is located 49 meters from the spin flipper. The result is $\Delta B = 1.5 \times 10^{-5}$ gauss. Experimentally we have measured $A_1 \sim 1.5 \times 10^{-5}$. Substituting these numbers into equation (3.4), we get

$$A_2 \sim 2 \times 10^{-10}$$

which is negligible relative to the statistical errors observed in this experiment.

Table 3.3: The ^{238}U target

weight(kg)	diameter(in)	thickness(in)	nt (1/barn)
1.0	2	$\frac{3}{4}$	0.12

3.6 ^{238}U target

The target is a 1 kg of ^{238}U metal, $\frac{3}{4}''$ thick and $2''$ in diameter (Table 3.3), pressed into a brass cylinder of $2''$ inner diameter and $2.5''$ outer diameter. The target is inserted into the exit of the spin flipper through a brass collimator, as shown in Figure 3.14. The spin flipper longitudinal field serves as the guide field for the neutron spins.

3.7 Detector

The detector consists of an array of seven NE905 ^{6}Li-loaded glass scintillators mounted directly on seven R1513 Hamamatsu photomultiplier tubes. The scintillators are 1 cm thick, $5''$ in diameter, and contain 6.6% lithium by weight (enriched to 95% ^{6}Li). The PMTs have photocathodes measuring 13 cm in diameter. The seven detector array is mounted on an aluminum frame, with one detector at the center and six detectors around it in a circle. The aluminum frame is located at the exit of the vacuum aluminum beam pipe, and the distance to the spallation source is 56.5 meters.

Neutrons are detected in the scintillators via the reaction ([Knol79])

$$\mathrm{n} + {}^6\mathrm{Li} \rightarrow {}^4\mathrm{He} + {}^3\mathrm{H} + 4.78\mathrm{MeV}.$$

For epithermal neutrons which have kinetic energies much smaller than 4.78 MeV, each neutron reaction deposits $\sim$ 4.78 MeV into the scintillator. Therefore the pulse shapes seen at the PMT anodes are independent of the neutron energy.

The detector efficiency (see appendix C) is shown in Figure 3.15 as a function of neutron energy. The efficiency is $\sim$ 86% at 1 eV, and $\sim$ 18% at 100 eV, because the

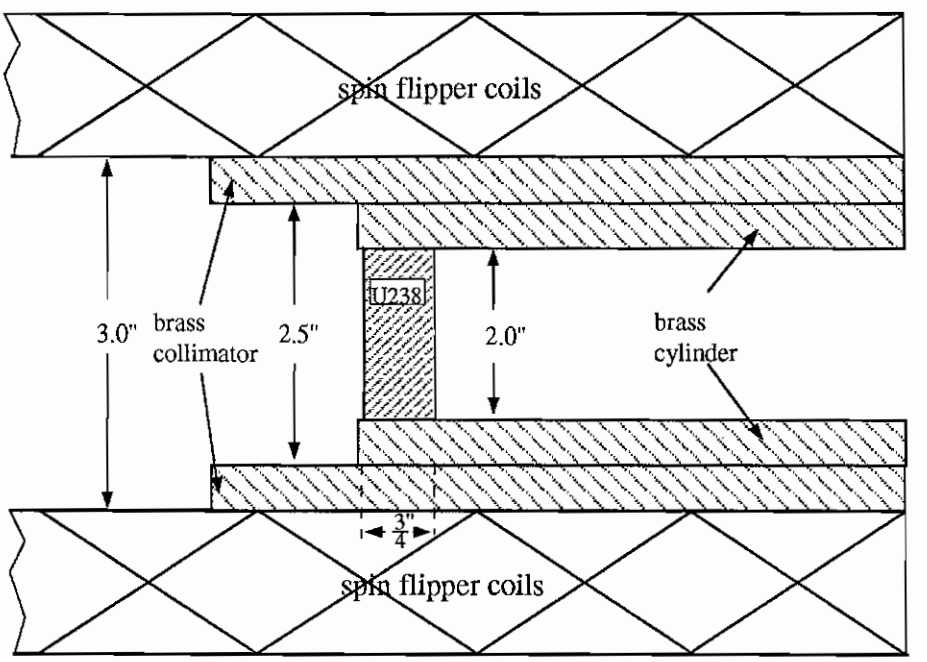

Figure 3.14: Mounting of the ^{238}U target

n $-^6$ Li cross section scales as $\frac{1}{v}$, where v is neutron velocity.

Because of the high instantaneous neutron flux, individual neutron pulses overlap. So it is necessary to use the anode current as a measure of the neutron count rate. The PMTs have S-20 type photocathodes which can provide currents as large as 1 μA and are suitable for large instantaneous count rate. The circuit diagram of the PMT base is shown in Figure 3.16. The cathode voltages are provided by a LeCroy 4032 multichannel high voltage power supply which can be controlled by the computer through a high voltage control(HVC) program. To assure that the gain does not degrade, the last four dynodes are connected to individual high voltage/high current power supplies. The phototube voltages were set so that a single neutron event produces a 5mV pulse at the anode.

The anode signals of the 7 detectors are summed, as shown in Figure 3.17. The summed current pulse is converted to a voltage with a $\times 10$ amplifier (model LRS 133BL dual linear amplifier). This amplifier has a short saturation recovery time and a maximum output voltage of 2V. Both these properties are important, since at the beginning of a beam burst, the large flash of gamma-rays and fast neutrons produces a signal as large as a few hundred volts. The amplifier saturates to 2V at this point. The short saturation recovery time minimizes the signal distortion.

As we will discuss later in this section, the voltage signal will be sampled using a transient digitizer at fixed time intervals (DWELL time) varying from 100 ns to 10 μs. Since the actual sampling time is small relative to the time intervals, a multipole filter was used to stretch the single neutron pulses to a width comparable to the width of the time interval, so neutrons arriving between two sampling points contribute to the voltage sampled.

The circuit diagram of the multipole filter is shown in Figure 3.18. The resistors are 50 Ω and the inductance L and the capacitance C are chosen such that $L = R^2C$. Under this condition, the filter is totally resistive with an input resistance of 50 Ω if the load is also 50 Ω.

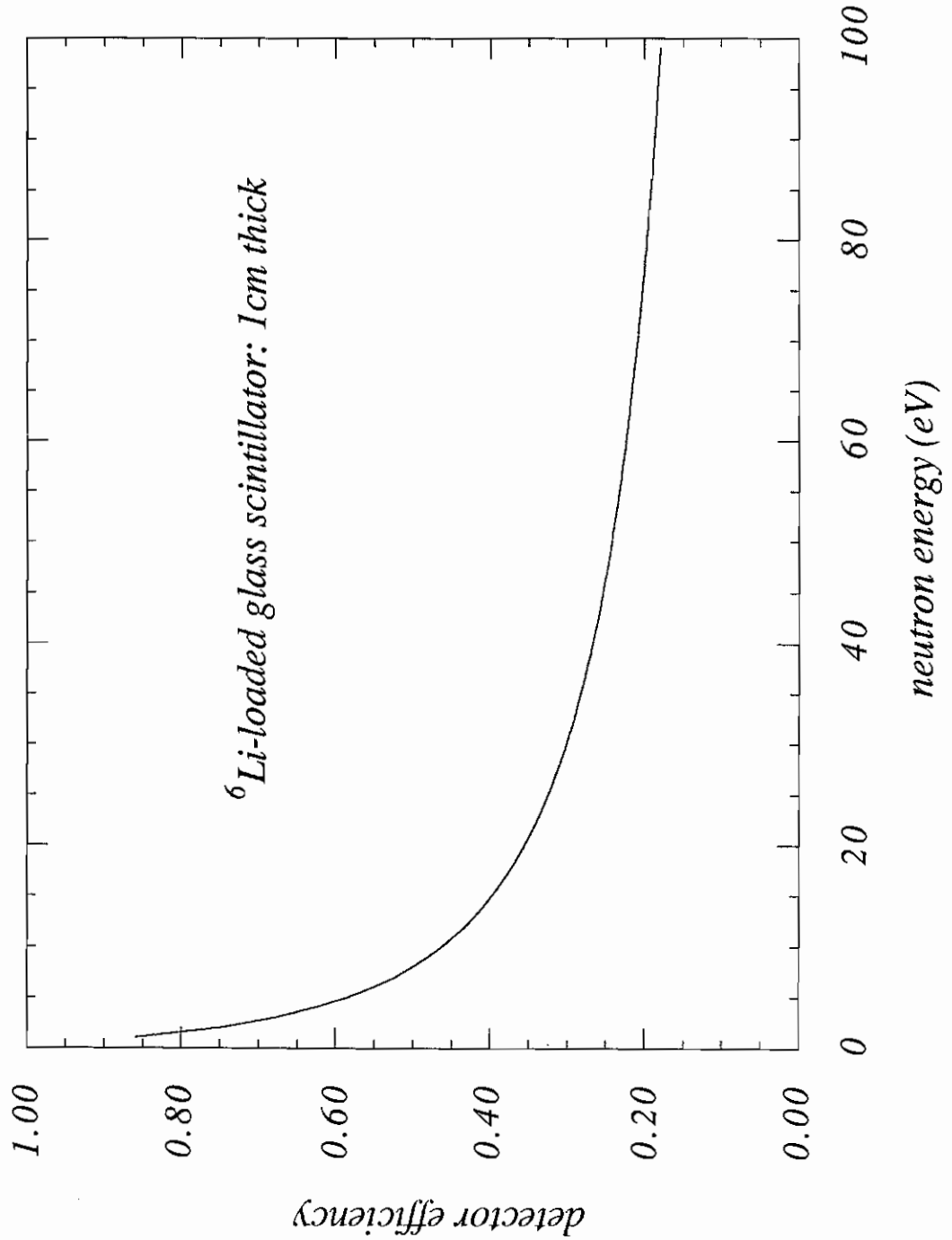

Figure 3.15: The detector efficiency vs neutron energy

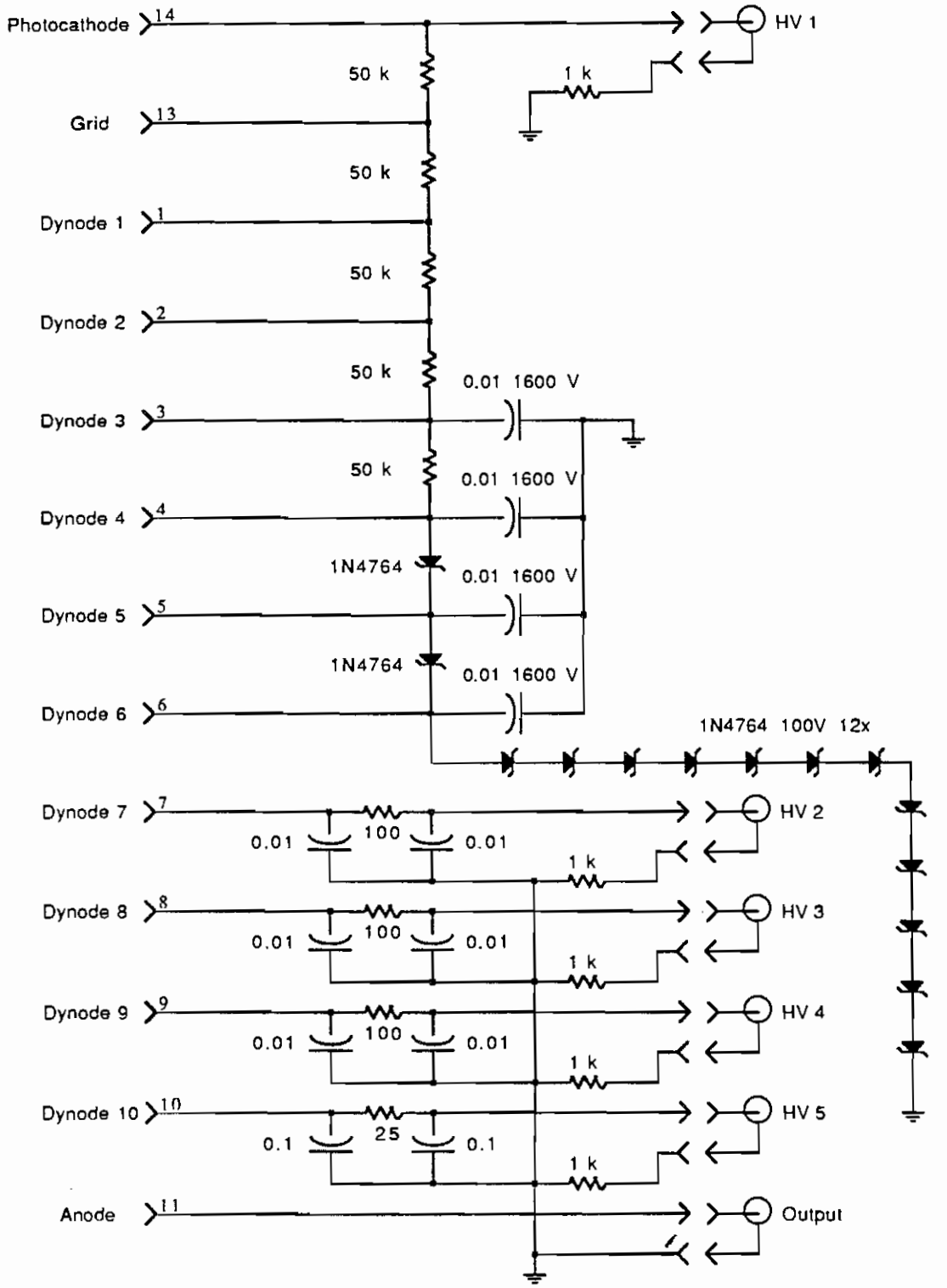

Figure 3.16: Circuit diagram of the PMT base

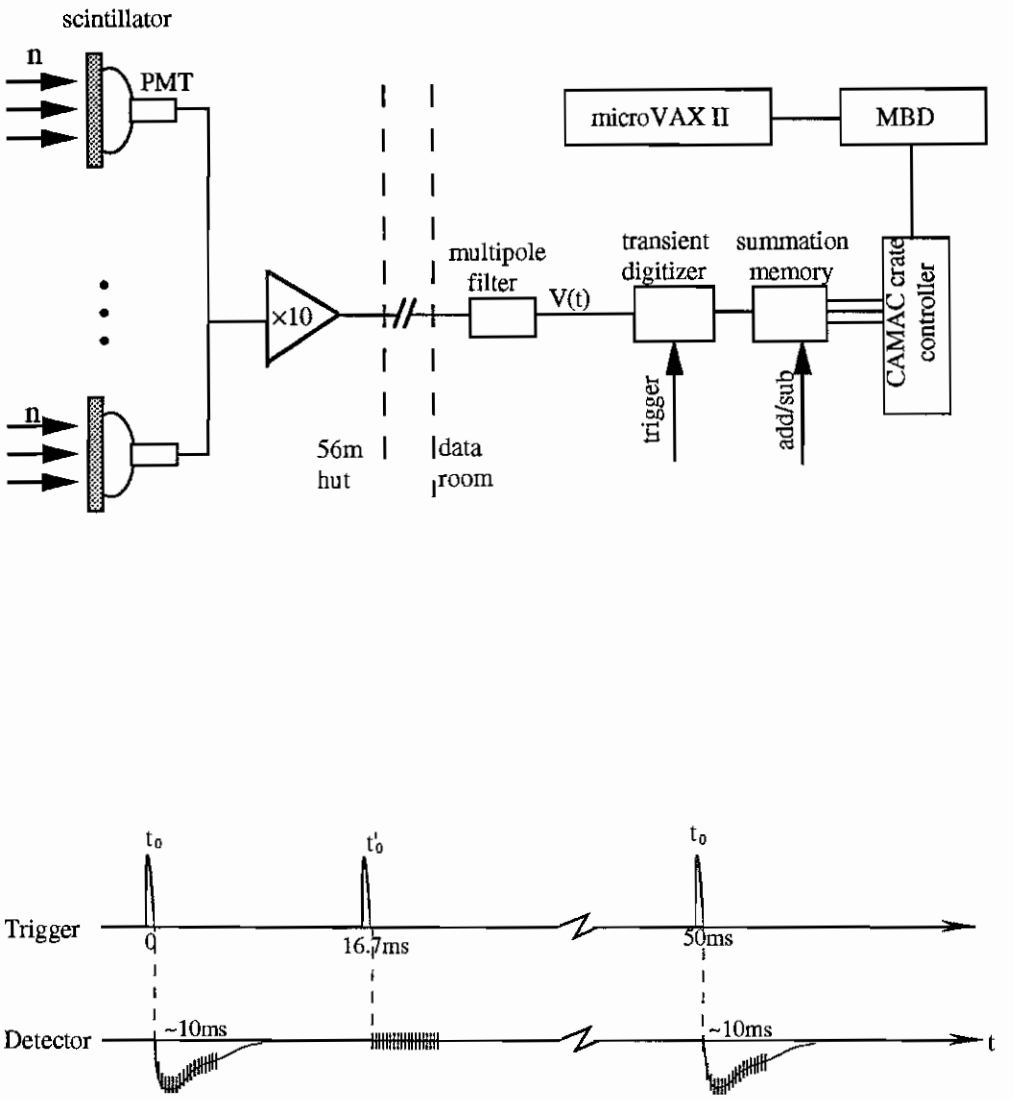

Figure 3.17: The detectors connected in current mode

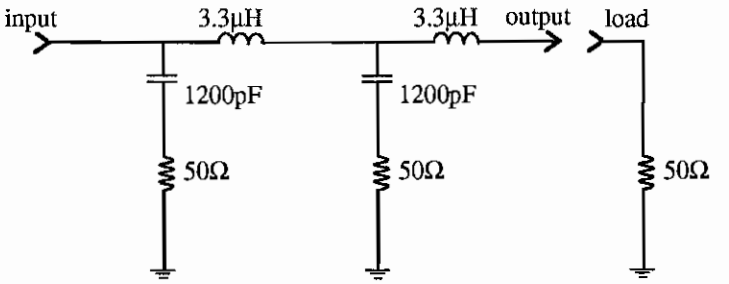

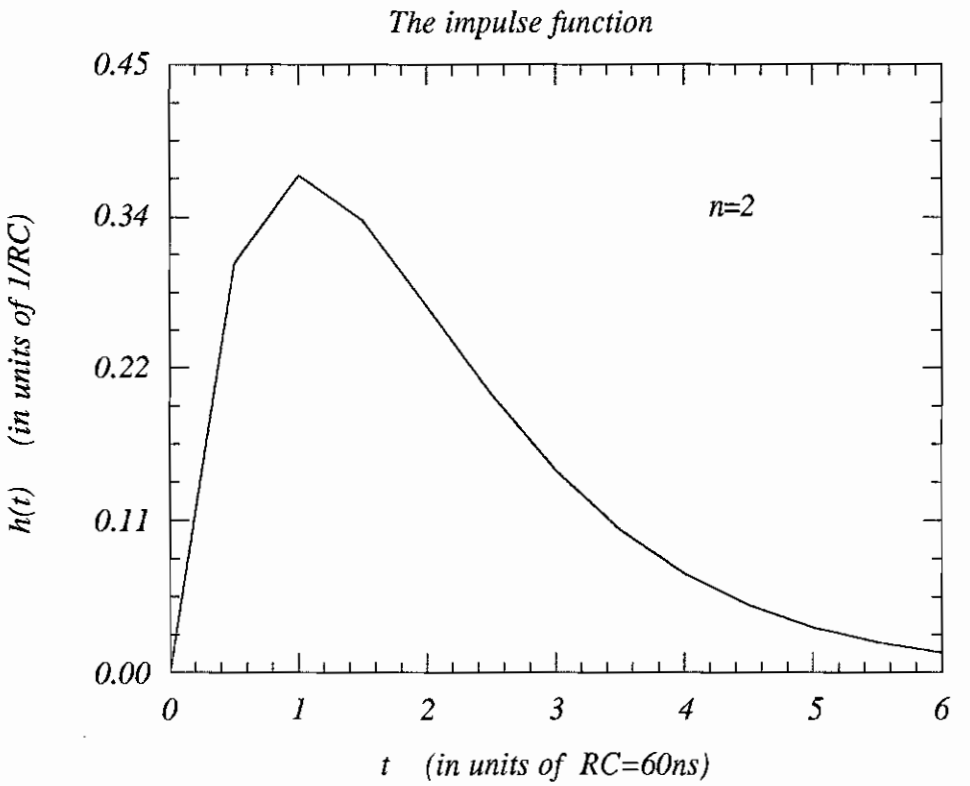

Figure 3.18: The multipole filter and its impulse function

The impulse response of the filter is given by

$$h(t) = \frac{1}{RC}\frac{(t/RC)^{n-1}}{(n-1)!}e^{-t/RC},$$

where $n = 2$ is the number of RC stages in the filter. The impulse function is plotted in the lower half of Figure 3.18 with $L = 3.3\mu H$, $C = 1200pF$ and $R = 50\Omega$.

It should be noticed that the filter conserves the area under the signal. That is

$$\int_{-\infty}^{+\infty} h(t)\,dt = \int_{-\infty}^{+\infty} \frac{(t/RC)^{n-1}}{(n-1)!}e^{-t/RC}\,d(t/RC) = 1.$$

A simple model can help us understand the relationship between the neutron flux and the anode voltage. Assuming that the filter stretches a single neutron event to a square pulse with a width of W and a height of v_0. Then neutrons that are detected between $t - W$ and t contribute to the signal at time t, as shown in Figure 3.19. If the neutron flux is $S(t)$, then the number of neutrons arriving between $t - W$ and t is $N = S(t)W$, and the voltage is

$$V(t) = S(t)Wv_0. \tag{3.5}$$

The voltage signal is digitized by a transient digitizer(DSP 2012S) which has a fast 12 bit ADC with 8K buffer memory. Upon a trigger signal, it digitizes 8K points on the voltage signal with fixed time interval which can range from 100 ns to 10 μs. The 8K points are subsequently accumulated in a summation memory(DSP 4101) which has 8K 24 bit memory. An option of the summation memory allows that the transient digitizer data can either be subtracted from or added to the content of the summation memory. For each beam burst, we digitizes the neutron signal, and subtract it from the summation memory; one sixtieth of a second later when the neutron signal is gone, we digitizes the baseline, and add it to the summation memory, as shown in the lower half of Figure 3.17. Therefore for each beam burst, we store an inverted neutron signal in the summation memory with baseline subtracted. The choice of 1/60 second is to eliminate any small 60Hz AC line noise associated with the operation of LAMPF linac. We can preprogram the summation memory to

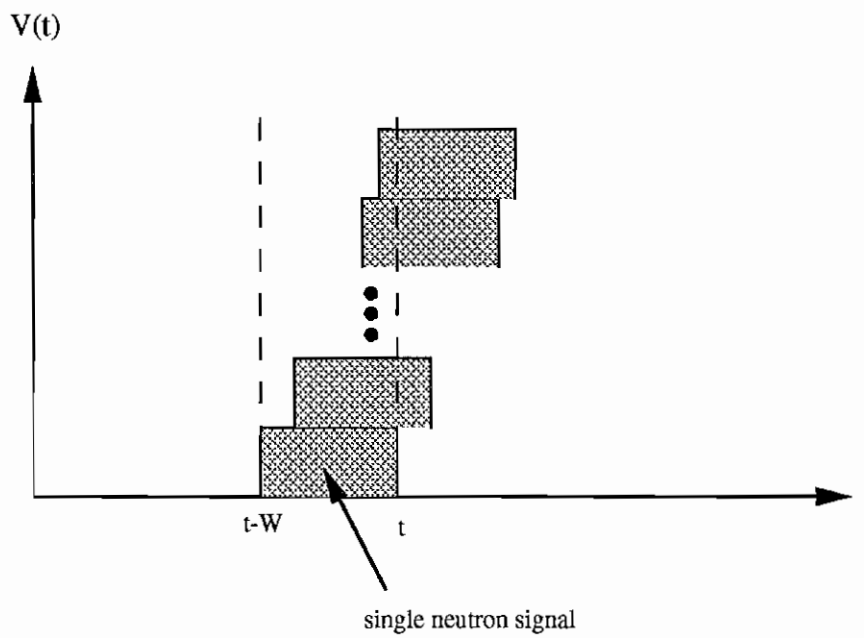

Figure 3.19: A simplified model relating the anode signal to the neutron flux

take certain number of sweeps before it interrupts the computer. The data in the summation memory is then transferred to the data acquisition computer through a MicroBranch Driver(MBD-11).

Figure 3.20 shows the effect of the subtraction. The top figure shows a spectrum taken with a 50Ω terminator without subtraction. The fluctuation is around 3000. The numbers are not centered at zero because of the DC offset of the transient digitizer. The bottom figure shows the effect of the subtraction. The fluctuation is less than 100 which is a 30 fold suppression.

In some situations (thick target, small detector, etc.) the count rate is low enough that the neutron pulses can be counted individually. A Canberra 8770 multiscaler with a summation memory(DSP 4100) is available for this purpose. Just like a transient digitizer, the multiscaler can record 8K points with fixed channel width which can vary from 100 ns to 10 μs. Figure 3.21 shows a simplified diagram of the detectors as they are used in the multiscaler mode. The neutron pulses were amplified, discriminated, and then sent through coaxial cables to the data room where they were reshaped to a width of 10 nsec. The reshaped pulses from the seven individual detectors were mixed together with a linear fan-in module, and are recorded by the multiscaler according to the neutron TOF.

3.8 Beam monitor

The beam monitor is a 1 mm thick, 6.35 by 6.35 cm square, ^{6}Li-loaded glass scintillator connected via a light guide to an AMP 2203B PMT. The scintillator was placed between the polarizer and the exit of the 2 inch diameter collimator. The PMT is placed inside sufficient magnetic shielding to reduce the effect of the fringe field from the cryostat superconducting magnet.

At the count rate encountered at this short flight path, there is a high probability for the neutron pulses to overlap. As a consequence, the normal pulse counting

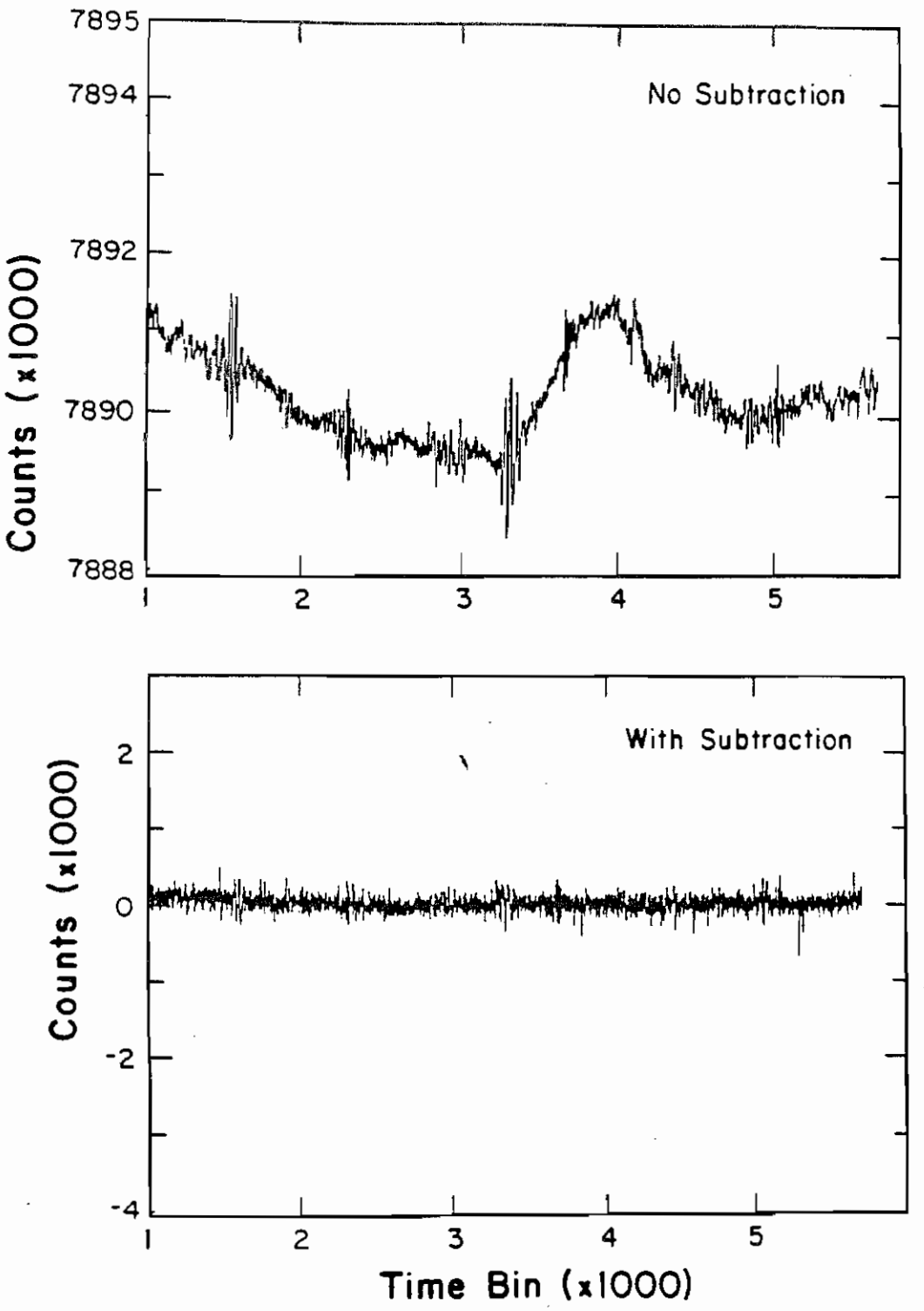

Figure 3.20: The effect of the subtraction

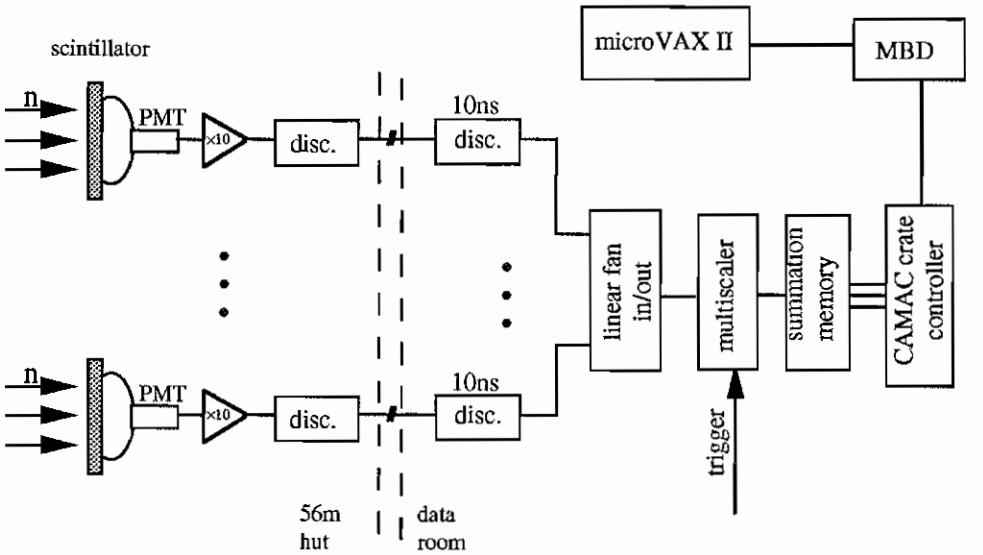

Figure 3.21: Detectors connected in multiscaler mode

technique is impossible. Instead the current signal from the anode is used as a measure of the count rate. From equation (3.1), the available neutron flux is

$$\Delta N \propto \frac{\Delta E_n}{E_n} \propto \frac{2\Delta T}{T},$$

where T is the neutron TOF. The count rate is then

$$\frac{\Delta N}{\Delta T} \propto \epsilon \frac{1}{T} \propto \sqrt{E_n}\,\epsilon,$$

where ϵ is the monitor efficiency. For ^{6}Li-loaded glass scintillators,

$$\epsilon \propto \frac{1}{v_n} \propto \frac{1}{\sqrt{E_n}},$$

therefore the anode current signal is approximately constant,

$$i \propto \epsilon\sqrt{E_n} \propto \frac{1}{\sqrt{E_n}}\sqrt{E_n} \sim \text{constant}.$$

The short flight path and the energy independence of the anode current signal combine to produce a pulse for each neutron burst that is approximately constant for a period of about 2 msec. The area of the pulse is an excellent measure of the total neutron flux.

The anode of the PMT is connected to a current-to-frequency converter (CFC) which produces a series of pulses. The pulses are gated and counted by a foreground scaler and a background scaler, as shown in Figure 3.22. The trigger signal t_0, which is obtained from a time pickoff for each neutron beam burst, is passed to a precision double pulser. At the *pulse* output, the pulser regenerates t_0 with little time delay and a second pulse t_0', exactly 1/60 second later. The pulse output goes to a gate generator which generates a 3 ms wide gate for each incoming pulse (t_0 or t_0'). At the *sub* output, the pulser produces a 5V DC level at the t_0 signal, and a 0V DC level at the t_0' signal, which is used to pass the gated CFC pulses to the desired scalers. At the t_0 signal when the neutron pulses are present, the coincidence to the foreground scaler is enabled, and a train of pulses, lasting 3 msec, is counted by the foreground scaler; similarly at the t_0' signal when neutron signals are gone, the coincidence to the

background scaler is enabled, and a train of pulses, 3 msec long, is counted by the background scaler. The two scalers are read by the data acquisition system, and the difference between the two scalers is a background corrected measure of the neutron flux for each beam burst (0.2% statistical error).

The monitor is not used for normalizing the data but rather for monitoring the stability of the beam. In a production run, the data is taken in units of the 8-step-sequences which we have discussed earlier. The monitor signal is measured for each beam burst and stored temporarily in computer memory. At the end of a 8-step-sequence, the mean of the monitor is calculated, and a gate with a width of $\pm 8\%$ of the mean is set around the mean. If all monitor readings in the 8-step-sequence are inside this gate, the beam is considered stable, and the neutron transmission data taken in the current 8-step-sequence will be accumulated; if any monitor reading is outside this 8% gate, the beam is considered unstable, and the transmission data will not be accumulated. The monitor data is then cleared out of the computer memory for the next 8-step-sequence. In this way, we rejected about 20% of the production data, but the quality of the remaining data is insured.

3.9 Data acquisition system

The data acquisition system consists of CAMAC modules, an intelligent CAMAC controller, the MBD-11, and a microVAX II. Block diagrams of the various parts of the system are seen in Figures 3.10, 3.17, 3.21, and 3.22. The data acquisition software was written using the IUCF XSYS data acquisition package.

The data acquisition is controlled by the 20 Hz timing signal t_0 which signals the arrival of the proton beam bursts at the spallation target. After each beam burst, the monitor foreground and background scalers are read by the MBD and the counts are transferred to the microVAX memory. The difference in the foreground counts and the background counts is, as discussed in section 3.8, proportional to the total

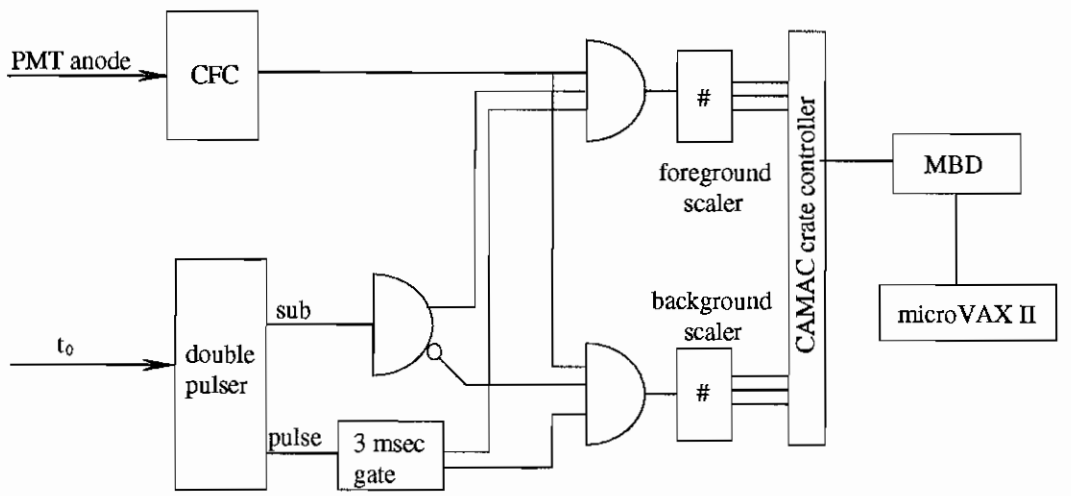

Figure 3.22: Schematic of the beam monitor circuit

neutron flux in each beam burst. These monitor counts are stored in a data area event by event, and are used to establish the beam stability during each 8-step-sequence.

Since the transient digitizer stores its data in a CAMAC module (the summation memory), no action is required by the MBD during a given spin state. After a fixed number of t_0 pulses (200), the summation memory module interrupts the MBD and requests that the contents of the summation memory to be transferred to the VAX memory.

A number of scalers are used to record the parameters of the experiment, such as the number of times the spin direction has been reversed, the number of t_0's in each spin state, and the elapsed time for each spin state. The scalers were read in every 2 seconds and at the end of each spin state, and displayed at the operator console, so that the state of the experiment could be monitored. In addition, a scanning ADC was used to read the spin flipper transverse coil current, and the results were used to test that the spin flipper was in the correct state, and to route the data to the proper data area.

3.10 Experimental procedure

The experimental data was taken in a series of measurements each lasting about 30 minutes. A NMR measurement was taken at the beginning of each run to monitor the proton polarization of the LMN crystal. From the NMR calibration (appendix B), we are able to determine the neutron polarization and make corrections for the slow time drifts of the polarization. In general, we found the polarization from run to run is constant to within a few percent. Following the NMR measurement are the neutron transmission measurements for 160 preprogrammed neutron spin sequences. The TOF bin width was chosen to be 200 ns to cover neutron energy of 6 eV to 1 keV. The 160 spin sequences are grouped into 8-step-sequences as discussed in section 3.5. For each spin state, data was accumulated for 200 beam bursts (about 10 seconds).

The data for each spin state ($\pm$ helicity) was accumulated in temporary data areas in the computer memory. At the end of a 8-step-sequence, the monitor data is examined for beam stability. If the monitor counts for each of the $8 \times 200 = 1600$ beam bursts are within $\pm 8\%$ of the average in the 8-step-sequence, then the data is transferred and accumulated in the "good" data areas (data areas 3 and 4). Otherwise, it is transferred and accumulated in the "bad" data areas (data areas 5 and 6). The temporary data areas are cleared before each 8-step-sequence. Occasionally, other errors occur, such as a failure in the spin flipper control relays. These conditions are also sensed and cause the data to be stored in the "bad" data areas. After the 20 8-step-sequences are finished, all the data is archived to the computer disk.

Approximately once a day, the proton polarization is reversed by changing the microwave frequency.

Chapter 4

Method of Data Analysis

4.1 Introduction

In this chapter, we will discuss the method of extracting the parity violating asymmetry for a p-wave resonance. As discussed in chapter 2, if we neglect the interference term, the total cross section of a p-wave resonance can be written as

$$\sigma = \sigma_{potential} + \sigma^{\pm}$$

where $\sigma^{\pm} = \sigma_p(1 \pm f_n p)$ is the resonance cross section for $+$ and $-$ helicity neutrons, respectively, σ_p is the p-wave resonance cross section as given by equation (2.5), f_n the neutron polarization, and p the parity violating asymmetry we are trying to determine.

The neutron transmission yield at the detector is given by

$$\begin{aligned} N^{\pm} &= F(E_n)e^{-nt[\sigma_{potential}+\sigma_p(1\pm f_n p)]} \\ &= C(E_n)e^{-nt\sigma_p(1\pm f_n p)} \end{aligned}$$

where $F(E_n)$ is the neutron flux, E_n the neutron energy, $C(E_n) = F(E_n)e^{-nt\sigma_{potential}}$, n the number density of the ^{238}U target nuclei, and t the thickness of the target. The

transmission asymmetry is

$$\varepsilon \equiv \frac{N^+ - N^-}{N^+ + N_-} = -\tanh(f_n n \sigma_p t p).$$

If p is small, the above equation reduces to

$$\varepsilon = -f_n n \sigma_p t p. \tag{4.1}$$

The neutron transmission yield and the transmission asymmetry are shown in Figure 4.1 for the 63.5eV p-wave resonance. The upper plot is the neutron transmission spectrum, the bottom one is the transmission asymmetry. The large asymmetry at the 63.5 eV resonance clearly indicates a strong parity violation.

Although the ε plot is efficient to demonstrate the existence of a large parity violation, it is difficult to use to extract p because σ_p is not known accurately. Furthermore, it has to be corrected for Doppler broadening. This method is also sensitive to the background which is not negligible in the current mode data. One may try to correct for these effects, but such corrections are difficult to make with accuracy.

We developed an alternate method of analysis which involves fitting the transmission spectra of both helicities simultaneously. With this method, we can reliably extract the parity violating asymmetries. The detail of this analysis is discussed below.

4.2 Doppler broadening of a p-wave resonance

Because of the thermal motion of the target nuclei, the resonances are broadened. This effect is called Doppler broadening. Since the total width of a typical p-wave resonance of ^{238}U is around 20 meV, and at room temperature the average thermal energy of the target nuclei is $\frac{1}{2}K_BT \sim 25$ meV (K_B the Boltzmann constant, T the effective target temperature), the Doppler broadening can not be neglected.

For simplicity, let us consider the one dimensional problem. A neutron of mass m_n and velocity v moves toward a target nucleus of mass M and velocity V, as shown

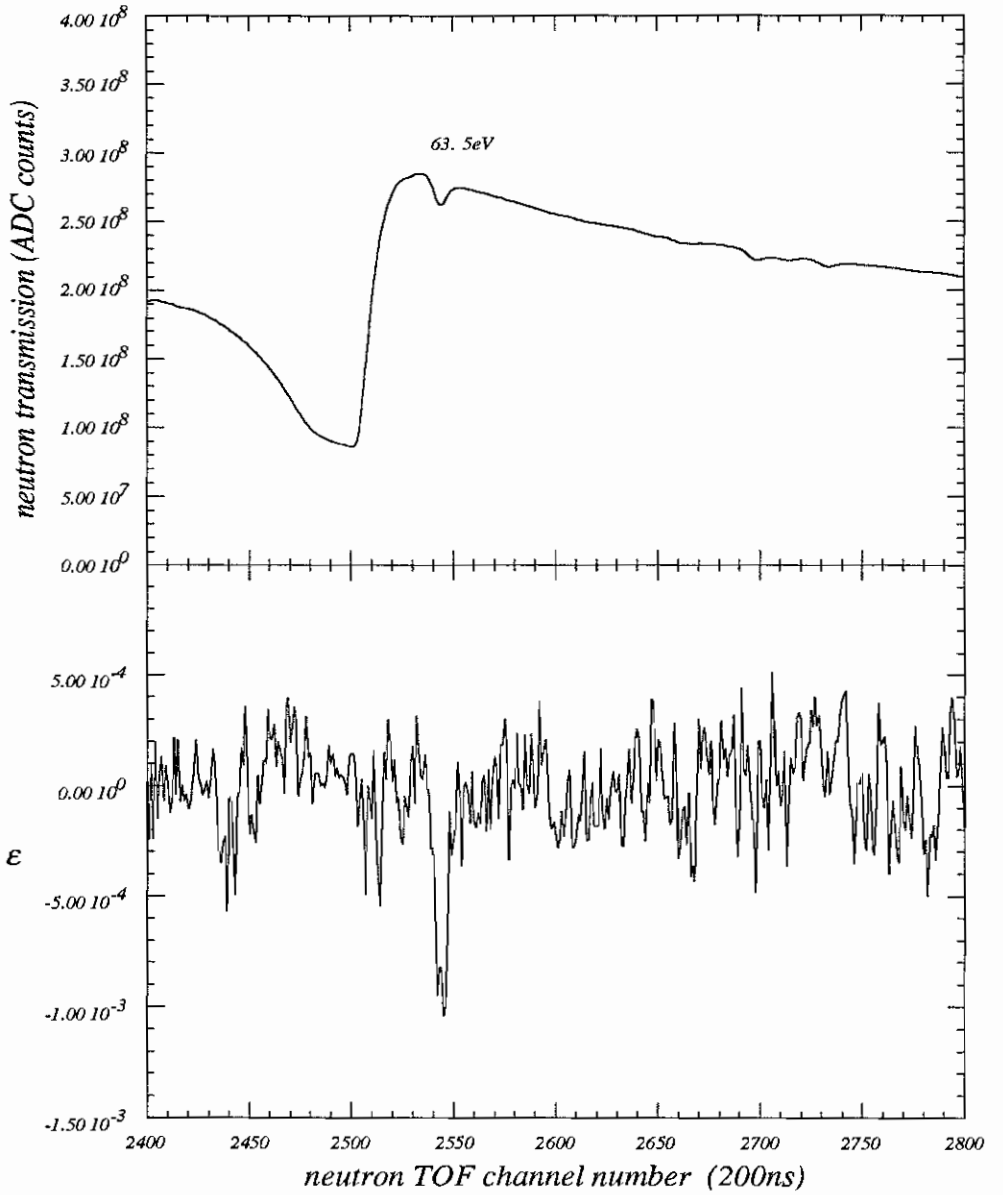

Figure 4.1: The transmission yield and the transmission asymmetry near the 63eV p-wave resonance

below

neutron	target
m_n, v	M, V
$\bullet\longrightarrow$	$\bullet\longrightarrow$

The velocity of the center of mass is

$$V_{cm} = \frac{m_n v + MV}{M + m_n},$$

and the kinetic energy of the pair in the center of mass system is

$$E = \frac{1}{2}\mu(\dot{\vec{r}}_{m_n} - \dot{\vec{r}}_M)^2 = \frac{1}{2}\mu(v - V)^2 \tag{4.2}$$

where $\mu = \frac{Mm_n}{M+m_n}$ is the reduced mass.

The p-wave resonance cross section is, as given by equation (2.5)

$$\sigma_p = \pi\lambda^2 \frac{\Gamma_p \Gamma_p^n}{(E_p - E)^2 + \Gamma_p^2/4}$$

where Γ_p is the total width, Γ_p^n the neutron width, E the center of mass energy, E_p the resonance energy, and λ the de Broglie length which is related to E by

$$E = \frac{\hbar^2 k^2}{2\mu} = \frac{\hbar^2}{2\mu\lambda^2}.$$

For a p-wave resonance, the neutron width Γ_p^n depends on energy as (see chapter 2)

$$\Gamma_p^n \propto E^{\frac{3}{2}},$$

therefore the p-wave resonance cross section can be written as

$$\sigma_p = \beta \frac{\sqrt{E}}{(E_p - E)^2 + \Gamma_p^2/4} \tag{4.3}$$

where β is a constant depending on the resonance parameters. The maximum cross section is then

$$\sigma_{max} = \frac{\beta\sqrt{E_p}}{\Gamma_p^2/4}. \tag{4.4}$$

Assuming that the target nucleus obeys the Boltzmann distribution

$$P(V) = \sqrt{\frac{M}{2\pi K_B T}} e^{-\frac{MV^2}{2K_B T}}, \tag{4.5}$$

the Doppler broadened cross section is then

$$\sigma_{eff}(E_n) = \int_{-\infty}^{+\infty} \sigma_p(v,V)P(V)\,dV. \tag{4.6}$$

Substituting equation (4.2) into (4.3), and (4.3), (4.5) into (4.6), one finds

$$\begin{aligned}
\sigma_{eff}(E_n) &= \beta\sqrt{\frac{M}{2\pi K_B T}}\int_{-\infty}^{+\infty} e^{-\frac{MV^2}{2K_BT}} \frac{\sqrt{\frac{1}{2}\mu(v-V)^2}}{[E_p - \frac{1}{2}\mu(v-V)^2]^2 + \Gamma_p^2/4}dV \\
&= \beta\sqrt{\frac{\mu}{2\pi}}\int_{-\infty}^{+\infty} e^{-u^2} \frac{\left|v - \sqrt{\frac{2K_BT}{M}}u\right|}{\left[E_p - \frac{1}{2}\mu\left(v - \sqrt{\frac{2K_BT}{M}}u\right)^2\right]^2 + \Gamma_p^2/4}du \\
&= \frac{\beta}{\sqrt{\pi}E_p^{\frac{3}{2}}}\int_{-\infty}^{+\infty} e^{-u^2} \frac{\left|\frac{v}{v_0} - \sqrt{\frac{2K_BT}{M}}\frac{u}{v_0}\right|}{\left[1 - \left(\frac{v}{v_0} - \sqrt{\frac{2K_BT}{M}}\frac{u}{v_0}\right)^2\right]^2 + \left(\frac{\Gamma_p}{2E_p}\right)^2}du
\end{aligned} \tag{4.7}$$

where we have used $E_p \equiv \frac{1}{2}\mu v_0^2$ and the substitution $u \equiv \sqrt{\frac{M}{2K_BT}}V$.
To simplify equation (4.7), we introduce two dimensionless parameters

$$\begin{aligned}
B^2 &\equiv \left(\frac{2E_p}{\Gamma_p}\right)^2, \\
C &\equiv \sqrt{\frac{E_pA}{K_BT}},
\end{aligned}$$

where A is the atomic number of the nucleus. Then

$$\sqrt{\frac{2K_BT}{M}}\cdot\frac{1}{v_0} = \sqrt{\frac{K_BT}{M/\mu}\frac{1}{E_p}} \cong \frac{1}{\sqrt{\frac{E_pA}{K_BT}}} = \frac{1}{C}$$

and

$$\frac{v}{v_0} = \frac{l}{(K-K_s)D}\cdot\frac{(K_0-K_s)D}{l} = \frac{K_0-K_s}{K-K_s}$$

where l is the length of the flight path, D the TOF bin width, K the TOF channel number, K_0 the channel number of the resonance peak, and K_s the zero TOF channel number. In the calculation, we have used $\mu \approx m_n$ and $M/m_n = A$.

In terms of the parameters B^2 and C, equation (4.7) can be written as

$$\sigma_{eff}(K) = \sigma'_{max}\int_{-\infty}^{+\infty} e^{-u^2} \frac{\left|\frac{K_0-K_s}{K-K_s} - \frac{u}{C}\right|}{1 + B^2[1 - (\frac{K_0-K_s}{K-K_s} - \frac{u}{C})^2]^2}du \tag{4.8}$$

where $\sigma'_{max} = \frac{\sigma_{max}}{\sqrt{\pi}}$.

As an example, we can calculate the Doppler broadening of a typical p-wave resonance of ^{238}U at room temperature. Assuming $E_p = 63.5$ eV, $\Gamma_p = 20$ meV, and $\frac{1}{2}K_BT = 1/40$ eV, we can calculate B^2 and C as

$$\begin{aligned} B^2 &\equiv \left(\frac{2E_p}{\Gamma_p}\right)^2 = 4.0 \times 10^7, \\ C &\equiv \sqrt{\frac{E_p A}{K_B T}} = 7.8 \times 10^2. \end{aligned}$$

To compare the Doppler broadened resonance with the unbroadened one, we express the unbroadened cross section (equation 4.3) in terms of the TOF channel numbers

$$\frac{\sigma_p}{\sigma_{max}} = \frac{v}{v_0} \frac{1}{1 + B^2\left[1 - \left(\frac{v}{v_0}\right)^2\right]^2} \tag{4.9}$$

$$= \frac{\frac{K_0 - K_s}{K - K_s}}{1 + B^2\left[1 - \left(\frac{K_0 - K_s}{K - K_s}\right)^2\right]^2}. \tag{4.10}$$

For a bin width of 200 ns, we have $K_0 = 2.5447 \times 10^3$, and $K_s = -18.57$ (see chapter 5). The normalized cross sections are shown in Figure 4.2. The solid line represents $\sigma_{eff}/\sigma_{max}$, the Doppler broadened resonance , and the dotted line represents σ_p/σ_{max}, the unbroadened resonance. At room temperature, the Doppler broadening reduces the peak strength by a factor of 20, while spreading the resonance by a factor of four. The Doppler broadening is indeed important and must not be neglected.

Before closing this section on Doppler broadening, it is useful to discuss the criteria for choosing the integration stepsize for equation (4.8). Notice that the integrand is the product of a Gaussian

$$e^{-u^2}$$

and a Lorenzian

$$\frac{\left|\frac{K_0 - K_s}{K - K_s} - \frac{u}{C}\right|}{1 + B^2\left[1 - \left(\frac{K_0 - K_s}{K - K_s} - \frac{u}{C}\right)^2\right]^2}.$$

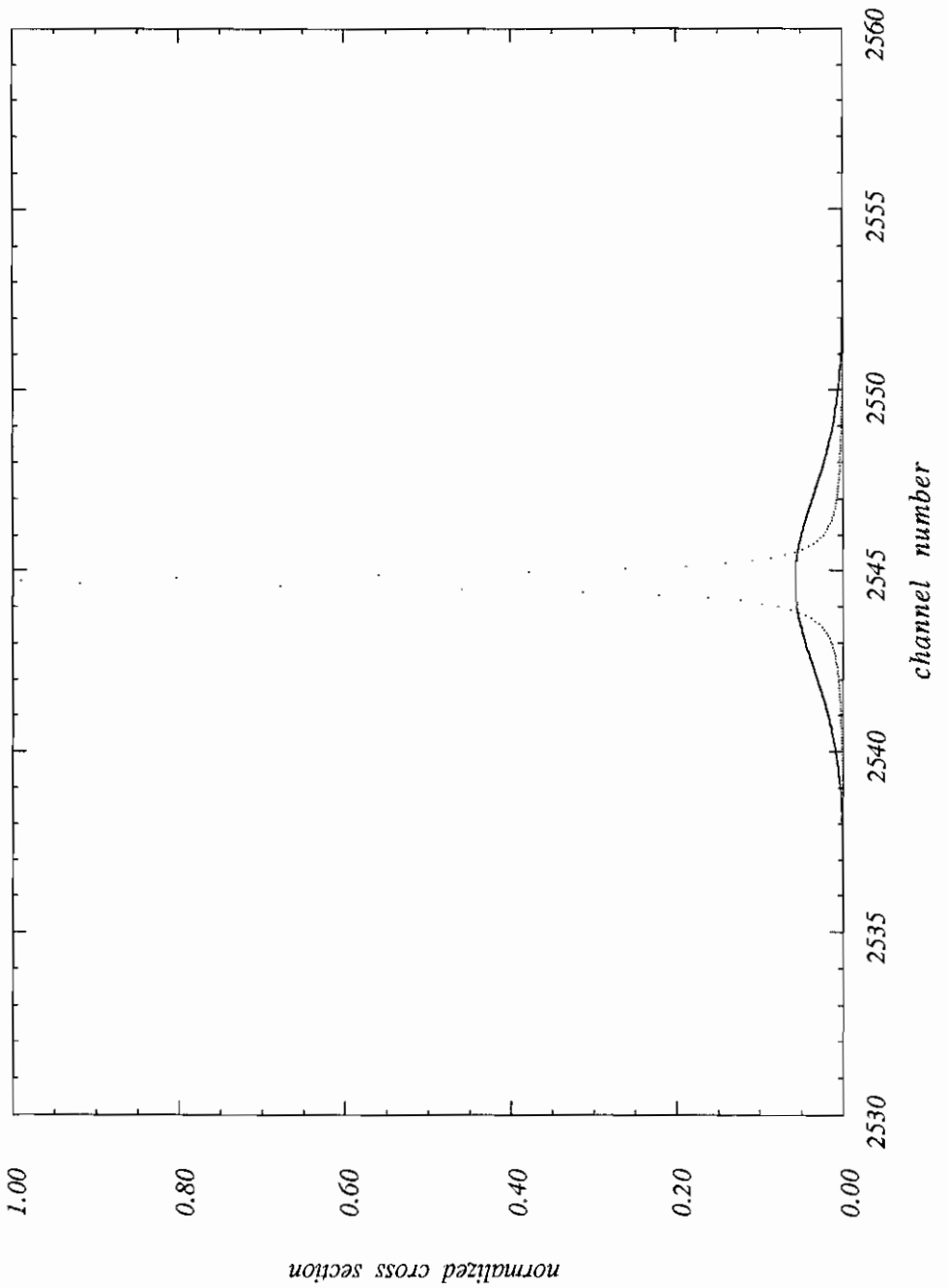

Figure 4.2: The Doppler broadening of a typical ^{238}U p-wave resonance at room temperature. E_p=63.5eV, Γ_p=20meV, $\frac{1}{2}K_BT = \frac{1}{40}$eV and TOF bin width=200 ns. The solid line represents the Doppler broadened resonance $\sigma_{eff}/\sigma_{max}$, the dotted line represents the unbroadened resonance σ_p/σ_{max}.

Therefore we can choose the stepsize to be 0.1, one twentieth of the Gaussian width, or one tenth of the Lorenzian width, whichever is smaller. The Lorenzian width can be determined as follows. Since

$$\begin{aligned} \frac{K_0 - K_s}{K - K_s} &\approx 1 \\ C &> 100 \\ u &< 4, \end{aligned}$$

the Lorenzian can be simplified as

$$\begin{aligned} \frac{|\frac{K_0-K_s}{K-K_s} - \frac{u}{C}|}{1 + B^2[1 - (\frac{K_0-K_s}{K-K_s} - \frac{u}{C})^2]^2} &\approx \frac{|1 - \frac{u}{C}|}{1 + B^2[1 - (1 - \frac{u}{C})^2]^2} \\ &= \frac{|1 - \frac{u}{C}|}{1 + (\frac{2B}{C})^2 u^2} \\ &= \left(\frac{C}{2B}\right)^2 \frac{1}{u^2 + (\frac{C}{2B})^2}. \end{aligned}$$

Therefore the Lorenzian width is approximately $\frac{C}{B}$, and the integration stepsize for equation (4.8) can be chosen to be 0.1 or $0.1\frac{C}{B}$, whichever is smaller.

4.3 The fitting function

As determined in appendix C, the neutron flux from the spallation source is inversely proportional to neutron energy

$$\Delta N \propto \frac{\Delta E_n}{E_n} \tag{4.11}$$

where ΔN is the number of neutrons with energies in the interval $E_n \rightarrow E_n + \Delta E_n$. The neutron energy E_n is related to the time-of-flight T through

$$E_n = \frac{1}{2} m_n \left(\frac{l}{T}\right)^2$$

where l is the length of the flight path. Therefore

$$\frac{\Delta E_n}{E_n} = -2\frac{\Delta T}{T}$$

or

$$\Delta N \propto \frac{\Delta T}{T}.$$

We use the following form to describe the transmission yield at the detector

$$\begin{aligned} N^{\pm} &= C_{\pm} \exp[-n\sigma'_{max}\varphi(1 \pm f_n p)] \\ &= \frac{N'(1 \pm \alpha)}{K - K_s} \left[1 + \sum_{i=1}^{5} \alpha_i \left(\frac{K - \frac{K_b+K_e}{2}}{1000}\right)^i\right] \exp[-n\sigma'_{max}\varphi(1 \pm f_n p)] \end{aligned} \quad (4.12)$$

where $C_{\pm}$ is the flux, $\sigma'_{max}\varphi$ the Doppler broadened p-wave resonance lineshape as given by equation (4.8), N' the normalization factor, K the TOF channel number, α the beam asymmetry in the two helicity states, and $[K_b,K_e]$ the range of channels we are interested in. The fifth order polynomial in the square brackets describes the slow energy dependent effects such as the potential scattering and the detector efficiency, as well as any deviation from the $\frac{1}{T}$ dependence in the neutron flux.

The voltage signal that the transient digitizer samples is related to $N^{\pm}$ as follows. As discussed in chapter 3, the detector gives the same response for all epithermal neutrons. Denoting the single neutron signal by $v(t)$ and the neutron flux by $S(t)$, the number of neutrons striking the detector at $t' \rightarrow t' + dt'$ is $S(t')\,dt'$, and the voltage signal in a beam burst is expected to be

$$\begin{aligned} V(t) &= \int_{-\infty}^{+\infty} S(t')\,dt' v(t - t') \\ &= \int_{0}^{t} S(t - \tau) v(\tau)\,d\tau \end{aligned} \quad (4.13)$$

where we have made the substitution $\tau = t - t'$ and used $v(\tau) = 0$ for $\tau < 0$. The multipole filter stretches the single neutron pulses such that $v(t)$ is approximately a square pulse of width W and amplitude v_0. For such a square pulse, equation (4.13) can be further simplified to

$$V(t) = S(t) W v_0$$

which is the same as equation (3.5) that we derived using a pictorial argument. If the bin width of the transient digitizer is W, we have $S(t)W = N^{\pm}$. Therefore the

transient digitizer data $Y^{\pm}$ is proportional to $N^{\pm}$. Using equation (4.12), one can write

$$Y^{\pm} = \frac{N(1 \pm \alpha)}{K - K_s} \left[1 + \sum_{i=1}^{5} \alpha_i \left(\frac{K - \frac{K_b + K_e}{2}}{1000} \right)^i \right] \exp[-n\sigma'_{max}\varphi(1 \pm f_n p)] \qquad (4.14)$$

where

$$\varphi = \int_{-\infty}^{+\infty} e^{-u^2} \frac{|\frac{K_0 - K_s}{K - K_s} - \frac{u}{C}|}{1 + B^2[1 - (\frac{K_0 - K_s}{K - K_s} - \frac{u}{C})^2]^2} du.$$

The adjustable parameters for $Y^{\pm}$ are summarized as follows:

index	parameter	description
1	α_1	
2	α_2	
3	α_3	flux parameters
4	α_4	
5	α_5	
6	N	normalization
7	K_0	location of the resonance peak
8	$B^2 \equiv (\frac{2E_p}{\Gamma_p})^2$	resonance parameter
9	$C \equiv \sqrt{\frac{E_p A}{K_B T}}$	Doppler broadening parameter
10	$\sigma'_{max} = \frac{\sigma_{max}}{\sqrt{\pi}}$	σ_{max}: peak resonance cross section
11	α	beam asymmetry
12	$f_n p$	product of the neutron polarization and the parity violating asymmetry.

The method of least square fit is discussed in appendix D.

4.4 Errors in the fitting parameters

As we showed in the last section, $Y^{\pm}$ is proportional to $N^{\pm}$

$$Y^{\pm} = aN^{\pm}$$

where a is a constant determined by the physical properties of the scintillator, the multipole filter, the gain of the amplifier, and the slope of the transient digitizer. The error in $Y^{\pm}$ is then

$$\sigma_{Y^{\pm}} = a\sqrt{N^{\pm}} = \sqrt{aY^{\pm}}.$$

Had we known the value of a exactly, we would have defined the χ^2 and the curvature matrix as follows

$$\chi_0^2 = \sum_i \frac{[Y_i^{\pm} - Y^{\pm}(K_i)]^2}{\left(\sqrt{aY_i^{\pm}}\right)^2}$$

$$\alpha^0_{jj'} = \sum_i \frac{1}{\left(\sqrt{aY_i^{\pm}}\right)^2} \frac{\partial Y^{\pm}(K_i)}{\partial a_j} \frac{\partial Y^{\pm}(K_i)}{\partial a_{j'}}$$

where $Y_i^{\pm}$ is the transient digitizer reading at TOF channel i, a_j is the j-th fitting parameter. The sum is performed over i as well as the helicities $\pm$. Since we do not know the exact value of a, we construct the χ^2 and the curvature matrix as follows instead:

$$\begin{aligned}
\chi^2 &= \sum_i \frac{[Y_i^{\pm} - Y^{\pm}(K_i)]^2}{\left(\sqrt{Y_i^{\pm}}\right)^2} \\
&= a\sum_i \frac{[Y_i^{\pm} - Y^{\pm}(K_i)]^2}{\left(\sqrt{aY_i^{\pm}}\right)^2} \\
&= a\chi_0^2,
\end{aligned}$$

$$\begin{aligned}
\alpha_{jj'} &= \sum_i \frac{1}{(\sqrt{Y_i^{\pm}})^2} \frac{\partial Y^{\pm}(K_i)}{\partial a_j} \frac{\partial Y^{\pm}(K_i)}{\partial a_{j'}} \\
&= a\alpha^0_{jj'}.
\end{aligned}$$

Therefore the error matrix ϵ is related the "correct" one ϵ^0 as

$$\epsilon = \frac{1}{a}\epsilon^0,$$

and the error in a_j is

$$\sigma_{a_j} = \sqrt{\epsilon^0_{jj}}$$

$$\begin{aligned} &= \sqrt{\epsilon_{jj}}\sqrt{a} \\ &= \sqrt{\epsilon_{jj}}\sqrt{\chi^2_\nu} \end{aligned} \tag{4.15}$$

where χ^2_ν is the χ^2 per degree of freedom (see appendix D). Since $\chi^2_{0,\nu} = 1$, we have

$$\chi^2_\nu = a\chi^2_{0,\nu} = a.$$

4.5 Effect of the background

In the presence of a beam related background, the transmission yield can be written as

$$Y^{\pm} = C_{\pm}\left[e^{-n\sigma'_{max}\varphi(1\pm f_n p)} + B\right] \tag{4.16}$$

where B is the ratio of the background to the true neutron signal. For the ^{238}U target, $nt = 0.12$/barn, $\sigma_{max} \approx 5$ barn, $\varphi \approx 0.1$ (for a typical p-wave resonance), so $nt\sigma'_{max}\varphi \approx 0.03$. We can then expand equation (4.16) as

$$\begin{aligned} Y^{\pm} &= C_{\pm}[1 + B - n\sigma'_{max}\varphi(1 \pm f_n p)] \\ &= C_{\pm}(1+B)\left[1 - n\frac{\sigma'_{max}}{1+B}\varphi(1 \pm f_n p)\right] \\ &= C'_{\pm}e^{-n\sigma''_{max}\varphi(1\pm f_n p)}, \end{aligned} \tag{4.17}$$

where

$$\begin{aligned} C'_{\pm} &= C_{\pm}(1+B), \\ \sigma''_{max} &= \frac{\sigma'_{max}}{1+B}. \end{aligned}$$

Therefore to first order, the background does not effect the extraction of the parity violating asymmetry. It only effects the overall normalization and the peak cross section.

Chapter 5

Data Analysis

5.1 The production data set

The ^{238}U production data was taken with a sampling period of 200 ns. While this covers the neutron energy range of 6 eV to 1 keV, poor energy resolution and low detector efficiency at the higher energies restrict the analyzable data to the energies below 300 eV.

Each run measures the NMR signal for polarization and the neutron transmission yields in both helicities. The neutron transmission yields are sorted according to the helicity as follows:

	"good"	"bad"
FLIP	3	5
NOFLIP	4	6

where "FLIP" and "NOFLIP" correspond to certain neutron helicities as described in appendix B. The data areas 3 and 4 hold the "good" data which was taken when the beam was stable, the data areas 5 and 6 hold the "bad" data which was taken when the beam was unstable.

All the production runs were inspected before being analyzed. As part of that inspection, an integrated neutron transmission yield was obtained for each run by

summing all the TOF spectra (3, 4, 5, 6) from channel 5000 to 6000 (11.6 eV to 16.7 eV). A plot of this summed data is shown in Figure 5.1 as a function of the run number. Each cross there represents a production run. It is clear that the polarized neutron flux started to decrease in the development period between runs 4520 and 4683 and finally dropped to below 30% of the original value. It was later determined that this decrease in flux was caused by ice buildup inside the cryostat due to a vacuum leak. Figure 5.2 shows the effect of the ice on the transmission data. Run 4110 is normal, and run 4768 is with ice and is normalized to run 4110 for comparison. Besides reducing the neutron flux, the buildup ice changes the shapes of the flux and the resonances as well. As the ice buildup is continuous, and likely non-linear, the analysis becomes very complicated. These runs were not analyzed. After excluding the ice buildup runs, we have 123 good runs with the higher microwave frequency (75.685 GHz) and 58 good runs with the lower microwave frequency (75.520 GHz). We refer these runs as the normal production runs.

The transmission asymmetry ε, the lineshape and the timing were inspected as well. We did not observe any significant false asymmetry in the ε plots other than the statistical fluctuation, and the lineshape of the resonances appears normal. The timing was essentially stable except in about 10 runs where it was shifted by a maximum of 200 ns (one channel).

Figure 5.3 shows the fraction of the data rejected in the normal production runs. The fraction is calculated as $\frac{\sum(5)+\sum(6)}{\sum(3)+\sum(4)+\sum(5)+\sum(6)}$ where the sum is over the same TOF channels as in Figure 5.1. Approximately 20% of the data was rejected, primarily due to the instability in the PSR beam current. But this rejection improves the over all quality of the data and reduces the probability of false asymmetries.

Figure 5.4 shows the background level in the transmission data. Since the strong ^{238}U s-wave resonances have peak cross sections over 1000 barns, these resonances should be black. We estimate the background in the data by interpolating the background under the strong s-wave resonances with straight lines. The background is

approximately 31% at 63 eV. The source of the background may be beam related such as the gamma rays in the neutron beam, or detector related such as scintillator afterglow. As discussed in chapter 4, the existence of such a background does not affect the extraction of the parity violating asymmetry to first order.

5.2 Neutron polarizations

The neutron polarization in a run is determined from the NMR signal taken at the beginning of the run. As discussed in appendix B, the NMR area s is obtained by fitting the Q-curve to a third order polynomial, and the neutron polarization is related to the NMR area as

$$f_n = \tanh(-1.2963 \times 10^{-6} s).$$

The neutron polarization of the normal production runs is listed in Table 5.1, and is plotted in Figure 5.5. The runs with positive neutron polarization were taken with the higher microwave frequency, while the runs with negative neutron polarization were taken with the lower microwave frequency.

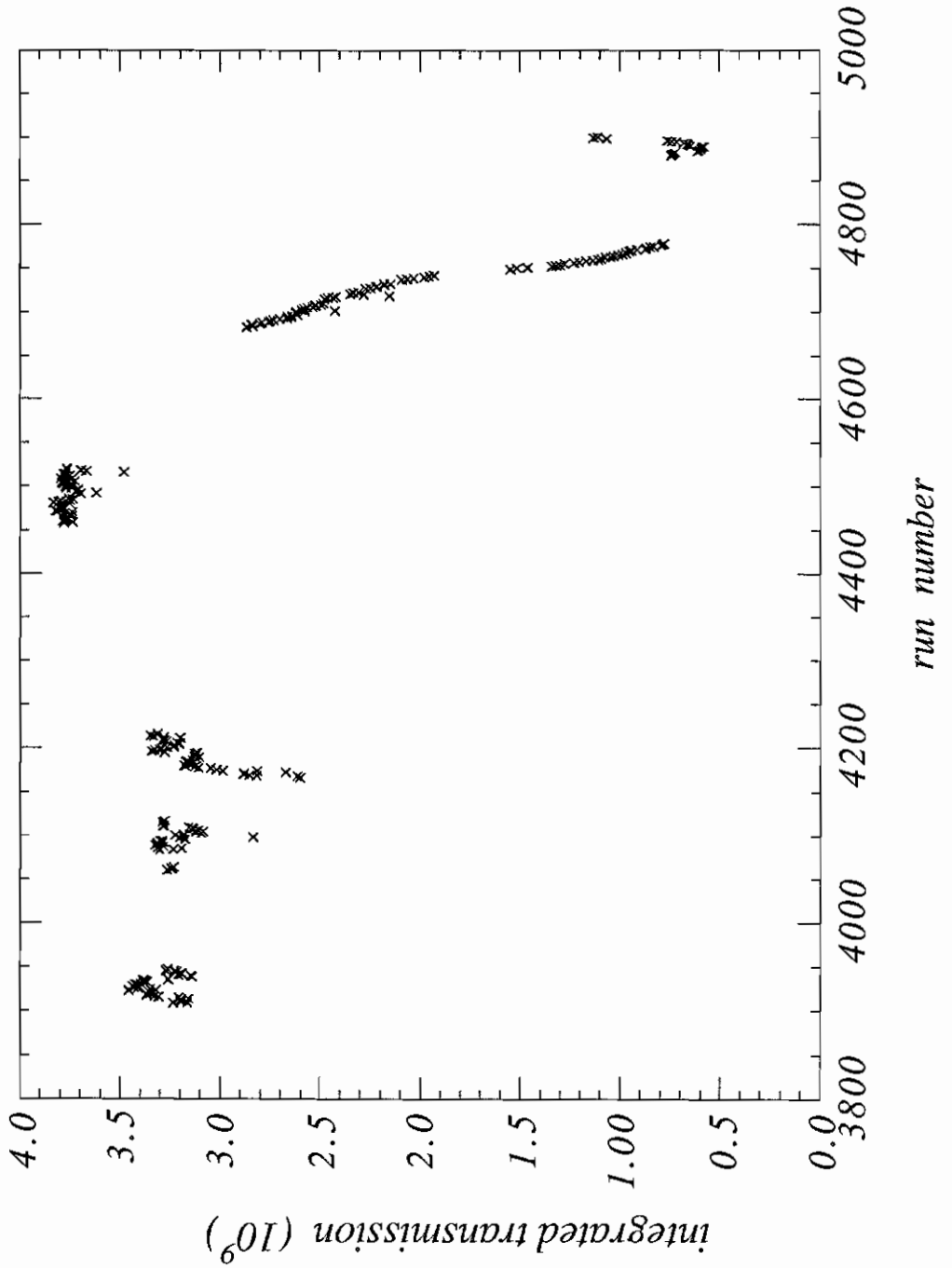

Figure 5.1: The integrated neutron transmission for all the production runs. The sum is from channel 5000 to 6000.

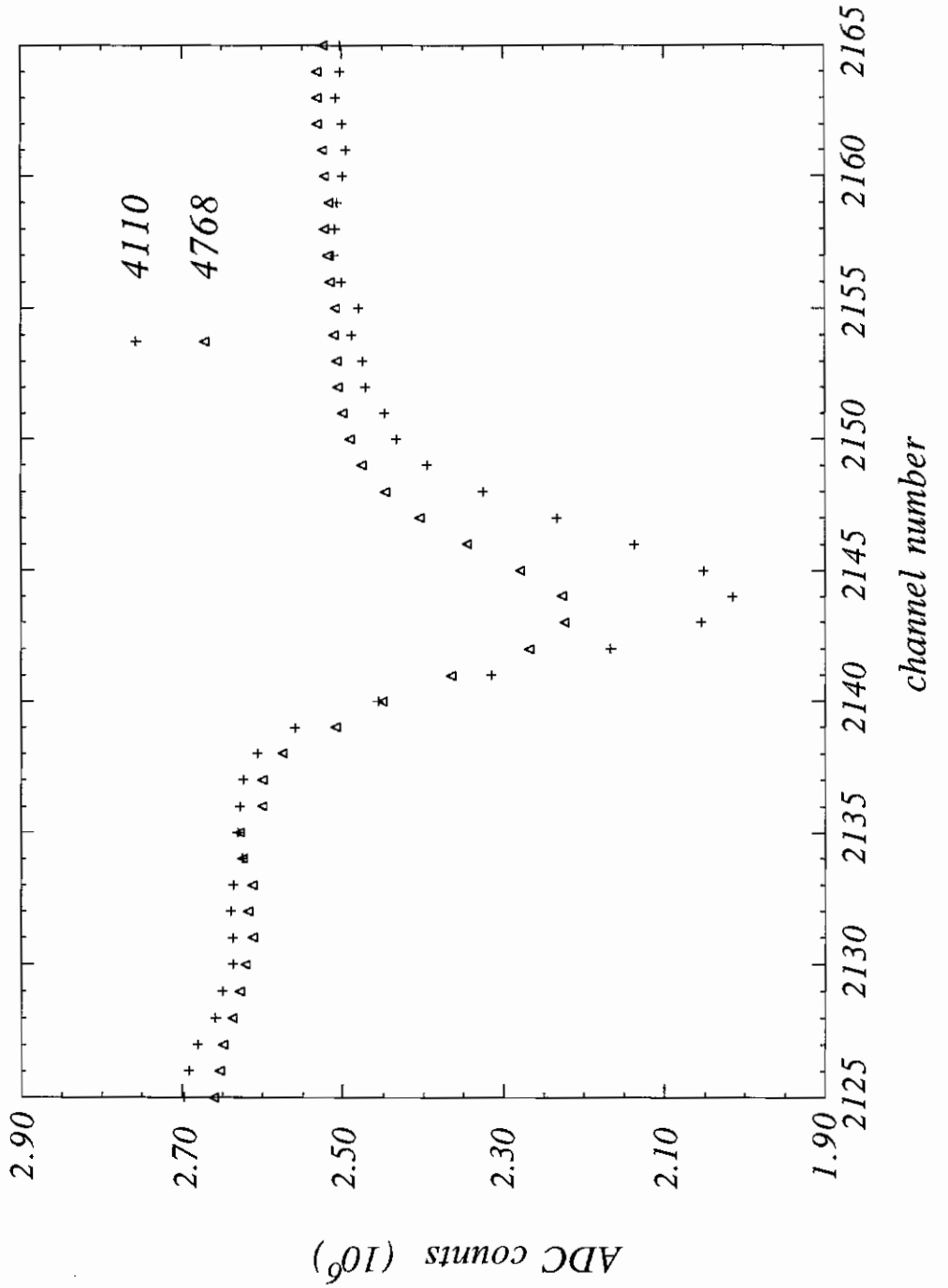

Figure 5.2: The effect of ice buildup. Run 4110 is a normal run. Run 4768 is a run with ice and is normalized to run 4110.

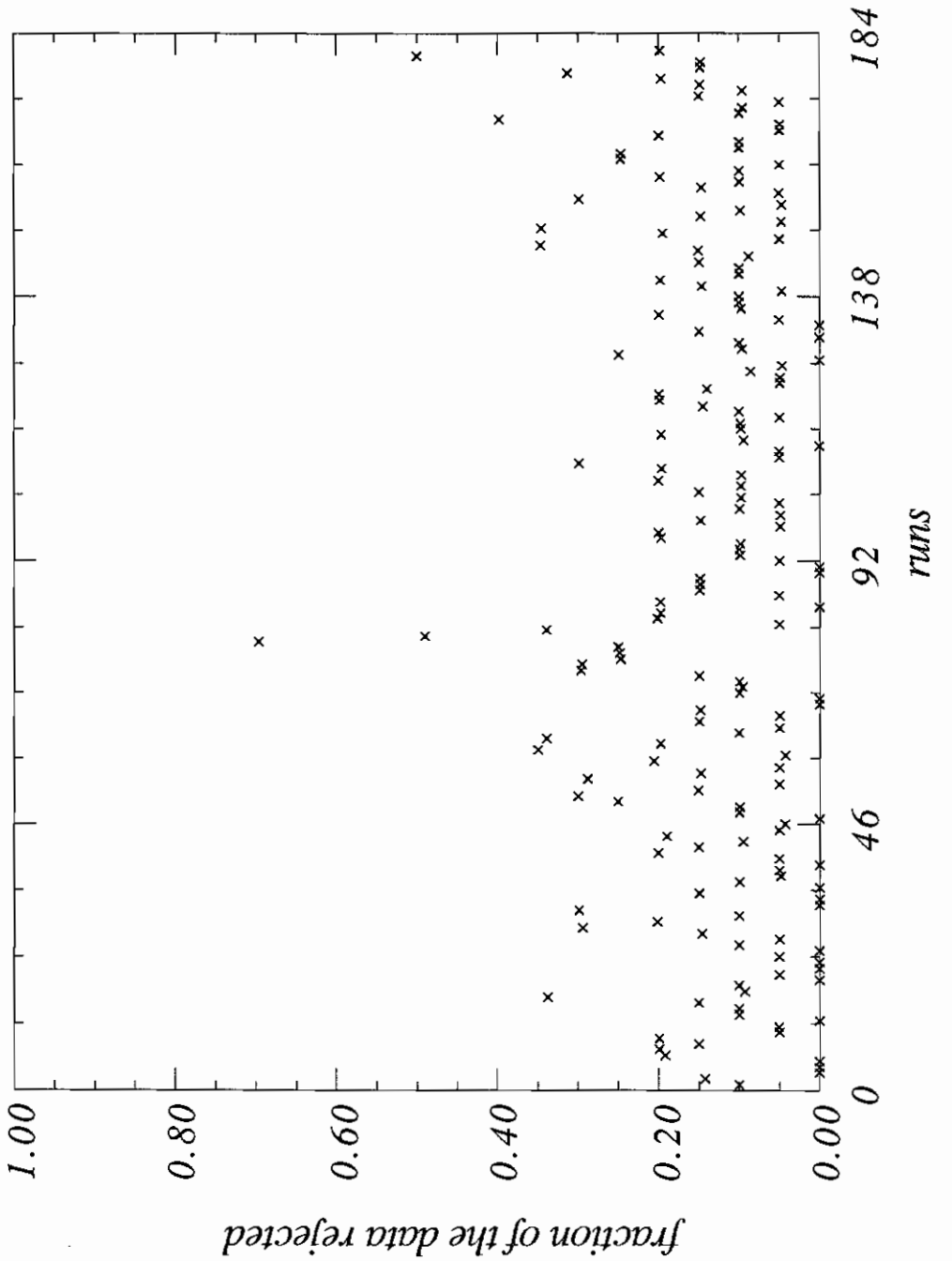

Figure 5.3: The fraction of the data rejected in the normal production runs

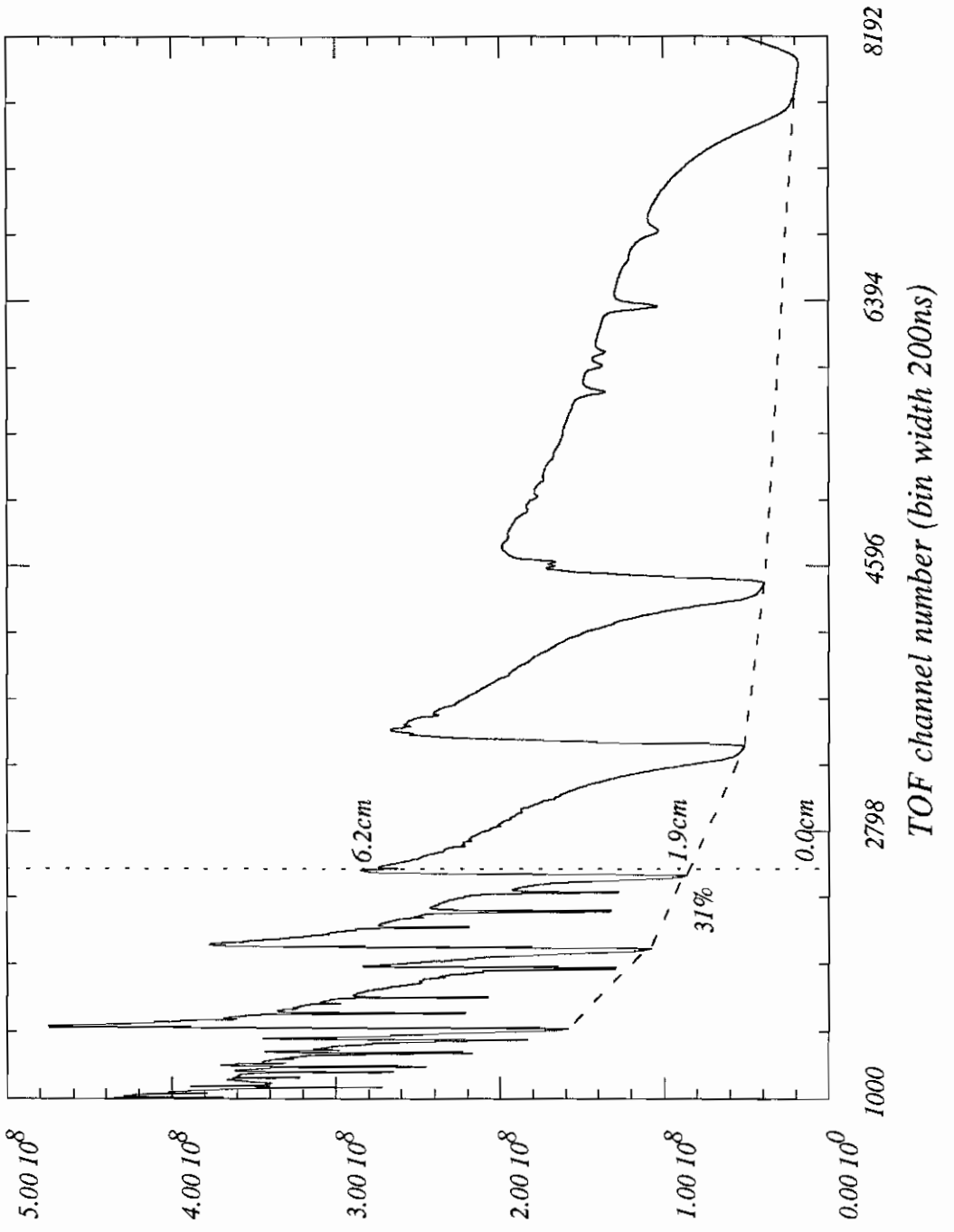

Figure 5.4: Background in the current mode data

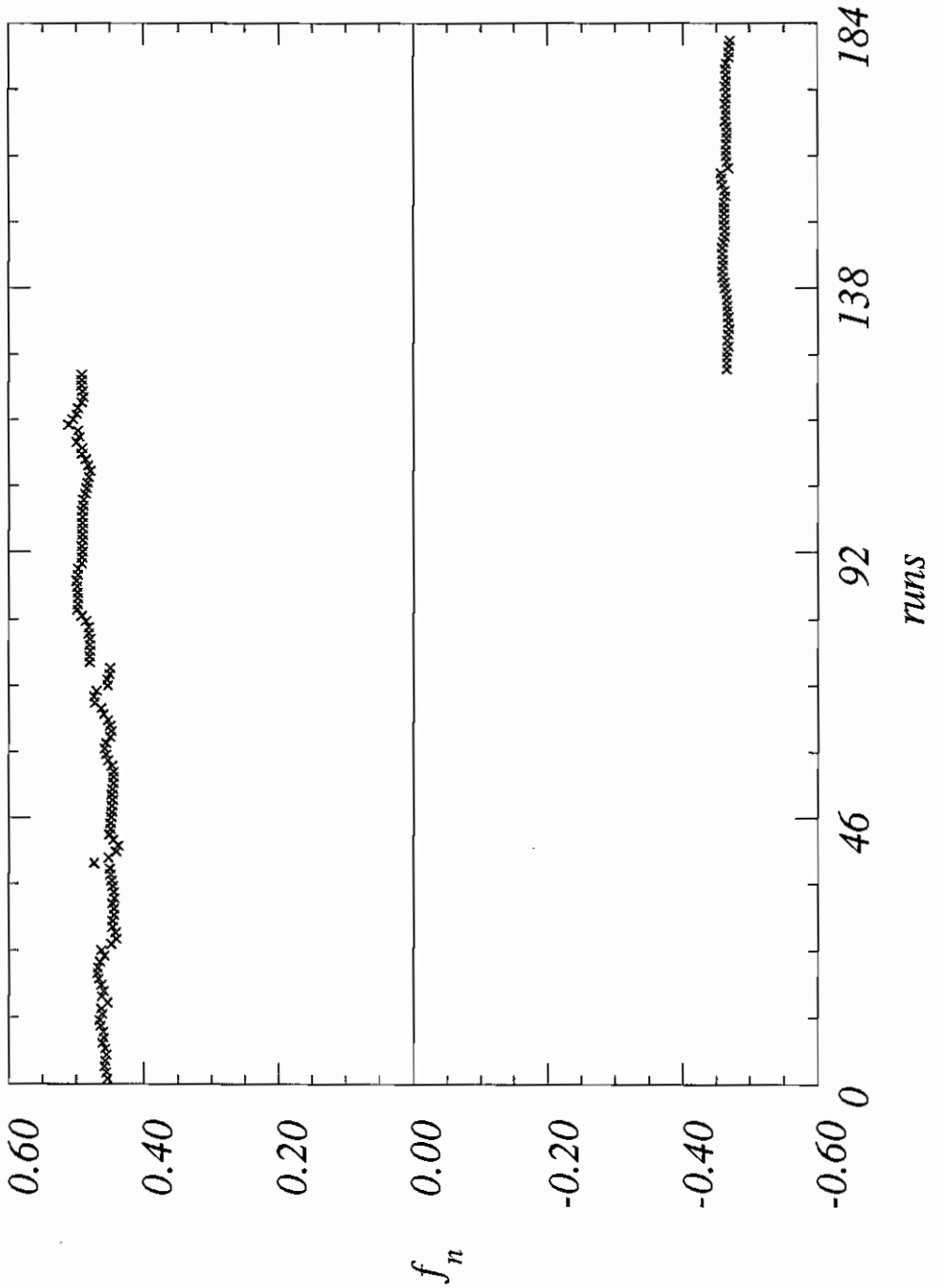

Figure 5.5: The neutron polarization of the normal production runs

run #	NMR area (s)	f_n	run #	NMR area (s)	f_n	run #	NMR area (s)	f_n
3908	-.377410E+06	0.454	4103	-.373605E+06	0.450	4216	-.415584E+06	0.492
3909	-.379202E+06	0.455	4104	-.376852E+06	0.453			
3910	-.381574E+06	0.458	4105	-.382453E+06	0.459	4458	0.388310E+06	-0.465
3911	-.380434E+06	0.457	4106	-.386642E+06	0.463	4459	0.388341E+06	-0.465
3912	-.379245E+06	0.455	4107	-.396518E+06	0.473	4460	0.388180E+06	-0.465
3913	-.380502E+06	0.457	4108	-.397907E+06	0.474	4461	0.389410E+06	-0.466
3914	-.384344E+06	0.461	4109	-.393479E+06	0.470	4462	0.390028E+06	-0.467
3915	-.383139E+06	0.459	4110	-.377246E+06	0.453	4463	0.389822E+06	-0.466
3916	-.383560E+06	0.460	4111	-.377325E+06	0.454	4464	0.390892E+08	-0.467
3917	-.387291E+06	0.464				4465	0.391147E+06	-0.468
3918	-.389416E+06	0.466	4115	-.375284E+06	0.451	4466	0.390326E+06	-0.467
3919	-.385025E+06	0.461	4116	-.374090E+06	0.450	4467	0.390449E+06	-0.467
3920	-.386835E+06	0.463				4468	0.389434E+06	-0.466
3921	-.377465E+06	0.454	4166	-.404670E+06	0.481	4469	0.389290E+06	-0.466
3922	-.385415E+06	0.462	4167	-.404493E+06	0.481	4470	0.388774E+06	-0.465
3923	-.383120E+06	0.459	4168	-.403601E+06	0.480	4471	0.387857E+06	-0.464
3924	-.386100E+06	0.463	4169	-.404939E+06	0.481	4472	0.385671E+06	-0.462
3925	-.390566E+06	0.467	4170	-.403666E+06	0.480	4473	0.384350E+06	-0.461
3926	-.392906E+06	0.469	4171	-.405067E+06	0.482	4474	0.382473E+06	-0.459
3927	-.391724E+06	0.468	4172	-.405833E+06	0.482	4475	0.381799E+06	-0.458
3928	-.388403E+06	0.465	4173	-.409772E+06	0.486	4476	0.382606E+06	-0.459
3929	-.382164E+06	0.458	4174	-.415607E+06	0.492			
3930	-.386701E+06	0.463	4175	-.422280E+06	0.499	4478	0.382461E+06	-0.459
3931	-.371805E+06	0.448	4176	-.422027E+06	0.498	4479	0.381902E+06	-0.458
3932	-.365662E+06	0.441	4177	-.422207E+06	0.498	4480	0.382157E+08	-0.458
3933	-.366237E+06	0.442	4178	-.421980E+06	0.498	4481	0.383812E+06	-0.460
3934	-.369884E+06	0.446	4179	-.422595E+06	0.499	4482	0.385482E+08	-0.462
3935	-.370243E+06	0.446	4180	-.423333E+06	0.500	4483	0.385266E+06	-0.462
3938	-.367648E+06	0.444	4181	-.422179E+06	0.498	4484	0.384870E+06	-0.461
3939	-.368196E+06	0.444	4182	-.421792E+06	0.498	4485	0.384591E+06	-0.461
3940	-.369677E+06	0.446	4183	-.416681E+06	0.493	4486	0.384356E+06	-0.461
3941	-.366746E+06	0.443	4184	-.415333E+06	0.492			
3942	-.367744E+06	0.444	4185	-.414791E+06	0.491	4401	0.384611E+06	-0.461
3943	-.370168E+06	0.446	4186	-.415432E+06	0.492	4492	0.384727E+06	-0.461
3944	-.371335E+06	0.447	4187	-.414312E+06	0.491	4493	0.386781E+06	-0.463
3945	-.373093E+06	0.449	4188	-.414417E+06	0.491	4494	0.385799E+06	-0.462
3946	-.374260E+06	0.450	4189	-.414805E+06	0.491	4495	0.382061E+06	-0.458
			4190	-.414694E+06	0.491	4496	0.380279E+06	-0.457
4060	-.397739E+06	0.474	4191	-.414189E+06	0.491	4497	0.379627E+06	-0.456
4061	-.376165E+06	0.452	4192	-.414233E+06	0.491	4498	0.390735E+06	-0.467
4062	-.305815E+06	0.441	4193	-.413927E+06	0.490	4499	0.388567E+06	-0.465
4063	-.361905E+06	0.438	4194	-.413957E+06	0.490	4500	0.387904E+06	-0.464
			4195	-.410379E+06	0.487	4501	0.388016E+06	-0.464
4083	-.369307E+06	0.445	4196	-.408810E+06	0.485	4502	0.387840E+06	-0.464
4084	-.374712E+06	0.451	4197	-.407717E+06	0.484	4503	0.388123E+06	-0.465
4085	-.373383E+06	0.449	4198	-.405055E+06	0.482	4504	0.388360E+06	-0.465
4086	-.373043E+06	0.449	4199	-.403625E+06	0.480	4505	0.388397E+06	-0.465
4087	-.371639E+06	0.448	4200	-.406627E+06	0.483	4506	0.386898E+06	-0.463
4088	-.371434E+06	0.447	4201	-.410421E+06	0.487	4507	0.387606E+06	-0.464
4089	-.371363E+06	0.447	4202	-.415556E+06	0.492	4508	0.387225E+06	-0.464
4090	-.370517E+06	0.446	4203	-.415687E+06	0.492	4509	0.386856E+06	-0.463
4091	-.370608E+06	0.447	4204	-.423505E+06	0.500	4510	0.387340E+06	-0.464
4092	-.369963E+06	0.446	4205	-.419286E+06	0.496	4511	0.387214E+06	-0.464
4093	-.369274E+06	0.445	4206	-.421735E+06	0.498	4512	0.386736E+06	-0.463
4094	-.388877E+06	0.445	4207	-.435970E+06	0.512	4513	0.387114E+06	-0.464
4095	-.369327E+06	0.445	4208	-.429547E+06	0.506	4514	0.387098E+06	-0.464
4096	-.370979E+06	0.447	4209	-.424101E+06	0.500	4515	0.386337E+06	-0.463
4097	-.376708E+06	0.453	4210	-.421212E+06	0.498	4516	0.387880E+06	-0.464
4098	-.380006E+06	0.456	4211	-.416382E+06	0.493	4517	0.391032E+06	-0.468
4099	-.381394E+06	0.458	4212	-.413901E+06	0.490	4518	0.391727E+06	-0.468
4100	-.379662E+06	0.456	4213	-.414426E+06	0.491	4519	0.392113E+06	-0.469
4101	-.374164E+06	0.450	4214	-.416422E+06	0.493	4520	0.393787E+06	-0.470
4102	-.372444E+06	0.448	4215	-.415418E+06	0.492			

Table 5.1: The neutron polarization of the normal production runs

5.3 Identifying the ^{238}U resonances

As discussed in appendix C, the neutron TOF, the neutron energy E_n and the length of the flight path l are related by

$$TOF = 7.23 \times 10^{-5} \frac{l}{\sqrt{E_n}}, \tag{5.1}$$

where TOF is in seconds, l in meters and E_n in eV.

We use the above formula to identify the strongest s-wave resonances by assuming $l = 60$ m. The total cross section of neutron on ^{238}U is plotted in Figure 2.1, and the resonances are listed in Table 5.2. By carefully comparing the strength of the resonances, some of the p-wave resonances are also identified as well as resonances from contaminations.

To make an accurate energy calibration of the TOF spectra, we perform a least square fit to the energies and the channel numbers of those well identified resonances the location of which could be read precisely. Since the target nucleus is much heavier than a neutron, the neutron energy E_n is approximately equal to the center of mass energy E. Therefore equation (5.1) can be written as

$$K - K_s = \frac{A}{\sqrt{E}}$$

or

$$(K\sqrt{E}) = K_s(\sqrt{E}) + A \tag{5.2}$$

where K is the TOF channel, K_s the zero-TOF channel, and $A = \frac{7.23\times10^{-5}l}{200\times10^{-9}}$ where 200×10^{-9} s is the TOF bin width.

The fit is shown in Figure 5.6. From this fit, we determined the length of the flight path and the zero-TOF channel to be

$$l = 56.51 \text{ m} \tag{5.3}$$

$$K_s = -18.57. \tag{5.4}$$

E (eV)	l	Γ (meV)	E (eV)	l	Γ (meV)
6.671	0	24.89	145.62	0	23.14
10.237	1		152.42	1	
11.309	1		158.98	1	
19.529	1		160.85	1	
20.872	0	33.7	165.26	0	26.4
36.680	0	57.3	173.18	1	
45.17	1		189.67	0	197
49.62	1		194.80	(1)	
57.9	1		200.69	1	
63.52	1		203.11	1	
66.02	0	48.1	208.49	0	72.8
80.73	0	26.9	214.88	1	
83.68	1		218.36	1	
89.24	1		224.60	1	
93.14	1		237.30	0	52.8
98.20	1		242.73	1	
102.54	0	94.4	253.90	1	
111.25	1		257.16	1	
116.87	0	47.8	263.94	1	
121.61	1		273.62	0	47.9
124.97	1		275.19	1	
133.30	(1)		282.46	1	

Table 5.2: ^{238}U resonances (taken from [Mugh84]). E is the resonance energy, l the orbital angular momentum, and Γ the total width of the resonance.

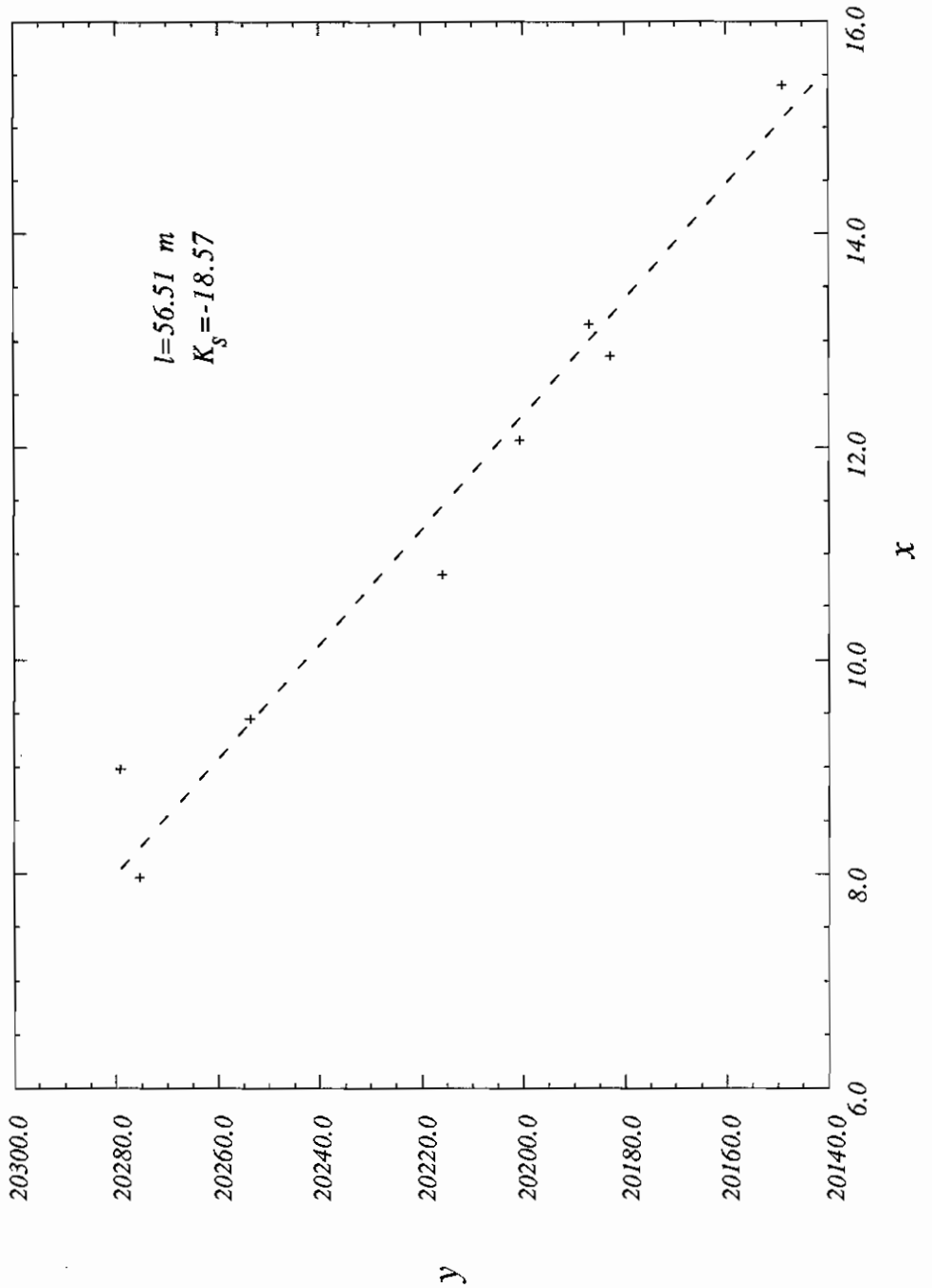

Figure 5.6: Energy calibration of the neutron TOF spectra. $x = \sqrt{E}$, $y = K\sqrt{E}$, where K is the TOF channel and E is in eV.

Using this calibration, we can identify all the resonances in the TOF spectra. The result is shown in appendix E. In general, the calibration agrees well with the listed resonance energies with a difference less than 0.3 eV up to 250 eV. Of the 40 listed p-wave resonances from 6 eV to 282 eV ([Moxo89]), we identified 17 p-wave resonances. In the following section, we discuss the extraction of the parity violating asymmetries for these p-wave resonances.

5.4 Analyzing a p-wave resonance

5.4.1 Outline

Since the two microwave frequencies correspond to opposite proton polarizations, runs with the same microwave frequency are analyzed together. For a given microwave frequency, we form the summed spectra by summing the "good" spectra of the runs. To analyze the parity violation on a p-wave resonance, we first fit the summed spectra to extract the lineshape parameters; then fit the individual runs to obtain the parity violating asymmetry p for each run. The p's of the individual runs are histogrammed to determine $\bar{p}$ the average and σ the standard deviation. The error in $\bar{p}$ is cited as $\sigma/\sqrt{N}$, where N is the number of runs with the given microwave frequency.

The analysis procedure described in chapter 4 is for the case of a well isolated p-wave resonance. For most of the p-wave resonances in ^{238}U, there is one or more nearby resonances which either distort the flux shape or overlap slightly with the p-wave resonance. To handle this problem, we modified the procedure, so that certain regions of the spectra can be blanked out, and the remaining data can be analyzed as an isolated p-wave resonance.

5.4.2 Fitting the summed spectra

The summed spectra were fitted in the following manner. The zero-TOF channel is obtained from the energy calibration ($K_s = -18.57$) , and the initial values of the

adjustable parameters are set at

index	Parameter	Initial Value
1	α_1	0
2	α_2	0
3	α_3	0
4	α_4	0
5	α_5	0
6	N	non-zero
7	K_0	from inspection
8	B^2	$\left(\frac{K_0}{\Delta K}\right)^2$, ΔK the width of the resonance
9	C	calculated at $T = 300°\mathrm{K}$
10	σ'_{max}	non-zero
11	α	0
12	$f_n p$	0

The initial value of the parameter B^2 is estimated as follows:

$$\frac{\Delta E}{E_0} = -2\frac{\Delta K}{K_0},$$

where E_0 is the energy of the resonance, and K_0 is the corresponding TOF channel, ΔK is the width of the resonance in terms of the TOF channel numbers, and ΔE is the corresponding width in energy. Assuming $\Delta E \approx \Gamma$, we obtain

$$\begin{aligned} B^2 &\equiv \left(\frac{2E_0}{\Gamma}\right)^2 \\ &= \left(\frac{K_0}{\Delta K}\right)^2. \end{aligned}$$

To ensure fast convergence, we followed the following steps in fitting the summed spectra:

1. Free N only to get the normalization roughly right. Since the fitting function is linear in N, one or two iterations will bring N near the correct value.

2. Free α_i $(i = 1, 2, \cdots, 5)$ one or two at a time and N.

3. Free K_0 and σ'_{max} to get the peak position and depth correct.

4. Now free B^2 and C in addition. These are the most difficult parameters to fit because they may be strongly correlated.

5. Free all the remaining parameters.

The parameters that determine the flux function should provide a smooth variation through the resonance. Since the parameters are correlated, a distorted or unphysical flux may give incorrect asymmetries. Figure 5.7 shows a fit to the 11.347 eV resonance. The fit was performed between the arrows. The dots represents the experimental spectrum, and the solid line through the dots is the fit. The smooth dotted line is the flux.

5.4.3 Fitting the individual runs

Once the lineshape parameters are obtained from the summed spectra, the individual runs can be fitted. In fitting the individual runs, the lineshape parameters are held fixed and only

$$N, \alpha, K_0 \text{ and } f_n p$$

are allowed to vary. Normally the fits converge after 6 or 7 iterations.

5.4.4 The average $\bar{p}$ and its error

In fitting an individual run k, we obtain the parameter $(f_n p)_k$ and its error estimate $\sigma_{(f_n p)_k}$. Since the neutron polarization f_n is known, we immediately obtain the parity violating asymmetry and its error for this run

$$\begin{aligned} p_k &= \frac{(f_n p)_k}{(f_n)_k} \\ \sigma_k &= \frac{\sigma_{(f_n p)_k}}{(f_n)_k} \end{aligned}$$

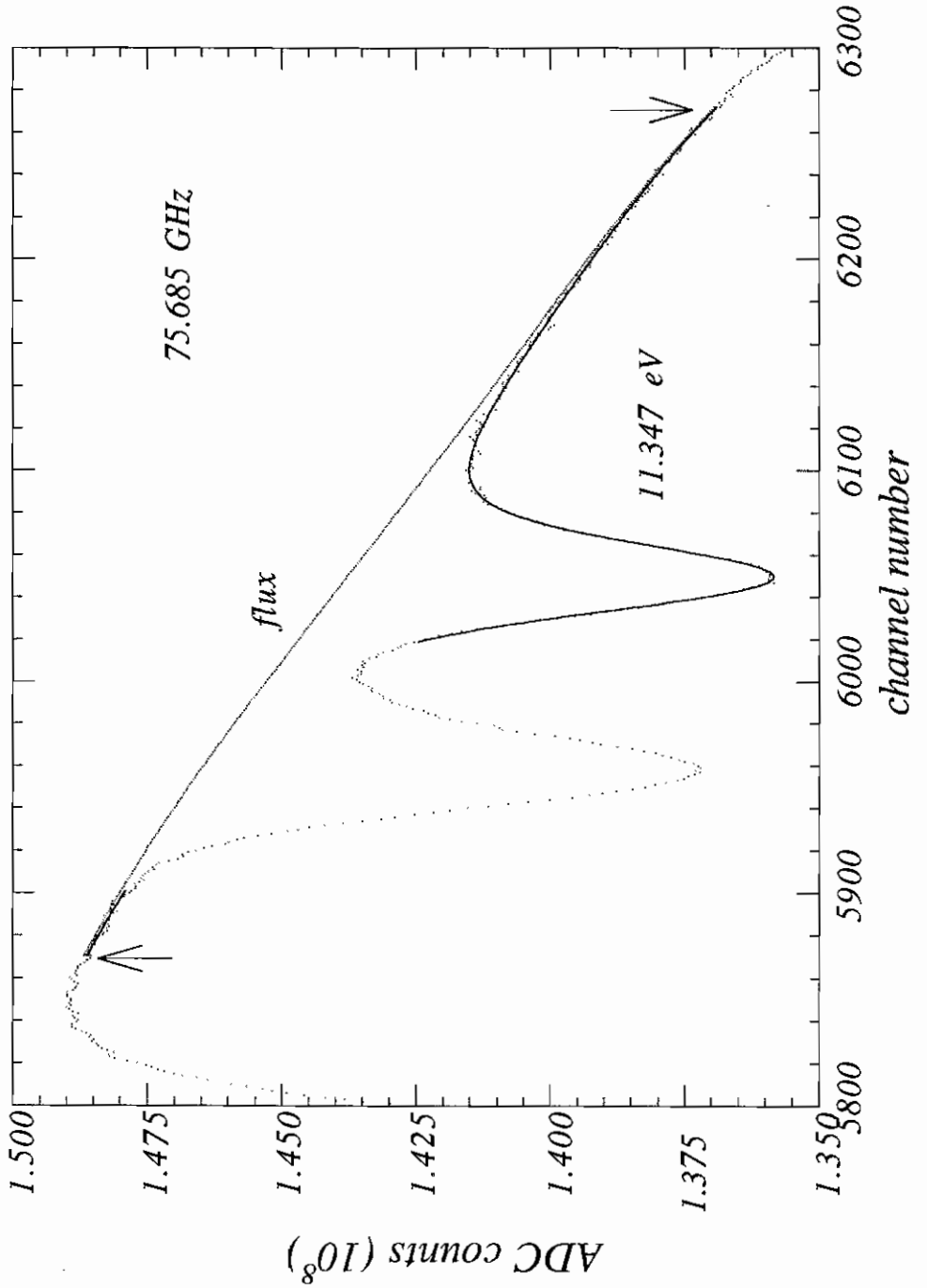

Figure 5.7: A fit to the 11.347 eV resonance in the summed spectra

The p_k's are histogrammed to determine the average parity violating asymmetry $\bar{p}$ and its error δ_2 as

$$\begin{aligned} \bar{p} &= \frac{\sum_k \frac{1}{\sigma_k^2} p_k}{\sum_k \frac{1}{\sigma_k^2}} \\ \delta_2 &= \frac{\sigma}{\sqrt{N}}, \end{aligned}$$

where N is the number of runs with the given microwave frequency ($N = 123$ for 75.685 GHz, and $N = 58$ for 75.520 GHz), and σ is the spread of the histogram as shown in Figure 5.8 and is determined as follows

$$\sigma^2 = \frac{1}{N-1} \sum_{k=1}^{N} (p_k - \bar{p})^2.$$

In the absence of non-statistical errors, σ should be determined by the statistics of a single run. Since δ_2 is obtained directly from the distribution, it should include all sources of error, and is the most robust way to determine an overall error. We refer δ_2 as the external error, and cite it as the error in $\bar{p}$.

Another way to estimate the error in $\bar{p}$ is from the counting statistics as follows:

$$\delta_1 = \frac{1}{\sqrt{\sum_k \frac{1}{\sigma_k^2}}}.$$

This is referred to as the internal error.

We found that for most cases, δ_2 was from 1.4 to 2.5 times bigger than δ_1. This does not mean that there are significant non-statistical errors in the system since for the multiscaler data taken as part of another experiment ([Yuan91]), δ_1 and δ_2 are approximately equal. The discrepancy of δ_1 and δ_2 in the transient digitizer data may be due to the fact that we do not know exactly how to convert the transient digitizer data to the neutron counts, therefore the statistical error in the transient digitizer spectra may be under-estimated.

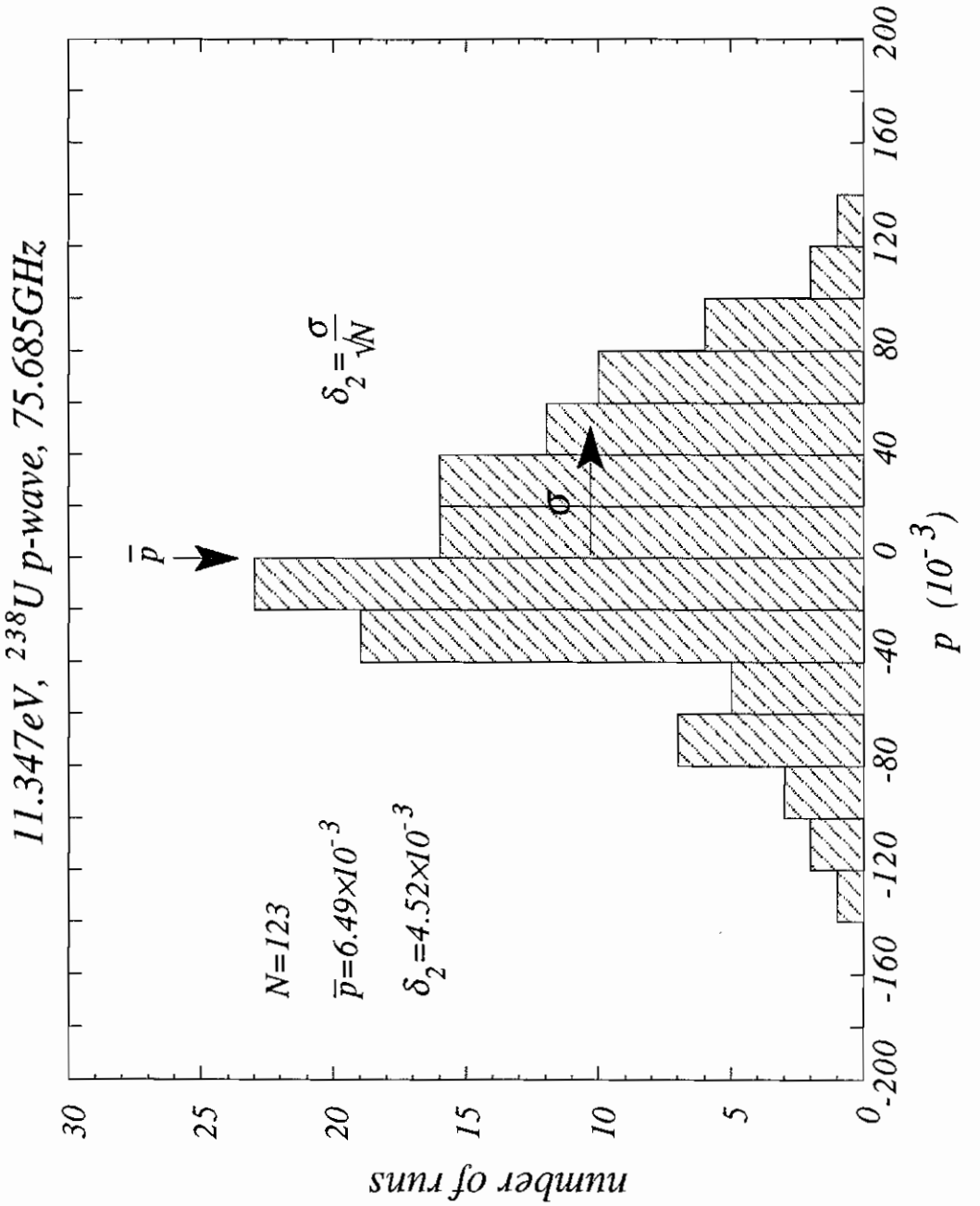

Figure 5.8: Histogram of the parity violating asymmetries of the 11.347 eV resonance

5.5 Summary of the analysis

Table 5.3 summarizes the analysis of the parity violating asymmetries on the 17 p-wave resonances. The first column is the resonance energy, the second and third columns are the parity violating asymmetries with errors for the two microwave frequencies, the fourth column is the combined parity violating asymmetry, and the seventh column indicates the significance of parity violation on the resonance. For the ^{238}U target, we observed 2σ or larger effect on 5 p-wave resonances, the largest being a 7σ effect which occurs at 63.5 eV.

The combined parity violating asymmetry is obtained from the results of the two frequencies as a weighted average

$$p_{com} = \frac{\frac{1}{\delta_h^2}p_h + \frac{1}{\delta_l^2}p_l}{\frac{1}{\delta_h^2} + \frac{1}{\delta_l^2}} \tag{5.5}$$

$$\delta_{p_{com}} = \frac{1}{\sqrt{\frac{1}{\delta_h^2} + \frac{1}{\delta_l^2}}} \tag{5.6}$$

where p denotes the parity violating asymmetries, δ the errors, h and l denotes the higher and lower microwave frequencies, respectively.

Appendix F shows the histograms of the parity violating asymmetries as well as the lineshape parameters obtained from the summed spectra.

5.6 Correction for spin flipper efficiency

In the analysis above, we assumed that the spin flipper efficiency is 100%. In practice, this is not the case, as shown in Figure 3.13. The spin preserving efficiency s_{flip} is almost 100% throughout the energy range of interest. The spin flipping efficiency r_{flip} is 100% at low energies, but oscillates noticably at high energies.

The spin flipper depolarizes the neutron beam if the efficiencies are not 100%. Assuming that the neutrons come out of the cryostat with polarization f_n. After passing through the spin flipper, the neutron polarization is $r_{flip}f_n$ if the transverse

$E^{\dagger}$(eV)	75.685GHz $p_h(10^{-3})$	75.520GHz $p_l(10^{-3})$	combined $p_{com}(10^{-3})$	sf. eff.	$p(10^{-3})$	$\frac{\|p\|}{\delta_p}$
p-wave resonances: ^{238}U						
10.228	-2.78± 1.07	0.03± 1.26	-1.60± 0.82	0.98	-1.64± 0.83	2.0
11.347	6.49± 4.52	7.04± 6.44	6.67± 3.70	0.99	6.74± 3.74	1.8
45.200	10.56±23.94	-57.28±33.73	-12.17±19.52	0.93	-13.10±21.02	–
57.936	49.98±33.17	56.31±41.38	52.46±25.88	0.89	59.22±29.22	2.0
63.500	24.19± 4.17	20.68± 6.50	23.17± 3.51	0.88	26.25± 3.98	6.6
83.695	4.97± 9.20	51.14±14.78	17.86± 7.81	0.91	19.56± 8.55	2.3
89.221	-2.22± 1.26	-2.35± 1.93	-2.26± 1.06	0.93	-2.44± 1.14	2.1
93.075	-20.16±24.86	59.07±42.96	-0.28±21.52	0.93	-0.30±23.02	–
98.000	-34.88±16.23	-1.14±18.92	-20.58±12.32	0.95	-21.77±13.03	1.7
124.99	7.03±10.44	17.78±14.73	10.62± 8.52	0.99	10.76± 8.63	1.2
152.42	-5.43± 6.64	8.96±10.68	-1.42± 5.64	1.00	-1.42± 5.64	–
158.94	1.92±16.58	-14.96±23.97	-3.54±13.64	1.00	-3.55±13.66	–
173.15	15.64± 8.93	1.34±11.60	10.32± 7.08	0.99	10.39± 7.13	1.5
242.70	-11.31± 6.83	8.56±10.84	-5.66± 5.78	0.92	-6.13± 6.25	–
253.88	7.30± 7.64	-14.49± 9.32	-1.46± 5.91	0.91	-1.60± 6.49	–
263.91	2.89± 4.74	-5.54± 6.37	-0.11± 3.80	0.90	-0.13± 4.24	–
282.40	14.61±14.77	-20.35±21.72	3.56±12.21	0.87	4.07±13.97	–
s-wave resonances: contaminations						
8.97	1.33±2.09	-0.59±2.36	0.49±1.56		U235-s	–
11.67	-3.25±4.17	0.83±5.46	-1.75±3.31		U235-s	–
12.43	-0.83±1.90	-6.00±3.25	-2.15±1.64		U235-s	1.3
72.17	0.42±0.53	-1.61±0.76	-0.24±0.43		La139-s	–
230	0.78±4.00	-1.24±5.77	0.12±3.29		Cu65-s	–

† obtained from Table 6.1

Table 5.3: Summary of the parity violating asymmetries

coil is on, and $s_{flip}f_n$ if the transverse coil is off. Let us take the case of higher microwave frequency as an example. The neutron spin directions at various part of the beamline is shown in Figure B.7. We have

$$\begin{aligned} \sigma^+ &= \sigma_p(1 + r_{flip}f_n p) \\ \sigma^- &= \sigma_p(1 - s_{flip}f_n p) \end{aligned}$$

where σ^+ and σ^- are the resonance cross sections for $+$ and $-$ helicity neutrons, respectively, and p is the true parity violating asymmetry. The parity violating asymmetry as obtained from the fitting program is

$$f_n p_{com} = \frac{\sigma^+ - \sigma^-}{\sigma^+ + \sigma^-} = f_n p \left(\frac{r_{flip} + s_{flip}}{2} \right)$$

Or

$$p = \frac{p_{com}}{\text{sf. eff.}}$$

where the spin flipper efficiency is defined as $(r_{flip} + s_{flip})/2$. The spin flipper efficiency and the corrected parity violating asymmetry are listed in columns 5 and 6 in Table 5.3.

5.7 Systematic errors

We checked for systematic error in four ways, and observed no significant effect. 1) We did not observe false asymmetries in the ε plots. 2) We do not expect to observe parity violation on the s-wave resonances because of the large spin independent cross sections. We analyzed 5 contamination s-wave resonances which have sizes comparable to that of the p-wave resonances in the transmission spectra. The result is listed in Table 5.3. Of the five s-wave resonances, only one showed a greater than 1σ effect (1.3σ), which is what is expected from random statistics. 3) We did not see any abnormal distributions in the histograms. 4) We can compare the internal (statistical) error δ_1 with the external (overall) error δ_2. In the multiscaler data, δ_1

is approximately equal to δ_2, which again indicates the absence of systematic error. Therefore, we are confident that systematic errors are small or absent in the data.

Of the 17 p-wave resonances, 5 show 2σ or larger effect. From random statistics, only $17 \times 4.5\% = 0.8$ resonances are expected. Therefore the p-violation we observed can not be contributed from random statistics.

Chapter 6

The RMS Matrix Element and the Parity Violating Spreading Width

Since the J of the p-wave resonances of ^{238}U is not definitively established, we can not analyze only those p-wave resonances with $J = \frac{1}{2}$, therefore the technique developed in chapter 2 for extracting the RMS matrix element can not be applied directly.

Of the 17 analyzed p-wave resonances, some of them may be $J = \frac{1}{2}$ and some of them may be $J = \frac{3}{2}$. Let us assume that the J of the p-wave resonances is completely unknown. From statistical nuclear physics, the level density in the compound nucleus ^{239}U can be written as ([Egid88])

$$\rho \propto (2J+1)\exp\left[-\frac{(J+\frac{1}{2})^2}{2\sigma^2}\right]$$

where σ is the spin cut-off parameter, and is approximately 4.8. For the low spin states we are interested in ($J = \frac{1}{2}, \frac{3}{2}$), the level density is approximately

$$\rho \propto (2J+1).$$

Therefore we have twice as many p-wave resonances with $J = \frac{3}{2}$ as with $J = \frac{1}{2}$. In

other words, a p-wave resonance has a probability of $\frac{1}{3}$ to be $J = \frac{1}{2}$, and a probability of $\frac{2}{3}$ to be $J = \frac{3}{2}$.

Let us assume $J = \frac{1}{2}$ for the p-wave resonance. The parity violating asymmetry on the resonance can be written as (see equation 2.7)

$$p_i = \sum_j A_{ij} V_{ij} + \gamma_i \tag{6.1}$$

where γ_i is the experimental uncertainty and

$$A_{ij} = \frac{2}{E_{s,j} - E_{p,i}} \sqrt{\frac{\Gamma^n_{s,j}(E_{p,i})}{\Gamma^n_{p,i}(E_{p,i})}}.$$

The energy and the neutron width are listed in Table 6.1 for the neutron resonances of ^{238}U. On the left-hand side of Table 6.1 are all the s-wave resonances. Since for a p-wave resonance, A_{ij} is negligibly small except for a few nearby s-wave resonances, the s-wave resonances are cut-off at 500 eV. One the right-hand side of Table 6.1 are all the p-wave resonances below 290 eV. We list the J assignment as well although it is not definitive. To calculate the A_{ij}'s for a p-wave resonance which is listed as $J = \frac{3}{2}$ in Table 6.1, we need to double the listed neutron width since the neutron width Γ^n depends on the J assignment as $(2J+1)\Gamma^n$ =constant.

In chapter 2, we made the assumption that the parity violating matrix elements V_{ij} are Gaussian distributed random variables with mean 0 and variance M^2

$$\begin{aligned} \langle V_{ij} \rangle &= 0 \\ \langle V_{ij}^2 \rangle &= M^2, \end{aligned}$$

and proved that p_i is also a Gaussian distributed random variable. Taking into account the experimental uncertainty γ_i, we can calculate the ensemble averages of p_i and p_i^2 as

$$\begin{aligned} \langle p_i \rangle &= \sum_j A_{ij} \langle V_{ij} \rangle + \langle \gamma_i \rangle \\ &= 0 \end{aligned} \tag{6.2}$$

index	E_s (eV)	Γ_s^n (eV)	E_p (eV)	$J^{\ddagger}$	Γ_p^n (eV)
1	-4.1330E+02	2.0330E-01	4.3930E+00	1.5	5.4000E-08
2	-3.9330E+02	8.2599E-02	7.7090E+00	1.5	1.3500E-08
3	-3.7330E+02	8.0475E-02	1.0228E+01†	0.5	1.6800E-06
4	-3.5330E+02	7.8288E-02	1.1347E+01†	1.5	2.0000E-07
5	-3.3330E+02	1.8300E-01	1.9628E+01	0.5	2.3200E-06
6	-3.1330E+02	7.3727E-02	2.4116E+01	1.5	2.3000E-07
7	-2.9330E+02	7.1332E-02	2.6917E+01	1.5	3.5000E-07
8	-2.7330E+02	3.3064E-01	4.3310E+01	0.5	8.5000E-07
9	-2.5330E+02	6.6292E-02	4.5200E+01†	1.5	1.0500E-06
10	-2.3330E+02	2.4438E-01	4.6759E+01	1.5	1.8000E-07
11	-2.1330E+02	6.0835E-02	4.9641E+01	0.5	1.2000E-06
12	-1.9330E+02	1.3900E-01	5.7936E+01†	1.5	2.4000E-07
13	-1.7330E+02	5.2600E-02	6.3500E+01†	1.5	6.6000E-06
14	-1.5330E+02	2.4800E-01	6.7500E+01	1.5	2.0000E-07
15	-1.3330E+02	2.3100E-02	7.2367E+01	0.5	3.0000E-06
16	-1.1330E+02	4.1600E-02	8.3060E+01	1.5	9.0000E-08
17	-9.3300E+01	1.9300E-02	8.3695E+01†	0.5	1.2300E-05
18	-7.3300E+01	1.7000E-02	8.9221E+01†	1.5	4.9000E-05
19	-5.3300E+01	7.3000E-03	9.3075E+01†	1.5	3.0000E-06
20	-3.3300E+01	8.0860E-04	9.8000E+01†	0.5	4.8000E-06
21	6.6740E+00	1.4930E-03	1.1115E+02	0.5	8.8000E-06
22	2.0871E+01	1.0260E-02	1.1928E+02	1.5	4.0000E-06
23	3.6682E+01	3.4130E-02	1.2499E+02†	1.5	1.1500E-05
24	6.6032E+01	2.4600E-02	1.3324E+02	0.5	8.0000E-06
25	8.0749E+01	1.8650E-03	1.3595E+02	1.5	1.5000E-06
26	1.0256E+02	7.1700E-02	1.5242E+02†	0.5	5.3000E-05
27	1.1690E+02	2.5490E-02	1.5894E+02†	1.5	9.5000E-06
28	1.4566E+02	8.4700E-04	1.6450E+02	1.5	1.0000E-06
29	1.6529E+02	3.3670E-03	1.7315E+02†	1.5	2.5000E-05
30	1.8967E+02	1.7320E-01	1.9480E+02	1.5	2.5000E-06
31	2.0851E+02	5.1110E-02	2.0070E+02	1.5	3.0500E-05
32	2.3738E+02	2.7160E-02	2.0307E+02	0.5	3.7000E-05
33	2.5722E+02	3.4000E-05	2.1481E+02	1.5	3.6000E-05
34	2.7366E+02	2.5780E-02	2.1828E+02	1.5	1.5500E-05
35	2.9100E+02	1.6870E-02	2.2906E+02	0.5	6.0000E-06
36	3.1132E+02	1.0890E-03	2.4270E+02†	1.5	9.7000E-05
37	3.4779E+02	8.2000E-02	2.5388E+02†	0.5	1.0900E-04
38	3.5345E+02	2.4000E-05	2.6391E+02†	0.5	2.7600E-04
39	3.7693E+02	1.1290E-03	2.7524E+02	1.5	1.0200E-04
40	3.9762E+02	6.2070E-03	2.7808E+02	1.5	5.0000E-06
41	4.1024E+02	2.0090E-02	2.8240E+02†	1.5	5.3500E-05
42	4.3407E+02	9.7870E-03			
43	4.6317E+02	5.6130E-03			
44	4.7843E+02	4.1260E-03			
45	4.8891E+02	8.8400E-04			
46	5.1836E+02	5.0470E-02			

† identified and analyzed in this experiment ‡ not definitive

Table 6.1: Neutron resonances of ^{238}U (taken from [Moxo89])

$$\begin{aligned}
\langle p_i^2 \rangle &= \langle (\sum_j A_{ij} V_{ij} + \gamma_i)(\sum_{j'} A_{ij'} V_{ij'} + \gamma_i) \rangle \\
&= \sum_{jj'} A_{ij} A_{ij'} \langle V_{ij} V_{ij'} \rangle + 2\langle \delta_i \rangle \langle \sum_j A_{ij} V_{ij} \rangle + \langle \gamma_i^2 \rangle \\
&= \sum_j A_{ij}^2 \langle V_{ij}^2 \rangle + \langle \gamma_i^2 \rangle \\
&= A_i^2 M^2 + \delta_i^2 \qquad (6.3)
\end{aligned}$$

where $A_i^2 = \sum_j A_{ij}^2$ and δ_i is the experimental error in p_i.

Therefore the probability for finding the parity violating asymmetry between p_i and $p_i + dp_i$ is

$$\begin{aligned}
\mathcal{P}(p_i)\, dp_i &= \frac{1}{\sqrt{2\pi \langle p_i^2 \rangle}} \exp\left[-\frac{p_i^2}{2\langle p_i^2 \rangle} \right] dp_i \\
&= \frac{1}{A_i \sqrt{2\pi (M^2 + \frac{\delta_i^2}{A_i^2})}} \exp\left[-\frac{(p_i/A_i)^2}{2\left(M^2 + \frac{\delta_i^2}{A_i^2}\right)} \right] dp_i \\
&= \frac{1}{\sqrt{2\pi (M^2 + \delta_{Q_i}^2)}} \exp\left[-\frac{Q_i^2}{2\left(M^2 + \delta_{Q_i}^2\right)} \right] dQ_i \qquad (6.4)
\end{aligned}$$

where

$$Q_i \equiv \frac{p_i}{A_i} \qquad (6.5)$$

$$\delta_{Q_i} = \frac{\delta_i}{A_i}. \qquad (6.6)$$

If instead, $J = \frac{3}{2}$ for the resonance, the probability can be obtained by setting $M = 0$ in equation (6.4)

$$\mathcal{P}(p_i)\, dp_i = \frac{1}{\sqrt{2\pi \delta_{Q_i}^2}} \exp\left[-\frac{Q_i^2}{2\delta_{Q_i}^2} \right] dQ_i. \qquad (6.7)$$

Since the resonance has a probability of $\frac{1}{3}$ to be $J = \frac{1}{2}$, and a probability of $\frac{2}{3}$ to be $J = \frac{3}{2}$, the probability for the resonance to show a parity violating asymmetry between p_i and $p_i + dp_i$ is

$$\mathcal{P}(p_i)\, dp_i = \left\{ \frac{1}{3} \frac{1}{\sqrt{2\pi (M^2 + \delta_{Q_i}^2)}} \exp\left[-\frac{Q_i^2}{2(M^2 + \delta_{Q_i}^2)} \right] \right.$$

$$+\frac{2}{3}\frac{1}{\sqrt{2\pi\delta_{Q_i}^2}}\exp\left[-\frac{Q_i^2}{2\delta_{Q_i}^2}\right]\Bigg\}\,dQ_i$$

where Q_i and δ_{Q_i} are defined in equations 6.5 and 6.6, and are listed in Table 6.2.

The likelihood function is the joint probability of all 17 p-wave resonances and can be written as

$$L(M) = N_0\prod_{i=1}^{17}\left\{\frac{1}{3}\frac{1}{\sqrt{2\pi(M^2+\delta_{Q_i}^2)}}\exp\left[-\frac{Q_i^2}{2(M^2+\delta_{Q_i}^2)}\right]\right.$$
$$\left.+\frac{2}{3}\frac{1}{\sqrt{2\pi\delta_{Q_i}^2}}\exp\left[-\frac{Q_i^2}{2\delta_{Q_i}^2}\right]\right\} \tag{6.8}$$

where N_0 normalizes the likelihood function as

$$\int_0^{M_{max}} L(M)\,dM = 1.$$

We chose $M_{max} = 10$ for the normalization.

The likelihood function is shown as the smooth curve in Firgure 6.1. The most compact region of 68% confidence level is represented by the shaded area. The value of M is

$$M = 0.59\ {}^{+0.50}_{-0.25}\qquad \text{meV}\qquad (68\%\ \text{CL.})$$

where 0.59 is the most probable value. The vertical bars in the plot represent the statistical significance of the p_i's. They are plotted at x-coordinates $|Q_i|$ with lengths proportional to $\frac{Q_i}{\delta_{Q_i}}$, the statistical significance of the Q_i.

One can then determine the parity violating spreading width as (equation 2.16)

$$\Gamma^{PV} = 2\pi\frac{M^2}{D} \equiv \begin{pmatrix} 1.0\ {}^{+1.7}_{-0.8} \end{pmatrix} \times 10^{-7}\ \text{eV}$$

and α_p as (equation 2.19)

$$|\alpha_p| = \sqrt{\frac{\Gamma^{PV}}{2\pi \times 10^5 \text{eV}}} \approx \begin{pmatrix} 4\ {}^{+4}_{-2} \end{pmatrix} \times 10^{-7}$$

E_p (eV)	$p \pm \delta_p$ (10^{-3})	A_i (1/eV)	$Q_i \pm \delta_{Q_i}$ (meV)
10.228	-1.64± 0.83	24.61	-0.07± 0.03
11.347	6.74± 3.74	47.13	0.14± 0.08
45.200	-13.10±21.02	34.82	-0.38± 0.60
57.936	59.22±29.22	65.74	0.90± 0.44
63.500	26.25± 3.98	34.42	0.76± 0.12
83.695	19.56± 8.55	13.58	1.44± 0.63
89.221	-2.44± 1.14	4.70	-0.52± 0.24
93.075	-0.30±23.02	24.59	-0.01± 0.94
98.000	-21.77±13.03	54.21	-0.40± 0.24
124.99	10.76± 8.63	10.56	1.02± 0.82
152.42	-1.42± 5.64	4.38	-0.32± 1.29
158.94	-3.55±13.66	8.57	-0.41± 1.59
173.15	10.39± 7.13	7.80	1.33± 0.91
242.70	-6.13± 6.25	4.87	-1.26± 1.28
253.88	-1.60± 6.49	3.25	-0.49± 2.00
263.91	-0.13± 4.24	2.46	-0.05± 1.72
282.40	4.07±13.97	4.95	0.82± 2.82

Table 6.2: Q_i's for the 17 p-wave resonances

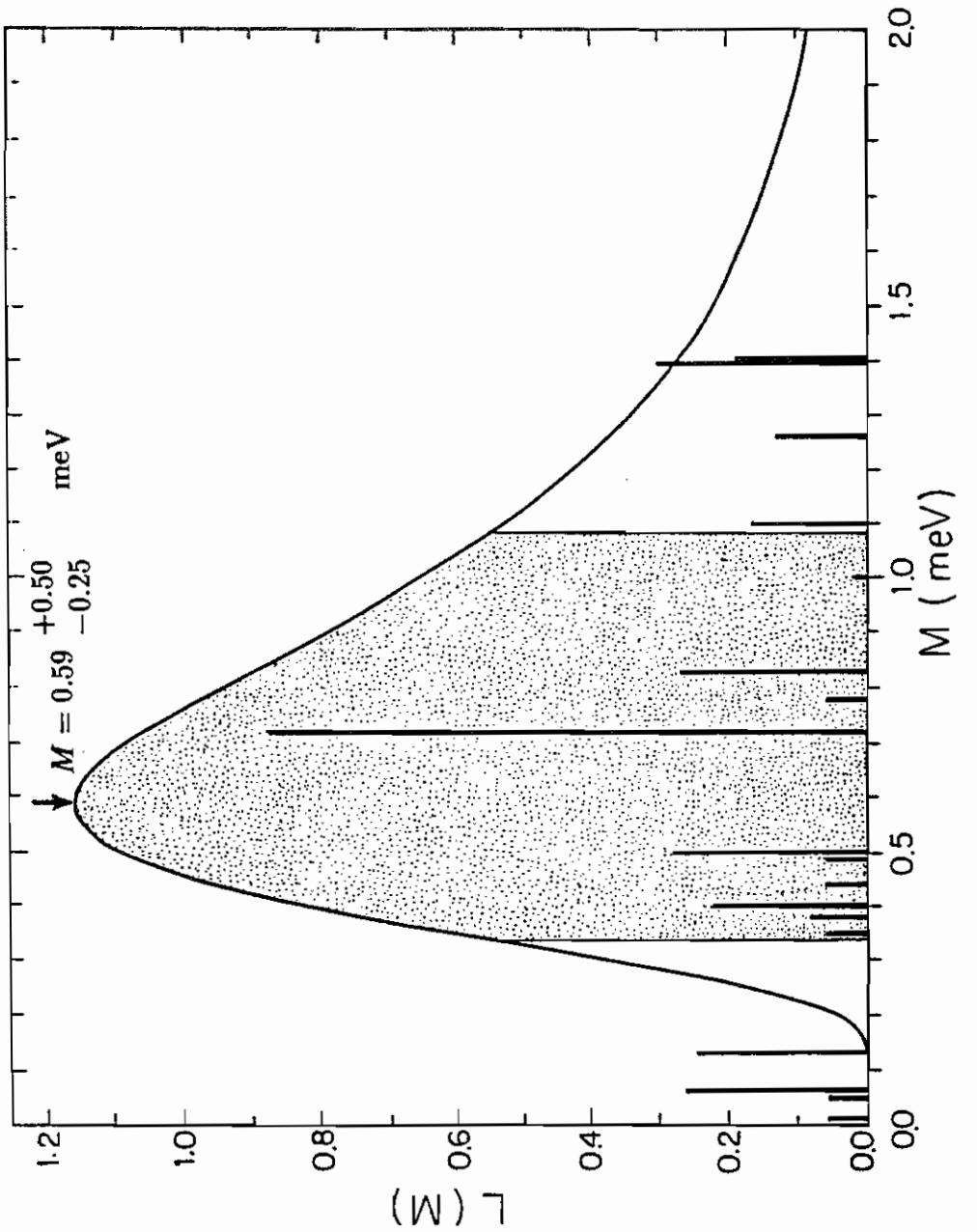

Figure 6.1: The likelihood function

where we took the level spacing D to be 21.0 eV (the level spacing for the s-wave resonances).

One can compare the Γ^{PV} obtained in this experiment with the value obtained in light nuclei. Near the ground states of light nuclei, D is a few MeV. Typical([Adel85]) measured mixing matrix elements are in the range of 0.03–3 eV. This gives a estimate in light nuclei of

$$\Gamma^{PV} \sim 6 \times 10^{-9} — 6 \times 10^{-5} \qquad \text{eV}$$

where we have used $D \sim 1$MeV.

One can compare the α_p we obtained for the effective NN interaction in the compound nucleus with the α_p of free NN interaction. In free NN interaction, the weak interaction amplitude can be estimated as

$$a_w = \frac{g_w^2}{m_W^2 + q^2}$$

where g_w is the weak coupling constant, m_W the W mass, and q the four momentum transfer; the strong interaction amplitude can be estimated as

$$a_s = \frac{f_{\pi NN}^2}{m_\pi^2 + q^2}$$

where $f_{\pi NN}$ is the pion-nucleon coupling constant and m_π is the pion mass. The strength of parity violation in the free NN interaction can be estimated as the ratio of the weak and strong interaction amplitudes as

$$\alpha_p = \frac{a_w}{a_s} = \frac{g_w^2}{f_{\pi NN}^2} \frac{m_\pi^2}{m_W^2} = 2 \times 10^{-7}$$

where we have used ([Frau74]) $g_w^2 = 0.65 \times 10^{-12} m_W^2$ (m_W in MeV), $f_{\pi NN}^2 = 0.08$ and $m_\pi = 140$ MeV.

Chapter 7

Summary and Conclusions

In this document, we reported the first determination of M, the Root-Mean-Square of the parity violating matrix elements.

We briefly reviewed the search for parity violation in the NN interaction. The large parity violation observed by Alfimenkov et al. stimulated our interest in this field. They observed a 10% parity violation at the 0.734 eV p-wave resonance in ^{139}La.

The observed large parity violation is explained by the mixing of the p-wave resonance with a nearby s-wave resonance in the CN. Due to the small energy spacing in the CN system, the parity violation can be enhanced by a factor as large as $\sim 10^5$ over the single-particle estimates. Explicit form of the parity violating asymmetry is given for spin zero targets. The model of two level mixing is generalized to include the mixing with many s-wave levels.

Before this experiment, the existing data in this field was insufficient to permit a determination of the parity violating matrix elements since all the data were taken with spin $I \neq 0$ targets and since the j-spin mixing ratios are not available. Furthermore parity violation was observed at most for one resonance per nucleus, and it is impossible to obtain the statistical properties of the matrix elements. All these obstacles are removed in this work. We chose a spin zero target ^{238}U; the j-spin mixing

ratios are 1. We studied parity violation simultaneously on many p-wave resonances of the same nucleus, and are able to extract the RMS parity violating matrix element without determining the individual matrix elements.

The experiment was performed using the intense pulsed epithermal neutron beam at the Los Alamos Neutron Scattering Center. A transmission measurement using polarized neutrons was carried out to determine the helicity dependence of the total cross sections. The neutron energy interval of 6 eV to 300 eV was studied. Different energy neutrons are separated by time-of-flight.

The parity violating asymmetry on p-wave resonances is extracted by fitting the neutron transmission spectra for both helicities simultaneously. Since the Doppler broadening of the p-wave resonances is not negligible, the Doppler broadening effect is treated in detail. Seventeen p-wave resonances are analyzed for parity violation. Amongst them, five show 2σ or larger effect. The largest is a 7σ effect at the 63.5 eV resonance which gives $p = 2.6\%$.

Using a likelihood analysis, we are able to determine the RMS parity violating matrix element as $M = 0.59 \begin{matrix} +0.50 \\ -0.25 \end{matrix}$ meV (68% CL), under the assumption that the parity violating matrix elements are Gaussian distributed random variables. The M obtained is free of detailed assumption about nuclear spectroscopy.

Using statistical nuclear spectroscopy, we are able to relate M to the effective NN interaction. For convenience, we introduce the parity violating spreading width $\Gamma^{PV} = 2\pi\frac{M^2}{D}$, where D is the level spacing in the CN. One can relate Γ^{PV} to the effective NN interaction as $\Gamma^{PV} = 2\pi(10^5\text{eV})\alpha_p^2$, where α_p is the ratio of the parity violating strength to the parity conserving strength in the effective NN interaction. Our measurement gives $\Gamma^{PV} = \begin{pmatrix} 1.0 \begin{matrix} +1.7 \\ -0.8 \end{matrix} \end{pmatrix} \times 10^{-7}$ eV which is consistent with the estimate in light nuclei, and $|\alpha_p| \approx \begin{pmatrix} 4 \begin{matrix} +4 \\ -2 \end{matrix} \end{pmatrix} \times 10^{-7}$ which agrees with the estimate of free NN interaction qualitatively.

The TRIPLE collaboration is making similar measurements on other nuclei, in an effort to map out the A dependence of Γ^{PV} and α_p.

The fact that Γ^{PV} and α_p agree with expectation is very encouraging. It suggests that the manifestation of the parity violating NN interaction in the CN is well understood. It has stimulated theoretical interest of relating the parity violation in compound nuclei to the DDH potential. In light of the large enhancement in the CN, direct measurement of time reversal violation is proposed. The TRIPLE collaboration is vigorously exploring this possibility. New instruments are under construction. A new ^{10}B-loaded scintillator will greatly increase the neutron detecting efficiency at higher energies, and a new polarizer will bring higher neutron polarization and larger neutron flux. With the new instruments in place, a 10 fold increase in sensitivity is expected.

Appendix A

S-wave Scattering of spin-$\frac{1}{2}$ particles

Consider a beam of particles colliding with a target. Choose the direction of the incident particles to be the z-axis. The incident beam can be described by the planewave e^{ikz} which contains many orbital angular momentum components. Explicitly,

$$\begin{aligned} e^{ikz} &= \sum_{l=0}^{\infty} i^l \sqrt{4\pi(2l+1)}\, j_l(kr) Y_l^0(\theta) \\ &\overset{kr\to\infty}{\cong} \sum_{l=0}^{\infty} i^l \sqrt{4\pi(2l+1)} \frac{\sin(kr - \frac{1}{2}l\pi)}{kr} Y_l^0(\theta). \end{aligned}$$

Since we are only interested in the scattering at low energies, the most significant contribution is from the s-wave term ($l = 0$). For spin 0 particles, the asymptotic wavefunction is

$$\psi = e^{ikz} + f\frac{e^{ikr}}{r} \cong \frac{\sin kr}{kr} + f\frac{e^{ikr}}{r}$$

where we retained only the $l = 0$ term in the e^{ikz} expansion. The total scattering cross section is then $4\pi f^2$. For spin-$\frac{1}{2}$ particles, the spin wave functions have to enter. If the initial and final spin wave functions are respectively ζ_i and ζ_f, the asymptotic s-wave scattering can be written as

$$\psi \cong \frac{\sin kr}{kr}\zeta_i + f\frac{e^{ikz}}{r}\zeta_f$$

Spin-$\frac{1}{2}$ particles have two spin states α and β with z-projections $+\frac{1}{2}$,$-\frac{1}{2}$, respectively. Now consider the interaction between two spin-$\frac{1}{2}$ particles, such as a neutron and a proton. If we are interested in the total angular momentum, we can choose the following spin wave functions,

$$\begin{aligned}
\zeta_s &= \frac{1}{\sqrt{2}}(\alpha_1\beta_2 - \beta_1\alpha_2) \\
\zeta_t^+ &= \alpha_1\alpha_2 \\
\zeta_t^0 &= \frac{1}{\sqrt{2}}(\alpha_1\beta_2 + \beta_1\alpha_2) \\
\zeta_t^- &= \beta_1\beta_2
\end{aligned}$$

whereas, if we want to keep track of the spins of the individual particles, we can use

$$\begin{aligned}
\zeta^{++} &= \alpha_1\alpha_2 = \zeta_t^+ \\
\zeta^{+-} &= \alpha_1\beta_2 = \frac{1}{\sqrt{2}}(\zeta_t^0 + \zeta_s) \\
\zeta^{-+} &= \beta_1\alpha_2 = \frac{1}{\sqrt{2}}(\zeta_t^0 - \zeta_s) \\
\zeta^{--} &= \beta_1\beta_2 = \zeta_t^-
\end{aligned}$$

Now introduce an operator A_0 such that

$$A_0\zeta_i = a_{0,fi}\zeta_f$$

The matrix element of A_0 taken between the initial state ζ_i and the final state ζ_f is the scattering amplitude between the two states:

$$a_{0,fi} = \langle f|A_0|i\rangle.$$

Now let us work out the matrix elements of the operator A_0. For two spin-$\frac{1}{2}$ particles, it is a 4×4 matrix. Let us use the total angular momentum representation. For s-wave scattering, A_0 should be diagonal because the total spin and its z-component have to be conserved. That is, it contains at most 4 non-zero elements: a_s, a_t^+, a_t^0 and a_t^-. Since we are considering only the s-wave scattering, there is no preferred axis. Therefore the last three amplitudes have to be the same: $a_t^+ = a_t^0 = a_t^- = a_t$.

Therefore the scattering amplitude matrix has the form,

$$A_0 = \begin{array}{c} \\ \zeta_s \\ \zeta_t^- \\ \zeta_t^0 \\ \zeta_t^+ \end{array} \begin{array}{c} \begin{array}{cccc} \zeta_s & \zeta_t^- & \zeta_t^0 & \zeta_t^+ \end{array} \\ \begin{pmatrix} a_s & 0 & 0 & 0 \\ 0 & a_t & 0 & 0 \\ 0 & 0 & a_t & 0 \\ 0 & 0 & 0 & a_t \end{pmatrix} \end{array}$$

where the ζ's represent the basis.

To simplify the calculation, let us introduce two projection operators, Λ_s and Λ_t. The eigenvalue of Λ_s (Λ_t) is 1 for the singlet (triplet) state, and 0 for the triplet (singlet) states. The operator A_0 is therefore

$$A_0 = \Lambda_s a_s + \Lambda_t a_t.$$

Now we calculate the matrix elements under the other representation.

$$\begin{aligned}
\langle \alpha_1 \alpha_2 | A_0 | \alpha_1 \alpha_2 \rangle &= \langle \zeta_t^+ | A_0 | \zeta_t^+ \rangle \\
&= a_t \\
\langle \beta_1 \beta_2 | A_0 | \beta_1 \beta_2 \rangle &= \langle \zeta_t^- | A_0 | \zeta_t^- \rangle \\
&= a_t \\
\langle \alpha_1 \beta_2 | A_0 | \alpha_1 \beta_2 \rangle &= \langle \frac{1}{\sqrt{2}}(\zeta_t^0 + \zeta_s) | A_0 | \frac{1}{\sqrt{2}}(\zeta_t^0 + \zeta_s) \rangle \\
&= \frac{1}{2}(a_t + a_s) \\
\langle \beta_1 \alpha_2 | A_0 | \beta_1 \alpha_2 \rangle &= \langle \frac{1}{\sqrt{2}}(\zeta_t^0 - \zeta_s) | A_0 | \frac{1}{\sqrt{2}}(\zeta_t^0 - \zeta_s) \rangle \\
&= \frac{1}{2}(a_t + a_s).
\end{aligned}$$

Using the same technique, we can calculate all matrix elements. They are

$$\begin{array}{c} \\ \alpha_1\alpha_2 \\ \alpha_1\beta_2 \\ \beta_1\alpha_2 \\ \beta_1\beta_2 \end{array} \begin{array}{c} \begin{array}{cccc} \alpha_1\alpha_2 & \alpha_1\beta_2 & \beta_1\alpha_2 & \beta_1\beta_2 \end{array} \\ \begin{pmatrix} a_t & 0 & 0 & 0 \\ 0 & \frac{1}{2}(a_t+a_s) & \frac{1}{2}(a_t-a_s) & 0 \\ 0 & \frac{1}{2}(a_t-a_s) & \frac{1}{2}(a_t+a_s) & 0 \\ 0 & 0 & 0 & a_t \end{pmatrix} \end{array}$$

The total cross section for any particular initial spin state is the sum of the square of the elements in the column times 4π, ie.

$$\begin{aligned} \sigma_{para} &= 4\pi|a_t|^2 \\ &= \sigma_t \\ \sigma_{anti} &= 4\pi\frac{1}{4}(|a_t+a_s|^2+|a_t-a_s|^2) \\ &= \frac{1}{2}4\pi(|a_t|^2+|a_s|^2) \\ &= \frac{\sigma_t+\sigma_s}{2}. \end{aligned}$$

Experimentally (Table2-10 of [Wils63]),

$$\begin{aligned} a_t &= (5.399 \pm 0.011) \times 10^{-13} \text{ cm} \\ a_s &= (-23.680 \pm 0.028) \times 10^{-13} \text{ cm} \end{aligned}$$

which gives

$$\begin{aligned} \sigma_t &= 4\pi a_t^2 = 3.66 \pm 0.01 \text{ barn} \\ \sigma_s &= 4\pi a_s^2 = 70.46 \pm 0.17 \text{ barn.} \end{aligned}$$

Therefore

$$\begin{aligned} \sigma_{para} &= \sigma_t = 3.66 \pm 0.01 \text{ barn} \\ \sigma_{anti} &= \frac{\sigma_t+\sigma_s}{2} = 37.06 \pm 0.09 \text{ barn} \end{aligned}$$

and

$$\sigma_p = \frac{\sigma_{anti} - \sigma_{para}}{2} = 16.7 \text{ barn.}$$

Appendix B

NMR Calibration

B.1 Introduction

The neutron polarization is monitored by the NMR signal. However, since the NMR signal is a function of the geometrical arrangement of the NMR coil relative to the location of the LMN crystal, it is necessary to calibrate the system. The calibration procedure basically involves measuring the NMR signal and the neutron transmission simultaneously at different proton polarizations, and using a least square fitting procedure to determine the calibration constant. The details will be discussed in the following sections.

B.2 Transmission of unpolarized neutrons through a polarized LMN crystal

Let us assume that the protons are polarized in the beam direction, and let us also choose the z-axis to be in the beam direction. Suppose in a cubic centimeter of the crystal, there are n_{p+} protons with spin $+\frac{1}{2}$, and n_{p-} protons with spin $-\frac{1}{2}$. By

definition, the proton polarization f_p and the proton number density n are

$$f_p = \frac{n_{p+} - n_{p-}}{n_{p+} + n_{p-}}, \tag{B.1}$$

$$n = n_{p+} + n_{p-}. \tag{B.2}$$

Solving for n_{p+} and n_{p-} from equations (B.1) and (B.2), we get

$$n_{p+} = \frac{n}{2}(1 + f_p) \tag{B.3}$$

$$n_{p-} = \frac{n}{2}(1 - f_p). \tag{B.4}$$

The n-p cross section, as discussed in appendix A, is strongly spin dependent. If σ_{para} is the spin parallel cross section, and σ_{anti} is the spin anti-parallel cross section, we can write

$$\sigma_{para} = \sigma_0 - \sigma_p \tag{B.5}$$

$$\sigma_{anti} = \sigma_0 + \sigma_p \tag{B.6}$$

where σ_0 represents the spin independent cross section, and $\sigma_p = \frac{\sigma_{anti} - \sigma_{para}}{2}$ is called the polarization cross section. For neutron energies 1 eV — 10 keV, σ_p is essentially constant at 16.7 barn ([Drag64]).

Now consider the transmission of N_0 unpolarized neutrons through the polarized LMN crystal. Since the N_0 incident neutrons are unpolarized, there are $\frac{1}{2}N_0$ neutrons with spin $+\frac{1}{2}$ and $\frac{1}{2}N_0$ neutrons with spin $-\frac{1}{2}$. If N_+ and N_- are the number of transmitted neutrons with spins $+\frac{1}{2}$ and $-\frac{1}{2}$, respectively, as shown in Figure B.1, we have

$$\begin{aligned} N_+ &= \frac{1}{2}N_0 e^{-\alpha} e^{-(n_{p+}\sigma_{para} + n_{p-}\sigma_{anti})t} \\ &= \frac{1}{2}N_0 e^{-\alpha} e^{-n\sigma_0 t} e^{+f_p n \sigma_p t} \end{aligned} \tag{B.7}$$

$$\begin{aligned} N_- &= \frac{1}{2}N_0 e^{-\alpha} e^{-(n_{p+}\sigma_{anti} + n_{p-}\sigma_{para})t} \\ &= \frac{1}{2}N_0 e^{-\alpha} e^{-n\sigma_0 t} e^{-f_p n \sigma_p t} \end{aligned} \tag{B.8}$$

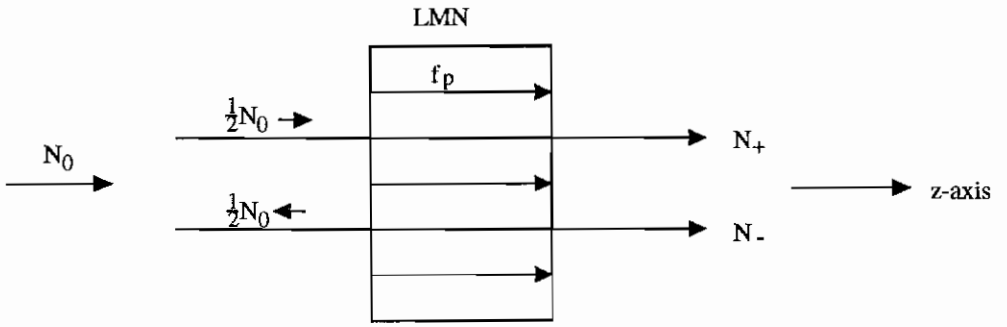

Figure B.1: Transmission of unpolarized neutrons through a polarized LMN crystal

where $e^{-\alpha}$ represents the spin independent absorption by the LMN nuclei other than the protons, and t is the thickness of the crystal in centimeters. Therefore the intensity and the polarization of the transmitted beam are

$$\begin{aligned} N &\equiv N_+ + N_- \\ &= N_0 e^{-\alpha} e^{-n\sigma_0 t} \cosh(f_p n \sigma_p t) \qquad \text{(B.9)} \\ f_n &\equiv \frac{N_+ - N_-}{N_+ + N_-} \\ &= \tanh(f_p n \sigma_p t). \qquad \text{(B.10)} \end{aligned}$$

B.3 Method of NMR calibration

The proton polarization f_p is related to the NMR area s by

$$f_p = c \cdot s$$

where c is a constant. By virtue of equation (B.10), the neutron polarization is related to s by

$$f_n = \tanh(a_2\, s) \qquad \text{(B.11)}$$

where $a_2 = n\sigma_p t\, c$ is a constant, and is the quantity to be determined by the NMR calibration procedure.

Take N of equation (B.9) to be the number of counts in the transmitted neutron spectrum. If we sum over some energy region, we have

$$\sum N = \left(\sum N_0 e^{-\alpha} e^{-n\sigma_0 t}\right) \cosh(a_2 s).$$

The number of counts in the monitor spectrum, m, is related to N_0 by $m = \epsilon N_0$, where ϵ is the monitor efficiency. Normalizing the detector counts to the monitor counts, we get

$$\begin{aligned} Z &= \frac{\sum N}{\sum m} = \frac{\sum (N_0 e^{-\alpha} e^{-n\sigma_0 t})}{\sum \epsilon N_0} \cosh(a_2 s) \\ &= a_1 \cosh(a_2 s) \end{aligned} \tag{B.12}$$

where a_1 is a constant.

During the experiment, the monitor experienced considerable radiation damage, and its efficiency dropped slowly with time t. We assume a quadratic monitor efficiency change as

$$\epsilon \approx (1 - a_3 t - a_4 t^2)\epsilon_0$$

where a_3 and a_4 are constants, and ϵ_0 is the monitor efficiency without radiation damage. Then equation (B.12) should be modified as

$$\begin{aligned} Z &= \frac{\sum N}{\sum m} = \frac{(\sum N_0 e^{-\alpha} e^{-n\sigma_0 t})}{(1 - a_3 t - a_4 t^2) \sum \epsilon_0 N_0} \cosh(a_2 s) \\ &= a_1 (1 + a_3 t + a_4 t^2) \cosh(a_2 s) \end{aligned} \tag{B.13}$$

where a_1, a_2, a_3 and a_4 are constants. In obtaining equation (B.13), we have used the expansion

$$\frac{1}{1 - a_3 t - a_4 t^2} \approx (1 + a_3 t + a_4 t^2).$$

As seen from equation (B.13), the calibration procedure can not determine the sign of a_2, since the hyperbolic cosine is an even function. The calibration procedure can only determine the amplitude of a_2. Equation (B.13) is equivalent to

$$Z = a_1 (1 + a_3 t + a_4 t^2) \cosh(|a_2|\,|s|). \tag{B.14}$$

The sign of a_2 will be discussed in section B.5.

B.4 Experimental procedure and data analysis

The seven detector array was set up in the pulse (multiscaler) mode, as discussed in chapter 3. The count rate in the array was reduced by placing a 2″ thick lead brick in the beam upstream the spin flipper, so that pulse mode could be used. A 20 mil thick Ta foil was put downstream the spin flipper to introduce a black resonance into the neutron TOF spectrum, which can be used as a check to ensure that everything is working properly. The spin flipper was off during the NMR calibration runs.

The NMR calibration procedure consists of a sequence of 63 runs, with the microwave power turned off after 20 runs to allow the proton polarization to relax toward 0. Each run measures 10 NMR sweeps at the beginning, followed by 2400 beam bursts ($\sim$ 2 minutes) of neutron transmission, and another 10 NMR sweeps at the end. A monitor reading was taken for each beam burst. A time pulse with a period of approximately 0.2 seconds was recorded with the data and allowed the relative beginning time t_b and the ending time t_e to be established.

Figure B.2 shows a typical neutron transmission spectrum. At short neutron flight times (TOF $<$ channel 20), the count rate is so high that the system saturates. But by channel 2000, the PMT and the amplifier have recovered. The integrated neutron transmission $\sum N$ is obtained by summing from channel 1981, the location of a black resonance, to channel 8191.

The average of the beginning and ending NMR signals is used as the NMR signal of the run. A typical NMR signal is shown in Figure B.3. Three gates were set in this spectrum:

Left gate:	[80, 150]
Resonance:	[156, 348]
Right gate:	[356, 436].

The NMR area is taken as the area of the resonance below the Q-curve. The Q-curve is determined by fitting the part of the spectrum contained within the left and right

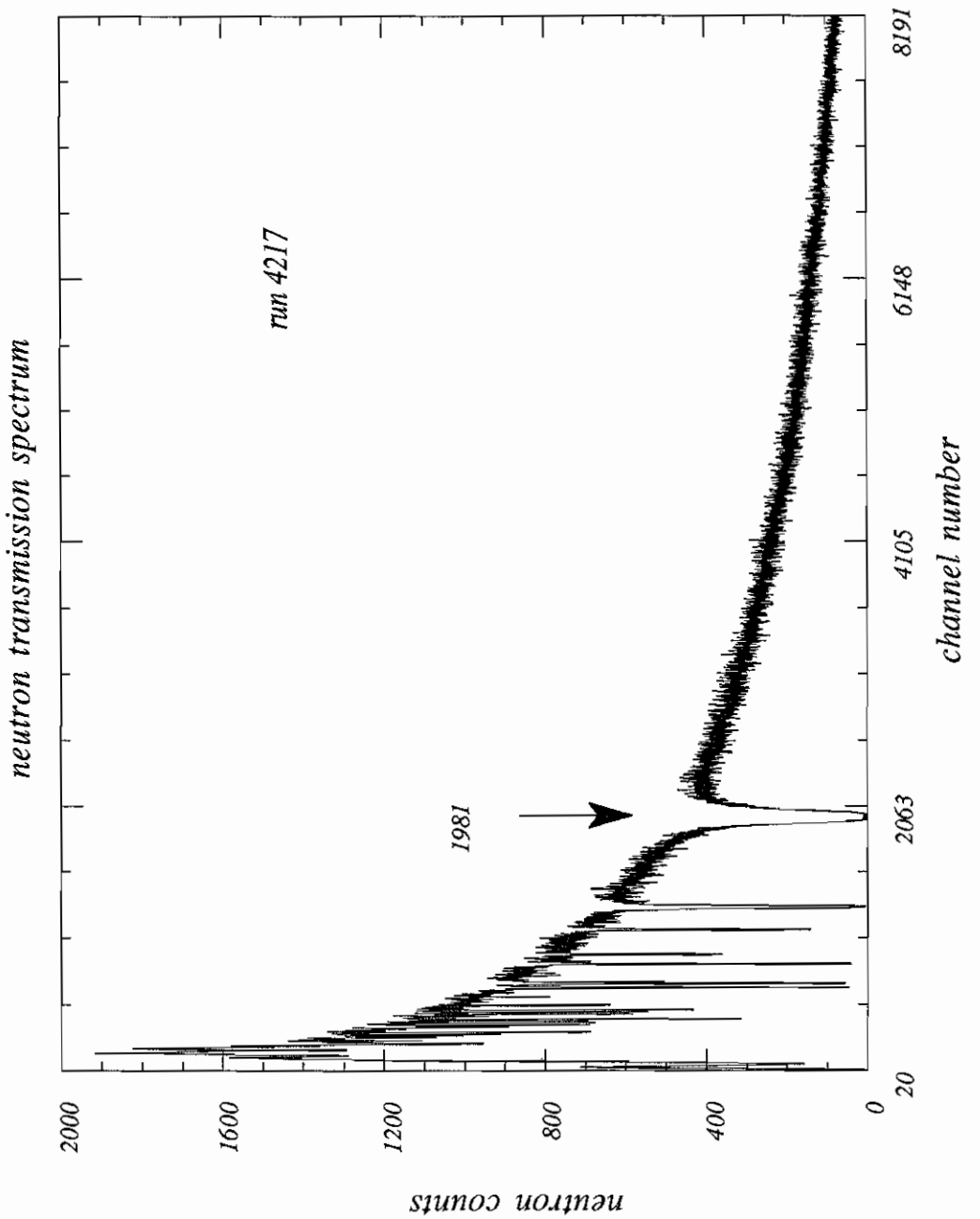

Figure B.2: Typical neutron transmission spectrum in the NMR calibration runs

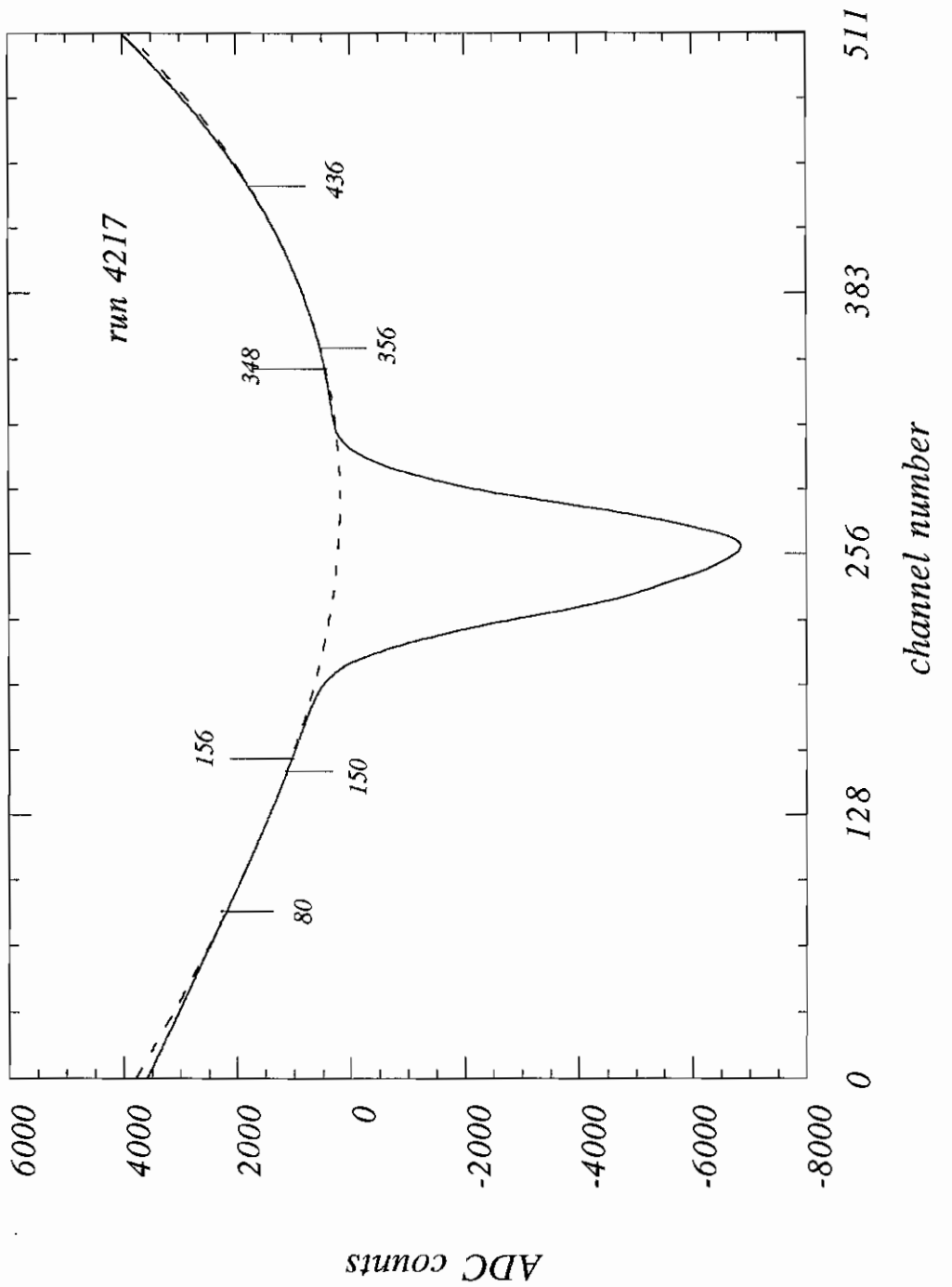

Figure B.3: Typical NMR signal with gate settings

gates to a third order polynomial

$$y = c_0 + c_1 x + c_2 x^2 + c_3 x^3,$$

as shown by the dashed line in Figure B.3.

The NMR area was extracted as

$$s = \sum_i (\mathrm{NMR}_i - Q_i)$$

where NMR_i and Q_i are respectively the readings of the NMR signal and the fitted Q-curve at channel i, and the sum is over the resonance gate.

The result of the NMR calibration measurement is listed in Table B.1. The time t is determined as the average of the beginning time and the ending time of the run

$$t = \frac{t_b + t_e}{2},$$

and Z is obtained as

$$Z = \frac{\sum N}{\sum m}$$

where $\sum m$ is the sum of the monitor counts for the 2400 beam bursts. The error in Z is determined by method of error propagation. Since the number of neutrons recorded by the monitor is much larger than the number of neutrons recorded by the main detector, the error in Z is mostly from the counting statistics of the main detector, ie.

$$\delta Z = \frac{\sqrt{\sum N}}{\sum m}.$$

Figure B.4 shows $\sum N$ (solid line) and $\sum m$ (dashed line) as a function of the run number. As seen from the figure, $\sum N$ drops as the proton target depolarizes while $\sum m$ is essentially flat. Beam fluctuation is apparent in the plot.

Figure B.5 shows the normalized transmission Z and the NMR area $|s|$ vs run number. It shows that both the neutron transmission and the NMR area drops after the protons started to depolarize.

run #	time(t)	Z	δZ	|NMR area| ($\|s\|$)
4217	233.	1.6382	0.0015	410793.2
4218	750.	1.6389	0.0015	411039.6
4219	1269.	1.6374	0.0015	410394.0
4220	2469.	1.6363	0.0015	410954.8
4221	3668.	1.6369	0.0015	410438.4
4222	4767.	1.6338	0.0015	410340.9
4223	5869.	1.6340	0.0015	410324.1
4224	6388.	1.6386	0.0015	409294.9
4225	6906.	1.6370	0.0015	409929.6
4226	7425.	1.6383	0.0015	409308.2
4227	7945.	1.6376	0.0015	408805.9
4228	8463.	1.6396	0.0015	409170.1
4229	9068.	1.6461	0.0016	408912.3
4230	9670.	1.6385	0.0015	409677.9
4231	10191.	1.6407	0.0015	409745.7
4232	10709.	1.6398	0.0015	409309.3
4233	11228.	1.6384	0.0015	408791.3
4234	11747.	1.6414	0.0015	409662.9
4235	12267.	1.6370	0.0015	409272.6
4236	12785.	1.6401	0.0015	408846.7
4237	13304.	1.6413	0.0015	408784.2
4238	13822.	1.6256	0.0015	397368.2
4239	14357.	1.6133	0.0015	380867.3
4240	14892.	1.5942	0.0015	365666.7
4241	15411.	1.5821	0.0014	351866.6
4242	15931.	1.5707	0.0014	337980.3
4243	16450.	1.5635	0.0014	325592.2
4244	16968.	1.5509	0.0014	313930.7
4245	17488.	1.5428	0.6614	301969.0
4246	18015.	1.5364	0.0014	288480.3
4247	18534.	1.5289	0.0014	277131.0
4248	19052.	1.5187	0.0014	265909.2
4249	19570.	1.5131	0.0014	256951.1
4250	20088.	1.5100	0.0014	246585.9
4251	20607.	1.5057	0.0014	237918.3
4252	21126.	1.5024	0.0014	226568.2
4253	21643.	1.5025	0.0014	220030.7
4254	22164.	1.4941	0.0014	212538.0
4255	22683.	1.4937	0.0014	204011.4
4256	23201.	1.4913	0.0014	195332.1
4257	23719.	1.4884	0.0014	187736.9
4258	24237.	1.4847	0.0014	180362.9
4259	24755.	1.4826	0.0014	173695.3
4260	25273.	1.4838	0.0014	166938.6
4261	25791.	1.4820	0.0014	160309.2
4262	26311.	1.4788	0.0014	154213.2
4263	26828.	1.4812	0.0014	148713.1
4264	27345.	1.4776	0.0014	143355.6
4265	27864.	1.4773	0.0014	137531.6
4266	28383.	1.4746	0.0014	132142.1
4267	28902.	1.4732	0.0014	126587.9
4268	29431.	1.4727	0.0014	120937.8
4269	29950.	1.4755	0.0014	117294.8
4270	30469.	1.4752	0.0014	112008.0
4271	30988.	1.4756	0.0014	108031.5
4272	31508.	1.4728	0.0014	103738.0
4273	32027.	1.4740	0.0014	100535.9
4274	32544.	1.4704	0.0014	96628.9
4275	33216.	1.4709	0.0014	91718.1
4276	33889.	1.4692	0.0014	87980.3
4277	34407.	1.4669	0.0014	64131.1
4278	34938.	1.4699	0.0014	80139.0
4279	35458.	1.4671	0.0014	76956.8

Table B.1: Summary of the NMR calibration runs

Figure B.6 shows a least square fit to equation (B.14). The calibration constant is determined to be

$$|a_2| = (1.2963 \pm 0.0044) \times 10^{-6}$$

and

$$\begin{aligned} a_3 &= (-2.54 \pm 0.48) \times 10^{-7} \\ a_4 &= (2.70 \pm 0.12) \times 10^{-11}. \end{aligned}$$

B.5 Sign of the calibration constant

We have determined the amplitude of the calibration constant in section B.4. In this section, we are going to determine the sign.

As discussed in chapter 3, the proton polarization is parallel to the superconducting magnetic field $\vec{B}$ for the lower microwave frequency, and anti-parallel for the higher microwave frequency. Since $\vec{B}$ is parallel to the beam direction, the proton polarization is parallel to the beam direction for the lower frequency, and anti-parallel for the higher microwave frequency, as shown in Figure B.7. The neutron polarization after the LMN crystal is, from equation (B.10), parallel to the proton polarization. The data is sorted according to the status of the spin flipper as follows: as the transverse field is on, the neutron spin is flipped, and the data is stored in data area 3; as the transverse field is off, the neutron spin is not flipped, and the data is stored in data area 4. Therefore for the lower microwave frequency, data area 3 holds negative helicity neutrons, while for the higher microwave frequency, data area 3 holds positive helicity neutrons. The neutron helicity in data area 4 is opposite to that in data area 3.

In extracting the parity violating asymmetries, we assumed that data area 3 holds positive helicity neutrons. This assumption is true for the higher microwave frequency, and is opposite for the lower microwave frequency. To account for this, we assign a

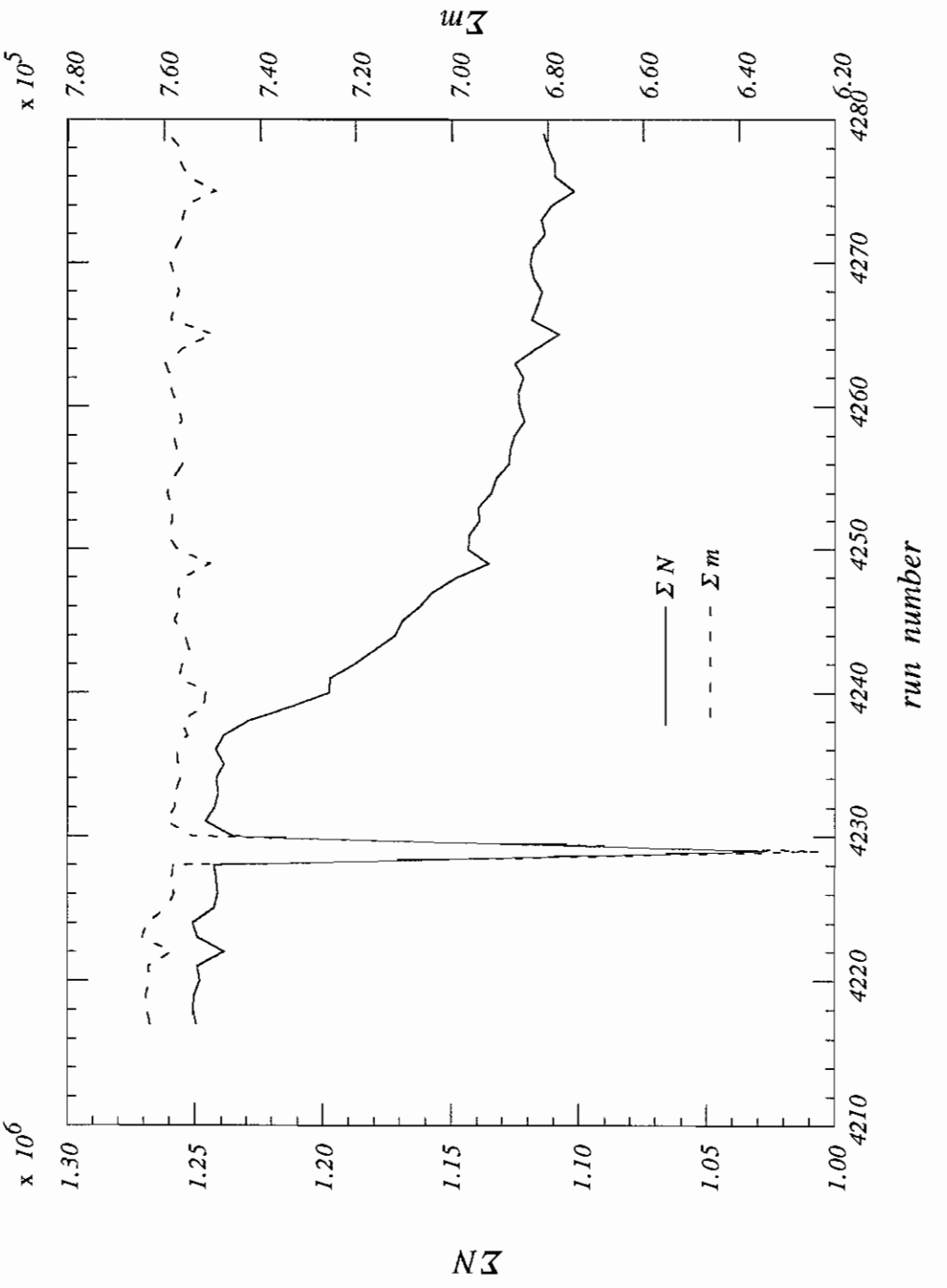

Figure B.4: Raw data vs run number

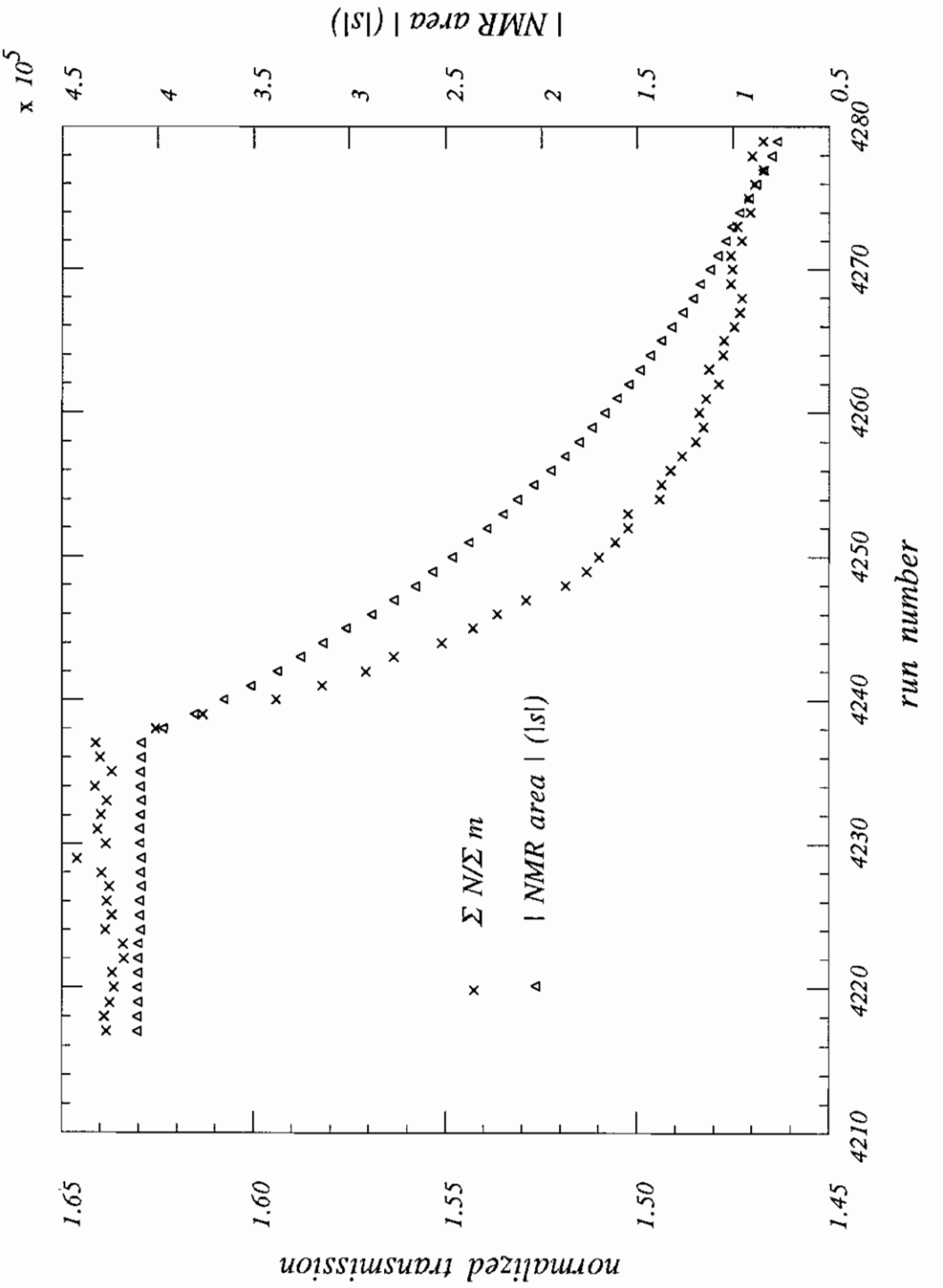

Figure B.5: Normalized data vs run number

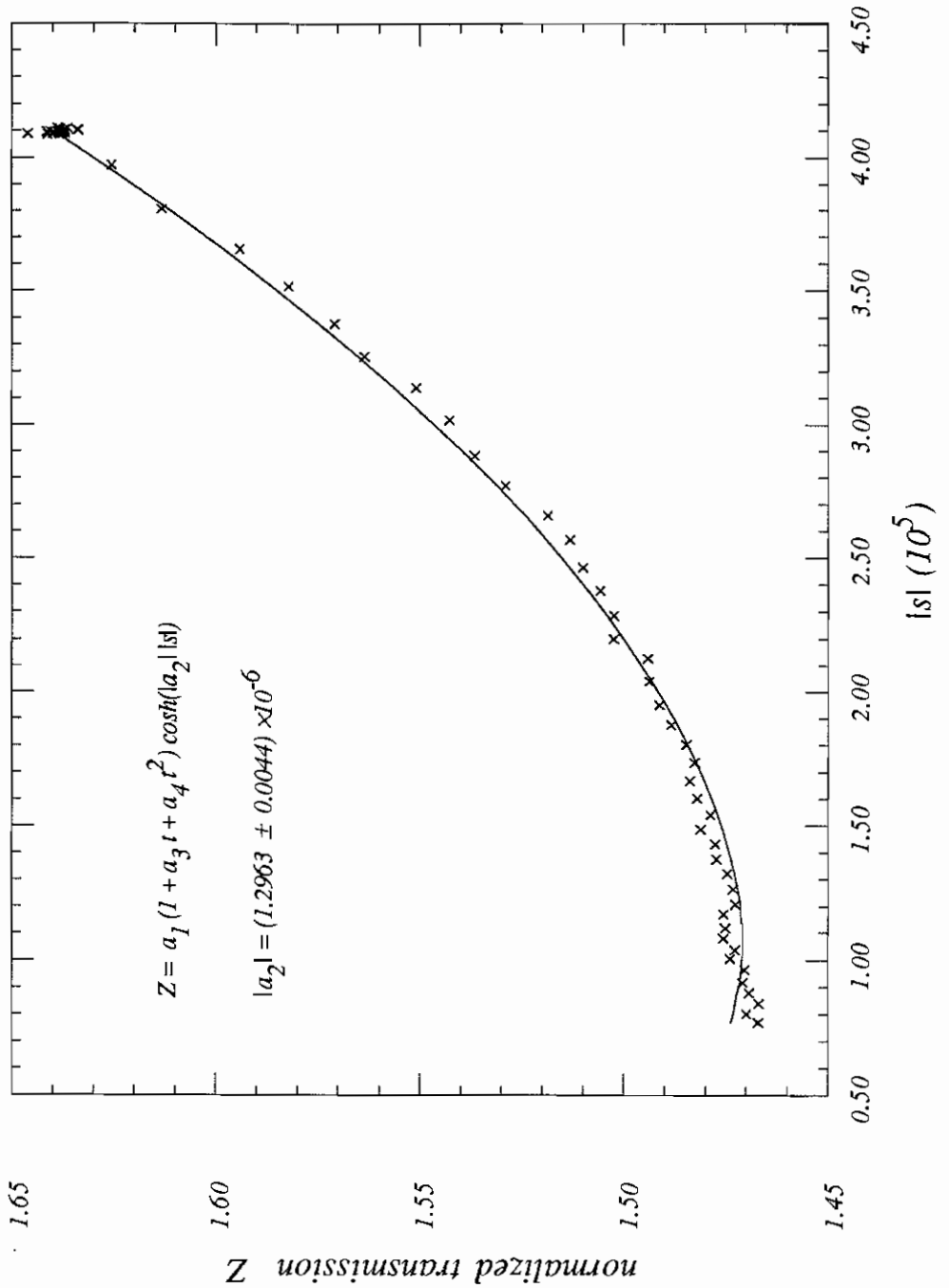

Figure B.6: NMR calibration fit

Figure B.7: Neutron spins at various parts of the beam-line. I_t is the transverse coil current, f_p and f_n are the proton and neutron polarizations, respectively.

	polarizer	spin flipper	target
	$\xrightarrow{\vec{B}}$		
75.520 GHz			
	$\xrightarrow{f_p}$	I_t on	3 $\xleftarrow{f_n}$
	$\xrightarrow[f_n]{}$	I_t off	4 $\xrightarrow[f_n]{}$
75.685 GHz			
	$\xleftarrow{f_p}$	I_t on	3 $\xrightarrow{f_n}$
	$\xleftarrow[f_n]{}$	I_t off	4 $\xleftarrow[f_n]{}$

negative sign to the neutron polarization for the lower microwave frequency. Since the NMR area is positive for the lower microwave frequency, a_2 should be negative and

$$a_2 = (-1.2963 \pm 0.0044) \times 10^{-6}.$$

For the higher microwave frequency, since the NMR area is negative, one obtains a positive neutron polarization as expected.

Appendix C

Neutron Flux from the LANSCE Spallation Source

C.1 Beam attenuation and detector efficiency

In this section, we discuss the attenuation of the neutron beam by various materials (the LMN crystal, the Los Alamos air, and the aluminum plates) and the efficiency of the ^{6}Li-loaded glass scintillators. The beam attenuating materials contain nuclei $^1_1$H, $^{12}_6$C, $^{14}_7$N, $^{16}_8$O, $^{24}_{12}$Mg, $^{27}_{13}$Al, and $^{139}_{57}$La. The total cross sections of neutron on these nuclei have been measured and can be obtained from reference [Garb73]. At neutron energies from 0.01 eV to 1 keV, the total cross sections have slow energy dependence, and are listed in Table C.1 for selected neutron energies. The total cross section at some other energy E_n can be obtained by interpolation as

$$\sigma = \frac{\sigma_1 \ln \frac{E_n}{E_{n,2}} - \sigma_2 \ln \frac{E_n}{E_{n,1}}}{\ln \frac{E_{n,1}}{E_{n,2}}}$$

where σ_1 and σ_2 are the total cross sections at $E_{n,1}$ and $E_{n,2}$, respectively.

The transmission of neutron through a material of thickness t can be expressed as

$$\exp\left[-\sum_i n_i \sigma_i t\right] = \exp\left[-\frac{t}{\lambda}\right] \tag{C.1}$$

Table C.1: Total cross sections of neutron on various targets

target nuclei	E_n (eV)	σ (barn)
$^{1}_{1}$H	0.01	47.
	0.032	29.
	0.09	22.
	1000.	21.
$^{12}_{6}$C	0.01 – 1000.	4.7
$^{14}_{7}$N	0.01	14.
	0.32	11.
	120.	9.9
	1000.	8.9
$^{16}_{8}$O	0.01 – 1000.	3.8
$^{24}_{12}$Mg	0.01 – 1000.	3.4
$^{27}_{13}$Al	0.01	1.86
	0.3	1.4
	1000.	1.35
$^{139}_{57}$La	0.01	35.0
	0.1	15.5
	1.6	11.8
	14.	8.0
	60.	5.0
	1000.	3.2

where n_i is the number density of the ith nuclei (in nuclei/cm^3), σ_i is the total cross section of the ith nucleus, and λ is the neutron mean-free-path in the material

$$\lambda = \frac{1}{\sum_i n_i \sigma_i}.$$

By definition, the neutron transmission through a one λ target is $e^{-1} = 36.8\%$.

LMN crystal

The molecular expression for the LMN crystal is

$$La_2Mg_3(NO_3)_{12}\cdot 24H_2O\ ,$$

and the molecular weight is

$$\begin{aligned} A &= 2\times \mathrm{La} + 3\times \mathrm{Mg} + 12\times \mathrm{N} + 60\times \mathrm{O} + 48\times \mathrm{H} \\ &= 1526. \end{aligned}$$

The LMN crystal has a density of 2.07g/cm^3 and a thickness of 1.8cm, as listed in Table 3.2. Therefore

$$\begin{aligned} \sum_i n_i\sigma_i t &= \frac{2.07\times 0.602\times 1.8}{1526}(2\sigma_{\mathrm{La}} + 3\sigma_{\mathrm{Mg}} + 12\sigma_{\mathrm{N}} + 60\sigma_{\mathrm{O}} + 48\sigma_{\mathrm{H}}) \\ &= 2.904\times 10^{-3}(\sigma_{\mathrm{La}} + 6\sigma_{\mathrm{N}} + 24\sigma_{\mathrm{H}} + 119.1) \end{aligned}$$

where the σ's are in barn, and we have used $\sigma_O = 3.8$ barn, $\sigma_{Mg} = 3.4$ barn, as listed in Table C.1.

Air

Standard air consists of 78.09% N_2 and 20.95% O_2 (p. F-205, [Weas77]). The air "molecule" has a molecular weight

$$A = 0.7809\times 28.0 + 0.2095\times 32.0 = 28.6.$$

We use the ideal gas model to calculate the number densities of the oxygen and nitrogen nuclei in the air of Los Alamos which has an elevation of approximately 7000 feet.

Using the ideal gas equation, we can relate the air density at Los Alamos to the air density at sea level

$$R = \frac{P}{nT} = \frac{P_0}{n_0 T_0},$$

where R is a constant, P, n, T are respectively the pressure, the density (moles/cm^3) and the temperature of air at Los Alamos, and P_0, n_0, T_0 are the corresponding quantities at sea level. Taking $T = T_0$, we can relate n to n_0 as

$$n = n_0 \frac{P}{P_0}. \tag{C.2}$$

The air pressure at Los Alamos has been measured to be $P = 11.6$ lb/in^2, and the air pressure at sea level is 14.7 lb/in^2. Therefore the ratio of the pressures is

$$\frac{P}{P_0} = \frac{11.6}{14.7}.$$

At room temperature (25 °C) at sea level, the density of air is $\rho_0 = 1.185 \times 10^{-3}$ g/cm^3 (p. F-11, [Weas77]), which corresponds to $n_0 = 0.0415$ moles/cm^3. Substituting these into equation (C.2), one finds

$$n = 0.0327 \qquad \text{moles/cm}^3.$$

Therefore the number densities of the oxygen and nitrogen nuclei in the Los Alamos air are

$$n_O = 8.25 \times 10^{-6}/(\text{cm}\cdot\text{barn})$$

$$n_N = 3.08 \times 10^{-5}/(\text{cm}\cdot\text{barn}),$$

and

$$n_O \sigma_O + n_N \sigma_N = (3.14 + 3.08\sigma_N) \times 10^{-3} \qquad \text{m}^{-1} \tag{C.3}$$

where we have used $\sigma_O = 3.8$ barn explicitly.

Table C.2: Neutron mean-free-paths

materials	λ (1 eV)	λ (1 keV)	typical λ
LMN	0.911cm	0.933 cm	0.92 cm
Los Alamos Air	29.5 m	32.4 m	30 m
Al	11.86 cm	11.86 cm	12 cm

Aluminum

Aluminum has $A = 27$ and density $\rho = 2.7$ g/cm^3. Therefore

$$n = 0.0602 \qquad \text{nuclei/(cm·barn)},$$

and

$$n\sigma_{\text{Al}} = 0.0602\sigma_{\text{Al}} \qquad \text{cm}^{-1}. \tag{C.4}$$

To get an idea of the attenuation by these materials, we calculate the neutron mean-free-path λ at 1 eV and 1 keV. The total cross sections of the nuclei at these energies are

	1 eV	1 keV
σ_{H}	20b	20 b
σ_{O}	3.8b	3.8 b
σ_{N}	10b	9 b
σ_{Mg}	3.4b	3.4 b
σ_{Al}	1.4b	1.4 b
σ_{La}	13b	3.3 b

The corresponding mean-free-path is listed in Table C.2.

Detector efficiency

Detector efficiency is a problem closely related to the problem of neutron transmission through the scintillator. In this case, we are interested in neutron absorption instead of transmission.

In the NE905 ^{6}Li-loaded glass scintillator, neutrons interact mostly with the ^{6}Li nuclei. The ^{6}Li number density in the scintillator is $n = 0.0156 \times 10^{24}$ nuclei/cm^3. The total cross sections of neutron with the ^{6}Li nuclei can be represented by [Szym90]

$$\sigma = \frac{125.}{\sqrt{E_n}} \qquad \text{barn},$$

where E_n is neutron energy in eV. Therefore the detector efficiency is

$$\text{eff} = 1 - \exp(0.0156\sigma t)$$

where t is the thickness of the scintillator in cm. The efficiency of a 1 cm thick scintillator is listed in Table C.3 and plotted in Figure 3.15.

C.2 Flux measurement

The neutron flux from the spallation source has been measured experimentally with a ^{6}Li-loaded glass scintillator 1 cm in diameter by 1 cm thick. The 1 cm detector was placed in front of the seven detector array at the 56 meter station. The small diameter of the detector makes it possible to take data in multiscaler mode. A brass collimator was placed approximately 4 meters from the spallation source, which defines the neutron emitting area of the moderator to a diameter of 1.75″. The polarizer, the ^{238}U target and the beam monitor were all removed from the beam, and the only absorption material in the beamline was 13.7 meters of air, and four $\frac{1}{32}$″ aluminum plates at the ends of the vacuum beam transport pipes. The geometry of this measurement is sketched below:

Table C.3: Efficiency of a 1cm thick ^{6}Li-loaded glass scintillator, E_n is the neutron energy in eV

E_n	eff.	E_n	eff.	E_n	eff.	E_n	eff.
1.0	0.86	26.0	0.32	51.0	0.24	76.0	0.20
2.0	0.75	27.0	0.31	52.0	0.24	77.0	0.20
3.0	0.68	28.0	0.31	53.0	0.24	78.0	0.20
4.0	0.63	29.0	0.31	54.0	0.23	79.0	0.20
5.0	0.58	30.0	0.30	55.0	0.23	80.0	0.20
6.0	0.55	31.0	0.30	56.0	0.23	81.0	0.20
7.0	0.52	32.0	0.29	57.0	0.23	82.0	0.19
8.0	0.50	33.0	0.29	58.0	0.23	83.0	0.19
9.0	0.48	34.0	0.29	59.0	0.23	84.0	0.19
10.0	0.46	35.0	0.28	60.0	0.22	85.0	0.19
11.0	0.45	36.0	0.28	61.0	0.22	86.0	0.19
12.0	0.43	37.0	0.28	62.0	0.22	87.0	0.19
13.0	0.42	38.0	0.27	63.0	0.22	88.0	0.19
14.0	0.41	39.0	0.27	64.0	0.22	89.0	0.19
15.0	0.40	40.0	0.27	65.0	0.22	90.0	0.19
16.0	0.39	41.0	0.26	66.0	0.21	91.0	0.19
17.0	0.38	42.0	0.26	67.0	0.21	92.0	0.19
18.0	0.37	43.0	0.26	68.0	0.21	93.0	0.18
19.0	0.36	44.0	0.26	69.0	0.21	94.0	0.18
20.0	0.36	45.0	0.25	70.0	0.21	95.0	0.18
21.0	0.35	46.0	0.25	71.0	0.21	96.0	0.18
22.0	0.34	47.0	0.25	72.0	0.21	97.0	0.18
23.0	0.34	48.0	0.25	73.0	0.21	98.0	0.18
24.0	0.33	49.0	0.24	74.0	0.20	99.0	0.18
25.0	0.32	50.0	0.24	75.0	0.20	100.0	0.18

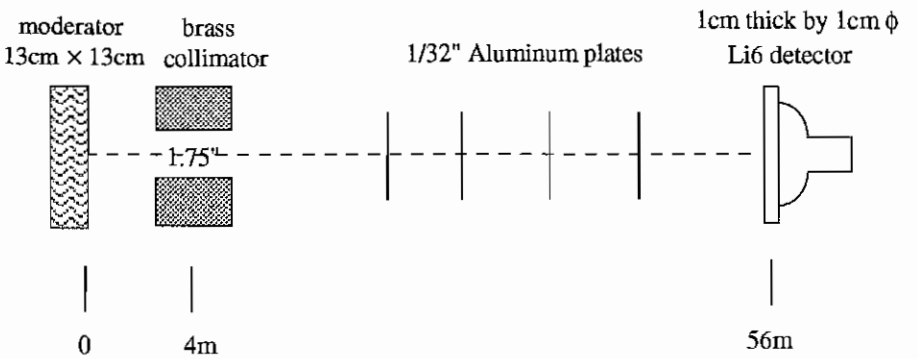

We assume that the neutron flux from the spallation source has the form

$$\begin{aligned} \Delta N &= 0.01 \frac{\Delta E_n}{E_n} \left(\frac{E_n}{E_0}\right)^{\beta} \frac{i}{eg} f\Omega \\ &= 0.02 \frac{\Delta T}{T} \left(\frac{E_n}{E_0}\right)^{\beta} \frac{i}{eg} f\Omega \qquad \text{per beam burst,} \end{aligned} \tag{C.5}$$

where ΔN is the number of neutrons with energies between E_n and $E_n + \Delta E_n$ (or TOF between T and $T + \Delta T$), i is the average proton current in amps, e the electron charge in Coulombs, f the fraction of the moderator surface the detector views, g the number of beam bursts per second, Ω the solid angle, and β and E_0 are the parameters to be determined.

From the geometry, we have

$$f = \frac{\pi(1.75 \times 2.54/2)^2}{13 \times 13\text{cm}^2} \approx 9.18 \times 10^{-2}$$

$$\Omega = \frac{\pi \times 0.5^2}{56^2 \times 10^4} \approx 2.50 \times 10^{-8} \qquad \text{sterad,}$$

where $13 \times 13\text{cm}^2$ is the total surface area of the moderator. Using $i = 55\mu\text{A}$ and $g = 20\text{Hz}$, we obtain the number of neutrons per channel per beam burst

$$\Delta N = \frac{790.5}{C}\left(\frac{E_n}{E_0}\right)^{\beta} \qquad \text{per beam burst,}$$

where $C = T/\Delta T$ is the TOF channel number, and E_n is related to C by

$$E_n = \left(\frac{4042.6}{C}\right)^2,$$

where we have used a flight path of l=56 m, and a channel width of $\Delta T = 1\mu\text{s}$.

Taking into account the beam attenuation and the detector efficiency, the measured neutron TOF spectrum Y is given by

$$\begin{aligned} Y \;=\; & \frac{790.5}{C}\left(\frac{E_n}{E_0}\right)^{\beta} \times 6400 && \text{raw flux} \\ & \times \exp[-(3.136 + 3.0763\sigma_N) \times 10^{-3} t_{air}] && \text{Air} \\ & \times \exp[-0.0602\sigma_{Al} t_{Al}] && \text{Al} \\ & \times D(E_n) && \text{det. efficiency,} \end{aligned} \tag{C.6}$$

where 6400 is the total number of beam bursts, $t_{air} = 13.7\text{m}$, $t_{Al} = 0.32\text{cm}$ and the detector efficiency is calculated for a 1cm thick scintillator.

A least-square fit of the data is shown in Figure C.1. The parameters were found to be

$$\begin{aligned} \beta &= 0.13 \\ E_0 &= 19 \qquad \text{eV.} \end{aligned}$$

C.3 Count rate at the seven detector array

In this section, we calculate the instantaneous count rate at the seven detector array. The beam attenuating materials in this case are the LMN crystal, 12.2 meters of Los Alamos air, four $\frac{1}{32}''$ aluminum plates, and an assumed 2λ target. The typical beam

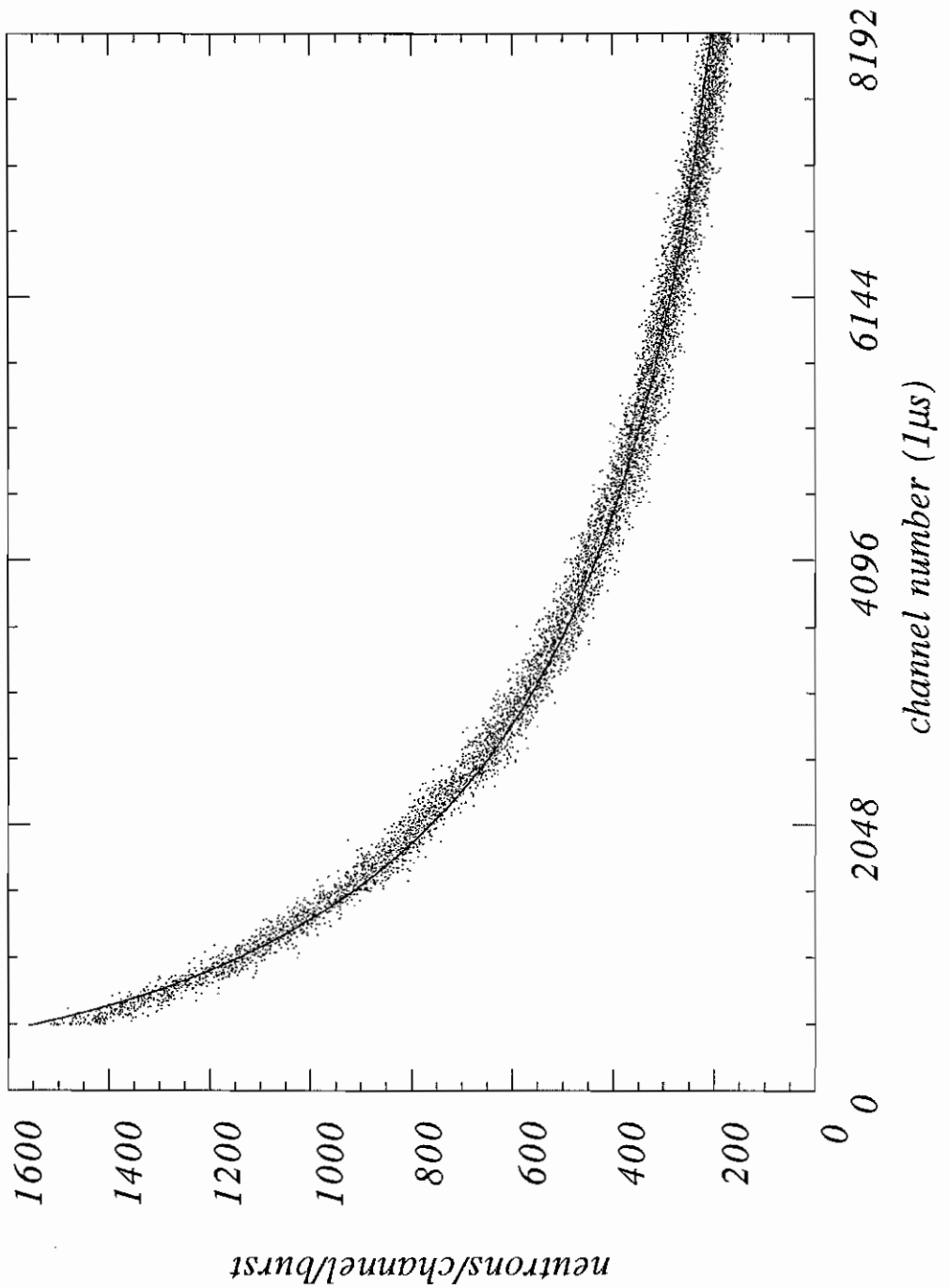

Figure C.1: A fit to the measured neutron flux for neutron energies 0.2 eV to 67 eV.

Table C.4: Typical neutron transmission in the beam attenuating materials. The transmission is calculated as $e^{-t/\lambda}$, where t is the thickness of the material and λ is the typical λ listed in Table C.2.

	LMN	Los Alamos air	Al
t	1.8 cm	12.2 m	0.32 cm
transmission (%)	15	70	97

transmission in these materials are listed in Table C.4.

Dividing equation (C.5) by ΔT, one obtains the instantaneous neutron rate during a beam burst

$$R = \frac{\Delta N}{\Delta T} = 0.02 \frac{1}{T} \left(\frac{E_n}{19\text{eV}} \right)^{0.13} \frac{i}{eg} f\Omega \qquad \text{(C.7)}$$

For $g = 20$Hz and TOF bin width of 200ns, we have

$$\begin{aligned} \frac{i}{eg} &= 3.125 \times 10^{11} i(\mu\text{A}) \\ T &= 2 \times 10^{-7} C \qquad \text{seconds} \end{aligned}$$

where C is the TOF channel number.

In general, the neutron energy E_n is related to the TOF T and the length of the flight path l by

$$T = \frac{l}{c} \sqrt{\frac{m_n c^2}{2E_n}} = 7.23 \times 10^{-5} \frac{l}{\sqrt{E_n}},$$

where T is in units of seconds, l in meters and E_n in eV. In obtaining the constant, we have used [Cohe89]

$$c = 2.99792458 \times 10^8 \qquad \text{m/s}$$

$$m_n c^2 = 939.56563 \qquad \text{MeV}.$$

To obtain f and Ω, we need to consider the aperture of the beamline. The aperture which defines the beam is the $1\frac{1}{8}''$ diameter collimator inside the cryostat which is

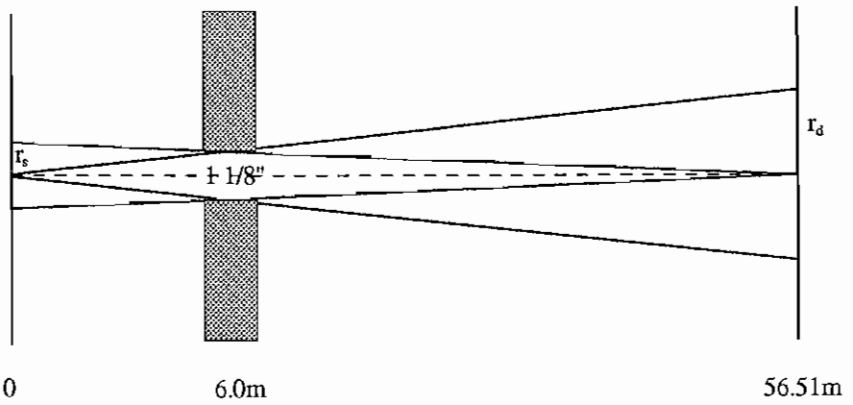

Figure C.2: The aperture of the beamline

located 6.0 meters from the spallation source, as shown in Figure C.2. The seven detector array is located 56.51 meters from the spallation source.

The detector sees only a circular part of the moderator surface with radius r_s given by

$$\frac{r_s}{1.43\text{cm}} = \frac{56.51}{56.51 - 6.0} \Longrightarrow r_s = 1.60\text{cm}$$

where 1.43 cm is the radius of the aperture $(1\frac{1}{8}''/2)$. Therefore

$$f = \frac{\pi r_s^2}{13 \times 13\text{cm}^2} = 0.047.$$

It takes some effort to calculate the solid angle the seven detector array extends with respect to the spallation source. The neutron beam is limited by the collimator to a cone which has a radius r_d at the detector. The radius r_d is given by

$$\frac{r_d}{1.43\text{cm}} = \frac{56.51}{6.0} \Longrightarrow r_d = 13.46\text{cm} = 5.30''.$$

As seen from the front of the detector, the seven detectors are arranged with one detector at the center and 6 detectors around it, as shown in Figure C.3. The

Figure C.3: The seven detector array and the polar coordinate system. The shaded area represents the beam spot at the 56 meter station. $r_0 = 2.5''$, $r_d = 5.30''$ and $\theta_0 = 1.70$.

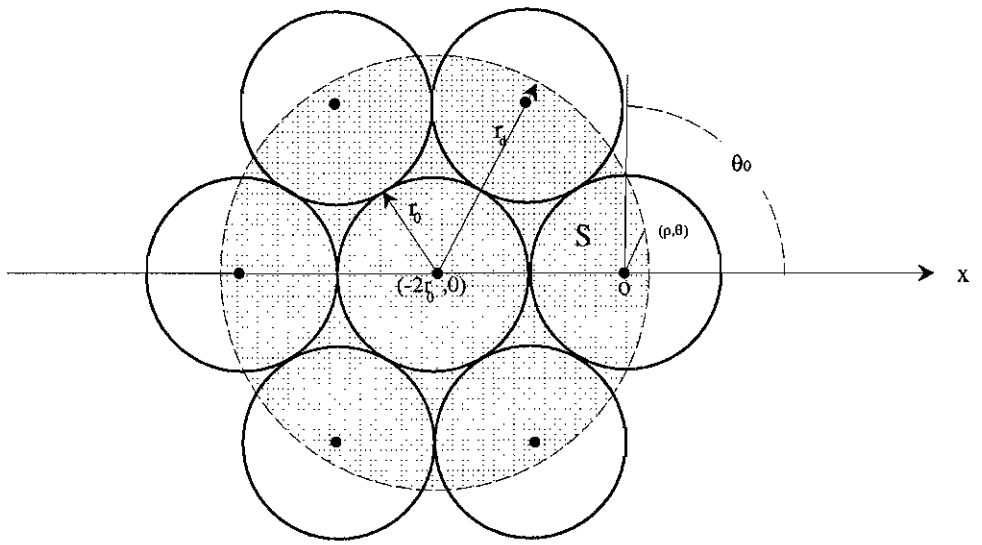

shaded area in Figure C.3 is the projection of the beam cone on the detector plane. Obviously, not all the areas of the outer detectors count. The active area S of an outer detector can be calculated as follows.

Let us choose a polar coordinate system as shown in Figure C.3. The origin is at the center of the outer detector, and the x-axis points away from the center of the inner detector. In the polar coordinate system, the circle of radius $r_d(> 2r_0)$ can be described by

$$(\rho\cos\theta + 2r_0)^2 + \rho^2\sin^2\theta = r_d^2,$$

or

$$\rho^2 + (4r_0\cos\theta)\rho + 4r_0^2 - r_d^2 = 0, \tag{C.8}$$

where (ρ, θ) is the polar coordinates. The angle θ_0 at which the circle intersects with

the outer detector can be found from equation (C.8) by setting $\rho = r_0$. The result is

$$\cos\theta_0 = \left(\frac{r_d}{2r_0}\right)^2 - \frac{5}{4} \Longrightarrow \theta_0 = 1.70.$$

The explicit form of ρ can be obtained from equation (C.8) as

$$\rho = \sqrt{r_d^2 - 4r_0^2 \sin^2\theta} - 2r_0\cos\theta.$$

Hence, the area of the outer detector inside the neutron cone is

$$\begin{aligned} S &= \pi r_0^2 - \int_{-\theta_0}^{+\theta_0} \frac{1}{2}(r_0+\rho)(r_0-\rho)\,d\theta \\ &= \pi r_0^2 - \frac{1}{2}\int_{-\theta_0}^{+\theta_0} (r_0^2-\rho^2)\,d\theta \\ &= \pi r_0^2\left[1 - \frac{1}{2\pi r_0^2}\int_{-\theta_0}^{+\theta_0}(r_0^2-\rho^2)\,d\theta\right] \\ &= \pi r_0^2[0.52] \end{aligned}$$

where the last step is obtained by numerical integration using

$$\begin{aligned} \theta_0 &= 1.70 \\ r_d &= 5.30'' \\ r_0 &= 2.5''. \end{aligned}$$

Therefore the solid angle is

$$\Omega = \frac{\pi(2.5\times 2.54)^2[1+6\times 0.52]}{56.51^2\times 10^4} = 1.64\times 10^{-5}\text{sterad.}$$

Substituting all these factors into equation (C.7), one obtains the instantaneous neutron rate at the seven detector array

$$R = 2.4396\times 10^{10}\frac{i}{C}\left(\frac{E_n}{19\text{eV}}\right)^{0.13} \qquad \text{neutrons/sec.}$$

Taking into account beam absorption and detector efficiency, the instantaneous count rate is

$$R = 2.4396\times 10^{10}\frac{i}{C}\left(\frac{E_n}{19\text{eV}}\right)^{0.13} \qquad \text{raw flux}$$

$$\times \exp[-2.904 \times 10^{-3}(\sigma_{La} + 6\sigma_N + 24\sigma_H + 119.1)] \qquad \text{LMN}$$

$$\times \exp[-(3.136 + 3.0763\sigma_N) \times 10^{-3} t_{air}] \qquad \text{Air}$$

$$\times \exp[-0.0602\sigma_{Al} t_{Al}] \qquad \text{Al}$$

$$\times \exp[-2] \qquad 2\lambda \text{ target}$$

$$\times D(E_n) \qquad \text{det. efficiency},$$

where i is the proton current in μA, C is the TOF channel number with 200ns time bins, $t_{air} = 12.2$m, $t_{Al} = 0.32$cm, the cross sections are in units of barn, the thickness of the scintillator is 1 cm, and R is in units of neutrons/sec. The instantaneous count rate is shown in Figure 3.6.

Appendix D

Least Square Fit

D.1 Concept of least square fit

Let us assume that we have a set of experimental data points $(x_i, y_i \pm \sigma_i, i = 1, 2, \ldots N)$, where σ_i is the error in y_i. We want to parameterize this set of data with a function $y(x, a_1, a_2, ..., a_m)$ where $a_j, j = 1, 2, ..., m$ are m independent parameters. This can be done by a least square fit.

To measure how good the function describes the data, we introduce

$$\chi^2 = \sum_{i=1}^{N} \frac{[y_i - y(x_i)]^2}{\sigma_i^2} \tag{D.1}$$

where $y(x_i)$ is a shortform for $y(x_i, a_1, a_2, ..., a_m)$. The optimum parameters are found by minimizing χ^2 with respect to the parameters

$$\frac{\partial \chi^2}{\partial a_j} = 0 \qquad\qquad j = 1, 2, ..., m. \tag{D.2}$$

Equation (D.2) can not be solved analytically except in the simplest case. Therefore numerical procedures have to be developed. More extensive discussions on least square fit can be found in reference [Bevi69]. In this appendix, we will first discuss the linear least square fit which can be handled analytically, then a general numerical fitting procedure ([Marq63]) which can, in principle, be applied to any function.

D.2 Linear least square fit

Let us assume that the fitting function is linear in the parameters, ie,

$$y(x) = \sum_{j=1}^{m} a_j f_j(x),$$

where $f_j(x)$'s are functions of x, and the a_j's are the parameters. The derivative of χ^2 with respect to a_j is then

$$\begin{aligned}
\frac{\partial \chi^2}{\partial a_j} &= -2 \sum_{i=1}^{N} \frac{y_i - y(x_i)}{\sigma_i^2} \frac{\partial y(x_i)}{\partial a_j} \\
&= -2 \sum_{i=1}^{N} \frac{y_i - y(x_i)}{\sigma_i^2} f_j(x_i) \\
&= -2 \left\{ \sum_{i=1}^{N} \frac{y_i}{\sigma_i^2} f_j(x_i) - \sum_{j'=1}^{m} \left(\sum_{i=1}^{N} \frac{f_j(x_i) f_{j'}(x_i)}{\sigma_i^2} \right) a_{j'} \right\} \\
&= 0 \qquad \text{for optimum parameters,}
\end{aligned}$$

therefore the optimum parameters satisfy

$$\sum_{j'=1}^{m} \alpha_{jj'} a_{j'} = \beta_j \qquad j = 1, 2, \ldots, m \tag{D.3}$$

where

$$\alpha_{jj'} = \sum_{i=1}^{N} \frac{f_j(x_i) f_{j'}(x_i)}{\sigma_i^2} \tag{D.4}$$

$$\beta_j = \sum_{i=1}^{N} \frac{y_i}{\sigma_i^2} f_j(x_i). \tag{D.5}$$

In matrix notation, equation (D.3) can be written as

$$\boldsymbol{\alpha} \cdot \boldsymbol{a} = \boldsymbol{\beta} \tag{D.6}$$

where $\boldsymbol{\alpha}$ is a $m \times m$ matrix with elements $\alpha_{jj'}$ given by equation (D.4), $\boldsymbol{\beta}$ is a $m \times 1$ column matrix with elements β_j given by equation (D.5), and $\boldsymbol{a}$ is a $m \times 1$ column matrix with elements a_j the optimum parameters.

Solving equation (D.6), one finds the optimum parameters

$$\boldsymbol{a} = \boldsymbol{\alpha}^{-1} \boldsymbol{\beta} = \boldsymbol{\epsilon} \boldsymbol{\beta},$$

or explicitly

$$a_j = \sum_{k=1}^{m} \epsilon_{jk}\beta_k \qquad\qquad j = 1, 2, \ldots, m \tag{D.7}$$

where $\boldsymbol{\epsilon}=\boldsymbol{\alpha}^{-1}$ is called the error matrix.

Using equation (D.7), we can estimate the errors in the parameters by the method of error propagation as

$$\begin{aligned}
\sigma_{a_j}^2 &= \sum_{i=1}^{N}\left[\left(\frac{\partial a_j}{\partial y_i}\right)^2 \sigma_i^2\right] \qquad\qquad j = 1, 2, \ldots, m \\
&= \sum_{k=1}^{m}\sum_{l=1}^{m}\left\{\epsilon_{jk}\epsilon_{jl}\sum_{i=1}^{N}\left[\frac{1}{\sigma_i^2} f_k(x_i) f_l(x_i)\right]\right\} \\
&= \sum_{k=1}^{m}\sum_{l=1}^{m}(\epsilon_{jk}\epsilon_{jl}\alpha_{kl}) \\
&= \sum_{k=1}^{m}\epsilon_{jk}\delta_{jk} \\
&= \epsilon_{jj},
\end{aligned}$$

or

$$\sigma_{a_j} = \sqrt{\epsilon_{jj}} \tag{D.8}$$

where we have used

$$\begin{aligned}
\frac{\partial a_j}{\partial y_i} &= \sum_{k=1}^{m}\epsilon_{jk}\frac{\partial \beta_k}{\partial y_i} \\
&= \sum_{k=1}^{m}\left[\epsilon_{jk}\frac{1}{\sigma_i^2} f_k(x_i)\right] \\
\alpha_{kl} &= \alpha_{lk} \qquad (\boldsymbol{\alpha} \text{ symmetric}) \\
\sum_{l=1}^{m}\epsilon_{jl}\alpha_{lk} &= \delta_{jk} \qquad (\boldsymbol{\epsilon}=\boldsymbol{\alpha}^{-1}).
\end{aligned}$$

Therefore the error in a_j is the square root of the j-th diagonal element of the error matrix.

D.3 General least square fit

In most cases, the fitting function is not linear in the parameters, the procedure discussed above can not be applied, and numerical procedures have to be employed. A

numerical least square fitting procedure searches through the χ^2 hypersurface to locate the minimum. In this section, we are going to discuss a numerical procedure which is a combination of the gradient search method and the linear expansion method: as the parameters are far from the optimum, it searches along the direction in which χ^2 decreases, so it always converges; as the parameters are close to the optimum, it searches for the minimum by a linear expansion of the fitting function, so it converges fast.

Let us assume that the parameters a_j, $j = 1, 2, \ldots, m$ are near the optimum values. In a linear expansion at this set of parameters, the fitting function can be written as

$$y(x, a_1 + \delta a_1, a_2 + \delta a_2, ..., a_m + \delta a_m) \approx y(x) + \sum_{j=1}^{m} \frac{\partial y(x)}{\partial a_j} \delta a_j, \tag{D.9}$$

where $y(x) = y(x, a_1, a_2, \ldots, a_m)$ as before.

The derivative with respect to δa_j is then

$$\frac{\partial}{\partial \delta a_j} y(x, a_1 + \delta a_1, a_2 + \delta a_2, ..., a_m + \delta a_m) = \frac{\partial y(x)}{\partial a_j}. \tag{D.10}$$

By definition, the χ^2 at $a_j + \delta a_j$, $j = 1, 2, \ldots m$ is

$$\begin{aligned} \chi^2 &= \chi^2(a_1 + \delta a_1, a_2 + \delta a_2, ..., a_m + \delta a_m) \\ &= \sum_{i=1}^{N} \frac{[y_i - y(x_i, a_1 + \delta a_1, a_2 + \delta a_2, \ldots, a_m + \delta a_m)]^2}{\sigma_i^2}, \end{aligned}$$

and the derivative of the χ^2 with respect to δa_j is

$$\begin{aligned} \frac{\partial \chi^2}{\partial \delta a_j} &= -2 \sum_{i=1}^{N} \frac{y_i - y(x_i, a_1 + \delta a_1, a_2 + \delta a_2, ..., a_m + \delta a_m)}{\sigma_i^2} \\ &\qquad \times \frac{\partial y(x_i, a_1 + \delta a_1, a_2 + \delta a_2, ..., a_m + \delta a_m)}{\partial \delta a_j} \\ &= -2 \left[\sum_{i=1}^{N} \frac{y_i - y(x_i)}{\sigma_i^2} \frac{\partial y(x_i)}{\partial a_j} - \sum_{j'=1}^{m} \left(\sum_{i=1}^{N} \frac{1}{\sigma_i^2} \frac{\partial y(x_i)}{\partial a_j} \frac{\partial y(x_i)}{\partial a_{j'}} \right) \delta a_{j'}' \right] \end{aligned} \tag{D.11}$$

where we have used equations (D.9) and (D.10).

The optimum parameters $a_j + \delta a_j$, $j = 1, 2, \ldots, m$ are found by setting equa-

tion (D.11) to zero, which gives

$$\sum_{j'=1}^{m} \alpha_{jj'} \delta a_{j'} = \beta_j \qquad\qquad j = 1, 2, \ldots, m \tag{D.12}$$

where

$$\alpha_{jj'} = \sum_{i=1}^{N} \frac{1}{\sigma_i^2} \frac{\partial y(x_i)}{\partial a_j} \frac{\partial y(x_i)}{\partial a_{j'}} \tag{D.13}$$

$$\beta_j = \sum_{i=1}^{N} \frac{1}{\sigma_i^2} [y_i - y(x_i)] \frac{\partial y(x_i)}{\partial a_j}. \tag{D.14}$$

In matrix notation, equation (D.12) can be written as

$$\boldsymbol{\alpha} \cdot \delta \boldsymbol{a} = \boldsymbol{\beta},$$

which leads to

$$\delta \boldsymbol{a} = \boldsymbol{\alpha}^{-1} \boldsymbol{\beta} = \boldsymbol{\epsilon} \boldsymbol{\beta} \tag{D.15}$$

where $\boldsymbol{\epsilon} = \boldsymbol{\alpha}^{-1}$ is the error matrix, and $\delta \boldsymbol{a}$ is a $m \times 1$ column matrix with elements δa_j. The optimum parameters are then $\boldsymbol{a} + \delta \boldsymbol{a}$.

In a real problem, the starting parameters may be far from their optimum values, therefore the above procedure may not converge. By introducing an arbitrary non-negative constant λ, this problem is solved beautifully as follows.

Let us modify the $\boldsymbol{\alpha}$ matrix (equation D.13) with the λ as below

$$\begin{aligned} \alpha_{jj} &\rightarrow \alpha_{jj}(1 + \lambda) \\ \alpha_{jj'} &\rightarrow \alpha_{jj'} \qquad\qquad j' \neq j. \end{aligned}$$

As the parameters are far from the optimum values, we choose λ large enough, such that the off-diagonal matrix elements are small as compared to the modified diagonal elements. Equation (D.12) then becomes

$$\lambda \alpha_{jj} \delta a_j = \beta_j,$$

or

$$\delta a_j = \frac{1}{\lambda} \frac{\beta_j}{\alpha_{jj}}. \tag{D.16}$$

It can be shown that

$$\beta_j = -\frac{1}{2}\frac{\partial \chi^2}{\partial a_j},$$

ie. $\boldsymbol{\beta}$ is the direction of steepest descent of χ^2 in the parameter space. Because both λ and α_{jj} are positive, equation (D.16) suggests that $\delta\boldsymbol{a}$ is in the direction of decreasing χ^2. Therefore, for large λ, this method is equivalent to the method of gradient search, which is able to find the approximate optimum values fast.

As the parameters are near the optimum, we can set $\lambda = 0$, then this method becomes the method of linear expansion, and the exact optimum values can be found.

To estimate the errors in the parameters, we realize that the fitting function can be linearly expanded near the optimum values, therefore we can borrow from the case of linear least square fit. In a linear least square fit, the error in the parameter is the square root of the corresponding error matrix element (equation D.8). We assume that this result can be generalized and estimate the error in a_j as

$$\sigma_{a_j} = \sqrt{\epsilon_{jj}} \qquad\qquad j = 1, 2, \ldots, m. \tag{D.17}$$

D.4 Implementation of a fitting program

In this section, we are going to discuss the implementation of a numerical least square fitting program which uses the procedure discussed in section D.3. The flow chart of the program is shown in Figure D.1.

Given the data set $(x_i, y_i \pm \sigma_i)$, $i = 1, 2, \ldots, N$ and the fitting function $y(x)$, we start the procedure with a set of trial parameters a_j $(j = 1, 2, ..., m)$, a large initial λ $(\sim 10^{-3})$, and a preset number of iterations. In every iteration, we calculate the χ^2, $\boldsymbol{\alpha}$, $\boldsymbol{\beta}$, $\boldsymbol{\epsilon}$, the parameter increase $\delta\boldsymbol{a}$, and the set of new parameters $\boldsymbol{a}+\delta\boldsymbol{a}$. Then the χ^2 is calculated at the new parameters. If the χ^2 at the new parameters is bigger than the χ^2 at the old parameters, the new parameters are further away from the optimum values, so it is discarded, and the λ is increases by two to make the procedure converge. If the χ^2 at the new parameters is smaller than the χ^2 at the

old parameters, the new parameters are closer to the optimum values, and are saved as the trial parameter for the next iteration. The λ is decreased by half. If λ is less than 10^{-5}, we set it to zero. After the preset number of iterations is finished, the computer waits for the operator to decide if the optimum values have been reached.

The following rules can help the operator to decide if the optimum parameters have been obtained:

1. χ^2_ν: χ^2 per degree of freedom

   If $y(x)$ is a suitable function to describe the data set, χ^2_ν is expected to be 1, where $\chi^2_\nu = \chi^2/\nu$, and $\nu = N - m$ is the degree of freedom.

2. Physical judgement:

   The parameters have physical meanings. The optimum parameters should agree with their physical meanings.

3. Different starting parameters:

   One may try with different starting parameters. If all the fits converge to the same parameter set, then one can be confident that he is not trapped in a local minimum on the χ^2 hypersurface.

As a practical problem, one may find it helpful to be able to conveniently fix certain parameters during a fit. In the remaining part of this section, we are going to discuss a simple prescription.

Let us assume that parameter a_j is going to be fixed. Then in equation (D.12), we have

$$\begin{aligned} \alpha_{jj'} &= \alpha_{j'j} = 0 \qquad\qquad j' = 1, 2, ..., m \\ \beta_j &= 0. \end{aligned}$$

In explicit matrix form, equation (D.12) can be written as

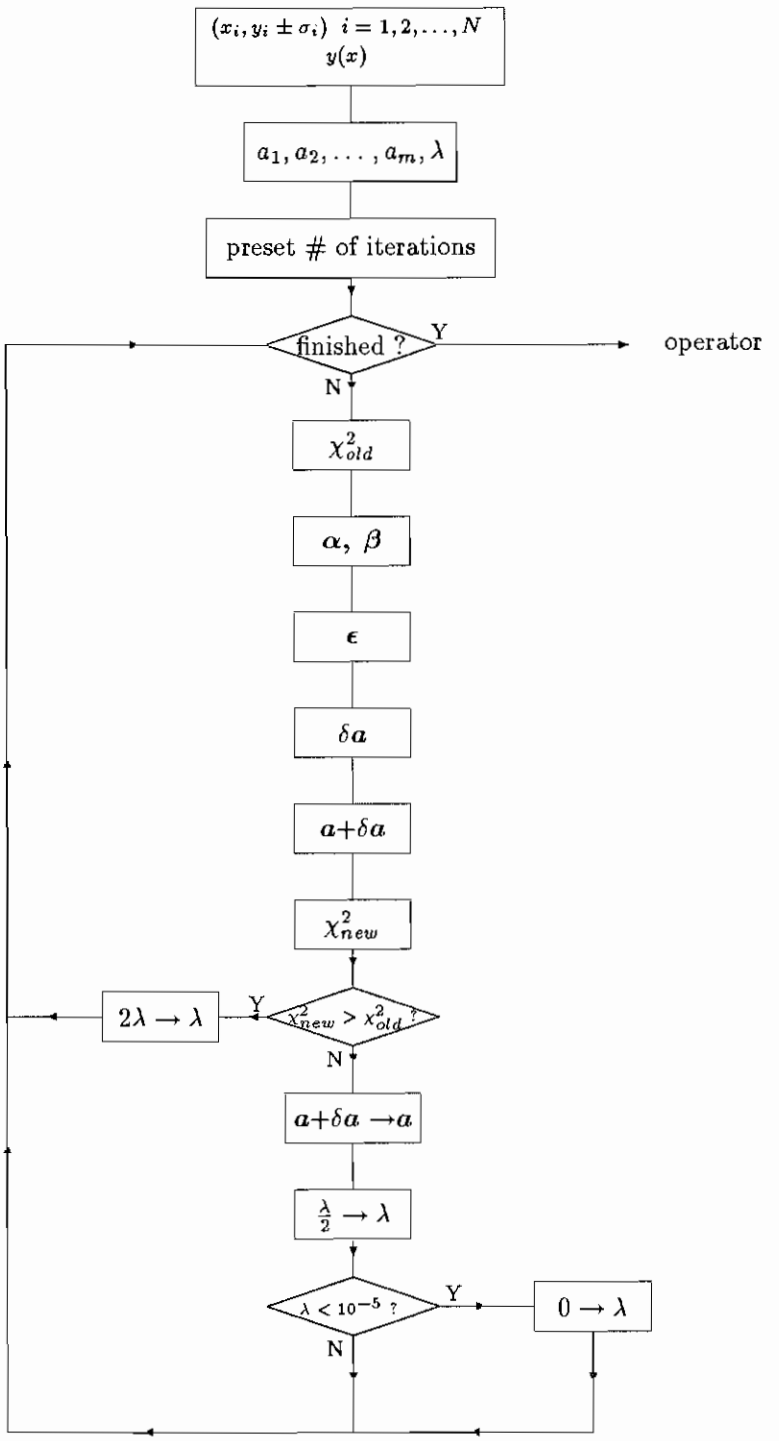

Figure D.1: Flow chart of the least square fitting program

$$
\begin{array}{c} \\ j \end{array}
\begin{array}{c} \mathrm{j} \\ \left(\begin{array}{ccccccccc} & & & & 0 & & & & \\ & & & & 0 & & & & \\ & & & & 0 & & & & \\ & & & & \vdots & & & & \\ 0 & 0 & 0 & \cdots & 0 & \cdots & 0 & 0 & 0 \\ & & & & \vdots & & & & \\ & & & & 0 & & & & \\ & & & & 0 & & & & \\ & & & & 0 & & & & \end{array} \right) \end{array}
\left(\begin{array}{c} \delta a_1 \\ \vdots \\ \delta a_j \\ \vdots \end{array} \right) = \left(\begin{array}{c} \beta_1 \\ \vdots \\ \beta_j = 0 \\ \vdots \end{array} \right). \qquad \text{(D.18)}
$$

To remove the singularity in the $\boldsymbol{\alpha}$ matrix, we can set $\alpha_{jj} = 1$, which is equivalent to adding the following equation to equation (D.18)

$$1 \cdot \delta a_j = 0,$$

which holds because $\delta a_j = 0$.

Therefore to fix parameter a_j, we only need to modify the matrix elements as follows:

$$
\begin{aligned}
\alpha_{jj} &= 1 \\
\alpha_{jj'} &= \alpha_{j'j} = 0 \qquad j' \neq j \\
\beta_j &= 0
\end{aligned}
$$

and the rest of the procedure does not need to be changed.

Appendix E

Identifying the Resonances in the TOF Spectra

This appendix identifies the resonances in the TOF spectra. Let us use the 63.50 eV resonance as an example to illustrate the labeling. For this resonance, the labeling is as follows:

2543

63.60

63.500p.

Here 2543 is the TOF channel number of the resonance peak rounded to the nearest integer, 63.60 eV is the energy of the resonance calculated from the calibration of $l = 56.51$ m and $K_s = -18.57$ (see chapter 5), 63.500[1] eV is the listed resonance energy, and the "p" means that this is a ^{238}U p-wave resonance. For the contamination s-wave resonances, we list the contamination nucleus as well.

[1]This is as listed in table 6.1 which is used in evaluating the RMS parity violating matrix element. It is a little different from the 63.52 eV we used for the energy calibration.

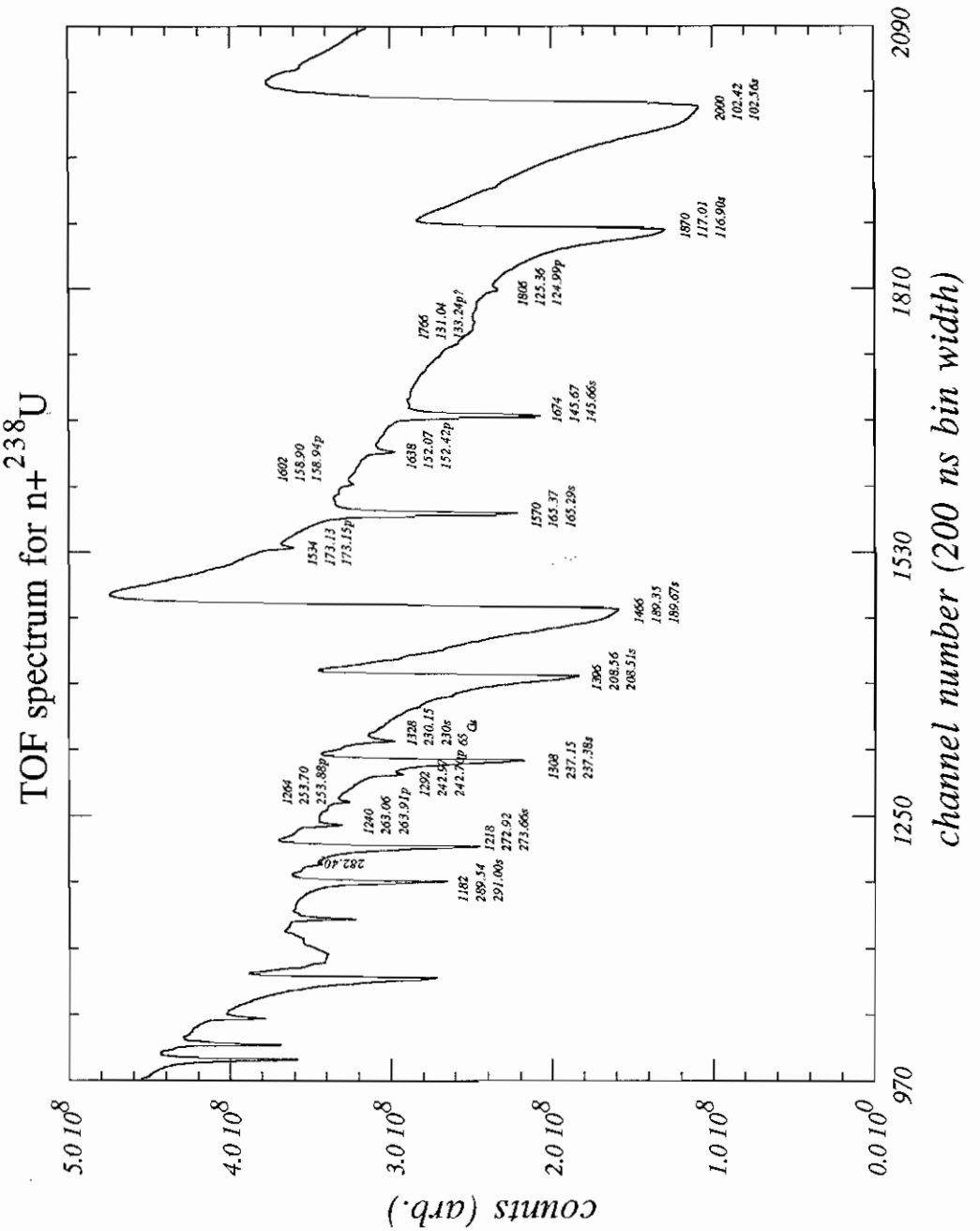
TOF spectrum for n+^{238}U
counts (arb.)
channel number (200 ns bin width)
5.0 10^8
4.0 10^8
3.0 10^8
2.0 10^8
1.0 10^8
0.0 10^0
970
1250
1530
1810
2090
1602 158.90 158.94p
1534 173.13 173.15p
1570 165.37 165.29s
1638 152.07 152.42p
1674 145.67 145.66s
1766 131.04 133.24p?
1808 125.36 124.99p
1870 117.01 116.90s
2000 102.42 102.56s
1264 253.70 253.88p
1240 263.06 263.91p
1292 242.54 242.70p
1328 230.15 230s
1218 272.92 273.66s
1182 289.54 291.00s
1308 237.15 237.38s
1395 208.36 208.51s
1466 189.35 189.67s

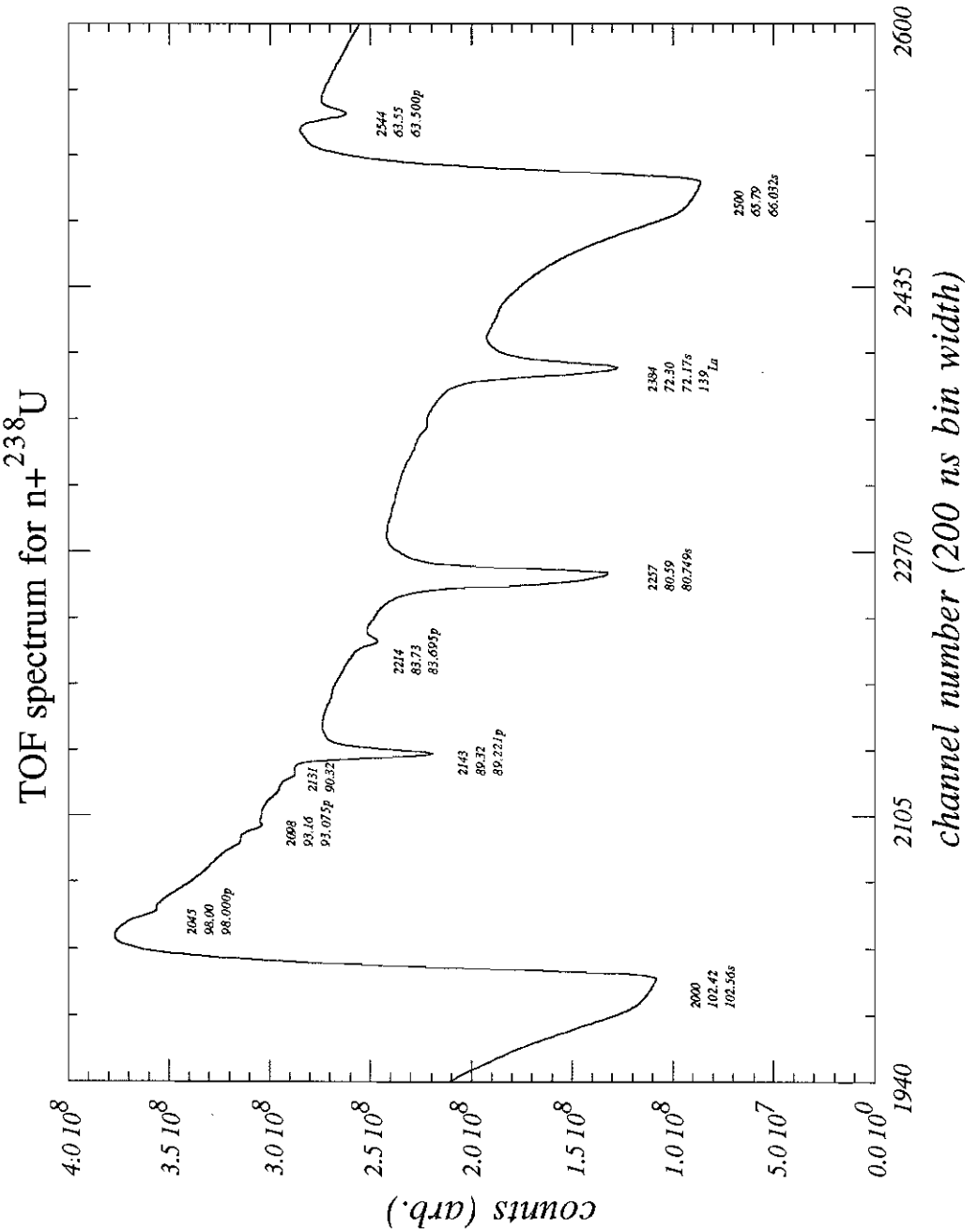
TOF spectrum for n+^{238}U
counts (arb.)
channel number (200 ns bin width)
4.0 10^8
3.5 10^8
3.0 10^8
2.5 10^8
2.0 10^8
1.5 10^8
1.0 10^8
5.0 10^7
0.0 10^0
1940
2105
2270
2435
2600
2045 98.00 98.000p
2098 93.16 93.075p
2131 90.32
2143 89.32 89.221p
2214 83.73 83.695p
2257 80.59 80.749s
2384 72.30 72.175 139La
2500 65.79 66.032s
2544 63.55 63.500p
2000 102.42 102.56s

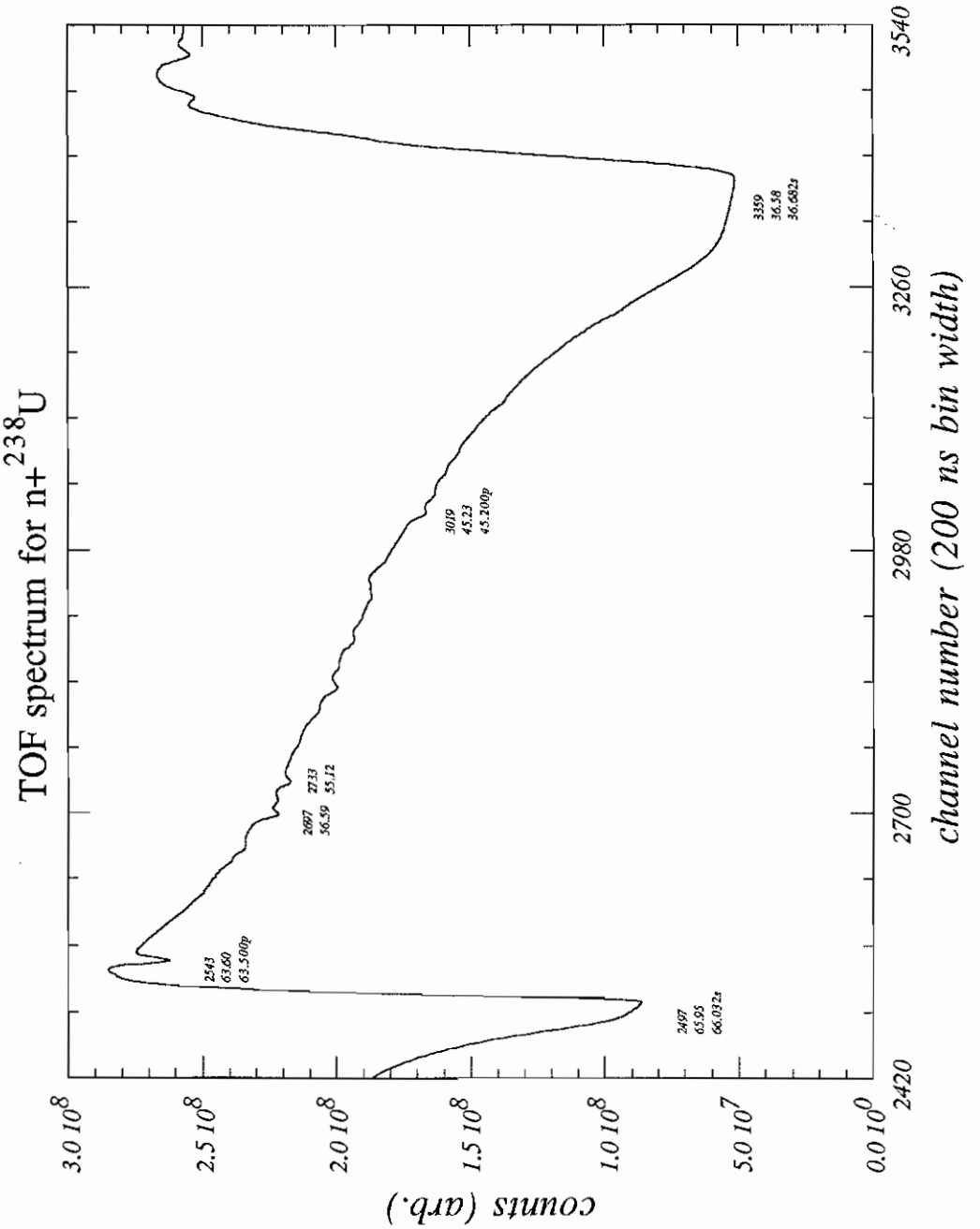
TOF spectrum for n+^{238}U
counts (arb.)
channel number (200 ns bin width)
3.0 10^8
2.5 10^8
2.0 10^8
1.5 10^8
1.0 10^8
5.0 10^7
0.0 10^0
2420
2700
2980
3260
3540
2543
63.60
63.500p
2697
36.59
2733
55.12
3019
45.23
45.200p
3359
36.58
36.682s
2497
65.95
66.032s

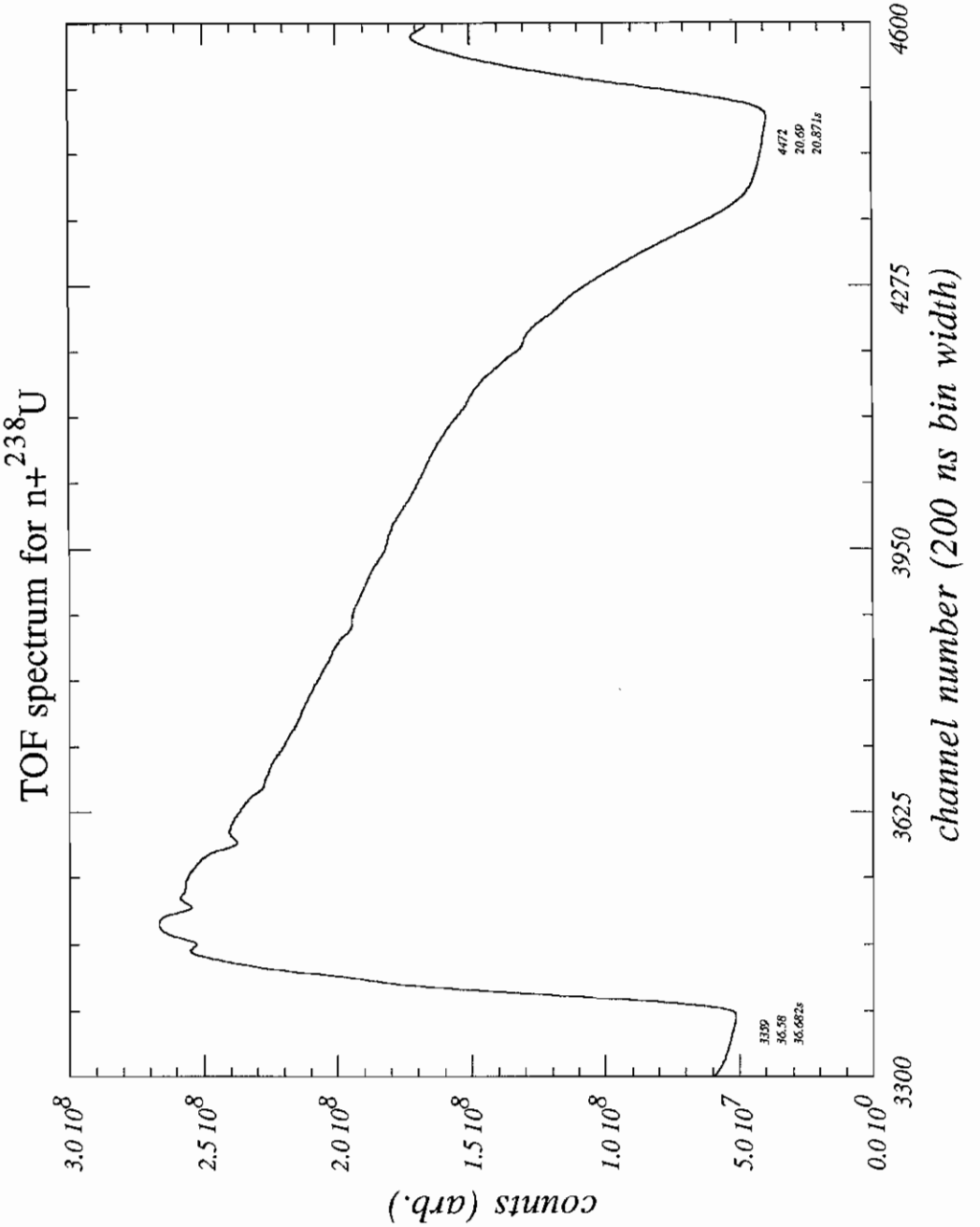
TOF spectrum for n+^{238}U
counts (arb.)
channel number (200 ns bin width)
3.0 10^8
2.5 10^8
2.0 10^8
1.5 10^8
1.0 10^8
5.0 10^7
0.0 10^0
3300
3625
3950
4275
4600
339
36.58
36.682s
4472
20.69
20.871s

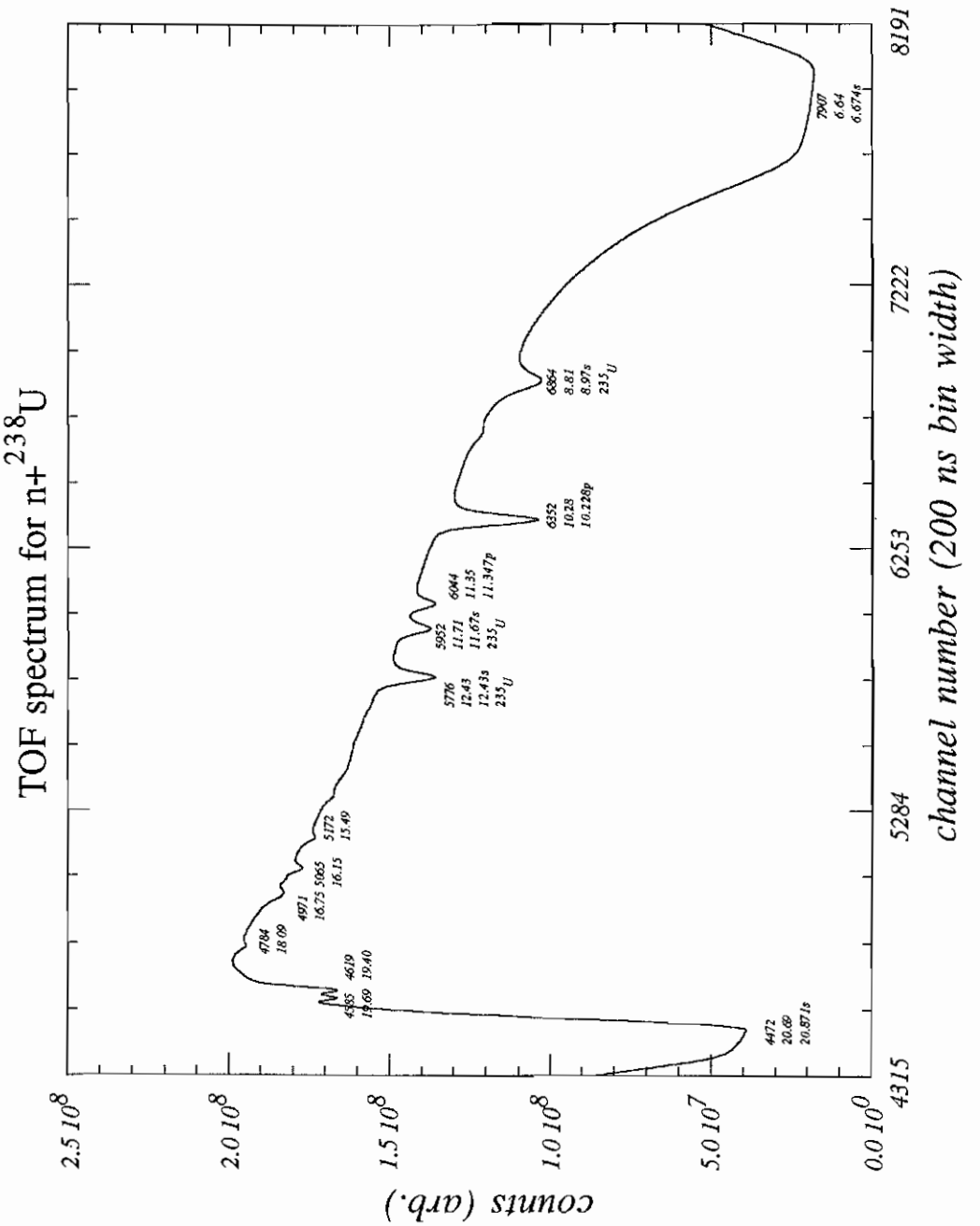
TOF spectrum for n+^{238}U
counts (arb.)
channel number (200 ns bin width)
2.5 10^8
2.0 10^8
1.5 10^8
1.0 10^8
5.0 10^7
0.0 10^0
4315
5284
6253
7222
8191
4784 18.09
4971 16.75
5065 16.15
5172 15.49
4619 19.40
4385 19.69
4472 20.69 20.871s
5776 12.43 12.43s 235U
5952 11.71 11.67s 235U
6044 11.35 11.347p
6352 10.23 10.228p
6854 8.81 8.97s 235U
7907 6.64 6.674s

Appendix F

Histograms

This appendix lists the histograms of the parity violating asymmetries of the 17 ^{238}U p-wave resonances and the 5 contamination s-wave resonances. The p-wave resonances are listed first, followed by the contamination s-wave resonances. In each category (p-wave or s-wave), the list is in the order of increasing energies of the resonances.

Each page lists the histograms for one resonance. The top histogram is for the higher microwave frequency while the bottom one is for the lower microwave frequency. The title of the histogram tells the energy of the resonance, the kind (p-wave or s-wave, ^{238}U or contamination) of the resonance, and the microwave frequency at which the data was taken; the text in the histogram tells N, $\bar{p}$, δ_1 and δ_2, where N is the number of runs analyzed, $\bar{p}$ is the average parity violating asymmetry, and δ_1 and δ_2 are respectively the internal and external errors (see section 5.4.4 for the definition of $\bar{p}$, δ_1 and δ_2). The external error δ_2 is cited as the error in $\bar{p}$. To the right of the histogram are the lineshape parameters obtained from the summed spectra. The lineshape parameters are listed according to the parameter index assigned in section 4.3, and are listed below for convenience:

index	parameter	description
1	α_1	
2	α_2	
3	α_3	flux parameters
4	α_4	
5	α_5	
6	N	normalization
7	K_0	location of the resonance peak
8	$B^2 \equiv (\frac{2E_p}{\Gamma_p})^2$	resonance parameter
9	$C \equiv \sqrt{\frac{E_p A}{K_B T}}$	Doppler broadening parameter
10	$\sigma'_{max} = \frac{\sigma_{max}}{\sqrt{\pi}}$	σ_{max}: peak resonance cross section
11	α	beam asymmetry
12	$f_n p$	product of the neutron polarization and the parity violating asymmetry.

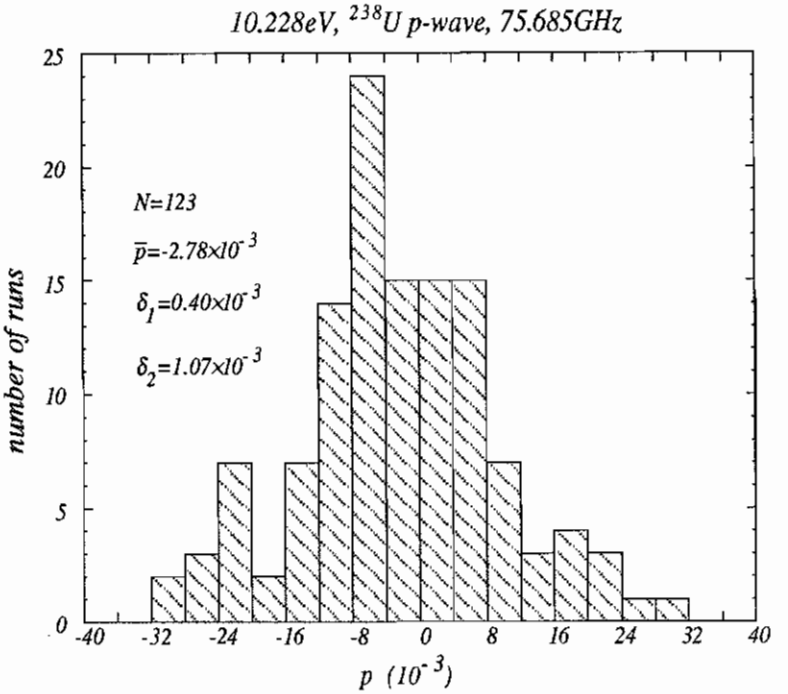

-1.46830E−01
3.58115E−02
2.66811E+00
-1.23368E+00
-2.87568E+01
9.10786E+11
6.35996E+03
1.21385E+06
2.59219E+02
1.09332E+01
-3.29829E−05
-1.20750E−03

Fitting range:
[6131 : 6579]

Blankout regions:
#1: [6248 : 6326]
#2: [6390 : 6490]

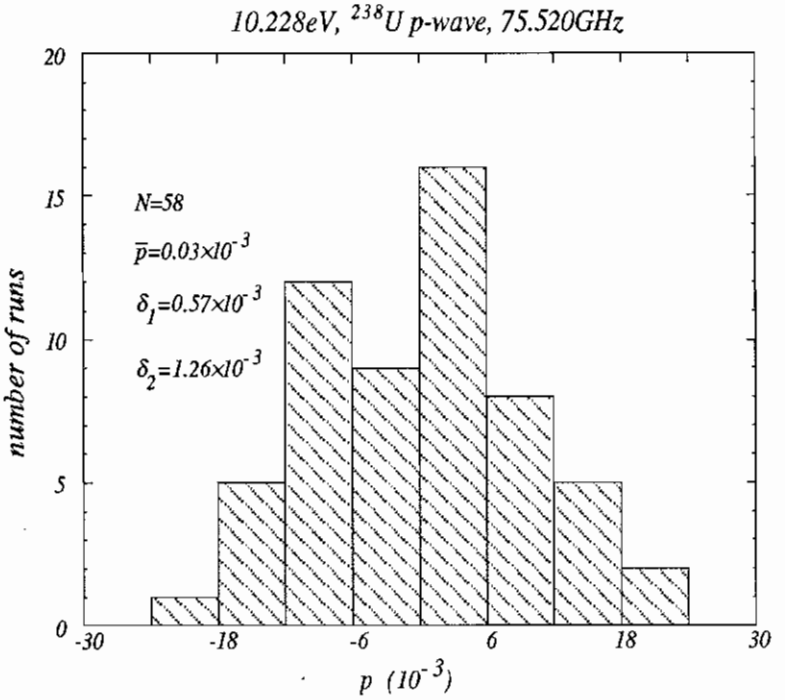

-1.53310E−01
1.49563E−01
3.15732E+00
-2.97455E+00
-3.57802E+01
4.94695E+11
6.35938E+03
1.19398E+06
2.59688E+02
1.05577E+01
8.33567E−06
2.32940E−05

Fitting range:
[6131 : 6579]

Blankout regions:
#1: [6248 : 6326]
#2: [6390 : 6490]

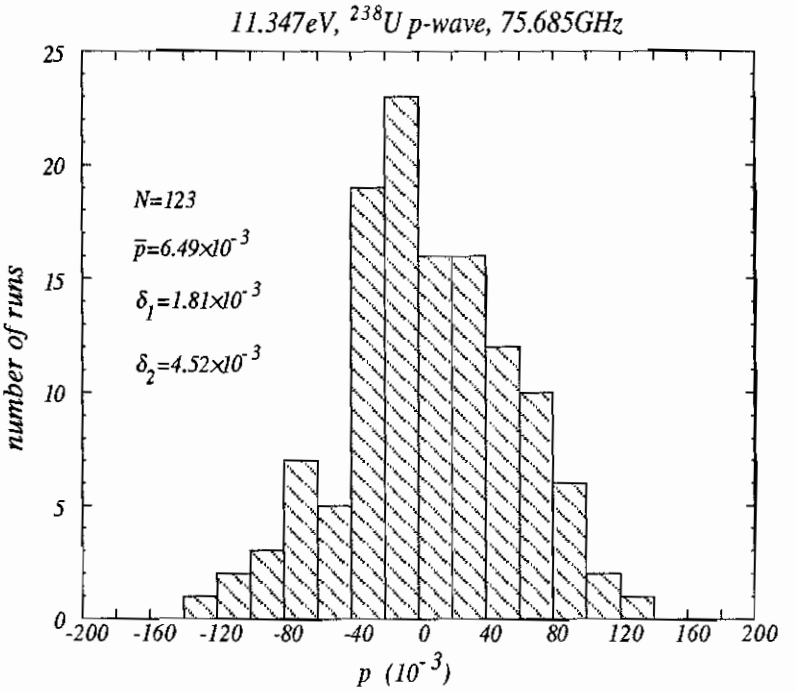

-4.89582E−02
5.93313E−03
4.94355E−01
-2.32732E+00
-6.84934E+00
9.30623E+11
6.04885E+03
5.93682E+04
4.05717E+02
6.43920E−01
-7.25972E−06
2.81407E−03

Fitting range:
[5870 : 6272]

Blankout region:
#1: [5902 : 6018]

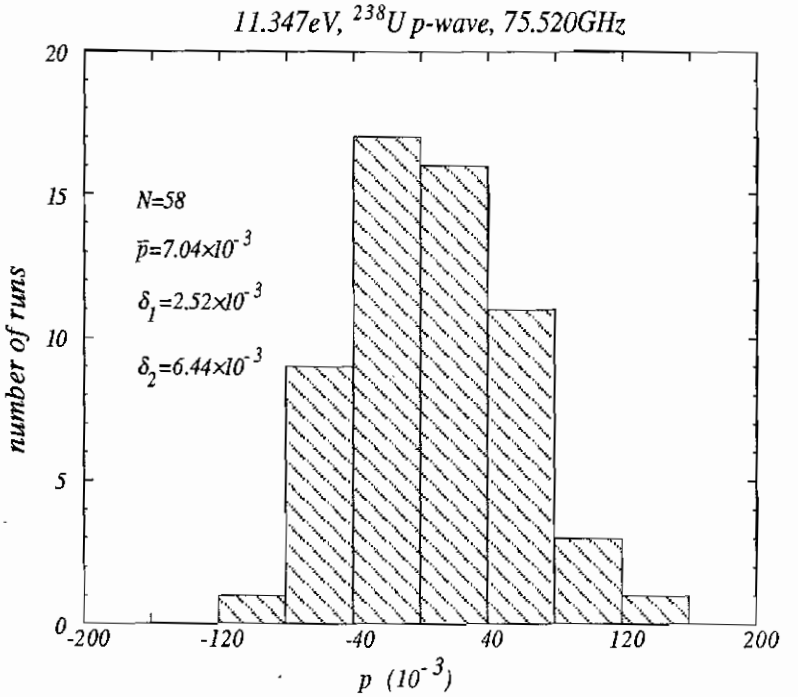

-4.96524E−02
1.32347E−02
6.05269E−01
-2.60832E+00
-9.29902E+00
5.06197E+11
6.04830E+03
4.81717E+04
4.42672E+02
5.91688E−01
9.49086E−07
-3.05043E−03

Fitting range:
[5870 : 6272]

Blankout region:
#1: [5902 : 6018]

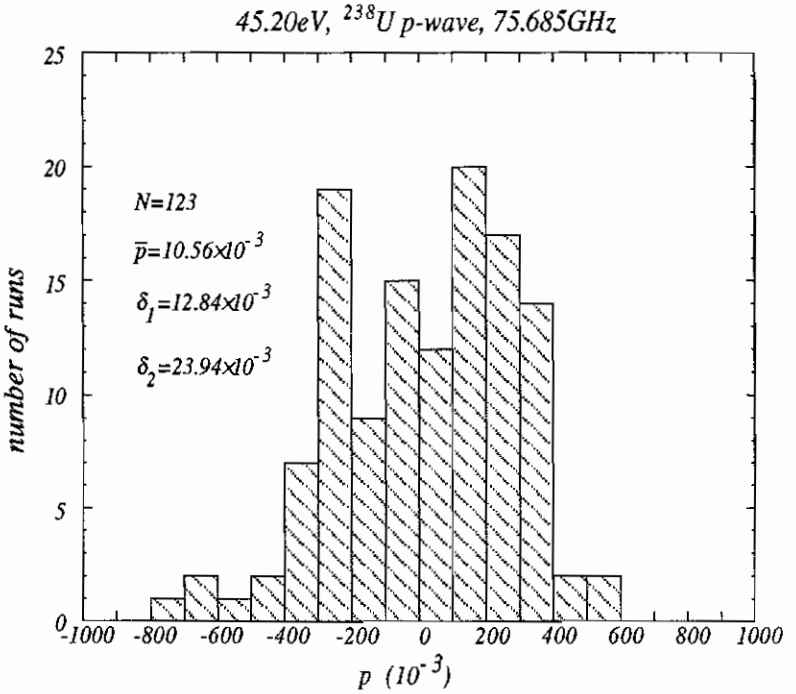

-1.56770E+00
-5.58811E+01
1.54486E+03
1.50727E+05
-2.36191E+06
5.23314E+11
3.01947E+03
3.11856E+06
6.59368E+02
5.28647E−01
2.42984E−04
1.08349E−02

Fitting range:
[2998 : 3027]

Blankout region:
none

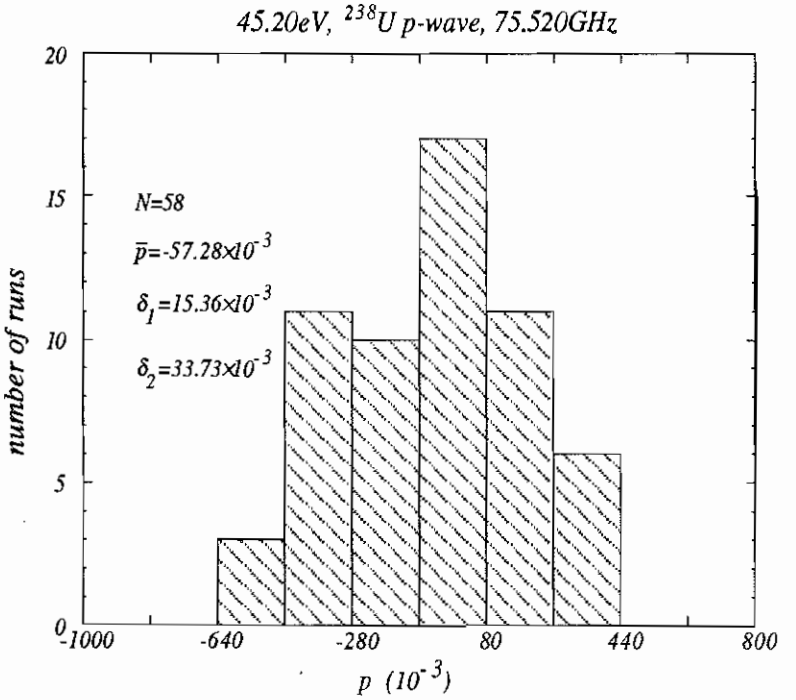

-1.34148E+00
-4.47233E+01
4.73744E+02
9.63788E+04
-8.29287E+05
3.05571E+11
3.01916E+03
8.62275E+06
5.87576E+02
1.01695E+00
1.75699E−04
2.61688E−02

Fitting range:
[2998 : 3027]

Blankout region:
none

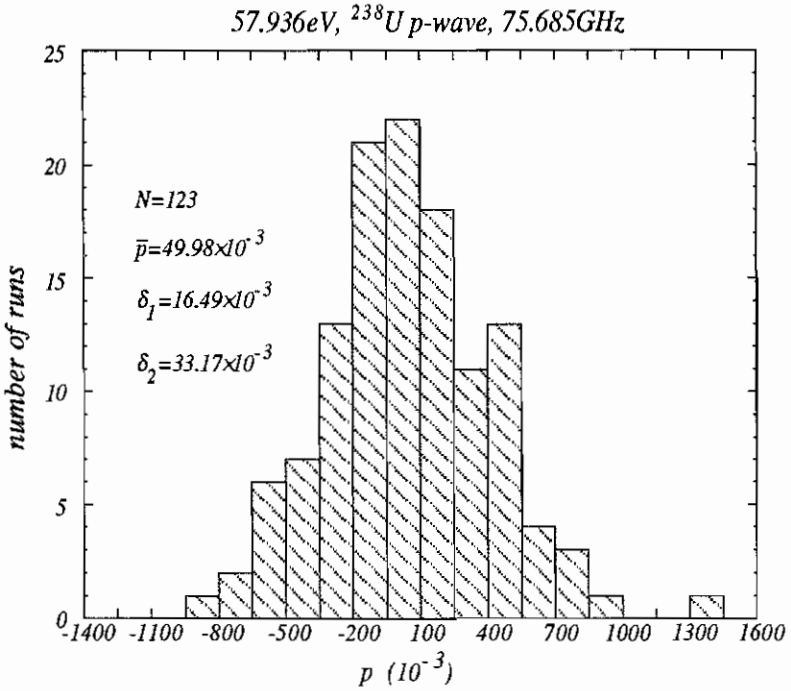

-6.54519E−01
1.85634E−01
0.00000E+00
0.00000E+00
0.00000E+00
6.36601E+11
2.66364E+03
4.34235E+04
7.44897E+02
1.35862E−01
1.68790E−04
2.52828E−02

Fitting range:
[2654 : 2682]

Blankout region:
none

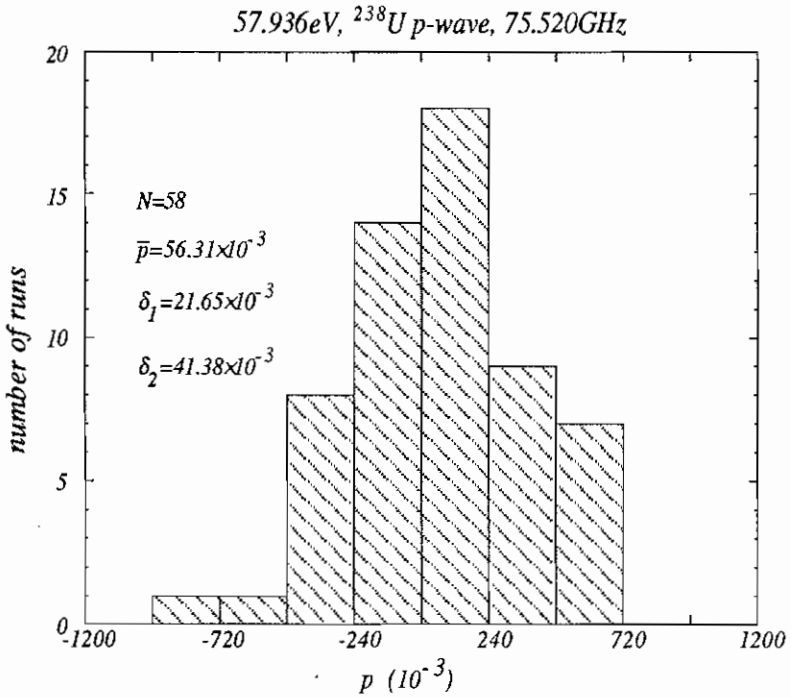

-7.52528E−01
4.48547E+00
4.03390E+02
0.00000E+00
0.00000E+00
3.70647E+11
2.66274E+03
3.25121E+04
1.46444E+07
1.27446E−01
-2.61747E−04
-3.44645E−02

Fitting range:
[2654 : 2682]

Blankout region:
none

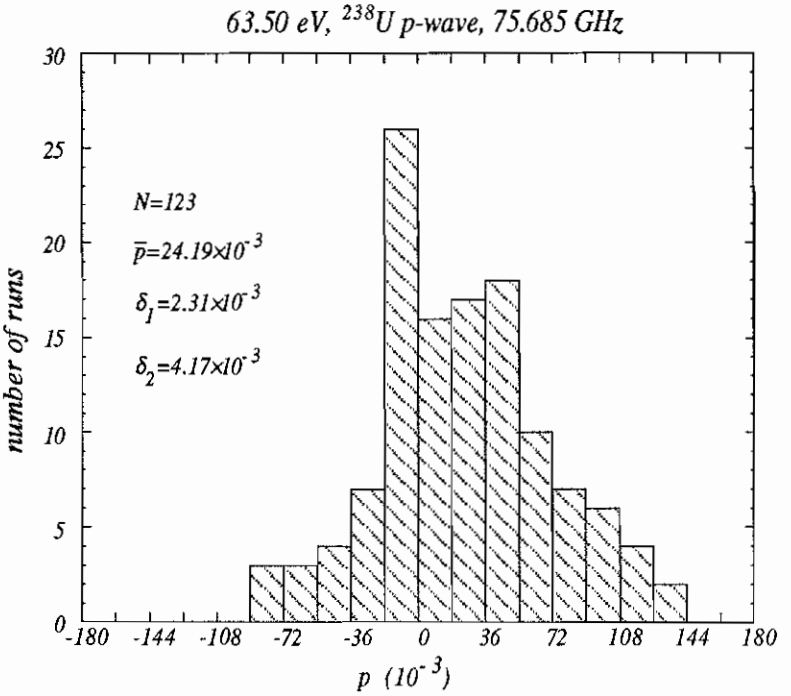

-1.47436E+00
3.07379E+01
-1.39241E+03
-2.37456E+04
1.69826E+06
7.06133E+11
2.54472E+03
1.41357E+05
1.15891E+03
7.86285E−01
3.96451E−05
1.12492E−02

Fitting range:
[2538 : 2586]

Blankout region:
none

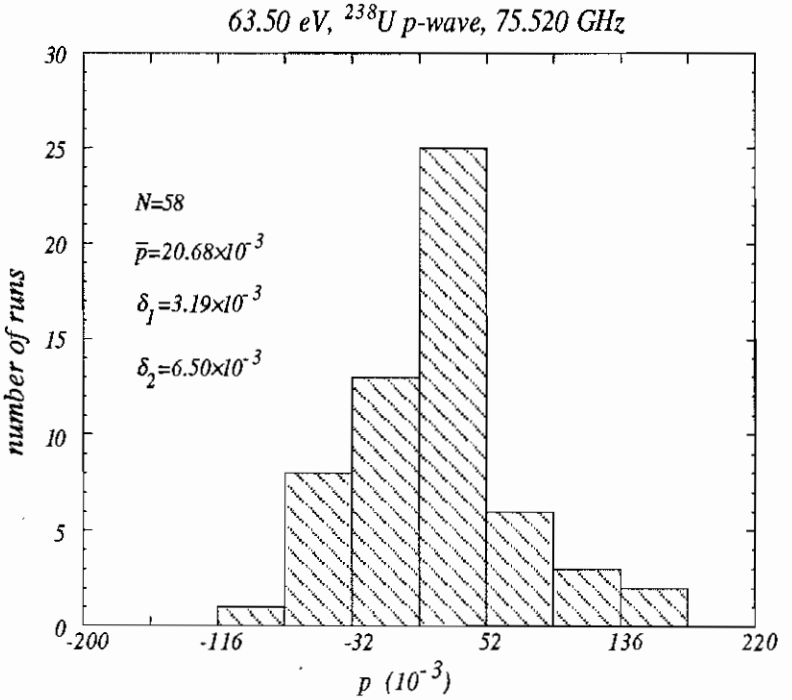

-1.43869E+00
2.45520E+01
-9.50556E+02
-1.39008E+04
9.08979E+05
4.10170E+11
2.54427E+03
1.52033E+05
1.10846E+03
7.79511E−01
1.69833E−04
-1.03783E−02

Fitting range:
[2538 : 2586]

Blankout region:
none

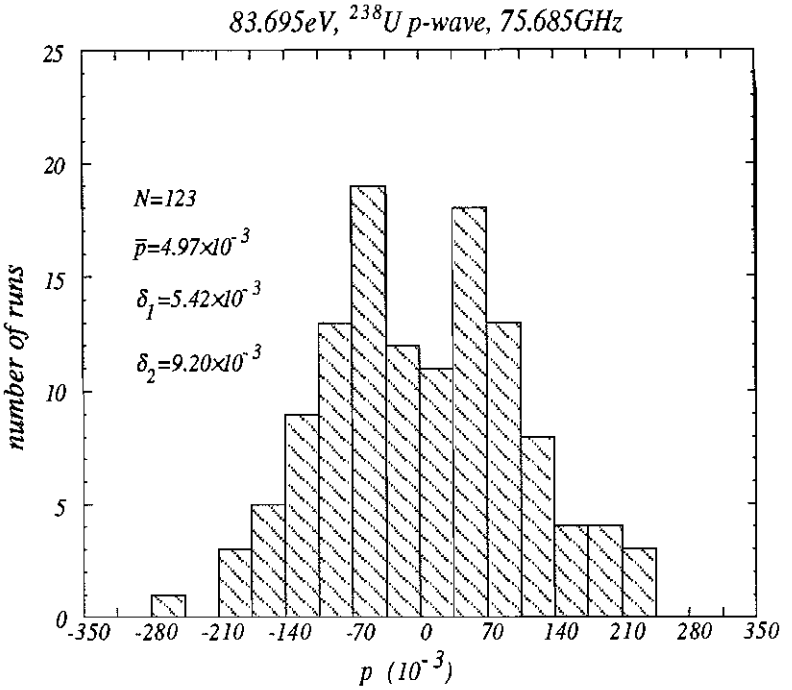

-1.17937E+00
3.69718E+00
-2.11725E+02
-2.19728E+04
-2.92645E+05
5.76730E+11
2.21527E+03
6.51165E+05
8.03696E+02
5.57629e−01
2.35556e−05
1.21542e−03

Fitting range:
[2187 : 2230]

Blankout region:
none

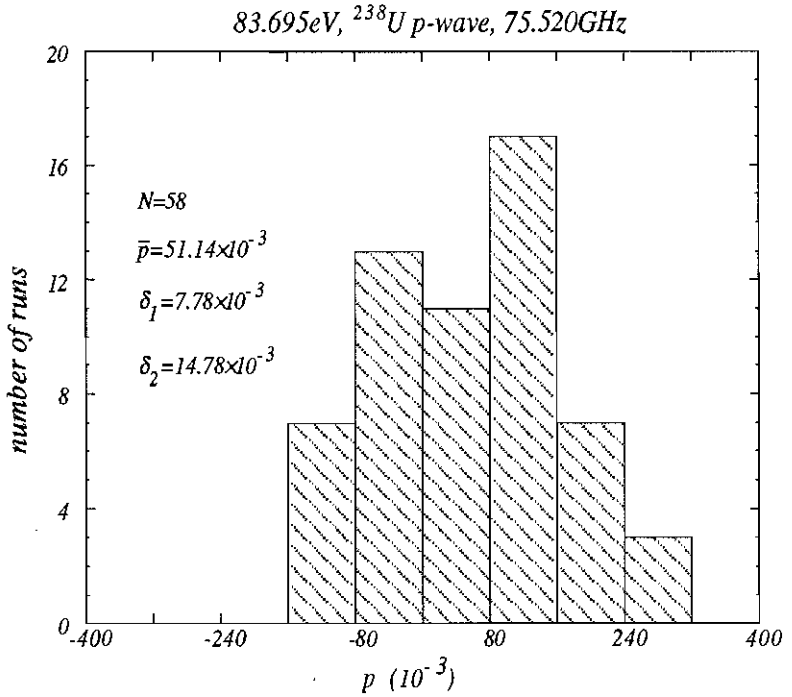

-1.26360E+00
7.32086E+00
2.48695E+02
-2.83222E+04
-8.42431E+05
3.36387E+11
2.21479E+03
8.38100E+05
7.88694E+02
5.71575e−01
-9.38890e−05
-2.35255e−02

Fitting range:
[2187 : 2230]

Blankout region:
none

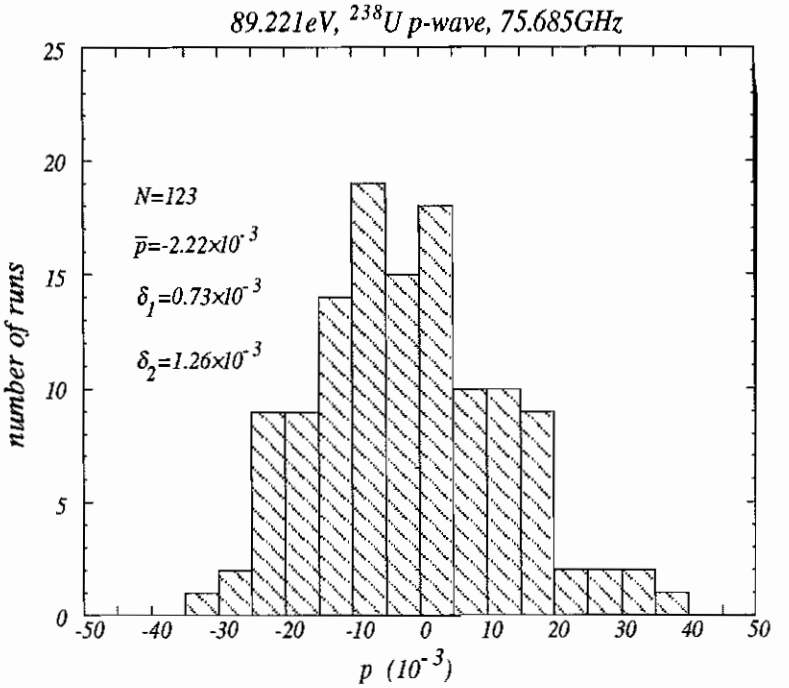

-1.00435E+00
6.86631E+00
-8.91585E+01
0.00000E+00
0.00000E+00
6.07414E+11
2.14506E+03
8.24912E+06
6.45423E+02
1.17729E+01
-6.59095e−05
-1.18484e−03

Fitting range:
[2110 : 2200]

Blankout regions:
#1: [2115 : 2140]
#2: [2149 : 2170]

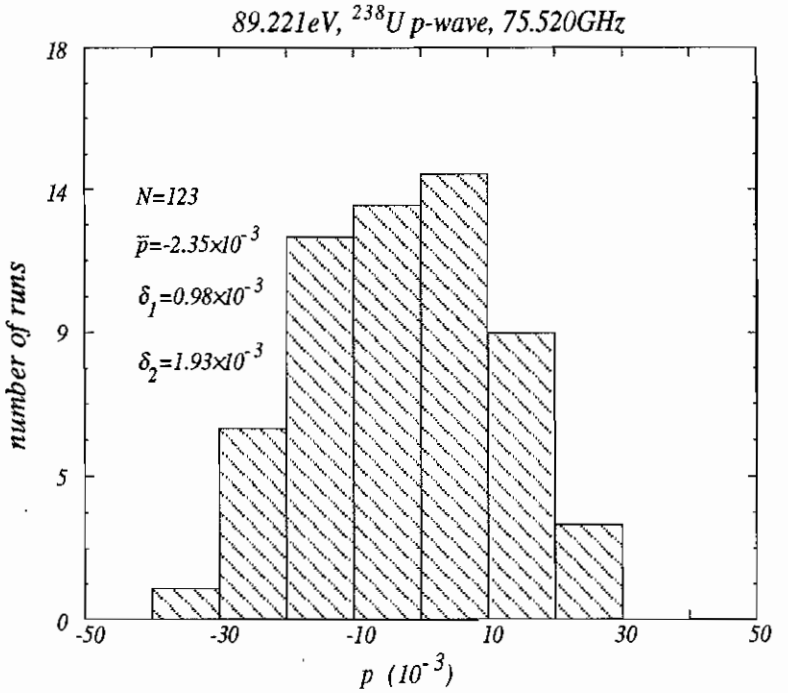

-1.21696E+00
1.87214E+01
2.87955E+01
-6.23482E+03
0.00000E+00
3.53906E+11
2.14459E+03
2.09351E+06
6.73545E+02
6.34948E+00
-6.17390e−05
1.03239e−03

Fitting range:
[2110 : 2200]

Blankout regions:
#1: [2115 : 2140]
#2: [2149 : 2170]

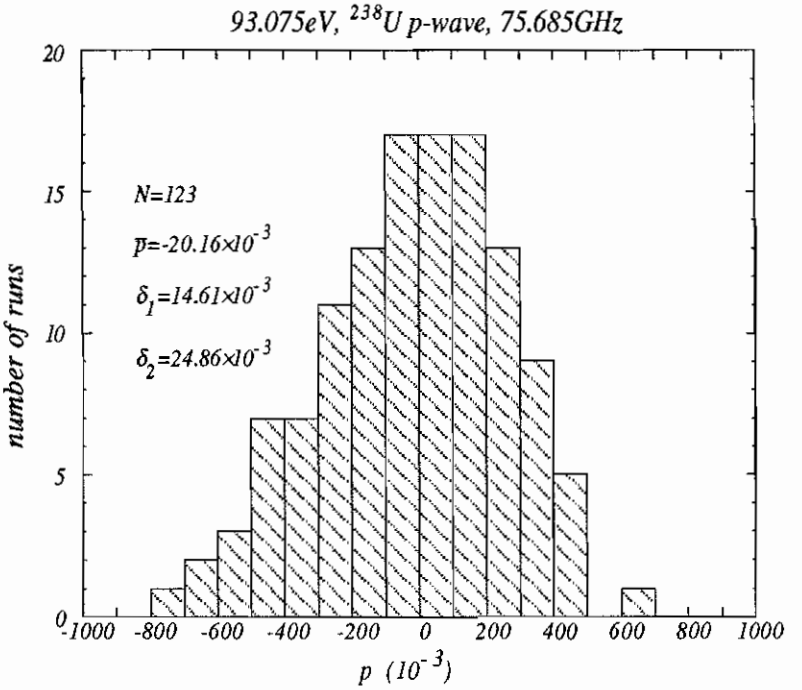

-2.41482E+00
-2.62828E+00
0.00000E+00
0.00000E+00
0.00000E+00
6.56328E+11
2.09938E+03
3.26995E+06
8.61140E+02
4.33563e−01
-2.00615e−05
-5.65376e−03

Fitting range:
[2094 : 2105]

Blankout region:
none

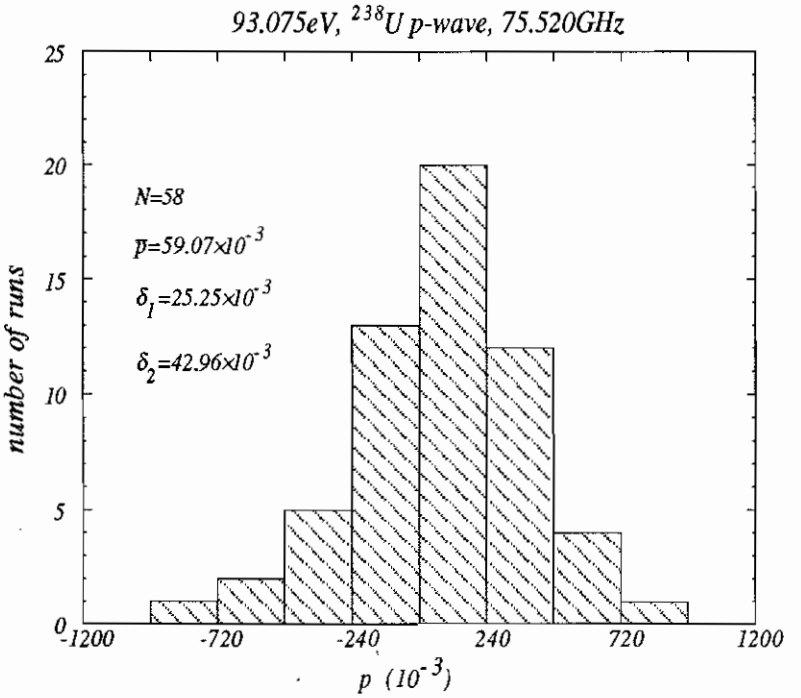

-2.36666E+00
9.39613E+01
0.00000E+00
0.00000E+00
0.00000E+00
3.80833E+11
2.09883E+03
3.94590E+06
9.03401E+02
3.71872e−01
-1.62240e−04
-2.63530e−02

Fitting range:
[2094 : 2105]

Blankout region:
none

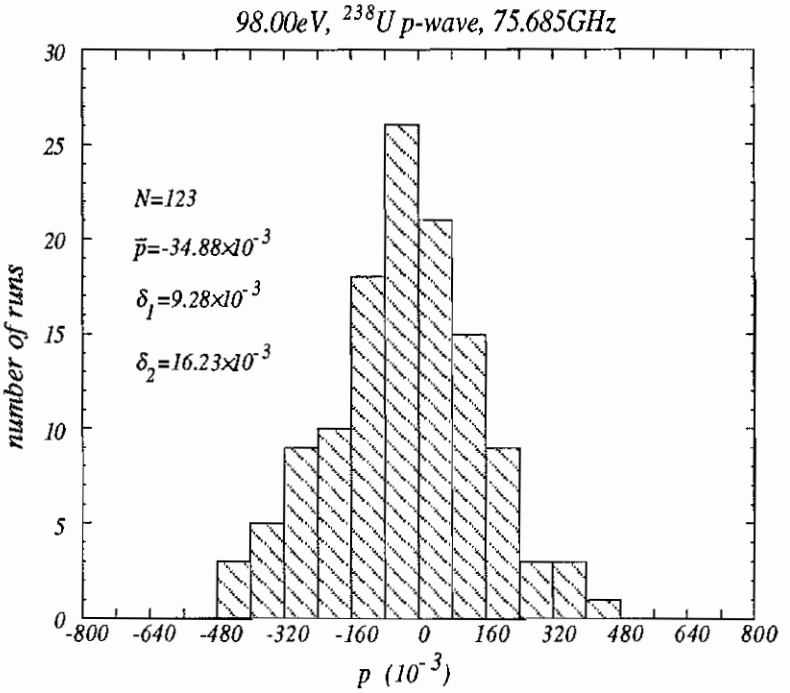

-3.58874E+00
-2.25554E+01
5.73925E+03
-6.52052E+04
-1.04006E+07
7.49396E+11
2.04609E+03
8.12489E+04
2.43641E+03
1.89751E−01
-1.52877E−04
-1.58936E−02

Fitting range:
[2034 : 2063]

Blankout region:
none

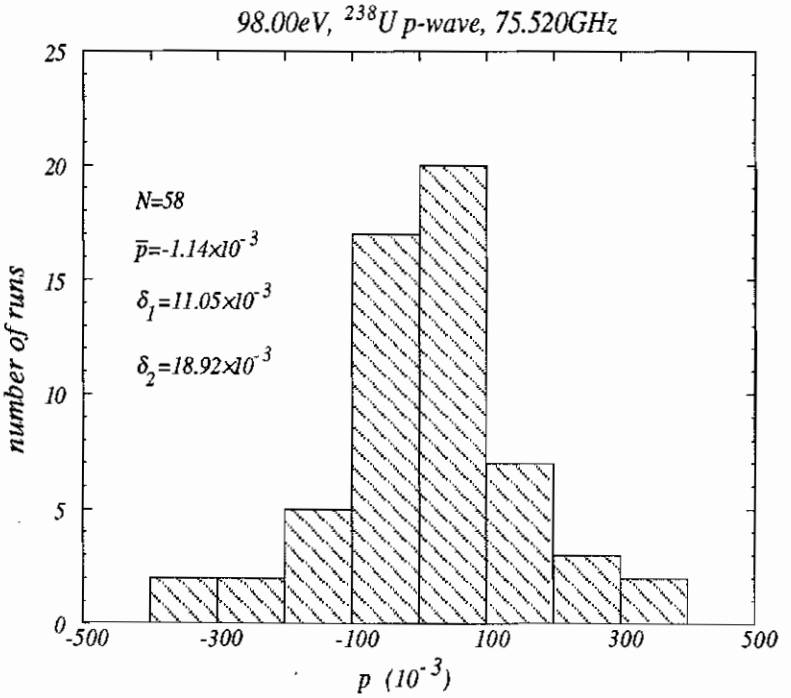

-3.74890E+00
-4.73594E+01
7.37964E+03
3.38821E+04
-1.48348E+07
4.35733E+11
2.04566E+03
8.50130E+04
1.67437E+03
2.14979E−01
-1.17990E−04
-4.32826E−03

Fitting range:
[2034 : 2063]

Blankout region:
none

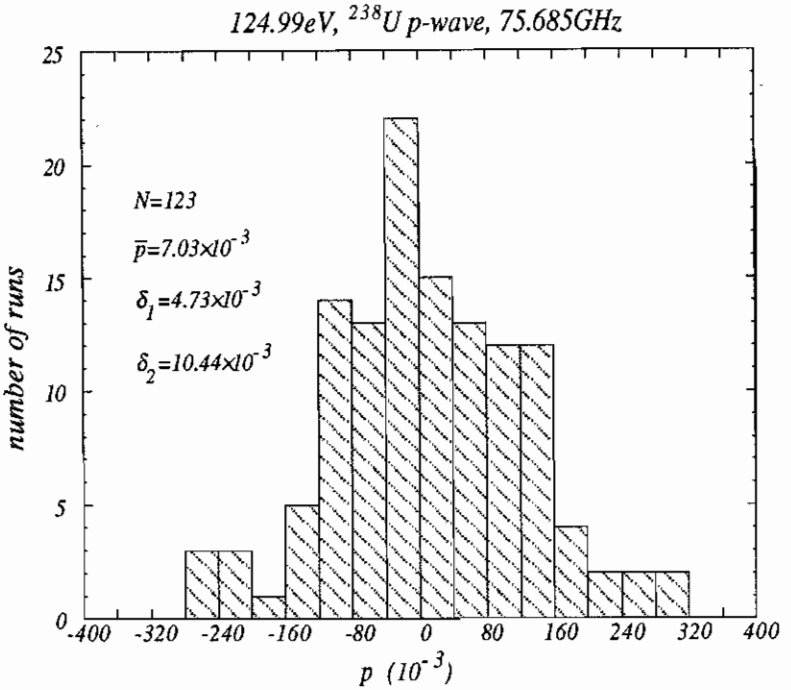

-1.18803E+00
7.21844E+00
3.99254E+01
-2.26877E+03
-9.99277E+03
4.94606E+11
1.81047E+03
1.33190E+05
3.65224E+03
2.66086E−01
-3.11204E−05
3.59919E−03

Fitting range:
[1693 : 1834]

Blankout region:
#1: [1725 : 1797]

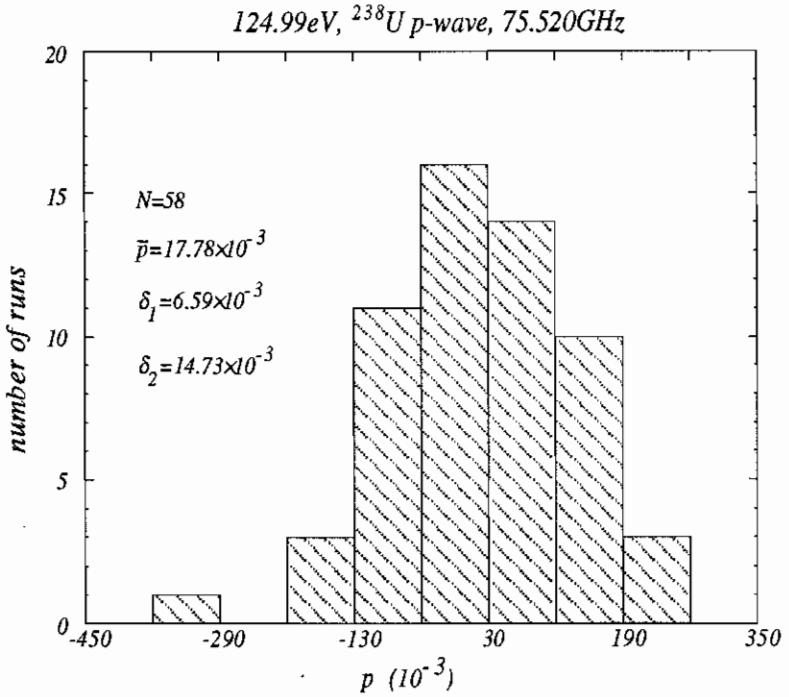

-1.13906E+00
7.84627E+00
1.17246E+01
-2.32790E+03
-5.73267E+03
2.71177E+11
1.81005E+03
2.37838E+05
1.24676E+03
3.08248E−01
1.18587E−04
-8.65266E−03

Fitting range:
[1693 : 1834]

Blankout region:
#1: [1725 : 1797]

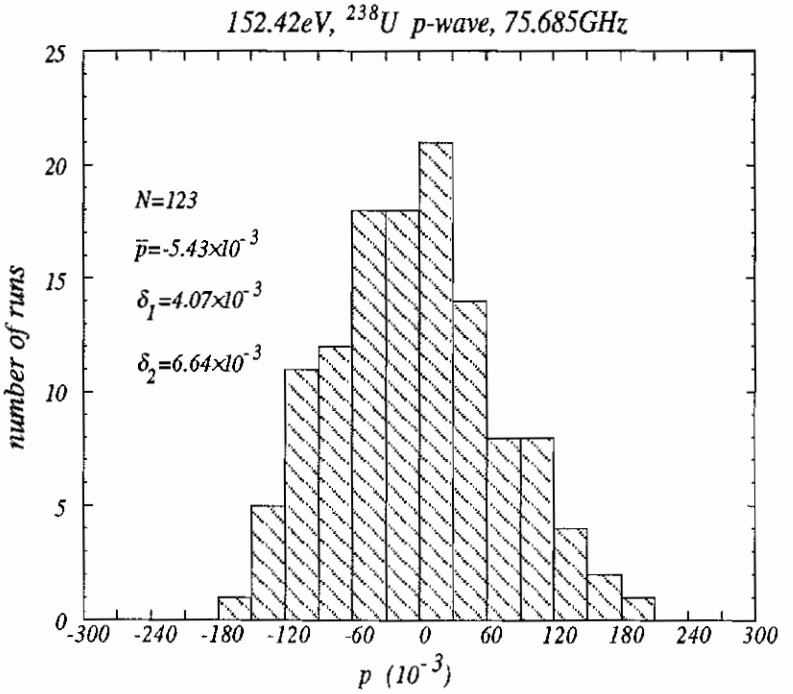

-1.07999E+00
3.35591E+00
7.16577E+02
-8.49079E+03
-2.58292E+05
5.52943E+11
1.63812E+03
3.52802E+06
8.14377E+02
1.39194E+00
4.44516E−05
-2.00761E−03

Fitting range:
[1620 : 1662]

Blankout region:
#1: [1641 : 1646]

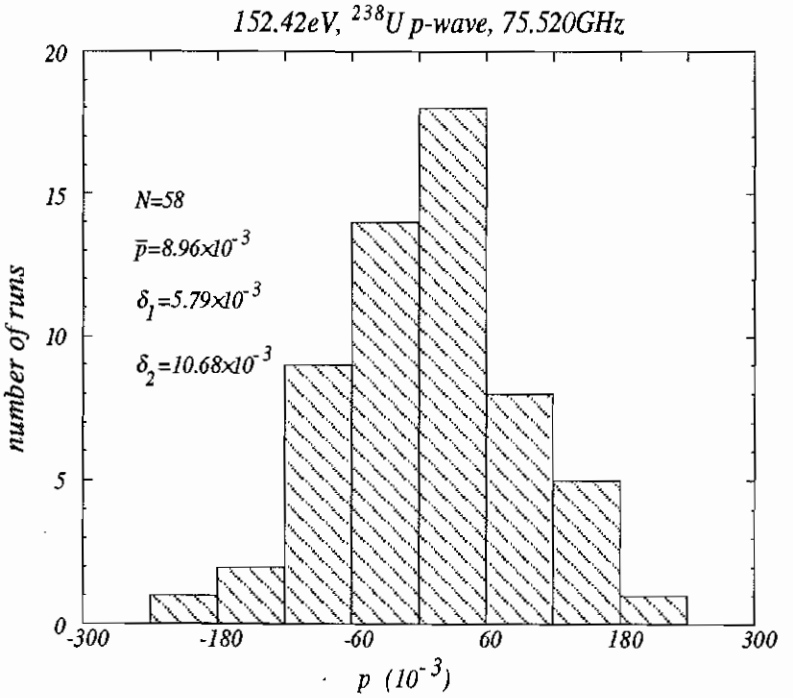

-1.05321E+00
1.24086E+01
6.42067E+02
-2.46551E+04
-1.76628E+05
3.02876E+11
1.63765E+03
4.07054E+06
8.03444E+02
1.44235E+00
-8.35682E−05
-4.57875E−03

Fitting range:
[1620 : 1662]

Blankout region:
#1: [1641 : 1646]

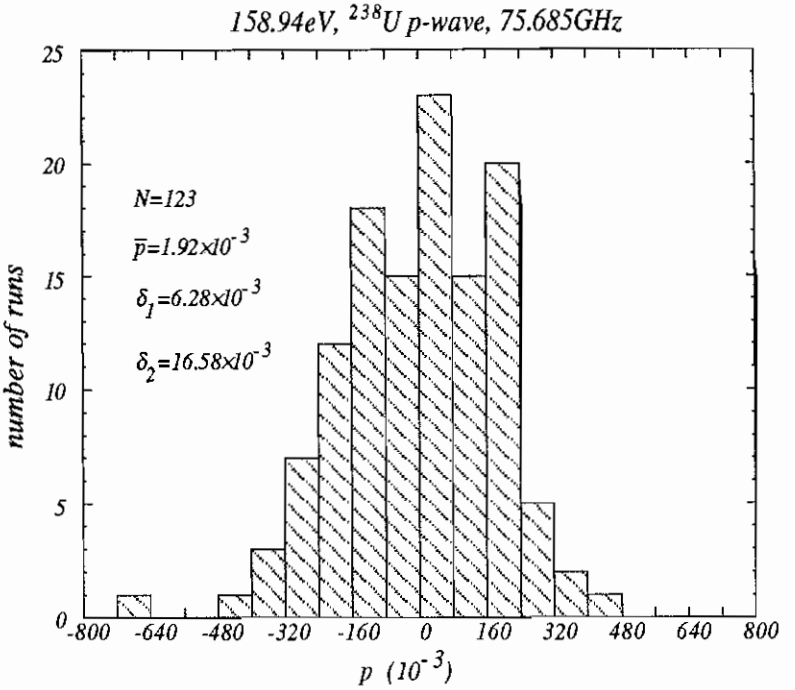

-1.46478E+00
-8.01958E+00
3.62120E+03
-2.74825E+03
-4.32505E+06
5.33983E+11
1.60389E+03
1.12236E+05
8.55146E+13
1.96053E−01
1.63074E−05
7.83352E−03

Fitting range:
[1589 : 1628]

Blankout regions:
#1: [1592 : 1598]
#2: [1608 : 1619]

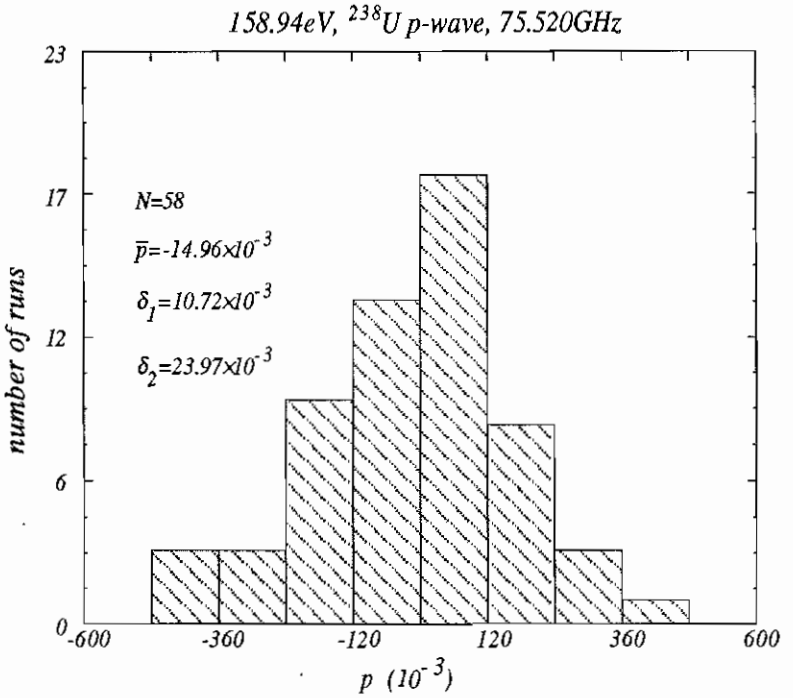

-1.33216E+00
7.94180E−01
3.12572E+03
-1.29502E+04
-3.94762E+06
3.11938E+11
1.60341E+03
1.33767E+05
8.55146E+13
1.79107E−01
-3.67811E−06
8.03548E−03

Fitting range:
[1589 : 1628]

Blankout regions:
#1: [1592 : 1596]
#2: [1608 : 1616]

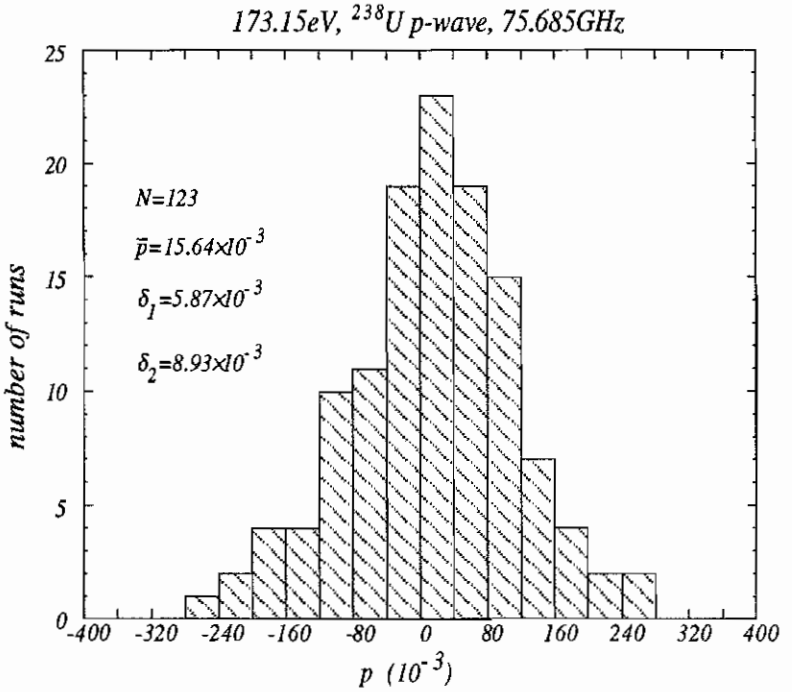

-3.30754E+00
5.42913E+01
5.89318E+03
-1.13562E+05
-1.39235E+07
5.84857E+11
1.53582E+03
2.40374E+06
8.70001E+02
8.73860E−01
2.70421E−06
3.29600E−03

Fitting range:
[1520 : 1551]

Blankout region:
none

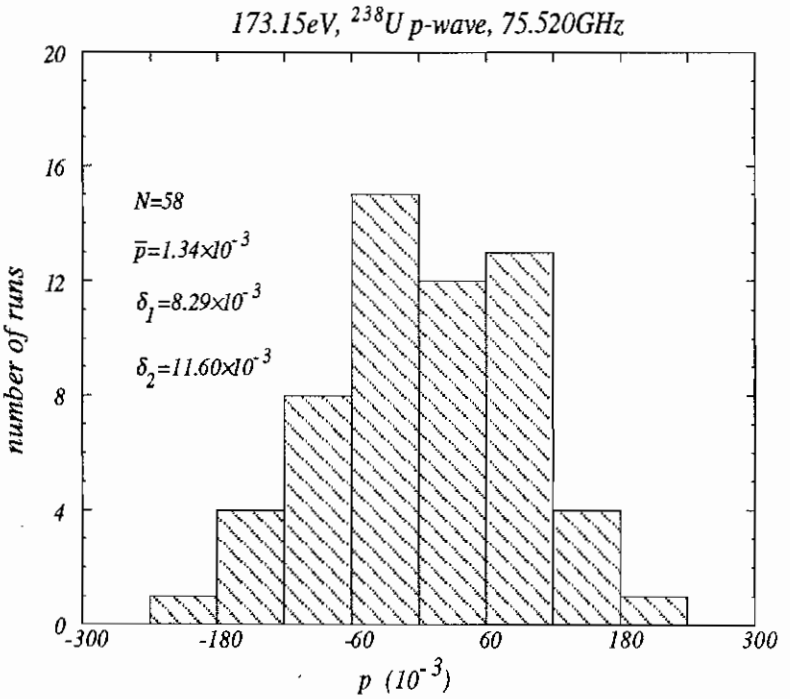

-3.19027E+00
6.03481E+01
5.36469E+03
-1.38678E+05
-1.28433E+07
3.41024E+11
1.53535E+03
2.45749E+06
8.90640E+02
8.60812E−01
-2.02970E−05
-2.64799E−03

Fitting range:
[1520 : 1551]

Blankout region:
none

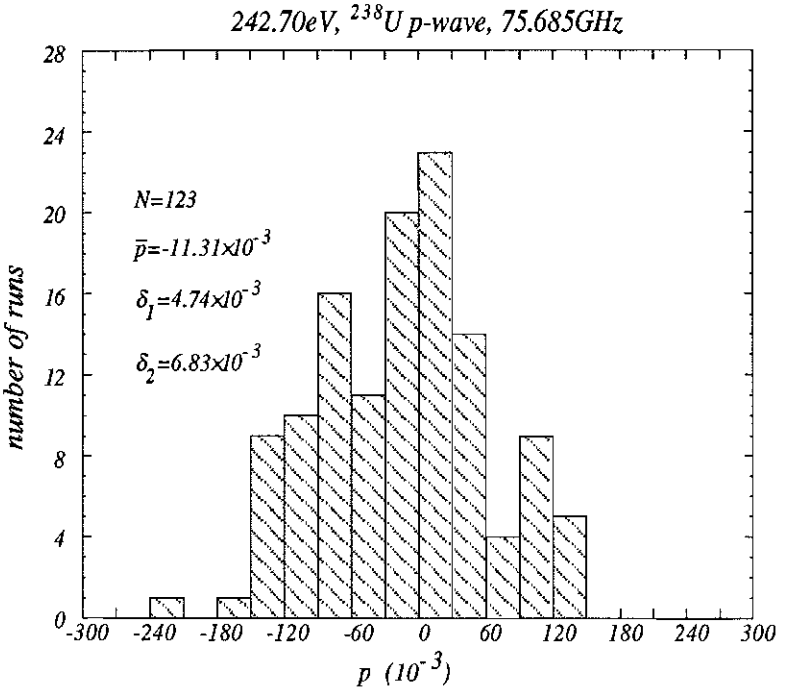

-3.37237E+00
-5.87779E+02
-7.52349E+04
4.58280E+06
8.50383E+08
4.12758E+11
1.29523E+03
1.96888E+07
7.92492E+02
2.90458E+00
-2.37641E−04
-3.91318E−03

Fitting range:
[1284 : 1300]

Blankout region:
none

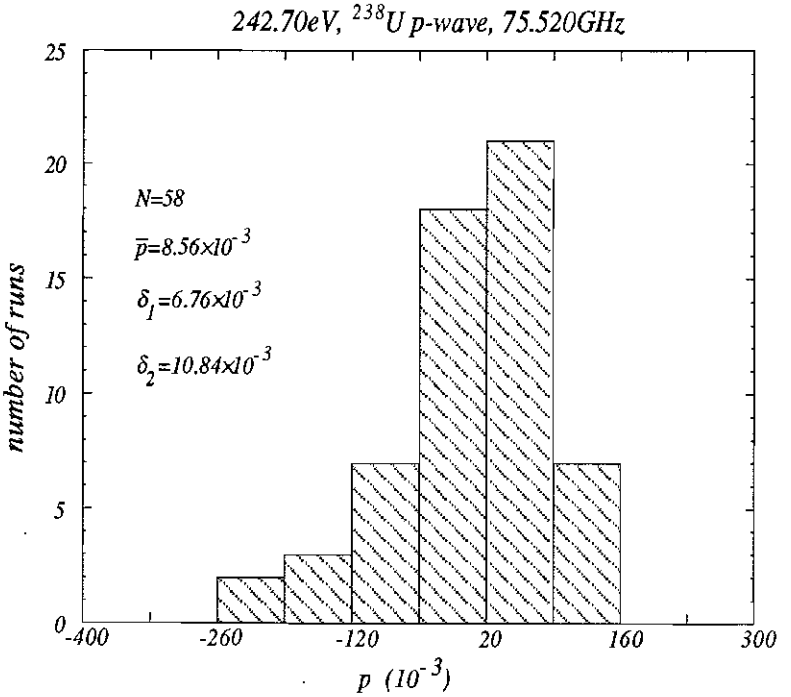

-3.82564E+00
-6.03423E+02
-5.81224E+04
4.93151E+06
6.87970E+08
2.42597E+11
1.29480E+03
1.85159E+07
7.89600E+02
2.79024E+00
3.44425E−05
-1.67095E−03

Fitting range:
[1284 : 1300]

Blankout region:
none

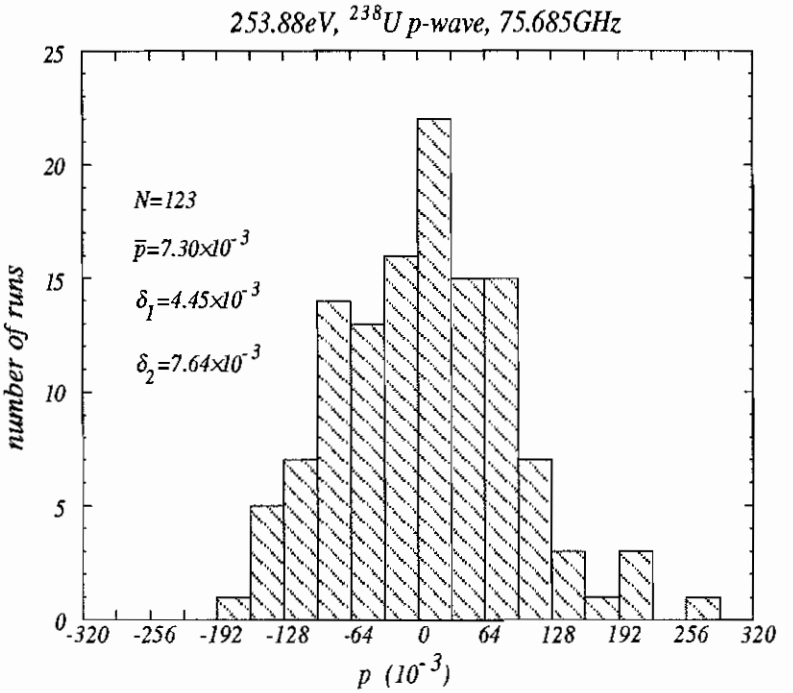

-1.85157E+00
-9.90212E+01
4.72074E+03
1.63442E+05
-8.53400E+06
4.35589E+11
1.26625E+03
1.22252E+05
1.62845E+14
3.30835E−01
6.08158E−05
5.99460E−03

Fitting range:
[1250 : 1284]

Blankout regions:
#1: [1256 : 1262]
#2: [1270 : 1273]

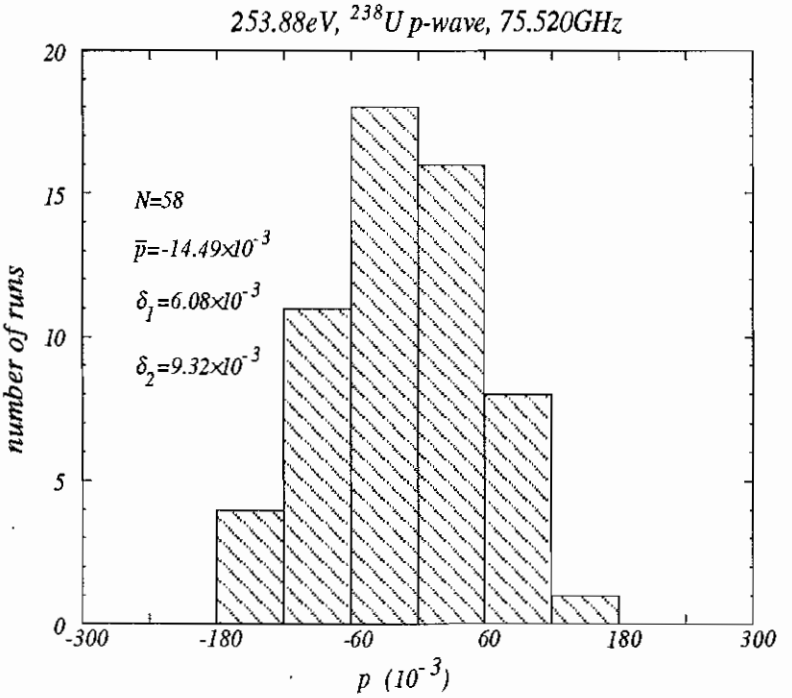

-1.45211E+00
-9.04500E+01
1.77034E+03
1.05767E+05
-1.19673E+06
2.57074E+11
1.26580E+03
1.27456E+05
1.62845E+14
3.23443E−01
1.00108E−04
6.55624E−03

Fitting range:
[1246 : 1284]

Blankout regions:
#1: [1254 : 1262]
#2: [1269 : 1273]

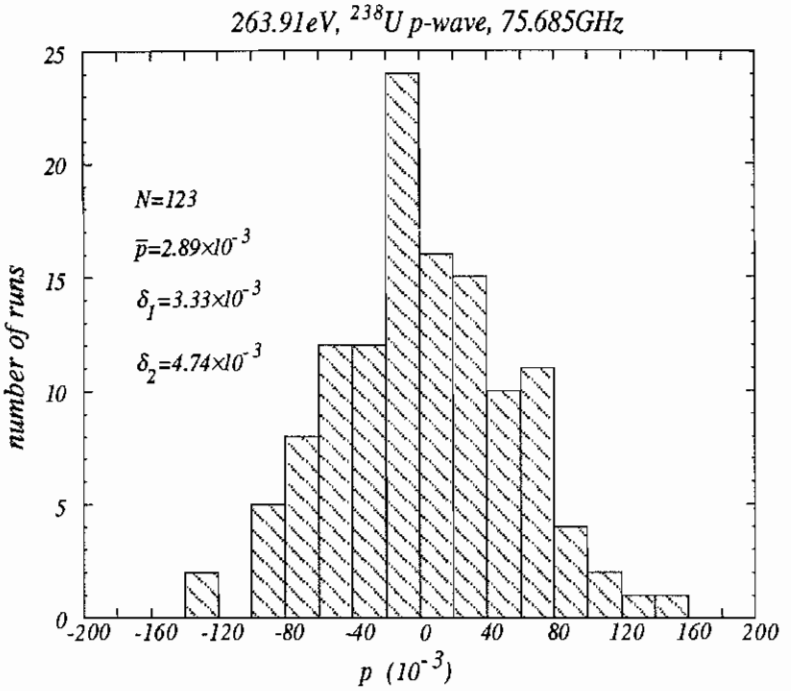

-2.73389E+00
-3.06497E+01
1.81912E+04
2.35690E+05
-6.22805E+07
4.44490E+11
1.24169E+03
3.97139E+07
7.54741E+02
5.70054E+00
6.30386E−05
1.71057E−03

Fitting range:
[1231 : 1254]

Blankout region:
#1: [1244 : 1250]

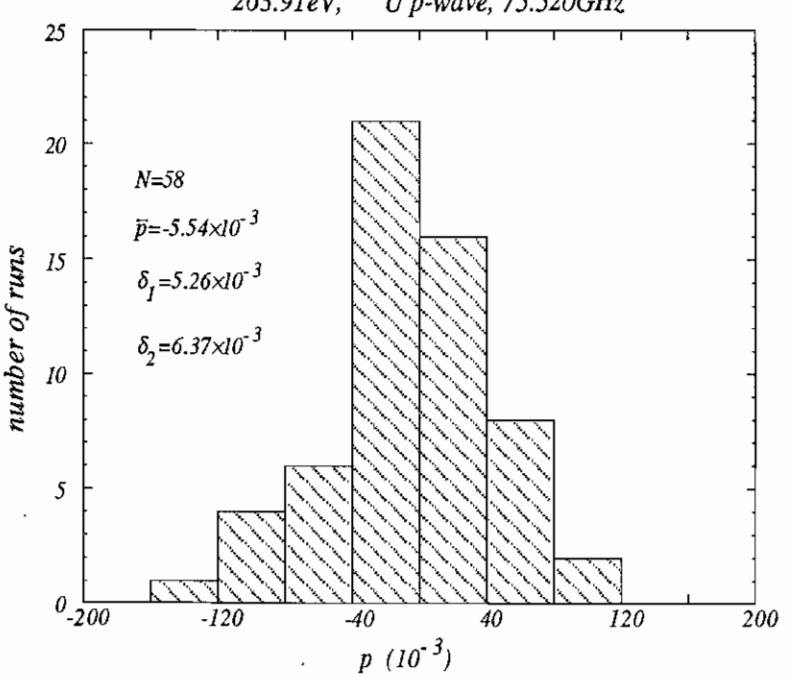

-2.24858E+00
-5.20737E+01
7.07394E+03
3.44840E+05
0.00000E+00
2.61864E+11
1.24131E+03
9.00888E+07
7.00881E+02
8.87953E+00
7.44632E−06
3.54136E−03

Fitting range:
[1231 : 1254]

Blankout region:
#1: [1244 : 1250]

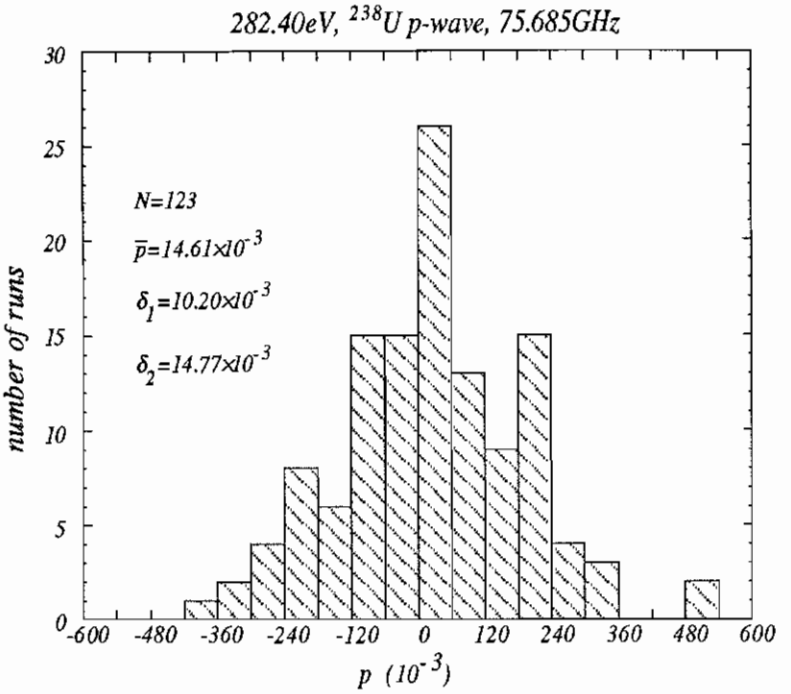

-4.15042E+00
-1.38581E+02
8.87224E+04
3.81288E+05
-1.05811E+09
4.27051E+11
1.19974E+03
1.45942E+07
7.87738E+02
1.11859E+00
-2.60431E−05
7.63324E−03

Fitting range:
[1193 : 1207]

Blankout region:
none

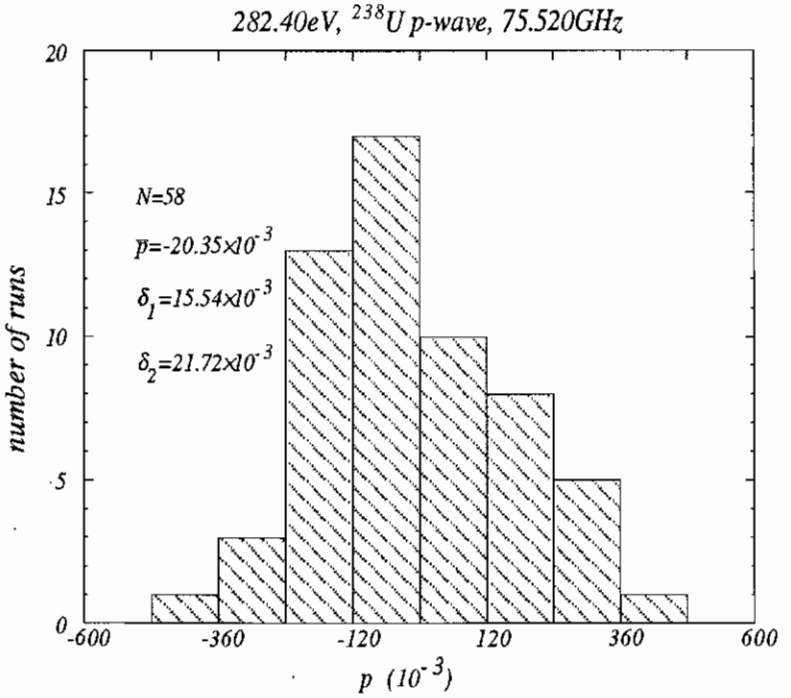

-4.25243E+00
-1.47166E+02
1.29413E+05
9.94111E+05
-2.04337E+09
2.51939E+11
1.19923E+03
2.11136E+07
8.46445E+02
1.11358E+00
7.51633E−05
8.74729E−03

Fitting range:
[1193 : 1205]

Blankout region:
none

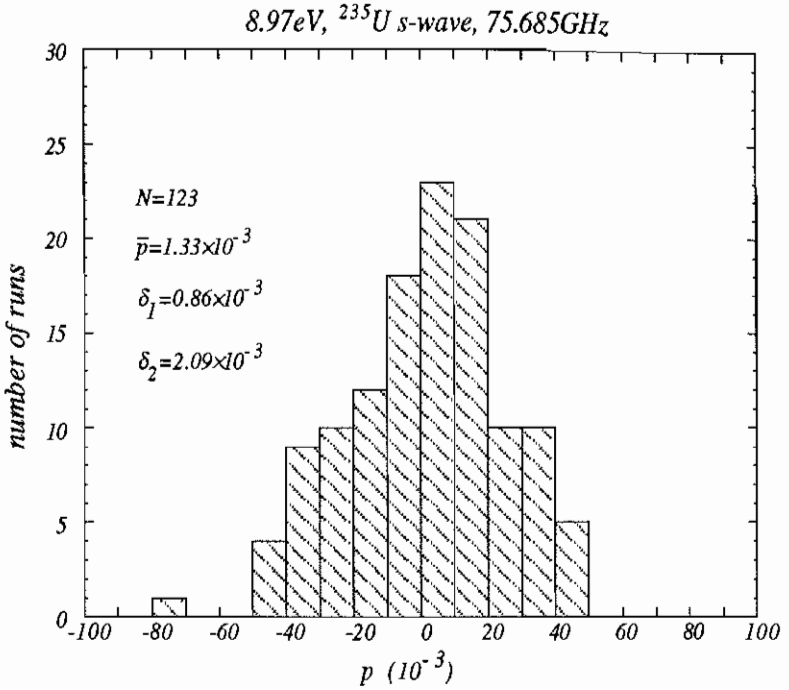

-2.22700E−01
-2.06057E−01
-1.94505E−01
-8.27351E−01
-5.18542E−01
7.99720E+11
6.87103E+03
1.15869E+04
3.16993E+02
1.10098E+00
1.92712E−05
8.86041E−04

Fitting range:
[6490 : 7225]

Blankout region:
#1: [6622 : 6750]

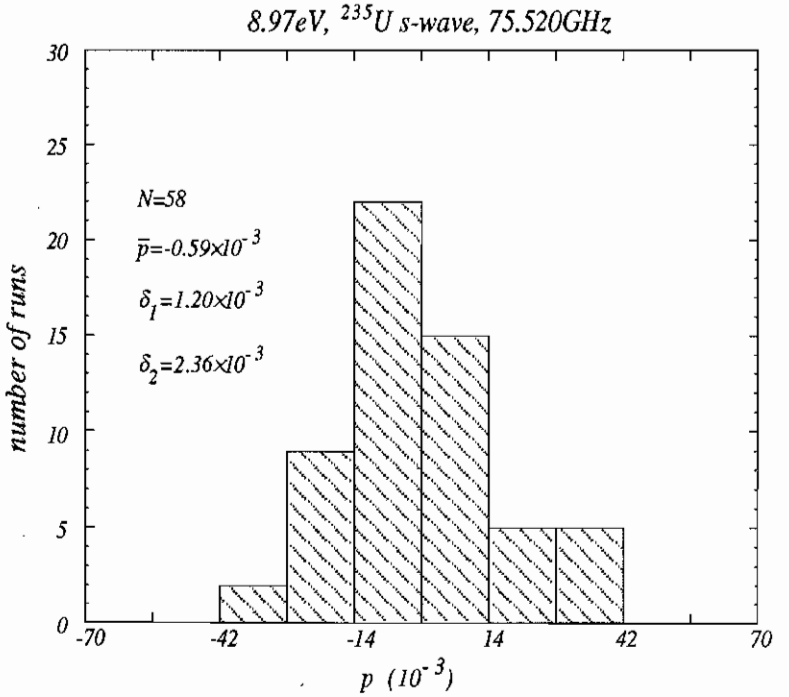

-2.16029E−01
-2.08929E−01
-2.35298E−01
-7.56751E−01
-2.53276E−01
4.65246E+11
6.87051E+03
1.18004E+04
3.08037E+02
1.08624E+00
-4.98015E−05
2.45560E−04

Fitting range:
[6490 : 7225]

Blankout region:
#1: [6622 : 6750]

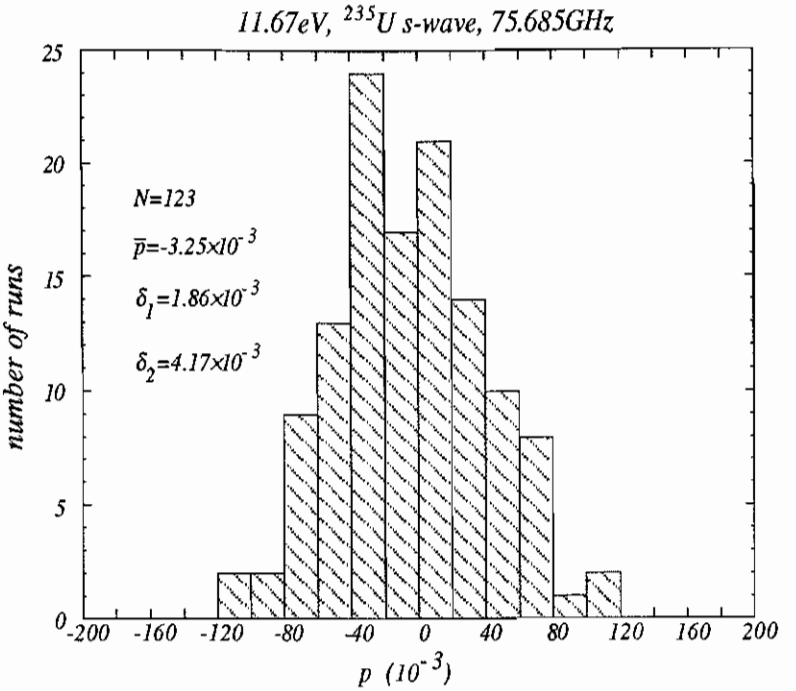

-4.89582E−02
5.93313E−03
4.94355E−01
-2.32732E+00
-6.84934E+00
8.71201E+11
5.95797E+03
3.18408E+07
2.46380E+02
1.37635E+01
-6.83504E−05
-2.10487E−03

Fitting range:
[5870 : 6272]

Blankout region:
#1: [5984 : 6150]

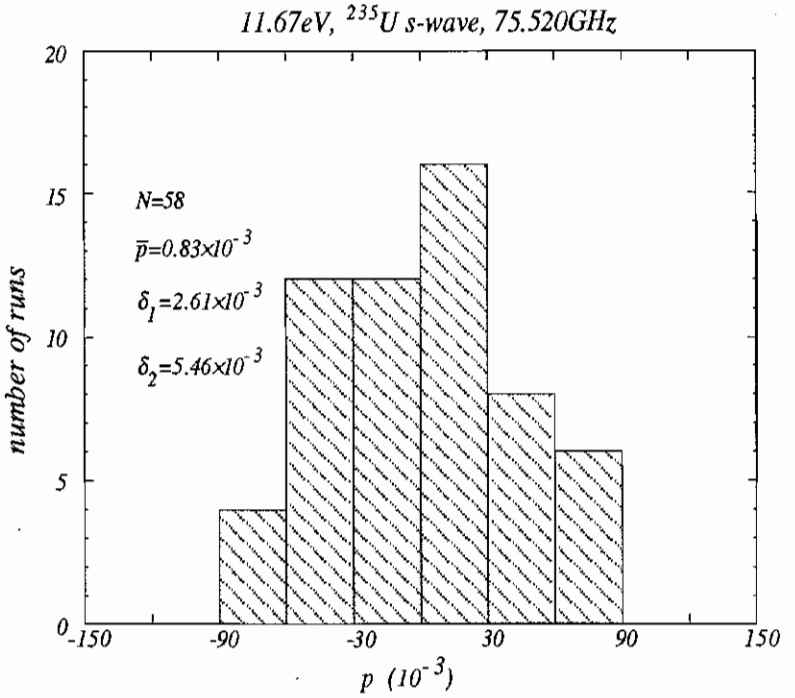

-4.96524E−02
1.32347E−02
6.05269E−01
-2.60832E+00
-9.29902E+00
5.05934E+11
5.95741E+03
2.39712E+07
2.46052E+02
1.18772E+01
5.74995E−05
-2.84332E−04

Fitting range:
[5870 : 6272]

Blankout region:
#1: [5984 : 6150]

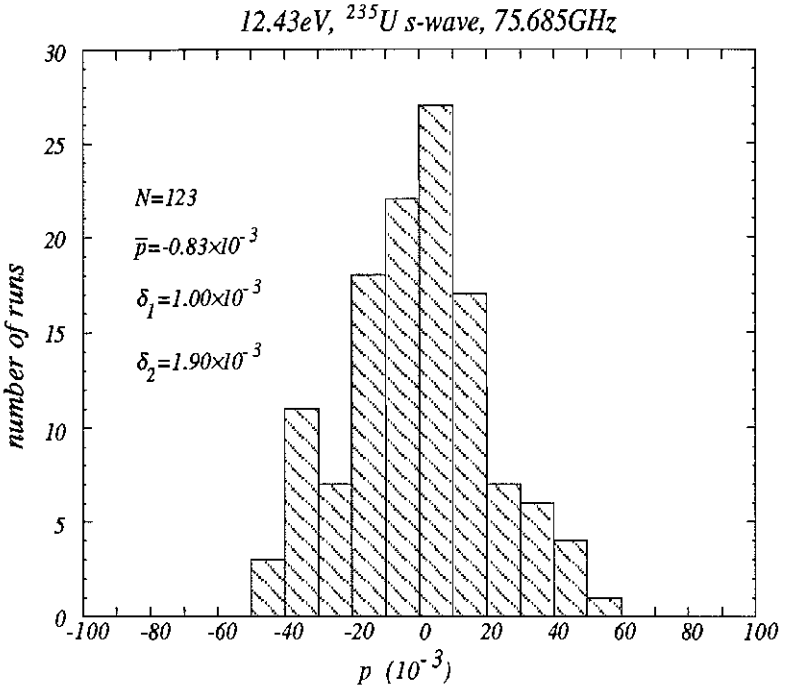

-8.80780E−02
5.42602E−02
7.27058E−01
-4.08872E−01
-3.45515E+00
8.78060E+11
5.77948E+03
1.46685E+05
2.76431E+02
2.10978E+00
-6.59016E−06
-6.79536E−04

Fitting range:
[5550 : 6250]

Blankout regions:
#1: [5640 : 5750]
#2: [5806 : 6130]

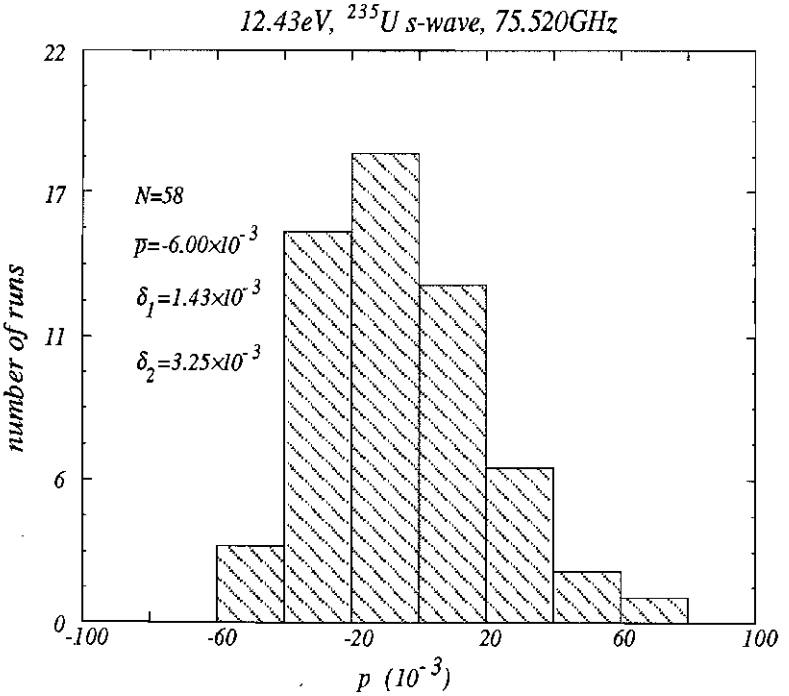

-7.90861E−02
1.16084E−01
5.67515E−01
-7.18282E−01
-2.70565E+00
5.08267E+11
5.77894E+03
1.57825E+05
2.80583E+02
2.06782E+00
5.72970E−05
2.77448E−03

Fitting range:
[5550 : 6250]

Blankout regions:
#1: [5640 : 5750]
#2: [5806 : 6130]

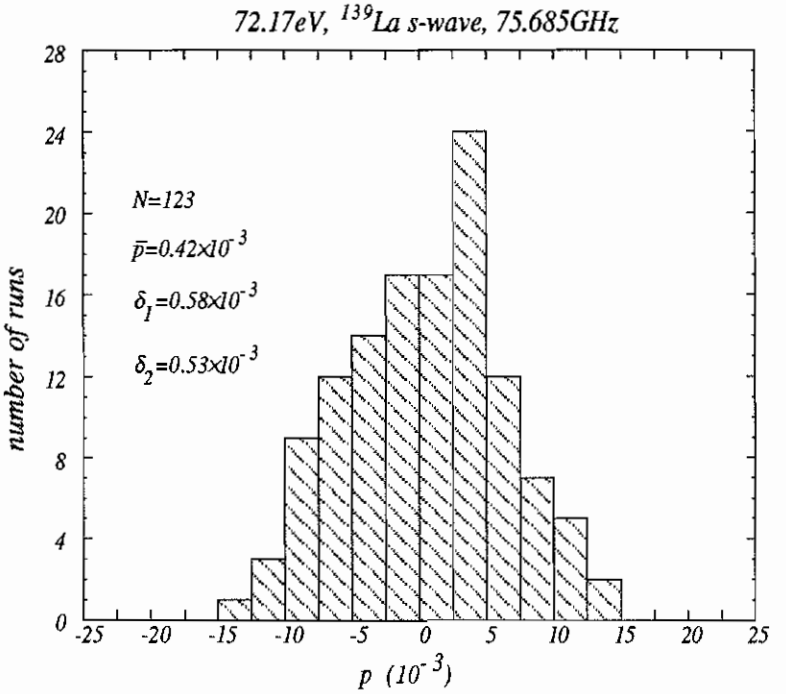

-2.07973E+00
-4.19207E+00
5.45607E+01
-1.92092E+03
-2.20451E+04
5.01892E+11
2.38518E+03
1.33493E+06
4.81792E+02
1.32450E+01
-2.80779E−05
2.98844E−04

Fitting range:
[2307 : 2460]

Blankout regions:
#1: [2327 : 2357]
#2: [2392 : 2423]

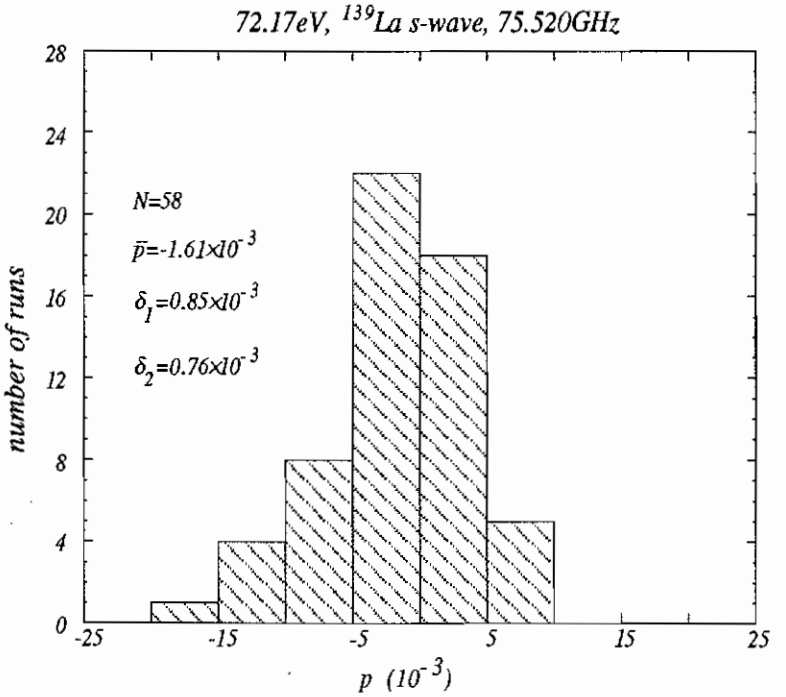

-2.06403E+00
-3.46165E+00
5.31235E+01
-2.03222E+03
-2.17557E+04
2.93285E+11
2.38473E+03
1.24493E+06
4.74807E+02
1.28129E+01
1.37291E−04
7.71673E−04

Fitting range:
[2307 : 2460]

Blankout regions:
#1: [2325 : 2357]
#2: [2392 : 2423]

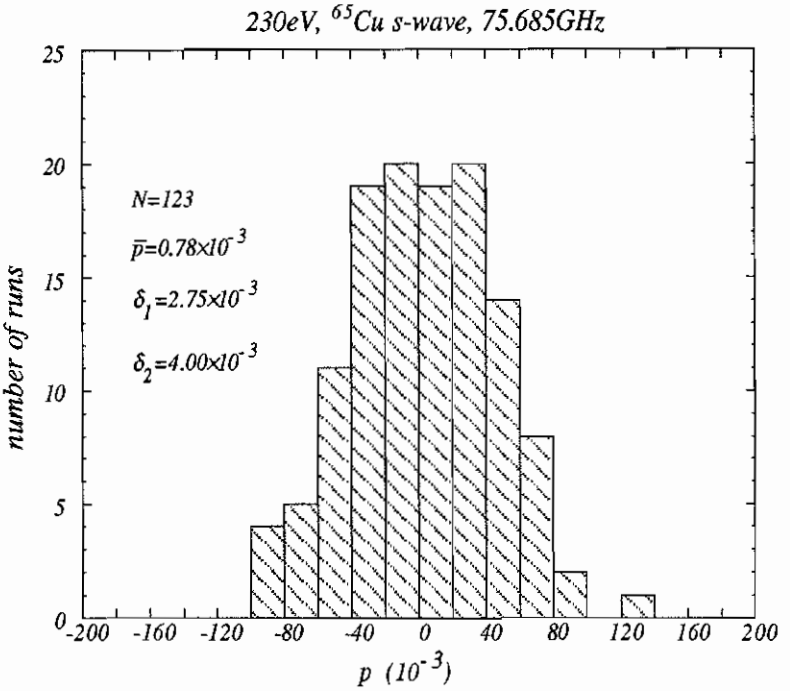

-3.59971E+00
5.11045E+01
-7.89563E+02
-1.22420E+05
9.47807E+06
4.34724E+11
1.33016E+03
8.74591E+04
1.47139E+07
7.18058E−01
-6.07545E−05
-3.77228E−04

Fitting range:
[1316 : 1350]

Blankout region:
#1: [1319 : 1324]

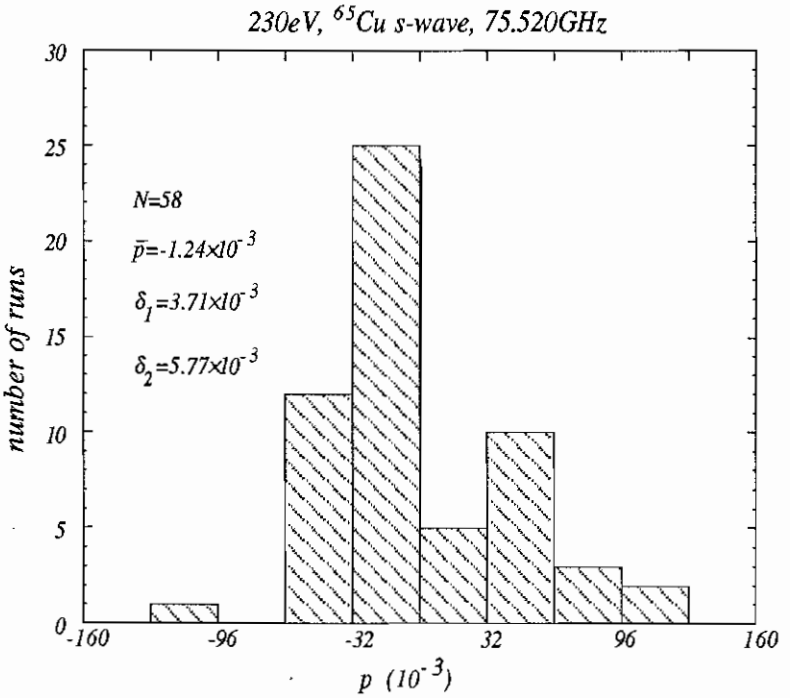

-3.75220E+00
3.93145E+01
1.70234E+03
-8.02548E+04
2.97075E+06
2.55751E+11
1.32969E+03
8.69146E+04
3.40959E+03
7.29579E−01
8.34633E−05
1.21783E−03

Fitting range:
[1316 : 1350]

Blankout region:
#1: [1319 : 1324]

Bibliography

[Abov64] Yu. G. Abov, P. A. Krupchitsky, and Yu. A. Oratovsky: Phys. Lett. **12**,25(1964).

[Abov73] Yu. G. Abov, O. N. Ermakov, and P. A. Krupchitsky: Sov. Phys. –JETP **38**,870(1974); Zh. Eksp. Teor. Fiz. **65**,1738(1973).

[Adel83] E. G. Adelberger, M. M. Hindi, C. D. Hoyle, H. E. Swanson, R. D. Von Lintig and W. C. Haxton: Phys. Rev. **C27**,2833(1983).

[Adel85] E. G. Adelberger and W. C. Haxton: Ann. Rev. Nucl. Part. Sci. **35**,501(1985).

[Ahre82] G. Ahrens, W. Harfst, J. R. Kass, E. V. Mason, M. Schober: Nucl. Phys. **A390**,486(1982).

[Albe72] J. L. Alberi, R. Wilson, and I. G. Schröder: Phys. Rev. Lett. **29**,518(1972).

[Alfi82] V. P. Alfimenkov, S. B. Borzakov, Vo Van Thuan, Yu. D. Mareev, L. B. Pikelner, A. S. Khrykin and E. I. Sharapov: Nucl. Phys. **A398**,93(1983).

[Alfi84] V. P. Alfimenkov: Sov. Phys. Usp. **27**,11(1984); Usp. Fiz. Nauk. **144**,361(1984).

[Balz84] R. Balzer, et al. : Phys. Rev. **C30**,1409(1984).

[Barn78] C. A. Barnes, et al. : Phys. Rev. Lett. **40**,840(1978).

[Ben77] H. Benkoula, J. C. Cavaignae, J. L. Charvet, D. H. Koang, B. Vignon and R. Wilson: Phys. Lett. **71B**,287(1977).

[Bevi69] P. R. Bevington: *Data Reduction and Error Analysis for the Physical Science*, McGRAW-HILL BOOK COMPANY, 1969.

[Bize80] P. G. Bizetti, T. F. Fazzini, P. R. Maurenzig, A. Perego, G. Poggi: Lett. Nuovo Cimento **29**,167(1980).

[Blat54] J. M. Blatt and V. F. Weisskopf: *Theoretical Nuclear Physics*, John Wiley & Sons, second printing.

[Bowm89] C. D. Bowman, J. D. Bowman and V. Yuan: Phys. Rev. **C39**,1721(1989).

[Bowm91] J. D. Bowman, B. Tippens: to be published.

[Cohe89] E. R. Cohen and B. N. Taylor: Physics Today **42** (No. 8, part 2),BG8(1989).

[Dani76] G. V. Danilyan, V. V. Novitskii, V. S. Pavlov, S. P. Borovlev, B. D. Vodennikov, and V. P. Dronyaev: JETP Lett. **24**,345(1976); Pis'ma Zh. Eksp. Teor. Fiz. **24**,380(1976).

[Desp80] B. Desplanque, J. F. Donoghue, B. R. Holstein: Ann. Phys. **124**,449(1980).

[Drag64] D. Draghicescu, V. I. Lushchikov, V. G. Nikolenko, Yu. V. Taran and F. L. Shapiro: Phys. Lett. **12**,334(1964).

[Eadi71] W. T. Eadie, D. Drijard, F. E. James, M. Roos and B. Sadoulet: *Statistical Methods in Experimental Physics*, North-Holland/American Elsevier.

[Earl83] E. D. Earle, A. B. McDonald, E. G. Adelberger, K. A. Snover, H. E. Swanson, et al. : Nucl. Phys. **A396**,221c(1983).

[Egid88] T. Von Egidy, H. H. Schmidt and A. N. Behkami: Nucl. Phys. **A481**,189(1988).

[Else84] K. Elsener, et al. : Phys. Rev. Lett. **52**,1476(1984).

[Feyn58] R. P. Feynman, M. Gell-Mann: Phys. Rev. **109**,193(1958).

[Fort76] M. Forte: ILL Research Proposal 03-03-002 (Grenoble,1976).

[Fort80] M. Forte, B. R. Heckel, N. F. Ramsey, K. Green, G. L. Greene, J. Byrne and J. M. Pendlebury: Phys. Rev. Lett. **45**,2088(1980).

[Frau74] Hans Frauenfelder and Ernest M. Henley: *Subatomic Physics*, Prentice-Hall, Inc. , 1974.

[Fren88] J. B. French et al. : Ann. Phys. (N. Y.) **181**,198(1988).

[Fren89] J. B. French, A. Pandey and J. Smith: in *Tests of Time Reversal Invariance in Neutron Physics*, edited by N. R. Roberson, C. R. Gould and J. D. Bowman, World Scientific,Singapore,1987.

[Garb73] D. I. Garber et al. :*Neutron Cross sections.* BNL-325, third edition volumn 2. National Neutron Cross Section Center, Brookhaven National Laboratory, Upton, New York. Available from National technical Information Service, US Department of Commence, 1973-.

[Goul90] C. R. Gould, D. G. Haase, N. R. Roberson, H. Postma, J. D. Bowman: Int. J. Mod. Phys. **A5**,2181(1990).

[Hale90] G. M. Hale: private communication,1990.

[Jeff63] C. D. Jeffries: *Dynamic Nuclear Orientation*, Interscience Publishers, 1963.

[Keyw73] G. A. Keyworth, J. R. Lemley, C. E. Olsen, F. T. Seibel, J. W. T. Dabbs and N. W. Hill: Phys. Rev. **C8**,2352(1973).

[Knol79] Glenn F. Knoll: *Radiation Detection and Measurement*, John Wiley & Sons, 1979.

[Knya84] V. A. Knyazkov, et al. : Nucl. Phys. **A417**,209(1984).

[Kolo81] E. A. Kolomensky, V. M. Lobashev, A. N. Pirozhkov, L. M. Smotritsky, N. A. Titov and V. A. Vesna: Phys. Lett. **107B**,272(1981).

[Krup87] P. A. Krupchitsky: *Fundamental Research with Polarized Slow Neutrons*, Springer-Verlag,1987.

[Lawr85] G. P. Lawrence, R. A. Hardekopf, A. J. Jason, P. N. Clout and G. A. Sawyer: IEEE Trans. Nucl. Sci. **32**(5),2662(1985).

[Lee56] T. D. Lee and C. N. Yang: Phys. Rev. **104**,254(1956).

[Mace88] R. J. Macek, in *Proceedings of the 10th Meeting of the International Collaboration on Advanced Neutron Sources*, Los Alamos, USA, October 3–7, 1988, edited by D. K. Hyer, p. 91.

[Marq63] D. W. Marquart: Soc. Indust. Appl. Math. **11**,431(1963).

[Mars58] R. E. Marshak,E. C. Sudarshan: Phys. Rev. **109**,1860(1958).

[Masu89] Y. Masuda, T. Adachi, A. Masaike and K. Morimoto: Nucl. Phys. **A504**,269(1989).

[Mcla88] V. McLane, C. L. Dunford, P. F. Rose: *Neutron Cross Sections*, Volume 2, Academic Press, Inc. ,1988.

[Mich64] F. C. Michel: Phys. Rev. **B133**,329(1964).

[Moxo89] ENDF/B-VI preliminary data file for ^{238}U (National Nuclear Data Center, Brookhaven National Laboratory, Upton, NY, July, 1989), resonance evaluation by M. Moxon.

[Mugh84] S. F. Mughabghab: *Neutron Cross Sections*, Volumn 1, part B, ACADEMIC PRESS, INC. , 1984.

[Nagl79] D. E. Nagle, J. D. Bowman, C. Hoffmann, J. L. Mckibben, and R. E. Mischke: *Proc. 3rd Int. Symp. on High Energy Physics with Polarized Beams and Polarized Targets*, Argonne, 1978. AIP conf. proc. **51**,24(1979).

[Perk87] D. H. Perkins: *Introduction to High Energy Physics*, third edition, Addison-Wesley Publishing Company, Inc. ,1987.

[Russ88] G. J. Russell, J. S. Gilmore, H. Robinson, G. L. Legate, A. Bridge, R. J. Sanchez, R. J. Brewton, R. Woods and H. G. Hughes, III: "LANSCE target system performance", ICANS-X, em Proceedings of the 10th meeting of the international collaboration on advanced neutron sources, Los Alamos, USA, October 3–7, 1988, edited by D. K. Hyer, p. 483.

[Saku84] J. J. Sakurai: *Advanced Quantum Mechanics*, Benjamin/Cummings Publishing Company, Inc. ,10th printing,1984.

[Snov78] K. A. Snover, R. Von Lintig, E. G. Adelberger, H. E. Swanson, T. A. Trainor: Phys. Rev. Lett. **41**,145(1978).

[Stod64] L. Stodolsky: Phys. Lett. **B50**,352(1974).

[Sush80] O. P. Sushkov and V. V. Flambaum: JETP lett. **32**,352(1980); Pis'ma Zh. Eksp. Teor. Fiz. **32**,377 (1980).

[Sush82] O. P. Sushkov and V. V. Flambaum, Sov. Phys. Usp. **25**,1(1982); Usp. Fiz. Nauk. **136**,3(1982).

[Szym90] J. J. Szymanski: private communication.

[Vanh88] J. R. Vanhoy, E. G. Bilpuch, J. F. Shriner, Jr. and G. E. Mitchell: Z. Phys. **A331**,1(1988).

[Weas77] R. C. Weast: *Handbook of Chemistry and Physics*, (57th edition, 1976–1977), CRC press.

[Weid88] O. Bohigas and H. A. Weidenmüller: Ann. Rev. Nucl. Part. Sci. **38**,421(1988).

[Weid89] H. A. Weidenmüller: in *Fundamental Symmetries in Nuclei and Particles*, World Scientific, edited by H. Henrikson and P. Vogel, p. 30.

[Wend90] S. A. Wender: private communication.

[Wilk58] D. H. Wilkinson: Phys. Rev. **109**,1603(1958).

[Wils63] Richard Wilson: *The Nucleon-Nucleon Interaction*, INTERSCIENCE PUBLISHERS, 1963.

[Wu57] C. S. Wu, E. Ambler, R. W. Hayward, D. D. Hoppes, R. P. Hudson: Phys. Rev. **105**,1413(1957).

[Yuan91] to be published in Physical Review.

BIOGRAPHY

Xianzhou (Joe) Zhu

Birth: February 4, 1966. Hubei Province, China

Education: M. A. Duke University,
Durham, North Carolina, 1987

B. S. Peking University,
Beijing, China, 1985

Positions: Research Assistant, Duke University, 1986-1991
Teaching Assistant, Duke University, 1985-1986

Membership: American Physical Society

Papers

1. Parity Non-Conservation for Neutron Resonances in ^{238}U, J. D. Bowman, C. D. Bowman, J. E. Bush, P. P. J. Delheij, C. M. Frankle, C. R. Gould, D. G. Haase, J. Knudson, G. E. Mitchell, S. Penttila, H. Postma, N. R. Roberson, S. J. Seestrom, J. J. Szymanski, B. Tippens, V. W. Yuan and X. Zhu: Phys. Rev. Letts. **65**, 1192(1990)

2. Parity Non-Conservation in Polarized Neutron Transmission Through ^{139}La, V. W. Yuan, C. D. Bowman, J. D. Bowman, J. E. Bush, P. P. J. Delheij, C. M. Frankle, C. R. Gould, D. G. Haase, J. Knudson, G. E. Mitchell, S. Penttila, H.

Postma, N. R. Roberson, S. J. Seestrom, J. J. Szymanski, B. Tippens and X. Zhu: (to Be Submitted to Physical Review)

3. Current Mode Detector for Neutron Time-of-Flight Studies, J. D. Bowman, J. J. Szymanski, V. W. Yuan, C. D. Bowman, A. Silverman, and X. Zhu: Nuclear Instruments and Methods in Physics Research **A297**,183(1990).

4. Fundamental Symmetry Studies at Los Alamos using Epithermal Neutrons, C. D. Bowman, J. D. Bowman, V. W. Yuan, P. Herczeg, J. Szymanski, R. N. Mortenson, J. M. Amaya, H. Postma, P. P. J. Delheij, O. K. Baker, C. R. Gould, D. G. Haase, G. E. Mitchell, N. R. Roberson, X. Zhu, A. B. McDonald, K. P. Coulter, D. Benton, B. Tippens and T. E. Chupp: in *Fundamental Symmetries and Nuclear Structure*, edited by J. N. Ginocchio and S. P. Rosen,World Scientific, Singapore, 1989, p. 1

5. Fast Transient Neutron Diffraction at LANSCE, C. D. Bowman, S. J. Seestrom, S. A. Wender, R. Richardson, V. W. Yuan, O. A. Wasson, X. Zhu, H. G. Priesmeyer, P. A. Egelstaff: (To be presented at International Conference on Neutron Scattering, B. A. R. C,1991)

6. Studies of Parity and Time Reversal Symmetries in Neutron Scattering from ^{165}Ho, D. G. Haase, C. R. Gould, J. E. Koster, N. R. Roberson, L. W. Seagondollar, J. P. Soderstrum, M. B. Schneider and X. Zhu: Hyperfine Interactions **43**, 133 (1988)

7. Facility for Parity and Time Reversal Experiments with Intense Epithermal (eV) Neutron Beams, C. D. Bowman, J. D. Bowman, P. Herczeg, J. Szymanski, V. W. Yuan, J. M. Anaya, R. Mortensen, H. Postma, P. P. J. Delheij, O. K. Baker, C. R. Gould, D. G. Haase, G. E. Mitchell, N. R. Roberson, X. Zhu, A. B. McDonald, D. Benton, B. Tippens and T. E. Chupp: Hyperfine Interactions **43**, 119 (1988)

Contributed Abstracts/Talks Presented

1. Parity Violation Matrix Elements for Neutron Resonances in ^{239}U, X. Zhu, N. R. Roberson, J. E. Bush, C. M. Frankle, C. R. Gould, D. G. Haase, G. E. Mitchell, C. D. Bowman, J. D. Bowman, J. Knudson, S. Penttila, S. J. Seestrom, J. J. Szymanski, V. W. Yuan, P. P. J. Delheij, H. Postma and B. Tippens: Bull. Am. Phys. Soc. 35,1039(1990)

2. Data Acquisition System for Fundamental Symmetries Studies with Epithermal Neutrons, Xianzhou Zhu, N. R. Roberson and C. R. Gould, Bull. Am. Phys. Soc. **33**, 2194 (1988)

Co-authored Abstracts

1. Polarized Epithermal Neutron Beam Facility at LANSCE, C. M. Frankle, J. E. Bush, C. R. Gould, D. G. Haase, G. E. Mitchell, C. D. Bowman, J. D. Bowman, J. Knudson, S. Penttila, S. J. Seestrom-Morris, J. J. Szymanski, V. W. Yuan, N. R. Roberson, X. Zhu, P. P. J. Delheij, H. Postma and B. Tippens: Bull. Am. Phys. Soc. **34**, 2360 (1989)

2. Polarization of the LANSCE Epithermal Neutron Beam, J. E. Bush, C. M. Frankle, C. R. Gould, D. G. Haase, G. E. Mitchell, C. D. Bowman, J. D. Bowman, J. Knudson, S. Penttila, S. J. Seestrom-Morris, J. J. Szymanski, V. W. Yuan, N. R. Roberson, X. Zhu, P. P. J. Delheij, H. Postma and B. Tippens: Bull. Am. Phys. Soc. **34**, 2360 (1989)

3. A Cryostat for Testing Time Reversal Invariance in Aligned Holmium, J. E. Koster, C. R. Gould, D. G. Haase, N. R. Roberson and X. Zhu: Bull. Am. Phys. Soc. **33**, 1589 (1988)

4. Beam Line for Study of Fundamental Symmetries at LANL, O. K. Baker, D. Benton, C. D. Bowman, J. D. Bowman, T. Chupp, P. P. J. Delheij, C. R. Gould, D. G. Haase, A. B. McDonald, G. E. Mitchell, H. Postma, N. R. Roberson, J. Szymanski, B. Tippens, V. Yuan and X. Zhu: Bull. Am. Phys. Soc. **33**, 2194 (1988)

5. Compound nuclear contributions to spin-spin cross section, J. Koster, C. R. Gould and X. Zhu: Bull. Am. Phys. Soc. **31**,1763(1986)